Microstructure, crystallography and stable isotope composition of *Crassostrea gigas*

Joanne MacDonald
B.Sc. (Hons) University of Glasgow

Thesis submitted for Degree of Doctor of Philosophy

School of Geographical and Earth Sciences
School of Chemistry
College of Science and Engineering
University of Glasgow

September 2011

Abstract

Many marine molluscs produce complex shells of calcium carbonate. These shells are formed under strict biological control to provide a range of functions to ensure the survival of the living organism. These inspiring biomineral structures can also provide an archive of environmental change via proxies such as $\delta^{18}O$ and $\delta^{13}C$ within the shell carbonate. However, the intimate relationship between the biological and environmental controls influencing biomineral production can often obscure the environmental signal, making it difficult to interpret environmental information from shell proxies. Understanding the design of biomineral structures will further our knowledge of biomineralisation as a whole, while understanding the controls that influence shell production will ensure that shell proxies applied to palaeoenvironmental studies are accurate.

Oysters are sessile bivalve molluscs that have evolved since the Triassic and expanded to occupy a range of habitats with almost global distribution, providing an example of a highly successful biomineral system. This study investigates the ultrastructure, crystallography and stable isotope composition of the Pacific oyster, *Crassostrea gigas* from estuarine and marine environments. The method by which oysters adhere to hard substrates is also investigated.

Both valves of the oyster shell are composed predominantly of low Mg calcite in three forms; an outer prismatic region, an inner foliated structure and chalk lenses which appear sporadically throughout the valves. Aragonite is restricted to the myostracum and parts of the hinge structure. Crystallographic analysis shows that, despite variations in structural morphology, the superimposed layers of the oyster shell maintain a single crystallographic orientation with the crystallographic c-axis orientated perpendicular to the outer shell surface. Varying crystal morphology, while maintaining crystallographic unity, may be a deliberate design to provide the oyster shell with both strength and flexibility.

In general, there is no difference in the overall ultrastructure or microstructural arrangement of estuarine and marine oysters. Estuarine oysters contain significantly more chalk than marine equivalents suggesting that the appearance

of chalk lenses is, to some degree, triggered by an external environmental stimulus.

Stable carbon and oxygen isotope analysis of folia and chalk provides further insights into the appearance of chalk in the oyster shell structure. There is no significant difference in the isotope composition of folia or chalky layers, although patterns of $\delta^{13}C$ and $\delta^{18}O$ of folia and chalk reveal key differences between the two structures. Folia display a narrower range of $\delta^{18}O$ values compared with chalk and exhibit significant interspecimen variation with respect to $\delta^{13}C$. Interspecimen variation, with respect to either $\delta^{18}O$ or $\delta^{13}C$ is absent in chalk samples. These patterns suggest that secretion of folia requires a more specific environmental stimulus and a greater input of metabolic carbon than chalk. Chalk is apparently secreted across a greater range of environmental conditions, with less metabolic regulation. Deviation from optimal environmental conditions, for example during periods of reduced salinity and/or cold or warm temperatures, may reduce metabolism causing the oyster to deliberately default from folia to chalk secretion. In general, folia and chalk in both estuarine and marine oysters is secreted in oxygen isotope equilibrium with the ambient environment.

Another aspect of the oyster biomineral system is their ability to adhere tightly, and usually permanently, to a range of hard substrates by cementation of the left valve. Investigation of the contact zone between oyster shells and biological (other oyster shells) and inorganic (rock) substrates reveals the influence of both biogenic and non-biogenic processes in oyster cementation. Original adhesion is brought about by secretion of an organic adhesive which acts as a nucleating surface onto which crystals precipitate which have random orientation and are composed of high Mg calcite. The lack of orientation and elevated Mg content suggests that these crystals are nucleating outwith the biological control experienced by the shell biomineralisation process and are formed from inorganic precipitation from seawater. It is proposed that oysters do not control, or secrete, the crystalline cement but instead they secrete an organic film onto which crystals precipitate from seawater. Oysters thus provide excellent examples of both biologically induced and biologically controlled mineralisation.

Table of Contents

Abstract I

Table of Contents III

List of Figures VII

List of Tables X

Acknowledgements XI

Declaration XIII

Chapter 1. Introduction 1

1.1 Biomineralisation 1
1.1.1 Biomineralisation in class Bivalvia (Phylum Mollusca) 3
1.1.1.1 Biomineral growth 5
1.2 Oysters 6
1.2.1.1 Crassostrea gigas 7
1.2.2 Oyster shell structure 7
1.2.2.1 Calcite prisms 9
1.2.2.2 Foliated calcite 10
1.2.2.3 Chalky calcite 11
1.3 Biominerals as environmental proxies 13
1.3.1 Oxygen isotopes 14
1.3.2 Carbon isotopes 16
1.4 Influence of environment on biominerals 19
1.5 Attachment mechanisms of marine organisms 20
1.5.1 Attachment mechanisms of bivalves 21
1.5.1.1 Byssal attachment 22
1.5.1.2 Cementation 22
1.6 Aims of this study 23

Chapter 2. Materials and methods 26

2.1 Specimen collection 26
2.1.1 Loch Fyne environmental setting 26
2.1.2 Loch Tuath environmental setting 29
2.1.3 Attached samples 32
2.1.3.1 Oyster-oyster attachment 32
2.1.3.2 Oyster-rock attachment 33
2.2 Sample preparation 35
2.2.1 Preparation of estuarine and marine samples 35
2.2.2 Cross sections 36
2.2.3 Growth line analysis 37
2.2.4 Fracture blocks 38
2.2.5 Resin blocks 40
2.2.6 Thin sections 41

2.2.7 Hinge sections 42
2.2.8 Preparation of attached samples 44
2.2.8.1 Oyster-oyster attachment 44
2.2.8.2 Oyster-rock attachment 46
2.3 Analytical techniques 48
2.3.1 Image analysis using Image J 48
2.3.2 Scanning electron microscopy 49
2.3.2.1 Secondary electron imaging 49
2.3.2.2 Backscattered electron imaging 50
2.3.3 Energy dispersive spectroscopic (EDS) elemental analysis 50
2.3.3.1 Quantitative analysis 50
2.3.3.2 Qualitative spot analysis and elemental mapping 52
2.3.4 Electron backscatter diffraction (EBSD) 53
2.3.4.1 EBSD technique 53
2.3.4.2 EBSD data analysis and representation 55
2.3.5 Raman spectroscopic analysis 57
2.3.5.1 Raman spectroscopy technique 58
2.3.5.2 Raman data analysis and representation 58
2.3.6 Isotopic analysis 59
2.3.6.1 Sample preparation for isotopic analysis 59
2.3.6.2 Mass spectrometry 61
2.3.6.3 Oxygen isotope analysis of Loch Tuath seawater sample 62
2.3.6.4 Isotopic equilibrium calculations 63
2.3.7 Statistical analysis 64
2.3.7.1 Student T-test 64
2.3.7.2 Two way analysis of variance (ANOVA) 64
2.3.7.3 Pearsons correlation coefficient 65

Chapter 3. Microstructure, chemistry and crystallography of *Crassostrea gigas* 66

3.1 Introduction 66
3.1.1 Oyster shell structure, previous work 67
3.1.2 Effect of environment on oyster shell structure 69
3.1.3 Aims of this study 70
3.2 Results 70
3.2.1 Physical characteristics of shells of estuarine and marine oysters 70
3.2.2 Macrostructure of shells of estuarine and marine oysters 72
3.2.3 Quantitative imaging analysis 74
3.2.4 Microstructure 75
3.2.4.1 Prisms 76
3.2.4.2 Foliated structure 80
3.2.4.3 Chalky lenses 83
3.2.4.4 Chalk morphology 84
3.2.5 Myostracum 88
3.2.6 Hinge region 89
3.2.6.1 Hinge region of the right valve 90
3.2.6.2 Hinge region of the left valve 92
3.2.7 SEM imaging analysis of cavities in marine samples 95
3.3 Chemistry 97
3.3.1 Chemical variation throughout three calcite microstructures 97
3.4 Crystallography 102

3.4.1 Crystallography of the prisms 102
3.4.2 Crystallography of the foliated structure 103
3.4.3 Crystallography of chalky lenses 106
3.4.4 Myostracum 108
3.4.5 Hinge region 109
3.4.5.1 Crystallography of the hinge region of the right valve 109
3.4.5.2 Crystallography of the hinge region of the left valve 112
3.5 Discussion 115
3.5.1 Comparison of estuarine and marine *Crassostrea gigas* 115
3.5.2 Cavities in marine *C. gigas* 116
3.5.3 Thick valves and reduction of chalk in marine *C. gigas*. 117
3.5.4 Microstructure, crystallography and chemistry of *C. gigas* 118
3.5.4.1 Functional morphology of oyster shell structure 119
3.6 Summary 124

Chapter 4. Stable isotope composition of estuarine and marine *Crassostrea gigas*. ... 126

4.1 Introduction 126
4.1.1 The stable isotope signature of oyster shells - previous studies 127
4.1.2 Aims of this study 130
4.2 Results 130
4.2.1 Carbon and oxygen isotope composition of estuarine *C. gigas*. 131
4.2.2 Carbon and oxygen isotope composition of marine *C. gigas*. 135
4.2.3 Comparison of the stable isotope signature of estuarine & marine *C. gigas*. 139
4.3 Discussion 143
4.3.1 Stable isotope composition of *C. gigas* 143
4.3.2 Through-valve stable isotope trends 146
4.3.3 Effect of environment on shell isotope signature. 146
4.3.4 Isotopic equilibrium and implications for palaeoclimatic studies. 148
4.3.4.1 Estuarine oysters 148
4.3.4.2 Marine oysters 150
4.4 Summary 153

Chapter 5. Attachment of oysters to natural substrata 155

5.1 Introduction 155
5.1.1 Cementation of oysters and other bivalves - previous studies 156
5.1.2 Aims of this study 158
5.2 Results 159
5.2.1 Ultrastructure of the contact zone 160
5.2.1.1 Temporal distribution of materials 163
5.2.2 Chemistry of the contact zone 165
5.2.2.1 Raman spectroscopic analysis 168
5.2.3 Crystallography of crystalline cement 169
5.2.4 Effect of cementation on shell structure 172
5.3 Discussion 174
5.3.1 Method of attachment 174
5.3.2 Marine cementation 176
5.3.3 Source of organic glue 177
5.3.4 Composition of organic glue 178
5.4 Summary 181

Chapter 6. Conclusions and discussion 183

6.1 Aims of this project 183
6.1.1 *Crassostrea gigas* samples and environments 184
6.2 Shell structure and stable isotope composition of *C. gigas* 184
6.2.1 Effect of environment on shell structure and stable isotope composition 186
6.2.1.1 Appearance of chalky lenses 187
6.3 Attachment mechanism of oysters 189
6.4 Future work 190
6.4.1 Shell structure and stable isotope composition 190
6.4.2 Cementation of bivalves 191

Appendix A 192

A.1 List of samples and valve dimensions 192
A.2 Cemented Samples 194

Appendix B EDS standardised analysis: List of standards 195

Appendix C Stable isotope results 196

List of References 203
Peer reviewed publications from this thesis 224

1. Alignment of crystallographic c-axis throughout the four distinct microstructural layers of the oyster *Crassostrea gigas*

2. Attachment of oysters to natural substrata by biologically induced marine carbonate cement

List of Figures

Chapter 1

Figure 1. Diagrammatic representation of typical bivalve shell structure and calcifying mantle. 4
Figure 2. The structure of the organic matrix in bivalve shell formation. 5
Figure 3. Inner and outer surfaces of both valves of the oyster shell (*Crassostrea gigas*).....8
Figure 4. Cross section of a typical oyster shell revealing internal microstructural arrangement. 9
Figure 5. SEM images of the prismatic shell structure. 10
Figure 6. SEM images of the foliated shell structure. 11
Figure 7. Details of the chalky calcite present within oyster shell structure. 12
Figure 8. Schematic representation of the main pathways & factors influencing shell carbon. 17
Figure 9. Attachment mechanisms common to epifaunal bivalves. 21

Chapter 2

Figure 10. Collection site of estuarine oyster samples from Loch Fyne Oyster Farm, Loch Fyne. ...27
Figure 11. Daily temperature and salinity values at Loch Fyne Oyster Farm. 28
Figure 12. Collection site of marine oyster samples from Ulva Oyster Farm, Loch Tuath. 30
Figure 13. Monthly seawater temperature at Loch Tuath. 31
Figure 14. Location of collection site of shell-shell cemented samples, La Baule, France. 32
Figure 15. Samples of shell-shell attachment, collected from La Baule, France. 33
Figure 16. Location of collection site of oysters attached to rocks in Linne Muirich, Loch Sween. .34
Figure 17. Samples of *C. gigas* attached to rock, collected from Linne Muirch, Loch Sween. 35
Figure 18. Representation of the three principle dimensions measured on all samples. 36
Figure 19. Preparation and position of valve cross sections. 37
Figure 20. Treatment of valve cross section for analysis of incremental growth lines. 38
Figure 21. Preparation of fracture shell sections for analysis by SEM imaging. 39
Figure 22. Preparation of valve hinge sections for analysis.....43
Figure 23. Preparation of samples of oyster-oyster attachment for analysis. 45
Figure 24. Preparation of samples of oyster-rock attachment. 47
Figure 25. Quantification of valve composition by cross section image analysis using Image J. 49
Figure 26. Representative example of EDS spot analysis data. 51
Figure 27. Representative example of EDS elemental mapping data.....52
Figure 28. Details of SEM chamber setup for EBSD analysis. 54
Figure 29. Crystallographic orientation colour keys for calcite and aragonite. 56

Figure 30. EBSD data as stereographic pole plots. 57
Figure 31. Analysis of Raman spectroscopic data. 59
Figure 32. Preparation of samples for isotopic analysis. 60

Chapter 3

Figure 33. Diagrammatic representation of the structural components of *C. gigas*. 68
Figure 34. Schematic section of the hinge of the oyster. 68
Figure 35. Comparison of *C. gigas* from estuarine & marine environments. 73
Figure 36. Quantification of chalk, folia and cavity distribution in shell cross sections. 75
Figure 37. SEM image of a fractured shell section revealing the prismatic layer. 76
Figure 38. SEM images of fracture sections revealing details of the prismatic layer. 78
Figure 39. SEM image of the transition zone between prismatic region and foliated structure. 80
Figure 40. SEM images revealing details of the foliated structure. 81
Figure 41. 3D model of foliated structure showing alternating lath orientation. 82
Figure 42. Optical microscopy images revealing distribution and shape of chalky lenses. 83
Figure 43. SEM images revealing structural components of chalky lenses. 84
Figure 44. Comparison of the amont of void space in chalky lenses within right & left valves. 86
Figure 45. SEM images of the interface between chalky and foliated microstructures. 87
Figure 46. SEM images of fracture shell sections revealing details of the myostracum. 89
Figure 47. Diagrammatic representation of the hinge region of the right valve. 90
Figure 48. SEM images of the hinge region of the right valve hinge region 92
Figure 49. Diagrammatic representation of the hinge region of the left valve. 93
Figure 50. SEM images of the hinge region of the left valve. 94
Figure 51. SEM images of cavities in marine specimens of *C. gigas.* 96
Figure 52. Elemental maps showing distribution of elements within a chalk lens. 99
Figure 53. Typical EBSD crystallographic orientation map of prismatic structure. 102
Figure 54. Typical EBSD crystallographic orientation map of foliated structure. 104
Figure 55. Crystal orientation within laths of type 1 and type 2 orientation. 105
Figure 56. Crystallographic orientation in foliated structure where laths are inclined. 106
Figure 57. EBSD crystallographic orientation of chalk lenses. 107
Figure 58. EBSD crystallographic orientation of the myostracum. 108
Figure 59. Crystallography of the structural components of the hinge region of the right valve. .111
Figure 60. Crystallography of the structural components of the hinge region of the left valve. ...113
Figure 61. Summary of crystallography of the mineralised parts of the hinge. 115
Figure 62. Summary diagram of the ultrastructure and crystallography of *C. gigas.* 125

Chapter 4

Figure 63. Valve division from hinge to ventral margin for isotopic analysis. 130
Figure 64. $\delta^{18}O$ – $\delta^{13}C$ cross plot of all isotopic data obtained for estuarine *C. gigas.* 132
Figure 65. $\delta^{18}O$ – $\delta^{13}C$ cross plot of the mean values of replicate samples for estuarine *C. gigas*.134
Figure 66. $\delta^{18}O$ – $\delta^{13}C$ cross plot of the mean isotope values obtained from estuarine *C. gigas,* where any individual effect has been removed.....135
Figure 67. $\delta^{18}O$ – $\delta^{13}C$ cross plot of all isotopic data obtained for marine *C. gigas.* 136
Figure 68. $\delta^{18}O$ – $\delta^{13}C$ cross plot of the mean values of replicate samples for marine *C. gigas.* ...138
Figure 69. $\delta^{18}O$ – $\delta^{13}C$ cross plot of the mean isotope values obtained from marine *C. gigas,* where any individual effect has been removed.....139
Figure 70. $\delta^{18}O$ – $\delta^{13}C$ cross plot of all estuarine and marine isotopic data for comparison. 140
Figure 71. $\delta^{18}O$ – $\delta^{13}C$ cross plot of all estuarine and marine isotopic data for comparison, removing individual effects.....141
Figure 72. Profile of $\delta^{13}C$ and $\delta^{18}O$ throughout the height of the oyster valve. 142
Figure 73. Isotopic temperatures calculated from $\delta^{18}O$ values of estuarine samples. 148
Figure 74. $\delta^{18}O$ – $\delta^{13}C$ cross plot of marine *C. gigas* data with salinity effects.....151
Figure 75. Isotopic temperatures calculated from $\delta^{18}O$ values of marine samples. 152

Chapter 5

Figure 76. Samples of cemented oysters analysed in this study. 159
Figure 77. SEM images revealing details of the crystalline cement. 161
Figure 78. SEM images revealing details of the organic glue. 162
Figure 79. Temporal sectioning of the contact zone between aterally attached oyster shells.....163
Figure 80. SEM images of the contract zone progressively from ventral to sections. 165
Figure 81. Elemental distribution maps of shell-shell contact zone. 166
Figure 82. Raman spectroscopic analysis of shell folia and contact zone cement. 169
Figure 83. EBSD analysis across the contact zone of laterally attached oyster shells. 171
Figure 84. Effect of cementation on shell ultrastructure. 173
Figure 85. Schematic diagram detailing the processes leading to cementation in *C. gigas*.....182

List of Tables

Table 1. Average valve dimensions of *C. gigas* from estuarine and marine environments. 71

Table 2. Elemental composition of calcite microstructures of estuarine *C. gigas*. 100

Table 3. Elemental composition of calcite microstructures of marine *C. gigas*. 101

Table 4. Quantitative EDS analysis of $CaCO_3$ and $MgCO_3$ composition of shell and cement.....168

Acknowledgements

This project was funded by a BBSRC Doctoral Training Award for which I am very grateful.

Thank you to Prof. Maggie Cusack and Dr Andy Freer who supervised this project and provided many great discussions over the past three years. Special thanks to Andy for reading and re-reading this thesis and picking up all those z's!! Additional supervision was provided by Prof. Tony Fallick at the Scottish Universities Research Centre (SUERC), many thanks Tony for all the advice and guidance in the world of isotope geosciences.

Special thanks to the staff at Loch Fyne Oyster Farm and Jamie Howard at Ulva Oyster Farm who provided the samples used in this study and provided seawater temperature and salinity data. Thanks also to Lighthouse Caledonia for providing seawater temperature data for Loch Tuath.

Thanks to Dr Mark Inall at the Scottish Association of Marine Science for providing salinity data for the Tiree Passage and for discussion on salinity. Many thanks to Prof. Martin Lee for help with SEM, EBSD and EDS and for assuring me that some things just are not meant for EBSD! I also thank Dr Colin Braithwaite whose knowledge of carbonate cements has made for many great discussions and contributed greatly to this work. Many thanks to Paula Lindgren for her assistance with Raman spectroscopy.

Considerable mentions go to all the technical staff at the School of Geographical and Earth Science: Les Hill for taking some fabulous pictures of my samples, Peter Chung for help with the SEM and its inevitable malfunction, Robert Macdonald for being able to fix just about anything and for helping to build the fantastic volcano!! Big big thank you to John Gilleece for not only helping with sample preparation and thin sectioning but for proving much needed good banter, laughs and of course for helping to construct the volcano. Thanks also to all the technical staff at SUERC, especially to Terry Donnelly.

Thanks also to Nick for collecting samples and always being on hand to answer random questions and help with sample preparation. I would almost definitely have gone insane if it wasn't for Kate and her constant help with all things Word – thank you!

This PhD has been a journey from start to finish, which I could not have completed without all the fabulous friends I have made in the post grad office. Big thanks go to Dr Clare Torney who set a mighty fine example of how to complete a PhD, livened up

conferences, listened to all my rants and provided great chat on everything from the axis of calcite crystals to weekly shopping lists to wedding dresses! Thanks to Laura for inventing ‘high heel Friday’ and for coordinating office lunches which always brightened up my day! Big thank you to Heidi for teaching me the Queens English, providing great banter and for coming running with me.

Massive thank you to Rachael for taking me on a once in a lifetime trip to Iceland. This provided me with a much needed return to the wonderful world of structural geology, I am now proud to say I know what a palagonite is and can identify it in the field! Thanks also to Rachael and Susan who provided much help with the dreaded adobe illustrator – you definitely need a structural geologist on hand to draw a 3D diagram!!

I would also like to thank everyone else in the office, Rebecca, Penne, Heiko, Mahmood, Bozhi and Ram for putting up with me for the last three years and for always being on hand to help.

Thank you to my dad for completing the near-impossible task of reading this entire thesis front to back, to my mum and Callum for always asking what I was doing so they could at least try and explain it to others and to Laurie for providing great humour and asking the million dollar question – have you not finished it yet??

Biggest thanks of all go to my wee brother for introducing me to the world of statistics, without his help and advice I couldn’t have reached many of the conclusions I have in this thesis. I hate to say it but...Neil you are genius.....

I would never have been able to complete this project without Greg. Thank you so much for putting up with me, listening to my rants (or at least pretending to!), laughing at my rants and for giving me constant support, I absolutely could not have done it without you. Massive thanks also to my dog Elli who, if she could speak, could almost definitely recite this thesis word for word!

Declaration

The material presented in this thesis is the result of three years independent research carried out at the School of Geographical & Earth Sciences and the Scottish Universities Environmental Research Centre. The research was supervised by Prof. Maggie Cusack and Dr Andy Freer. This thesis represents my own research and any published or unpublished work by other authors has been given full acknowledgement in the text.

Joanne MacDonald

Chapter 1. Introduction

1.1 Biomineralisation

The natural world is host to a variety of elaborate biomineral structures, the formation and properties of which have both intrigued and inspired researchers for many decades (e.g. Taylor and Layman 1972, Weiner and Traub 1984, Lowenstam and Weiner 1989, Weiner et al. 2000, Addadi et al. 2006, Cusack and Freer 2008, Lee et al. 2008a).

Since the beginning of the Phanerozoic (542 Ma) many multi-cellular living systems have controlled the secretion of mineralised hard parts to provide a specific function (Dove 2010). Over the course of evolution, organisms of many phyla have refined and perfected the process of biomineralisation facilitating the production of complex biomineral structures, under strict biological control. The diverse array of functions performed by biomineral structures includes internal support and mobility (endoskeletons) (e.g. Dauphin 2002), protection (exoskeletons) (e.g. Addadi et al. 2006), cutting and grinding (teeth, e.g. Evans and Alvarez 1999), sight (Lee et al. 2007), orientation (magnetic receptors, e.g. Faivre and Schüler 2008) and balance (fish otolith, e.g. Shengrong et al. 2011).

Biominerals encompass over 60 different mineral types (Lowenstam and Weiner 1989), with the Ca-bearing minerals, calcium carbonate ($CaCO_3$), calcium phosphate ($Ca_3(PO_4)_2$) and silica by far the most abundant. Within these common biomineral groups there is a distinct vertebrate-invertebrate divide whereby $Ca_3(PO_4)_2$ is responsible for the formation of vertebrate bone while $CaCO_3$ and silica contribute to the skeletal material of most invertebrates (Cusack and Freer 2008). Despite this divide, the close association of mineral phase with organic material, in the form of proteins, polysaccharides and lipids, is common to all biomineral groups. The composite structure of biominerals unites the flexible fracture resistance of organic materials with the hardness of inorganic minerals, resulting in structures with exceptional properties (e.g. Gilbert et al. 2005), many of which have offered inspiration in the design of advanced materials (e.g. Jackson et al. 1988, Lee et al. 2008a, Yoon et al. 2011).

The organic component, although not abundant (typically <5% in mollusc shells, (Marin et al. 2007)), performs a critical role in the mineralisation process, providing a framework which mediates crystal growth, probably from an amorphous precursor (e.g. Lowenstam and Weiner 1989, Marin and Luquet 2005, Addadi et al. 2006, Marin et al. 2007, Pokroy et al. 2007). Organic matrix mediated crystal growth provides strict control over microstructure, crystallographic orientation and chemistry leading to the formation of specialised mineral structures with complex crystal arrangements (e.g. Lowenstam and Weiner 1989, Weiner et al. 2000). The intriguing ability of relatively simple organisms, such as marine invertebrates, to produce exquisite biomineral structures at normal temperatures and pressures has founded a drive to identify the biochemical constituents responsible for mediating crystal growth. Analysis of the organic matrix of many biomineralising organisms has unravelled some of the key proteins and macromolecules involved in crystal nucleation, as well as those that inhibit crystallogenesis, preventing spontaneous crystallisation of the amorphous phase where present; a comprehensive review of which is given in Marin et al. (2007). Most molluscan proteins identified to date are rich in aspartic acid (Asp) which is reported to be critical in controlling mineral formation (Zhang and Zhang 2006). For example, Asp as well as glycine (Gly) are intimately involved in determining the shape and orientation of calcite crystals (Hou and Feng 2006). Acidic proteins are associated with calcium binding, for example Suzuki et al. (2009) report the acidic protein Pif as central to the binding and regulation of aragonite in nacre formation. The most acidic proteins however are associated with calcite structures (Cusack and Freer 2008). For example, Samata et al. (2008) identified a novel, highly acidic 52 kDa protein, in the organic matrix of the calcitic oyster shell, noting the association of the protein with Ca^{2+} binding. Recently, much work has been focussed on the Aspirich proteins, an unusually acidic protein family, which induces and stabilises the formation of amorphous calcium carbonate (ACC) preventing uncontrolled crystallisation in the prismatic shell layer (Politi et al. 2007). Indeed, rigorous analysis of proteins from different shell layers has revealed compositional differences in proteins associated with calcite and aragonite structures, a detailed review of which is given by Zhang and Zhang (2006).

Understanding the complex relationships between individual proteins and the resulting biomineral structure is far from complete. Extraction and analysis of proteins from a variety of species continues to reveal new insights into the biomineralisation process and is essential to advancing controlled crystal growth *in-vitro*.

1.1.1 Biomineralisation in class Bivalvia (Phylum Mollusca)

Molluscs are a diverse phylum of invertebrates including both aquatic and terrestrial forms that have evolved and expanded over 540 million years since their first appearance in the earliest Cambrian (e.g. Marin et al. 2007 and references therein). Most molluscs form shells of $CaCO_3$ for protection with an impressive array of complex biomineral structures reported from across the phylum (e.g. Kobayashi and Samata 2006). Amongst the most intensively studied are the bivalves, on which this study focuses. Bivalves have been at the forefront of biomineralisation research given their ability to form bi-mineralic shells (e.g. Cusack et al. 2007, Cusack and Freer 2008). Many bivalves utilise more than one $CaCO_3$ phase in their shell structure, alternating between calcite and metastable aragonite with apparent ease (Cusack and Freer 2008). In addition, many bivalve shell structures, such as nacre, have attractive mechanical properties as they are both tough and strong yet light (e.g. Jackson et al. 1988, Cusack and Freer 2008). Indeed, bivalve shell structures have been a key interest in many research fields since the early 19^{th} century (e.g. Gray 1833, Bøggild 1930, Watabe and Wilbur 1961, Watabe 1965, Wise and Hay 1968, Taylor et al. 1969, Carter 1990, Checa et al. 2009, Harper et al. 2009, Okumura et al. 2010).

Bivalve shells are complex structures composed of a series of superimposed layers, each with monomineralic composition and unique crystal arrangement (Figure 1). Adjacent layers may alternate between calcite and aragonite. Crystals of each layer are associated with an organic matrix that not only enhances the material properties of the shell layers (e.g. Marin and Luquet 2005) but provides a framework for crystal growth (e.g. Weiner and Traub 1984, Checa et al. 2005, Addadi et al. 2006).

Bivalve shell construction begins with the secretion of the periostracum (Figure 1), a tough organic sheet composed of quinone-tanned proteins (Simkiss and Wilbur 1989). The periostracum acts to seal off the external environment and in doing so creates a minute gap between the inner surface of the periostracum and the mantle (the layer of tissue which covers the visceral mass of the organism and is responsible for shell secretion). In this 'gap', known as the extrapallial (EP) cavity (Figure 1), the building blocks of the shell are secreted from epithelial cells of the mantle in a solution known as EP fluid, and includes both the mineral ions and organic components of the matrix (Marin and Luquet 2005).

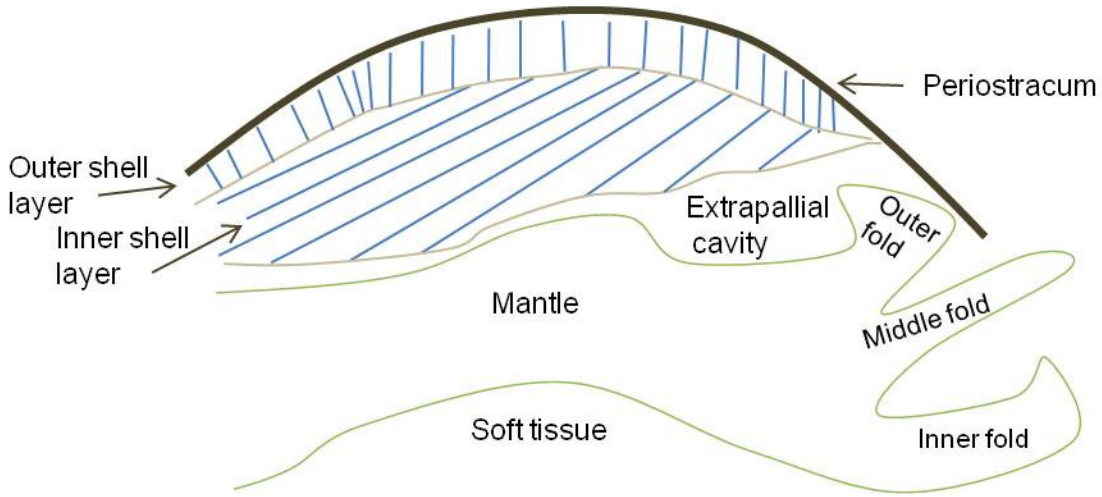

Figure 1. Diagrammatic representation of typical bivalve shell structure and calcifying mantle.
Bivalve shells are composed of a series of superimposed layers, usually two (outer shell layer and inner shell layer). The construction of these layers begins with the secretion of the periostracum. Organic matrix components and mineral ions are secreted in solution, the extrapallial fluid, into the extrapallial cavity from epithelial cells of the mantle. Schematic diagram - not to scale.

The organic matrix forms prior to the mineral phase and is composed of soluble and insoluble components (Figure 2) (Addadi et al. 2006). The soluble component is dominated by acidic macromolecules of mainly acidic sulphated polysaccharides and hydrophilic proteins rich in aspartic acid (Weiner and Traub 1984, Lowenstam and Weiner 1989). These acidic macromolecules are responsible for binding and organising the ions responsible for mineral formation. Indeed, much work has been conducted to uncover the individual proteins responsible for crystal nucleation and polymorph selection (Marin et al. 2007). For example, recently, Ji et al. (2010) reported the dominant 28 kDa protein, isolated from the extrapallial fluid of *Mytilus edulis*, as central to Ca^{2+} binding and subsequent mineral formation. Changes in amino acid composition of

the soluble components are reported to be associated with determining microstructure type by controlling crystallisation (Lee et al. 2009). The insoluble component of the organic matrix is essential to prevent dissolution in the aqueous environment and comprises hydrophobic macromolecules including β-chitin and hydrophobic silk proteins (Addadi et al. 2006). This insoluble complex provides support and spatial control to the mineralised component (Weiner and Traub 1984) and is the main shaping agent in crystal growth (Checa et al. 2005) (Figure 2).

1.1.1.1 Biomineral growth

The stages leading to crystal nucleation and growth have been most intensively studied for the aragonite structure nacre (e.g. Nakahara 1983, Weiner and Traub 1984, Addadi et al. 2006). These studies report that nacre forms on a preformed organic framework from an amorphous calcium carbonate (ACC) precursor (e.g. Marin and Luquet 2005, Pokroy et al. 2007, Cusack and Freer 2008). Addadi et al. (2006) review early observations of nacre formation (e.g. Nakahara 1983) and propose a detailed model of nacre growth. The authors describe the nucleation of nacre crystals on specific nucleation sites composed of acidic proteins, which lie within a silk hydrogel layer rich in glycine (Gly) and alanine (Ala) amino acids, bound by layers of chitin (Figure 2) (Weiner and Traub 1984, Addadi et al. 2006, Nudelman et al. 2007).

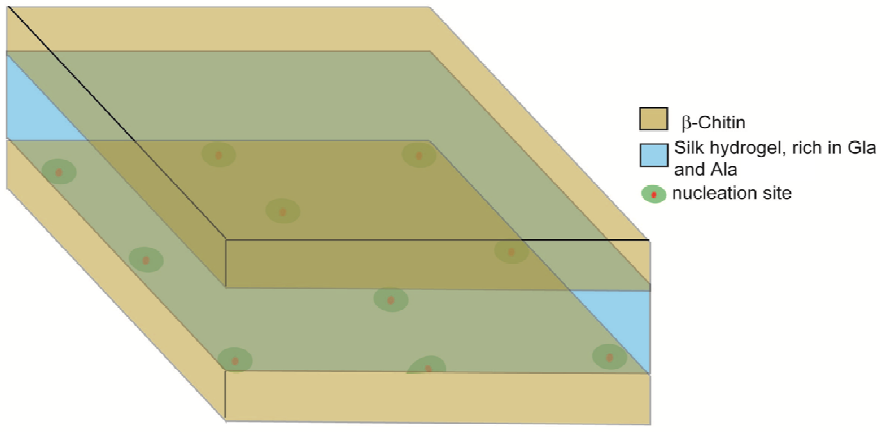

Figure 2. Diagrammatic representation of the structure of the organic matrix in bivalve shell formation (modified after (Addadi et al. 2006).
Model presented represents the organic matrix involved in nacre formation (Addadi et al. 2006) and is exaggerated for clarity. Organic matrix is arranged in a layered structure where a silk hydrogel rich in Gly and Ala amino acids is bound between layers of β-chitin. Within the hydrogel acidic proteins form nucleation sites onto which crystals nucleate and grow.

Addadi et al. (2006) describe transport of the mineral phase, in the form of ACC to the nucleation site where nucleation is induced by, and on, acidic proteins. Chemical and biochemical constituents, namely Mg, P and proteins of the silk gel temporarily stabilise the metastable ACC preventing uncontrolled crystallisation before it reaches the nucleation site (Addadi et al. 2006). Once crystallisation is induced crystals begin to grow by epitaxy on the organic framework (Lowenstam and Weiner 1989). This model describes the formation of nacre and may be applicable to other bivalve shell structures such as calcite prisms however this has yet to be proven.

Mineral growth by classical crystallisation involves the progressive growth or enlargement of a single crystal by unit cell replication (Cölfen and Mann 2003). Recently however, identification of nanocrystals within larger mesocrystal structures (e.g. Okumura et al. 2010) suggests that biominerals grow by non classical crystal growth, whereby nanocrystals are secreted individually, surrounded by organic matrices, and are assembled and fuse to form a mesocrystal structure (Cölfen and Mann 2003). Indeed, complex sub-domains composed of nanocrystals have been identified within individual calcite prisms in *Pinctada margaritifera (Dauphin 2003)*, *Pinctada fucata* (Okumura et al. 2010) and *Crassostrea gigas* (Esteban-Delgado et al. 2008, Checa et al. 2009).

1.2 Oysters

Oysters are amongst the most common and well known bivalves. The true oysters (Order Ostreoida) have provided a critical marine resource since the prehistoric (Yonge 1960) and currently support a global industry worth an estimated $2.8 billion (2004 data, Fisheries and Aquaculture Organisation database). As well as being of considerable economic importance, oysters are amongst the most successful bivalves with a long geological history and almost global distribution. This success is undoubtedly a reflection of their unique shell structure and impressive ability to alter their physiology and biomineralisation regimes to withstand a wide range of environmental conditions. Indeed, since their first appearance in the Triassic (Stenzel 1971), oysters have evolved and expanded to occupy habitats across a wide range of salinities and are present in all continents with the exception of the Antarctic (Yonge 1960).

1.2.1.1 Crassostrea gigas

This study will focus on the oyster *Crassostrea gigas*, the classification of which is given below.

Pacific oyster – *Crassostrea gigas (Thunberg, 1793)*

Phylum – Mollusca

Class - Bivalvia

Order – Ostreoida

Family – Ostreidae

Genus – *Crassostrea*

Species - *gigas*

Crassostrea gigas, commonly known as the Pacific or Japanese oyster, is a sessile suspension feeding bivalve mollusc (e.g. Yonge 1960, Troost 2010). Native to the Pacific coast of Japan, the species has been successfully introduced globally and has become a dominant indigenous animal around the coasts and estuaries of much of northwest Europe, Australia and parts of North America where they thrive as both wild and farmed populations. The dominance and success of *C. gigas* in the many environments in which it has been introduced is a tribute to the physiological adaptability and robust shell characteristics of the species. These phenotypes make *C. gigas* particularly well suited to this study.

1.2.2 Oyster shell structure

The oyster shell is composed of two asymmetrical valves defined as the right (upper) and left (lower) valve (Figure 3). These valves, like those of most bivalves, are a composite of $CaCO_3$ and organic matter (e.g. Watabe and Wilbur 1961, Watabe 1965, Wise and Hay 1968, Taylor et al. 1969, Lowenstam and Weiner 1989, Carter 1990). Calcite, specifically low Mg calcite, is the dominant mineral phase present with aragonite restricted to specialised areas, such as

sites of attachment of the adductor muscle and parts of the hinge structure (e.g. Galtsoff 1964, Stenzel 1971, Carriker et al. 1980).

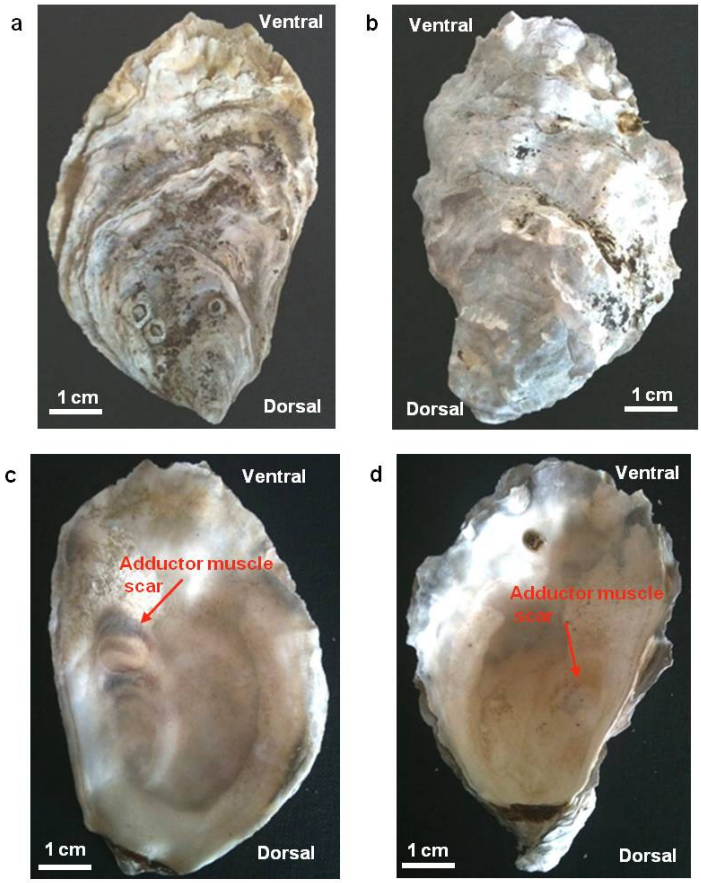

Figure 3. Photographs of the inner and outer surfaces of both valves of the oyster shell (*Crassostrea gigas*).
(a) Outer surface of the right (upper) valve. (b) Outer surface of the left (lower) valve which is larger than the right and is deeply cupped. The outer surface of both valves is cover by a thin periostracum. (c) & (d) show the inner surface of right and left valves respectively.

The periostracum, which provides a nucleation surface for crystal growth, is present on the outer surface of both valves, however can be < 0.5 µm thick and is easily eroded from older shells (Carriker et al. 1980, Harper 1992, Todd 1993). The mineralised part is composed predominantly of low Mg calcite in two forms, namely the prismatic region and foliated structure (Figure 4). The dominant foliated structure may be irregularly interrupted by lenses of porous calcite, termed chalk (Figure 4).

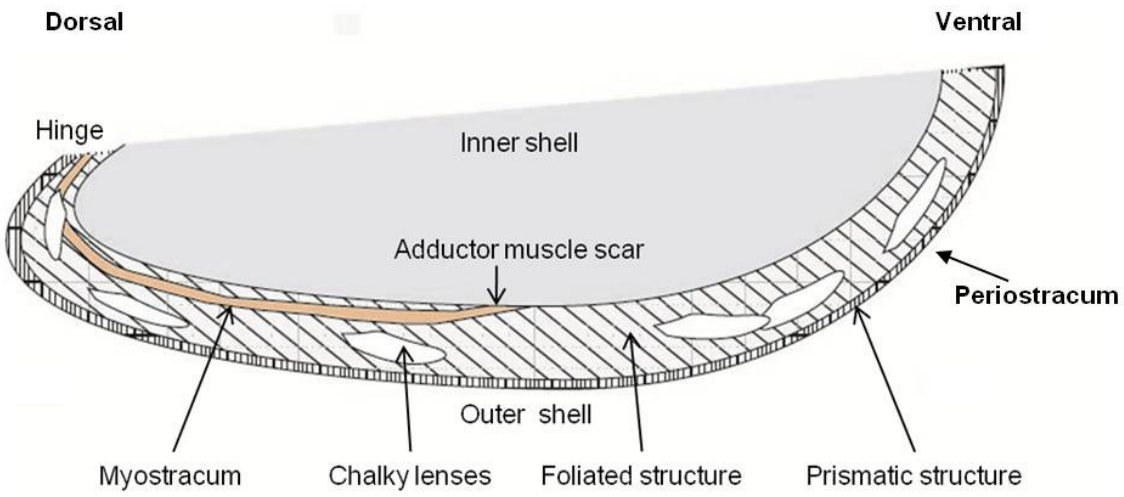

Figure 4. Diagrammatic cross section of a typical oyster shell revealing details of the internal microstructural arrangement.
Both valves are composed predominantly of low Mg calcite in three forms: prismatic structure which directly underlies the periostracum at the outer shell surface. Foliated structure which occupies the bulk of both valves and is frequently interrupted, and occasionally dominated by lenses of chalky calcite. The myostracum is the only significant aragonite structure and attaches the adductor muscle to the shell carbonate.

1.2.2.1 Calcite prisms

The prismatic structure, which occupies the outermost mineralised layer of the oyster, is a common shell structure found in many bivalves (Taylor et al. 1969, Taylor and Layman 1972, Checa et al. 2005, Kobayashi and Samata 2006, Kobayashi 2008, Checa et al. 2009). First reported by (Bøggild 1930), the prismatic structure has been investigated in a number of studies with the mineral phase (e.g. Taylor et al. 1969, Kobayashi and Samata 2006, Esteban-Delgado et al. 2008), organic matrices (Dauphin 2003, Freer et al. 2010, Okumura et al. 2010) and recently the crystallographic texture (e.g. Checa et al. 2005, Checa et al. 2009, Okumura et al. 2010) being discussed. These found the prismatic shell structure to be composed of hexagonal columnar prisms (Figure 5a) surrounded by thick organic sheaths (Figure 5b). Individual prisms are composite structures comprising nanocrystals of uniform orientation in terms of the crystallographic c-axis (Figure 5c) (Esteban-Delgado et al. 2008). Indeed, Okumura et al. (2010) identified a three part hierarchical structure in the prismatic region of *P. fucata*, similar to that described by Dauphin (2003) for *P. margaritifera*, revealing that prisms are composed of several sub-domains each containing sub-grains (<~200 nm) and organic macromolecules. Despite this complex internal structure, mesocrystal prisms generally exhibit crystallographic

properties of a single crystal, with crystallographic c-axis aligned parallel with the long axis of the prism (Checa et al. 2009).

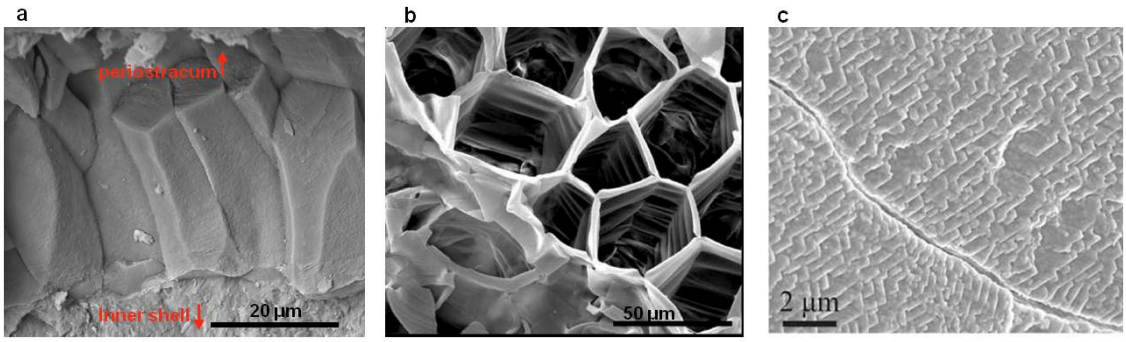

Figure 5. Scanning electron images of the prismatic shell structure.
(a) Backscattered electron SEM image of the prisms of *C. gigas* showing hexagonal morphology. (b) SEM image of decalcified prisms of *Anodonta cygnea* revealing details of the organic sheaths surrounding individual prisms (Image from Freer et al. 2010 Figure 2a). (c) SEM image of the internal surface of the prismatic structure of *C. gigas* revealing details of the composite internal structure of prism mesocrystals (Image from Checa et al. 2009 Figure 2H).

1.2.2.2 Foliated calcite

Foliated calcite occupies the majority of both valves of the oyster and is common in other bivalves such as Pectinidae (Checa et al. 2007a), and is analogous to the cross bladed lamination of the brachiopods (e.g. Schmahl et al. 2004). The foliated microstructure has been defined in many studies (Watabe and Wilbur 1961, Watabe 1965, Wise and Hay 1968, Taylor et al. 1969, Taylor and Layman 1972, Runnegar 1984, Carter 1990, Checa et al. 2007a) as being composed of elongate lath or blade shaped crystals joined laterally to form sheets termed folia (Figure 6a). These sheets are stacked vertically to form the foliated structure. The foliated structure contains significantly less organic material than the overlying prismatic region (Carriker et al. 1980). However, a significant organic component is present at the interface of the folia and underlying myostracum (Lee and Choi 2007). Furthermore, from a detailed study of lath surfaces, Lee et al. (2008b) report that individual laths are surrounded by a discrete layer of nanograins enclosed in a continuous organic membrane.

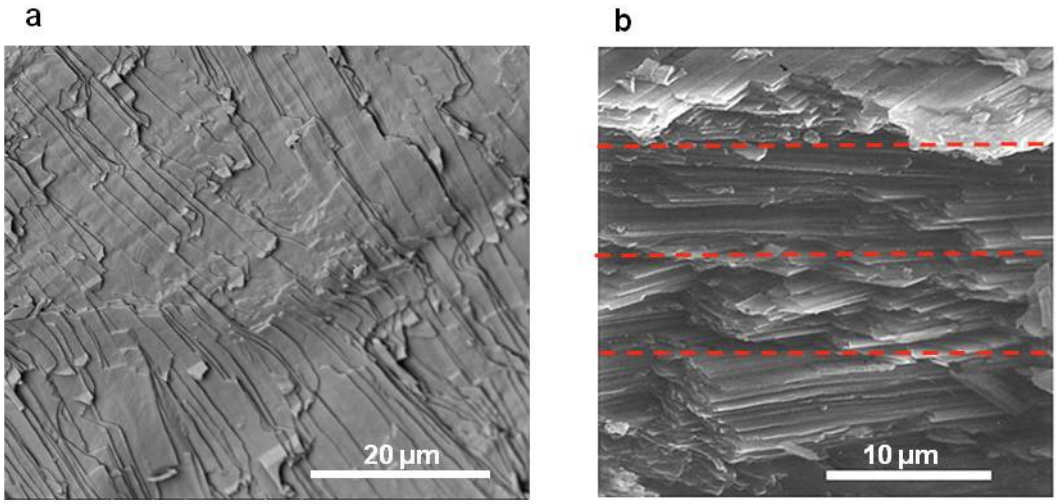

Figure 6. Scanning electron microscope images of the foliated shell structure. (a) Backscattered electron SEM image of the foliated structure of the inner shell, revealing details of the calcite lath arrangement. (b) Cross section SEM image of the foliated structure revealing clusters of laths with alternate morphological orientation (Image modified from Lee et al. 2008a, Figure 3b), red dashed lines highlight lath clusters with alternate morphological orientation.

Checa et al. (2007a) report that the orientation of the crystallographic c-axis within the foliated structure is sub-perpendicular to the elongation of the lath (c-axis tilted back from lath growth front). A similar crystallographic orientation is also noted by Lee et al. (2008a), who report that the crystallographic c-axis has a similar orientation to that of nacre i.e. perpendicular to the shell exterior and laminated layer (Bruet et al. 2005, Freer et al. 2010). However, Lee et al. (2008a) report that the morphological orientation of lath sheets to one of two possible types (Figure 6b), defined as type 1 and type 2. Earlier studies also report lath orientation to be variable (see Checa et al. 2007a for summary), for example Runnegar (1984) defines three types of lath orientation. The complex relationship between lath orientation and crystallographic orientation is still unclear. However it is apparent that these properties, together with those of the surrounding organic matrices (Lee and Choi 2007, Lee et al. 2008b), gives the foliated structure the unique ability to resist fracture by inhibiting crack progression through the shell (Lee et al. 2008a, Lee et al. 2008b).

1.2.2.3 Chalky calcite

The foliated layers of the oyster shell are frequently interrupted and occasionally dominated by lenses of chalky calcite. Although not continuous, these lenses are normal shell structures which appear irregularly throughout both valves (Carriker et al. 1980). These curious shell structures were first

reported by Gray (1833) and have since been described by many authors when investigating oyster shell structure (Galtsoff 1964, Stenzel 1971, Carriker et al. 1980, Harper 1992, Higuera-Ruiz and Elorza 2009). Chalky shell deposits can be identified with the naked eye as porcelain-like patches on the shell (Figure 7a). Internally the chalk is composed of fine blades of calcite from which leaflets branch at varying angles to enclose a system of pores, giving the chalk a characteristic porous structure (Figure 7b).

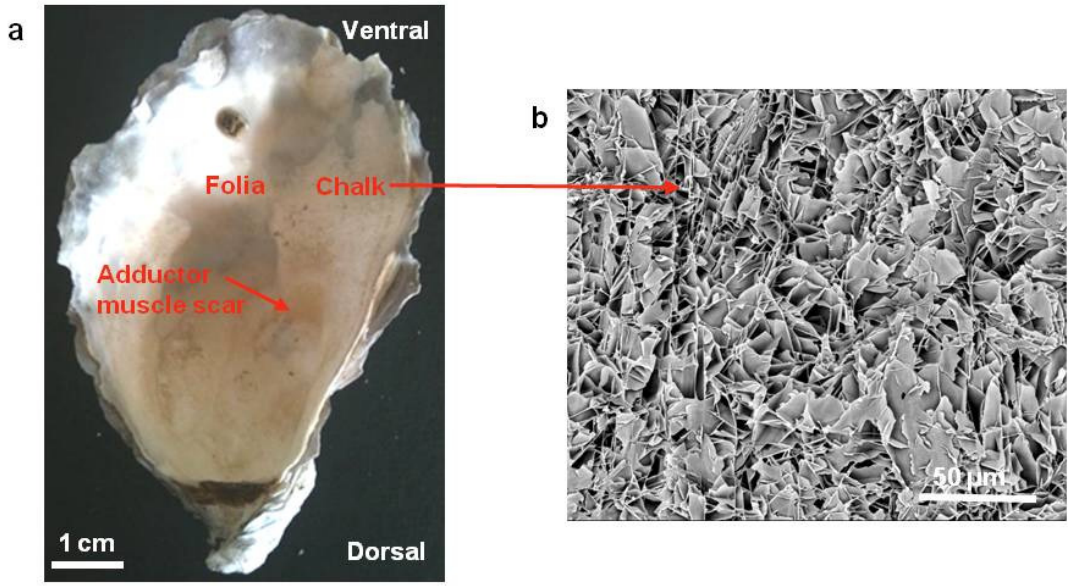

Figure 7. Details of the chalky calcite present within oyster shell structure. (a) Picture of the left valve of *C. gigas* showing white chalky areas and opaque areas comprising folia. (b) Backscattered electron SEM image of the chalk structure revealing internal structure.

Chalk lenses are common in nearly all oysters, certainly those of family Ostreidae, yet the appearance of chalk lenses in other bivalves is rare, suggesting that the ability to produce chalk is largely unique to oysters. Morton and Harper (2001) note the presence of a 'chalk-like' structure in *Cleidothaerus albidus* (Lamarck 1819), however the function of the structure is not elaborated. Many different models have been offered over the last century to explain the distribution and function of these peculiar structures. Orton et al. (1927) suggested that chalky deposits form where the mantle is temporarily detached from the shell. This model was refuted by Korringa (1951) and later by Galtsoff (1964) both of whom demonstrated that detachment of the mantle from the shell was uncommon and when mantle detachment was forced, deposition of chalk was not always evident. Korringa (1951) suggested that chalky deposits were secreted to 'smooth out' the inner shell where irregularities were present.

Chalky material occupies more space than an equal volume of folia (Korringa 1951, Galtsoff 1964, Stenzel 1971, Carriker et al. 1980, Lee et al. 2011) and so, to fill a void, chalk would provide 'cheap padding' as less material per unit volume would be required. Margolis and Carver (1974) suggested that chalky deposits are formed during times of maximum ventilation due to decrease in $CaCO_3$ saturation state. This has been widely disregarded, as a change in saturation would presumably affect the whole surface of the valve and so cannot explain the localised appearance of the lenses (Carriker et al. 1980). The appearance of chalky deposits in some fossil oysters has been attributed to mode of life as an adaption to life on a soft substrate (Komatsu et al. 2002). However, this does not account for the presence of chalk in oysters cemented to a hard substrate where there is no obvious requirement for a 'lightweight shell'. Palmer and Carriker (1979) note variation in the volume of chalk present in oysters grown in different environments. Indeed, prevailing environmental conditions can influence the biomineralisation process in many marine organisms, affecting growth rate and microgrowth patterns (Kanazawa and Sato 2008), mineral production (Lowenstam and Weiner 1989) and shell thickness & density (Palmer and Carriker 1979, Higuera-Ruiz and Elorza 2009). The occurrence of chalk in oysters may be a response to environmental changes, however this hypothesis requires further investigation.

Detailed descriptions of chalk morphology have been given in most studies concerning oyster shell structure (e.g. Palmer and Carriker 1979, Carriker et al. 1980, Higuera-Ruiz and Elorza 2009) though few have focussed on the nature of the chalky lenses and little is known of the crystallography of the structure. As a result, the mode of formation and function of the chalky deposits remains largely enigmatic.

1.3 Biominerals as environmental proxies

Many marine organisms construct exquisite biomineral structures of $CaCO_3$ under strict biological control. The ions from which the mineral phase is formed are incorporated by the organism from the surrounding aqueous environment. As a result, chemical signatures of the mineral can often reflect the environmental conditions at the time of shell formation.

For example, seawater temperature may be recorded via temperature dependant proxies such as $\delta^{18}O$ (e.g. Lowenstam 1961) and Mg/Ca ratio (e.g. Kamenos et al. 2009). Shell $\delta^{18}O$ and $\delta^{13}C$ may also be utilised to determine salinity (e.g. Kirby et al. 1998, Surge et al. 2001) and marine productivity (e.g. Wang et al. 1995), and recently boron has been considered as a proxy of oceanic pH (e.g. Kasemann et al. 2009).

Environmental factors have a major influence on biomineral stable isotope and trace element composition (e.g. Lowenstam and Weiner 1989). However, in many organisms, superimposed on the environmental influence is biological control. Biological or 'vital effects' can modify the isotopic composition and trace element ratio of the shell, such that they are no longer in equilibrium with the ambient environment. In such cases unravelling the complex physiological 'vital' effects and environmental signals can be challenging and can limit the use of marine organisms as environmental proxies. The biological control exerted during bivalve shell secretion can strongly regulate the incorporation of trace elements, specifically Mg, into the shell structure as a means of controlling and modifying biomineral growth (Meldrum and Hyde 2001). As a consequence, the reliability of some trace element proxies from bivalves is limited. For example, physiological impacts on shell Mg/Ca ratios have been observed in *Mytilus edulis* and *Pecten maximus* (Freitas et al. 2008), *Mytilus californianus* (Ford et al. 2010) and *Crassostrea virginica* (Surge and Lohmann 2008). Consequently, the use of bivalves as environmental proxies is mainly focussed on the stable isotopes of oxygen and carbon.

1.3.1 Oxygen isotopes

During the precipitation of calcite from water, oxygen isotopes ($^{18}O/^{16}O$) undergo temperature dependant fractionation whereby the $\delta^{18}O$ of the resulting carbonate is a function of the $\delta^{18}O$ and temperature of the water from which the precipitate was formed. This phenomenon was first reported by Urey (1948), who proposed that the relationship between $\delta^{18}O$ and temperature could enable estimation of ancient seawater temperatures from carbonate $\delta^{18}O$. This aspiration instigated a series of pioneering studies (McCrea 1950, McKinney et al. 1950, Epstein et al. 1951, Epstein et al. 1953, Craig 1957) from which the classic

palaeotemperature scale was developed. Further refinements to this original palaeotemperature technique were made over the following decades as more accurate quantification of the isotopic fractionations involved were realised (O'Neil et al. 1969, Tarutani et al. 1969, Anderson and Arthur 1983, Kim and O'Neil 1997). Ultimately, these developments have enabled palaeoclimatologists to estimate ancient seawater temperatures from carbonates dating back to the Jurassic (e.g. Brigaud et al. 2008).

Biominerals make particularly attractive palaeoclimatic tools as they offer the possibility of detecting fine scale climatic changes, through the presence of annual to seasonal growth lines within the shell carbonate (Lutz and Rhoads 1980, Kirby et al. 1998, Surge et al. 2001, Elliot et al. 2003, Gillikin et al. 2005). However, underpinning the use of biominerals as temperature proxies is the assumption that the carbonate is secreted in oxygen isotope equilibrium with the ambient environment. This critical assumption is complicated by the metabolism of the organism where processes such as calcification, metabolic changes, growth rate and stress can cause unquantifiable kinetic isotope fractionations. Kinetic isotope effects result in depletions in carbonate $\delta^{18}O$ and $\delta^{13}C$, and probably result from kinetic isotope fractionation during calcification (McConnaughey 1989).

The potential problem of isotopic disequilibrium in biomineral carbonate was first noted by Urey (1948) and Epstein et al. (1951), however Lowenstam (1961) was the first to rigorously test the assumption of isotopic equilibrium in shell carbonate. Lowenstam (1961) analysed the $\delta^{18}O$ signatures of modern calcite secreting brachiopods collected from waters where temperature and $\delta^{18}O$ of the seawater had been recorded. Lowenstam reported that the $\delta^{18}O$ values measured from the shell carbonate fell within the expected range for equilibrium and so concluded that fossil brachiopods may be used to determine palaeoenvironmental conditions (on the premise that the shell had not undergone any diagenetic alteration). This influential study prompted similar investigations in molluscs (e.g. Mook 1971, Margolis et al. 1975, Williams et al. 1982, Donner and Nord 1986, Margosian et al. 1987, Aharon 1991, Klein et al. 1996, Rahimpour-Bonab et al. 1997, Chauvaud et al. 2005) and other calcite precipitating organisms such as corals (e.g. McConnaughey 1989) and Foraminifera (Spero and Lea 1993), through which it became apparent that not

all phyla, or indeed all species comply to the equilibrium model. For example, $\delta^{18}O$ disequilibrium as a result of considerable kinetic fractionation during calcification, is widely reported for coral skeletons (Gonzalez and Lohmann 1985, McConnaughey 1989, Aharon 1991, Rahimpour-Bonab et al. 1997). Conversely, many studies report that most molluscs, particularly bivalves, and many brachiopods faithfully record temperature via shell $\delta^{18}O$ (e.g. Lowenstam 1961, Lecuyer et al. 2004, Parkinson et al. 2005, Fan et al. 2011). The absence of kinetic isotope effects in these phyla is thought to result from a lower pH and the presence of carbonic anhydrase at the calcification site which slow the calcification process. However, some cases of isotopic disequilibria have been reported in bivalves (e.g. Krantz et al. 1987) and brachiopods (Lepzelter et al. 1983, Popp et al. 1986). Disequilibrium in these phyla is often further complicated by complex physiological controls that can cause localised kinetic fractionation. Indeed, within single shells, $\delta^{18}O$ may vary between different shell microstructures (Carpenter and Lohmann 1995, Hickson et al. 1999, Owen et al. 2002, Brand et al. 2003, Parkinson et al. 2005), between different valves of a single specimen (Curry and Fallick 2002), and at different ontogenic intervals (Auclair et al. 2003).

1.3.2 Carbon isotopes

Stable carbon isotopes ($^{13}C/^{12}C$) obtained from many marine invertebrates have been utilised as proxies of salinity (e.g. Surge et al. 2001), productivity (e.g. Wang et al. 1995) and as a means of reconstructing organism diet (e.g. Riera and Richard 1997). However, accurate interpretation of the carbon isotope ratios from many organisms, especially bivalves, is challenging. The complex pathways and factors, summarised in Figure 8, that influence the shell carbon isotope ratio make it inherently difficult to isolate and identify the origin of the carbon signal (McConnaughey and Gillikin 2008).

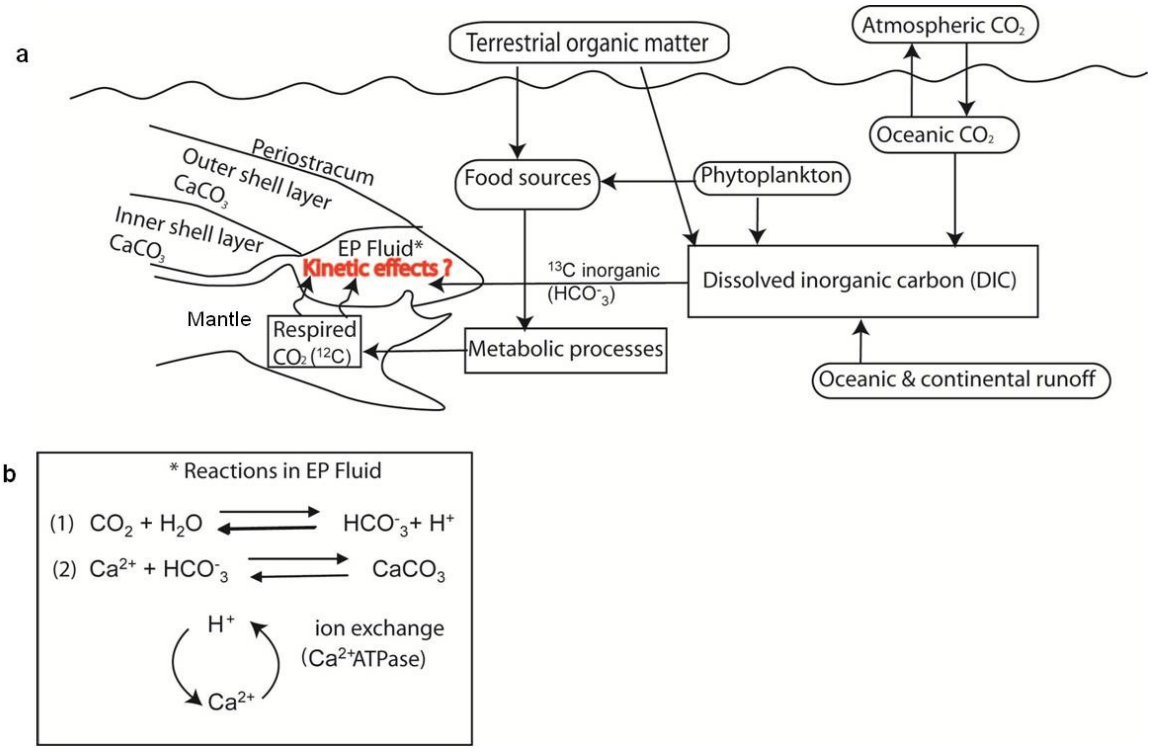

Figure 8. Schematic representation of the main pathways and factors influencing shell carbon.
(a) Main pathways in which dissolved inorganic carbon (DIC) in the form of HCO_3^-, and metabolic carbon respired from food sources in the form of CO_2 enter the EP fluid directly by fluid exchange and by diffusion from the mantle respectively. Both metabolic carbon and DIC undergo a series of reactions, detailed in (b), in the EP fluid to form $CaCO_3$ During this time isotopes may be subject to kinetic isotope fractionations (after McConnaughey et al. 1997, Cusack and Freer 2008, McConnaughey and Gillikin 2008, Lartaud et al. 2010b).

Bivalve shells are composite structures composed of ~95% $CaCO_3$ and ~5% organic material (Lowenstam and Weiner 1989, Zhang and Zhang 2006, Marin et al. 2007). Carbonate ions utilised in the construction of the mineral phase are derived from two principle sources. Inorganic carbon, in the form of bicarbonate ions (HCO_3^-) dissolved in ambient seawater, are incorporated into the calcifying EP fluid by fluid exchange, where they are de-protonated by the alkaline EP fluid (Figure 8b) (McConnaughey and Gillikin 2008). Metabolic CO_2 enters the EP fluid by diffusion from mantle tissues (Figure 8a) where it undergoes hydration and hydroxylation to produce bicarbonate (Figure 8b). The carbon incorporated to the resulting mineral structure is therefore a combination of metabolic and environmental carbon.

Where the inclusion of metabolic carbon is minimal, the $^{13}C/^{12}C$ ratio of shell carbonate will reflect the $^{13}C/^{12}C$ ratio of the ambient dissolved inorganic carbon (DIC) pool. The $^{13}C/^{12}C$ ratio of the DIC pool (Figure 8a) is a function of a number of complex global (long term) and local (short term) processes, the understanding of which can uncover a wealth of environmental information.

Global changes in $\delta^{13}C$ of DIC is controlled by changes in atmospheric and oceanic CO_2 and can fluctuate in response to volcanic degassing, anthropogenic CO_2 release, burial of organic carbon and carbonate and ice volume. Locally, the $^{13}C/^{12}C$ ratio of the DIC pool is affected by marine productivity where photosynthesising organisms, such as phytoplankton, preferentially uptake light ^{12}C leaving the DIC pool relatively enriched in ^{13}C. Decay of phytoplanktonic blooms releases ^{12}C leaving the DIC pool depleted in ^{13}C (Wang et al. 1995). Freshwater input can lower $\delta^{13}C$ by transport of isotopically light terrestrial carbon to the system. Hence, potentially, in the absence of metabolic input, bivalve shell carbon can record changes in the marine DIC pool on a global and local scale.

McConnaughey et al. (1997) considered that > 90% of carbon utilised by aquatic invertebrates is derived from the ambient DIC pool with negligible metabolic influence. Indeed, DIC is the dominant carbon source in many bivalves such as *C. virginica* (Kirby et al. 1998, Surge et al. 2001), and *Aequipecten opercularis* (Hickson et al. 1999). Conversely, Lartaud et al. (2010b) demonstrate that metabolic carbon can account for up to 69% of shell carbon in *C. gigas* and can fluctuate as a function of metabolic rate.

Inclusion of metabolic carbon can suppress the influence of DIC on shell carbon isotope profiles making it difficult to isolate the environmental signal. On the other hand, incorporation of metabolic carbon can reveal insights into the physiological and biomineralisation processes of the organism. For example, Parkinson et al. (2005) demonstrated that $\delta^{13}C$ values in some brachiopod shells show considerable metabolic influence, the extent to which varies dependent upon shell part, suggesting some degree of metabolic prioritisation (Parkinson et al. 2005). In addition, inclusion of metabolic carbon derived from respired CO_2 can provide details of organism diet (e.g. Riera and Richard 1997).

Factors affecting the carbon isotope composition of bivalve shell carbonate are complex and it is clear that both metabolic carbon and inorganic carbon (DIC) influence shell $\delta^{13}C$, which may be further complicated where kinetic isotope effects are also in play.

1.4 Influence of environment on biominerals

Marine organisms produce biomineral structures of $CaCO_3$ under biological control. Prevailing environmental conditions however, can also play a major role in shaping the resulting biomineral structure. The extent to which environmental changes affect biomineralisation is a function of the degree of biological control present (Lowenstam and Weiner 1989).

Seawater temperature, Mg/Ca ratio and PCO_2 are the main controlling factors in determining the polymorph (calcite or aragonite) of inorganic carbonate cements (Burton and Walter 1987). Similarly, in some biological systems including species of cnidarians, arthropods and molluscs, the weight percent of aragonite present is reported to increase with increasing temperature (Lowenstam and Weiner 1989, Table 1.11). Conversely, Neri et al. (1979) reported that shell mineralogy is not controlled by either temperature or salinity and Falini et al. (1996) propose that polymorphism is, in most cases, biologically controlled by macromolecules. Kennedy et al. (1969) also reported genetic factors as the main determinant in bivalve shell mineralogy. Interestingly, (Checa et al. 2007b) reported that increasing Mg concentration can induce aragonite precipitation in some calcite secreting bivalves such as *Ostrea edulis*.

The influence of temperature on shell growth rate and mineral deposition is apparent in most organisms, and many bivalves are unable to mineralise above, or below, a certain temperature range (e.g. Kirby et al. 1998, Hickson et al. 1999, Elliot et al. 2003, Schöne 2008).

Temperature is also reported as the dominant control on trace element, especially Mg, incorporation into biomineral structures and has enabled the use of Mg:Ca ratio as a temperature proxy. Where biological control is present however, the environmental influence on the Mg:Ca ratio can be over-ruled by the physiological processes of the organism (e.g. Freitas et al. 2008). Interestingly, the temperature dependence of $\delta^{18}O$ in biogenic carbonates tends to increase with increasing biological control. For example, in the secondary shell of the brachiopods, which is secreted under strict biological control, $\delta^{18}O$ is a function of temperature. In the primary layer however, which is apparently

secreted faster and under less control, $\delta^{18}O$ is subject to kinetic isotope effects removing the environmental influence on $\delta^{18}O$ (Parkinson et al. 2005).

Energy, predation, salinity, pollution and acidity have all been reported to influence growth rate, shell thickness and structure in a number of organisms (e.g. Kirby 2001, Higuera-Ruiz and Elorza 2009, Beniash et al. 2010). Changes in growth rate and mineral deposition as a response to such stresses can affect the incorporation of trace elements and the isotopic composition of the resulting biomineral structure. Indeed, environmental changes can affect characteristics such as growth rate, polymorph type and mineral abundance which themselves can influence the degree of environmental control, specifically temperature dependence, on trace element concentration and the stable isotope signature of the resulting biomineral structure.

1.5 Attachment mechanisms of marine organisms

The attachment of many marine and freshwater organisms permanently, or semi-permanently, to a hard substrate has long been of interest (e.g. Nelson 1924, Coe 1932, Cranfield 1973b, a, c, Cranfield 1974, 1975, Yonge 1979, Waite 1983, Harper 1992, Yamaguchi 1993, Harper 1997, Yamaguchi 1998, Braithwaite et al. 2000, Harper and Morton 2000, Morton and Harper 2001, Waite 2002, Bromley and Heinberg 2006, Kamino 2008). The ability of aquatic invertebrates to produce an array of strong robust adhesives in the presence of water, a skill currently beyond the scope of modern synthetic glues (liquid or semi-liquid adhesives), has intrigued researchers and promoted a drive to understand the materials and techniques involved.

A detailed review of most attachment strategies is given in Bromley and Heinberg (2006). In this review Bromely & Heinberg classify attachment mechanisms utilised by marine benthic organisms to six broad styles; muscular sucker attachment, holdfasts (e.g. byssal threads), organic glue secretions, hapterons, etchings and extensive/subtle cementation. With the exception of cementation (wholly cemented or calcified byssus, Yonge 1979), the above attachment styles involve the secretion of an organic or ‘chemical’ adhesive (viscoelastic gel of Smith 2002). Organic adhesives are often referred to as

'cement' (e.g. barnacle cement of Kamino et al. 2000, Kamino 2008), yet Bromley and Heinberg (2006) define cement as 'mineral precipitations'. To avoid confusion, the term 'cement' shall be used in this study in reference to crystalline or mineralised adhesives which form between the shell and substrate and will not refer to organic adhesives or calcified byssal threads. The term 'organic adhesive' will be used to describe any non-mineralised 'mucus-like' secretion directly involved in attachment.

1.5.1 Attachment mechanisms of bivalves

With the exception of a few free living forms (e.g. Pecten (Kauffman 1971)), the life habit of adult bivalves involves either permanent or semi-permanent attachment to the substrate by one of two closely related mechanisms, namely byssal attachment (Figure 9a) or cementation (Figure 9b) (Kauffman 1971, Stanley 1972, Yonge 1979, Harper 1991).

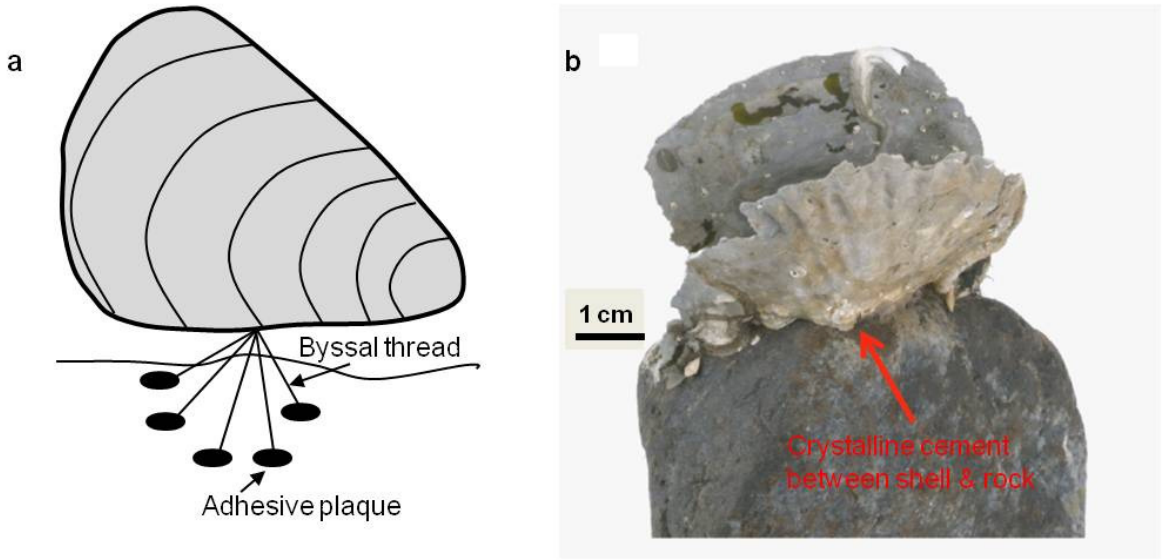

Figure 9. Attachment mechanisms common to epifaunal bivalves.
(a) Schematic representation of the byssal method of attachment. Diagram represents the byssal attachment of the common mussel *Mytilus edulis* (after Waite 1983) and is not to scale. (b) Picture of an oyster (*Crassostrea gigas*) cemented to a rock.

First appearing in the early Paleozoic, the byssal attachment is both the most common and most primitive method of attachment and appears in both epifaunal (epibyssate) and infaunal (endobyssate) forms (Stanley 1972, Yonge 1979). The first known cemented forms however did not appear until the Mesozoic (Yonge 1979, Harper 1991). This course of evolution has led many

authors to conclude that the cemented habit is an adaptation of the original byssal attachment (Kauffman 1971, Yonge 1979, Harper 1991).

1.5.1.1 Byssal attachment

Byssal attachment occurs in the post larval stage of most bivalves (Yonge 1979), and is retained into adult life in a number of families such as Mytilidae. In others, such as Ostreidae, the byssal attachment is lost soon after initial settlement of the larvae when cementation takes over (e.g. Cranfield 1973b, Yonge 1979).

The byssal attachment forms by the secretion of a protein-rich fluid from specialised glands in the foot (byssal glands). On contact with water this fluid sets to form byssal threads (e.g. Waite 1983, Weigemann 2004, Bromley and Heinberg 2006). The byssal attachment takes the form of multiple threads, each attached individually at the distal ends to the substrate by an adhesive plaque (Figure 9a) (e.g. Waite 1983, Weigemann 2004). The number and strength of the threads varies between families (Waite 1983, Pearce and LaBarbera 2009) and is a response to environmental conditions and stresses (Price 1980, Waite 1983, Young 1985, Lesin et al. 2006).

The byssal attachment remains as a non-mineralised protein based adhesive in all byssal families. The exception to this is the Anomiidae (Young 1985, Yamaguchi 1998) in which a single byssal 'plug' is released which is composed of $CaCO_3$ crystals and organic material arranged in a highly organised hierarchical structure (Yamaguchi 1998, Eltzholtz and Birkedal 2009).

1.5.1.2 Cementation

From an original byssal attachment, many bivalves evolved independently to adopt a cemented mode of life (Figure 9b) (e.g. Yonge 1979, Harper 1991, 1992, 1997). Harper (1991) notes that the appearance of cemented bivalves coincides with the Mesozoic marine revolution (as described by Vermeij 1977), and suggests that this expansion occurred as a response to an increase in predation as the rigid permanent attachment offered by cementation impedes manipulation and dislodgement by predators (Harper 1991).

Harper (1991 and references therein) recognises cementation in 16 bivalve families, most of which are marine, with only a few freshwater forms, such as Etheriidae (Yonge 1962) and Corbiculidae (Bogan and Bouchet 1998). Although cementation occurs in many unrelated taxa, it is generally accepted that adhesion occurs by deposition of calcareous cement (e.g. Kauffman 1971, Yonge 1979, Harper 1992, 1997) following a brief period of larval byssal attachment (e.g. Yonge 1979, Harper 1991, 1992).

The independent evolution of the cemented habit in most families has resulted in differences between families in terms of attachment orientation, timing of cementation and presence or absence of the foot (Yonge 1979). For example, pectinids are invariably dextrally attached while oysters are, without exception, sinistrally attached. Common to most cementing bivalves however is an early stage of byssal attachment. Most larval bivalves settle by way of the foot and become temporally byssally attached to provide stability during metamorphosis to adult form (Yonge 1979). Eventually, the byssal attachment is lost and the valves become wholly cemented to the substrate. Although the duration of the byssal period and timing of the onset of cementation is variable between taxa, Yonge (1979) proposed that following the dissoconch stage there is a common method of attachment deployed by all cementing bivalves. It is generally accepted that cementation involves precipitation of a mineral phase (usually $CaCO_3$) to form crystalline cement between the shell and substrate (Yonge 1979, Bromley and Heinberg 2006). The precise method involved in the formation of the mineralised cement however is largely unclear.

1.6 Aims of this study

Oysters have a long geological history and almost global distribution making them potentially ideal candidates for palaeoenvironmental studies. Indeed many authors have demonstrated that estuarine oysters faithfully record environmental conditions at the time of shell secretion (e.g. Kirby et al. 1998, Surge et al. 2001, 2003). However, oysters inhabit a range of environmental settings and many are descendants of fully marine ancestors (e.g. Kirby 2000). Changes in shell growth rate, stress and shell structure in response to external environmental pressures could alter the stable isotope signature of the shell.

Despite this, the effect of changing external environmental conditions on shell stable isotopes has never been explored. Understanding the effect of environment on shell microstructure and stable isotope signature is imperative before oysters from non estuarine environments can be applied to palaeoclimatic studies. Further, understanding the influence of environment on shell structure and isotope signature may provide new insights into the biomineralisation regime of the oyster and will identify key differences between the foliated and chalky calcite of the oyster. In addition, many marine biominerals continue to provide inspiration in the design of super tough materials and underwater adhesives. Oysters form a strong and permanent attachment to the substrate via cementation however the exact methods deployed by oysters to achieve adhesion are largely unknown.

The overall aim of this project is to characterise the microstructure, chemistry, crystallography and stable isotope signature of estuarine and marine specimens of the Pacific oyster, *Crassostrea gigas*. Specifically this study will address three inter-dependant principle aims:

1. Gain a full understanding of shell structure of both estuarine and marine oysters to provide a context for subsequent isotopic analysis. Explore the appearance and function of the chalk lenses in the oyster shells from different environments. This aim is addressed in Chapter 3.

2. Assess the ability of oysters from both estuarine and marine environments to record climate conditions at the time of shell secretion through stable isotope signature of the shell. This aim in addressed in Chapter 4.

3. Understand the methods by which oysters cement to hard substrates. This aim in addressed in Chapter 5.

A thorough comparison of estuarine and marine specimens of *C. gigas* is carried out at macrostructure and microstructural level through a range of techniques. Macrostructural analysis of estuarine and marine specimens is carried out by determination of the physical shell attributes including comparison of shell dimensions and by imaging analysis (detailed in section 2.3.1). Detailed analysis of the microstructure, chemistry and crystallography of estuarine and marine *C.*

gigas is carried out by a suite of scanning electron microscopy based techniques namely secondary electron and backscatter electron imaging, energy dispersive spectroscopic analysis (EDS) and electron backscatter diffraction (EBSD), detailed in sections 2.3.2, 2.3.3, 2.3.4 respectively. Mass spectrometry is used to determine the stable carbon and oxygen isotope composition of different shell microstructures of estuarine and marine valves (detailed in section 2.3.6).

A characteristic trait of oysters is their ability to adhere tightly to a range of substrate types. To understand the methods utilised by the oyster to achieve adhesion, samples of *C. gigas* attached to both inorganic (rock) and biological substrates (other oyster shells) were collected and analysed. From each sample the zone of attachment between shell and substrate is isolated and examined in detail by SEM imaging, EDS, EBSD and Raman spectroscopic analysis (detailed in section 2.3.5).

Chapter 2. Materials and methods

2.1 Specimen collection

This project utilises four sets of oyster samples to address two principle aims. Firstly, the project aims to compare the shell ultrastructure, crystallography, chemistry and stable isotope signature of oysters from estuarine and open marine environments. To address this, samples of *Crassostrea gigas*, from an estuarine environment, were sourced from a commercial oyster farm in Loch Fyne, Scotland (56. 241°N, -5.045°W) (Figure 10). Samples of *C. gigas* farmed in an open marine environment in Loch Tuath, Island of Ulva, Scotland (56.499°N, -6.229°W) (Figure 12) were provided by Ulva Oyster Farm.

The project also investigates the methods by which wild oysters adhere to hard substrates. For this, wild specimens of *C. gigas* cemented to shell substrates were collected from the intertidal zone at La Baule, northwest France (47.280°N, -2.394°W) (Figure 14) and wild *C. gigas* cemented to rock were collected from the intertidal zone at Linne Muirich, Loch Sween, Scotland (56.001°N, -5.651°W) (Figure 16).

Full details of all samples used in this study are given in Appendix A.

2.1.1 Loch Fyne environmental setting

Specimens of *C. gigas* from a sheltered brackish water environment were provided by Loch Fyne Oyster Farm (Figure 10). Oysters were grown using a tressel and bag technique at a depth of 0.5 m from the seabed during high tides and were periodically exposed during low tides. Oysters were three years old at the time of collection and a total of 13 oysters labelled as F1, F2, F3 etc. were utilised in this study.

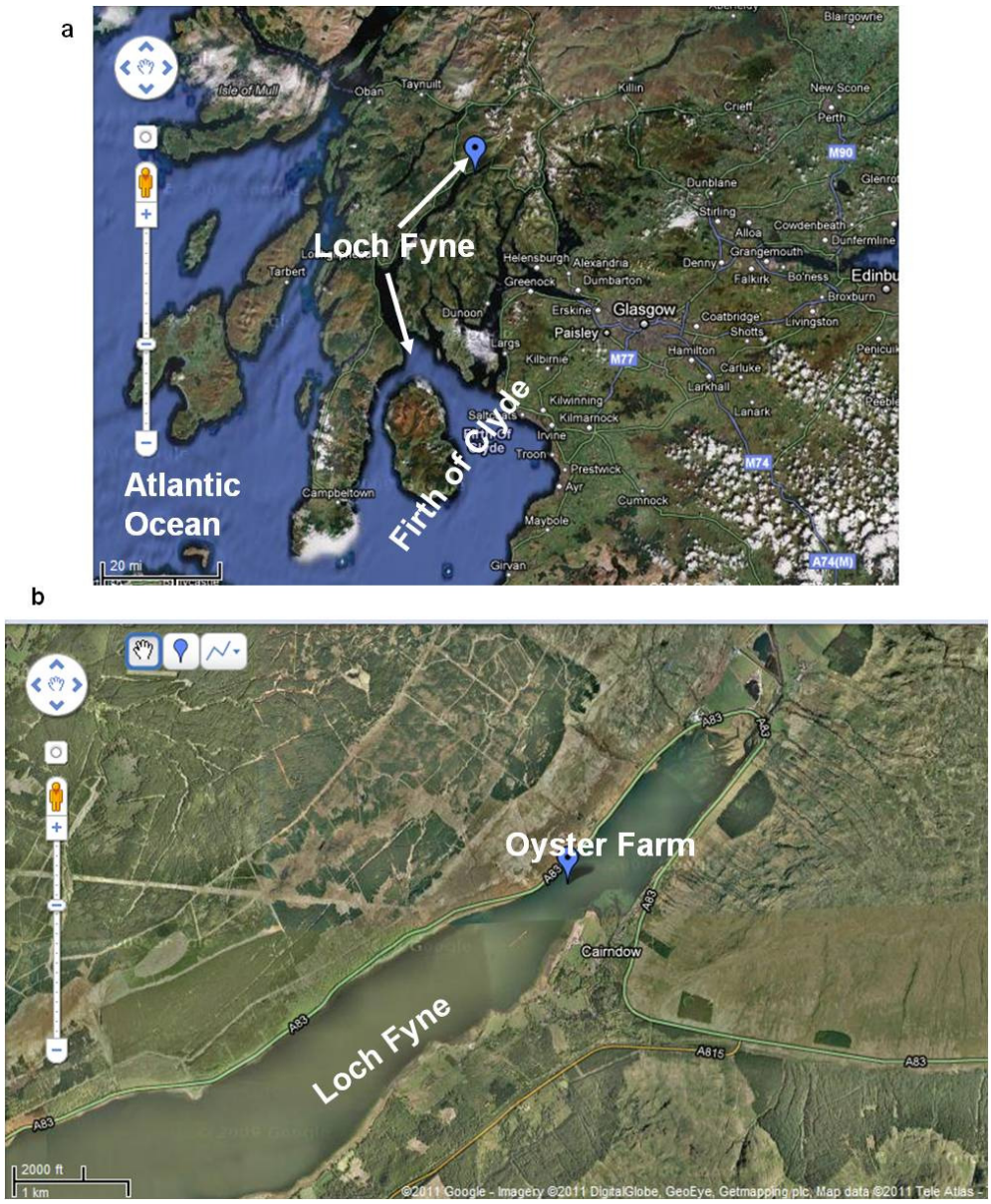

Figure 10. Collection site of estuarine oyster samples from Loch Fyne Oyster Farm, Loch Fyne.
(a) Location of Loch Fyne on the west coast of Scotland, arrows highlight the position of Loch Fyne from the head of the loch in the north-east to the mouth at the Firth of Clyde. Blue marker marks the position of Loch Fyne Oyster Farm. (b) Map showing location of Loch Fyne Oyster Farm (highlighted by blue marker). Maps from Google Maps.

Loch Fyne Oyster Farm is located at the head of Loch Fyne (Figure 10), a northeast – southwest trending sea loch extending 64 km inland from the loch mouth at the Firth of Clyde. Loch Fyne narrows from approximately 10 km in the south west to less than 2 km at the head of the loch in the northeast. The hills bounding the loch to the north and east provide significant freshwater runoff with rivers flowing into the loch responding rapidly to rainfall (Gillibrand 2001). Average annual freshwater runoff for Loch Fyne is 1340 x 10^6 m^3/year (Edwards and Sharples 1986).

From May 2010-March 2011 seawater temperature and salinity were recorded daily at Loch Fyne Oyster Farm. These data provide a near annual on-site record of water temperature and salinity for use in this study (Figure 11). Salinity is measured on the Practical Salinity Scale (PSS) which represents the conductivity ratio of a seawater sample to a standard KCl solution. The PSS is therefore a ratio and has no unit of measurement.

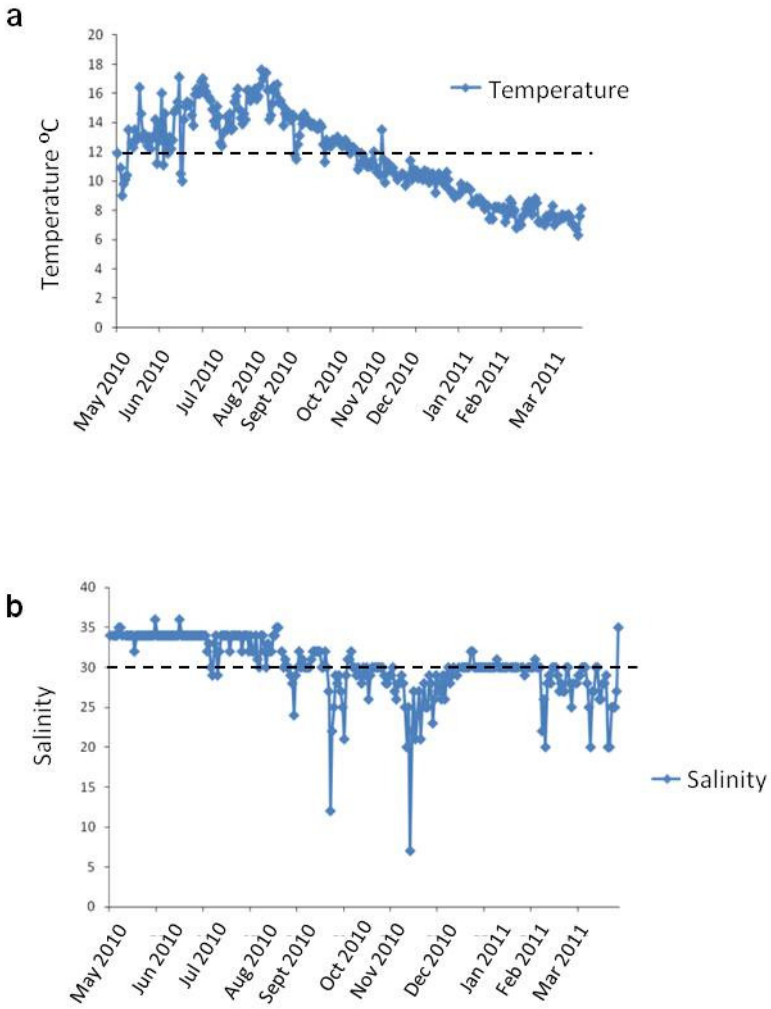

Figure 11. Daily temperature and salinity values at Loch Fyne Oyster Farm. (a) Daily seawater temperature record, dashed line indicates the average annual water temperature of 11.6˚C. (b) Daily water salinity record, dashed line indicates the average annual salinity of 30. Temperature and salinity records were measured by Loch Fyne Oyster Farm staff.

Temperatures range from 17.6˚C in July to 6.3˚C in February, with an average annual temperature of 11.6˚C. Salinity generally fluctuates from 20 to 36, but can drop as low as 7 during periods of high rainfall in November. Average salinity for the period of May 2010 to March 2011 was 30. The relationship between

salinity and $\delta^{18}O_{water}$ for west coast Scottish waters was defined by Austin and Inall (2002) and is expressed as follows:

$$\delta^{18}O_{water} = 0.18S - 6.0 \qquad \textbf{Equation 1}$$

Where S=salinity and $\delta^{18}O_{water}$ is expressed in ‰ relative to the International Atomic Agencies international standard - Standard Mean Ocean Water (SMOW). An average $\delta^{18}O_{water}$ value for Loch Fyne of -0.6‰ was calculated from an average salinity of 30.

2.1.2 Loch Tuath environmental setting

Samples of *C. gigas* grown in a marine environment were provided by Ulva Oyster Farm. Oysters were grown using the tressel and bag technique at a high tide depth of 4.5 m and were completely submerged throughout the year with the rare exception of extreme low spring tides. Oysters were three years old at time of collection. A total of ten marine oyster samples labelled as U1, U2, U3 etc. were utilised in this study.

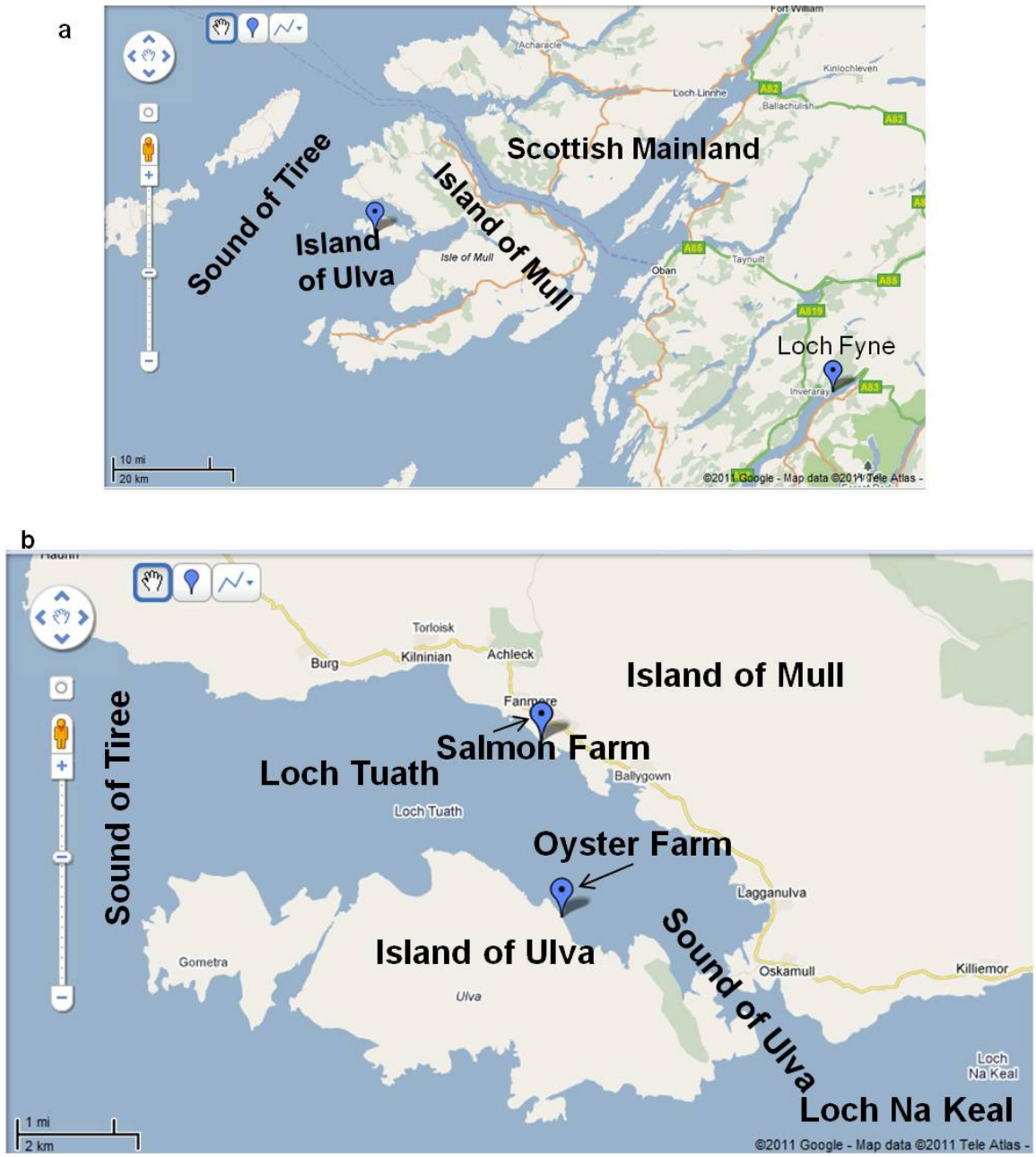

Figure 12. Collection site of marine oyster samples from the Island of Ulva Oyster Farm, Loch Tuath.
(a) Location of the Island of Ulva on the west coast of Scotland. (b) Map showing the location of Ulva Oyster Farm.

Ulva Oyster Farm is located on the east coast of the Island of Ulva in the waters of Loch Tuath (Figure 12). Loch Tuath is a 10 km long northwest - southeast trending sea loch separating the Island of Mull, to the northeast, and the Island of Ulva to the southwest. In the northwest the mouth of Loch Tuath forms a 4 km wide bay which is completely open to the Sound of Tiree. Towards the loch head the loch gradually narrows to approximately 2 km in the southeast where it is connected to neighbouring Loch Na Keal by the Sound of Ulva. Freshwater input to the system is marginal with no significant freshwater bodies entering the loch. Although total runoff volume entering Loch Tuath is unknown, the

average annual freshwater runoff for Loch Na Keal (Figure 12) is 250.3 x 10^6 m^3/year (Edwards and Sharples 1986).

Seawater temperature is recorded monthly in Loch Tuath by Lighthouse Caledonia Caged Salmon Farm on the Mull coast of Loch Tuath (Figure 12). Seawater temperatures from January 2007-May 2010 were made available for use in this study (Figure 13). Continuous salinity records could not be sourced for Loch Tuath.

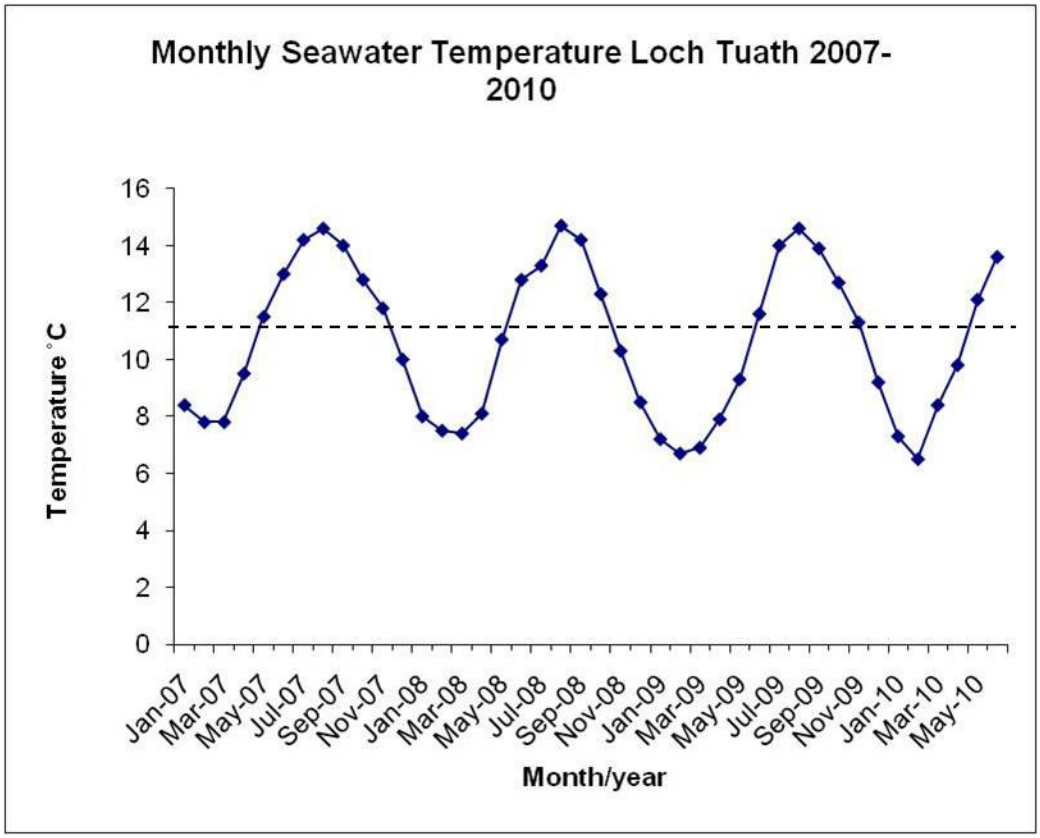

Figure 13. Monthly seawater temperature at Loch Tuath.
Seawater temperature is measured monthly at Lighthouse Caledonia Caged Salmon Farm, on the Mull coast of Loch Tuath (Figure 12). Dashed line represents the average annual water temperature of 10.6˚C.

Temperatures range from 14.7˚C in August to 6.5˚C in February, with an average annual temperature of 10.6˚C. The $\delta^{18}O$ of the water, measured during this study, was -0.42‰. The salinity of the water was calculated, using Equation 1, as 31.

2.1.3 Attached samples

This project also investigates the adhesion of wild oysters to both biological (other oyster shells) and non-biological (intertidal rock) substrates, to determine the methods by which oysters adhere and the effect that this has on shell structure.

2.1.3.1 Oyster-oyster attachment

Three pairs of cemented oyster shells (*C. gigas*) were collected from the intertidal zone at La Baule, northwest France (47.280ºN, -2.394ºW) (Figure 14) in July 2008.

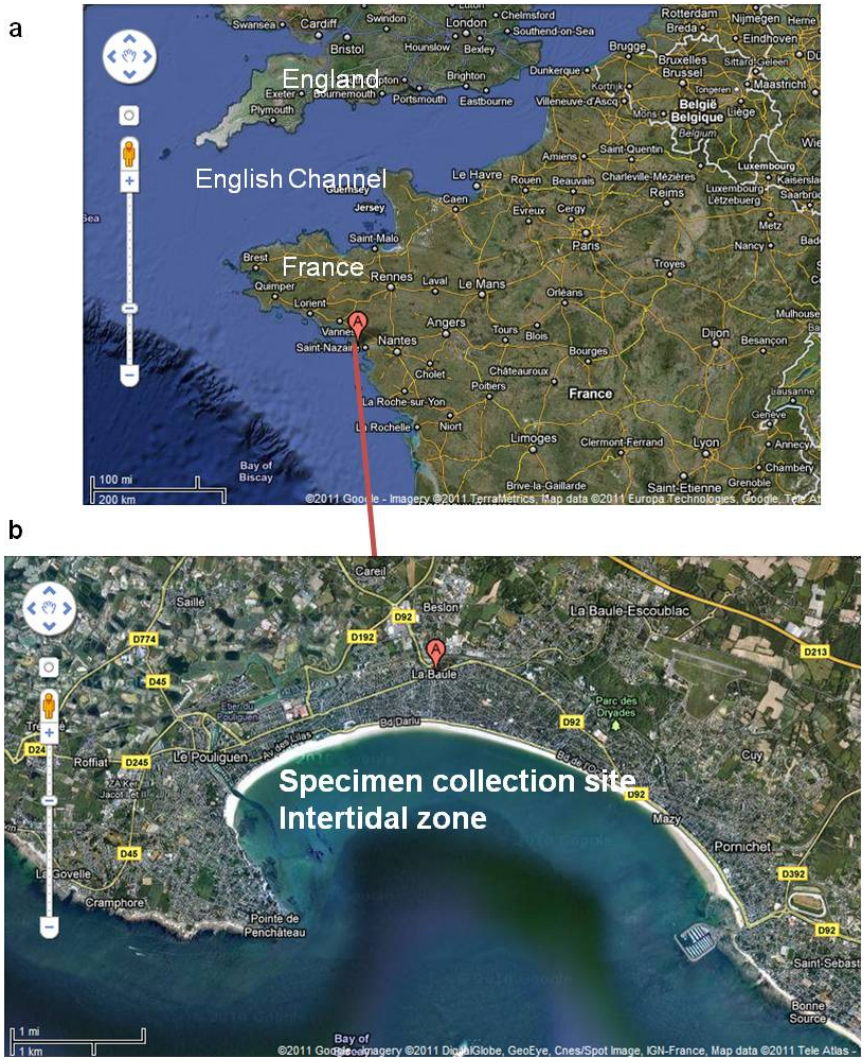

Figure 14. Location of specimen collection site, La Baule, France.
(a) Location of La Baule on the west coast of France. (b) High scale map of intertidal zone where attached samples were collected.

These cemented oysters included two pairs of laterally attached oyster shells (samples AL1 and AL2) and one pair of vertically attached oyster shells (sample AV1) (Figure 15).

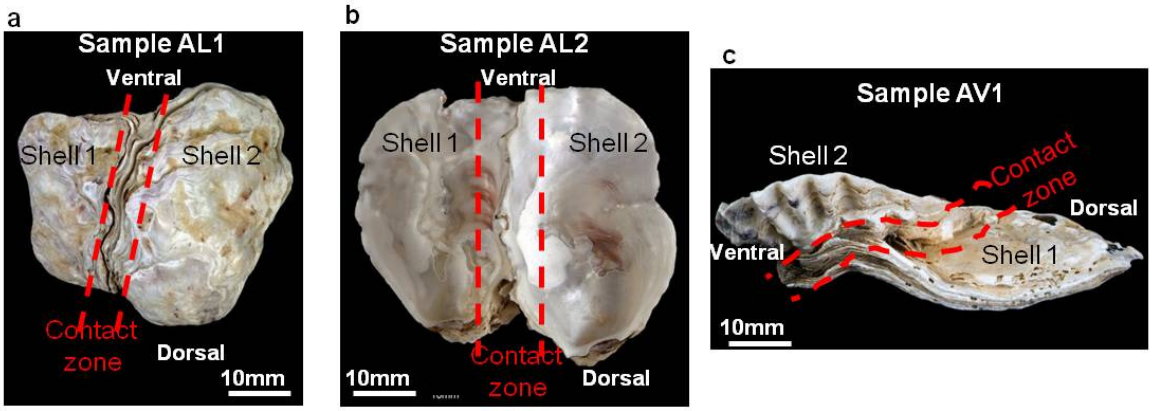

Figure 15. Samples of oyster shells attached to other oyster shells, collected from La Baule, France.
(a) & (b) Sample AL1 & AL2 both comprise two oyster shells attached laterally where shell 2 is attached on the anterior side to the posterior of shell 1. (c) Sample AV1 comprises two oyster shells attached vertically where the outer surface of the left valve of shell 2 is attached to the outer surface of the right valve of shell 1. In a-c the contact zone between the two fused shells is highlighted by dashed red lines.

2.1.3.2 Oyster-rock attachment

Individuals of *C. gigas* attached to rocks were collected from the intertidal zone at Linne Murich, Loch Sween, Scotland (56.001ºN, -5.651ºW) (Figure 16).

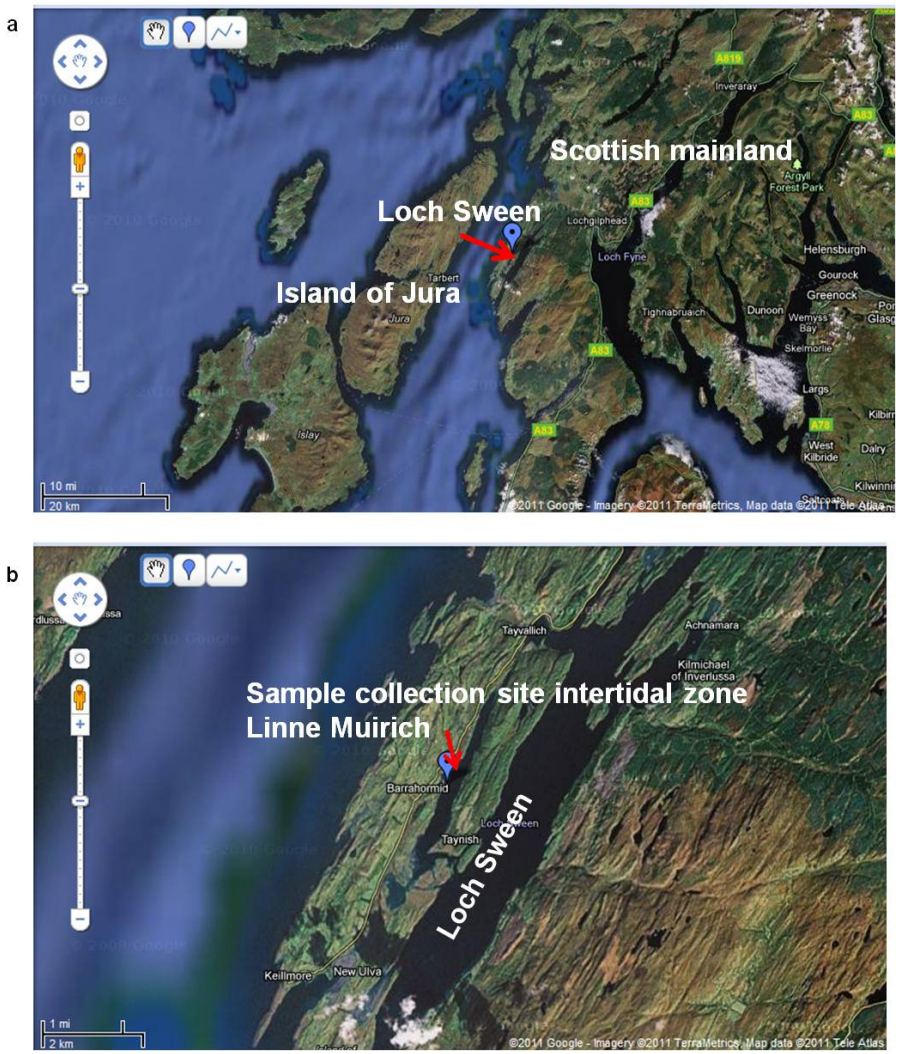

Figure 16. Location of collection site of oysters attached to rocks in Linne Muirich, Loch Sween, Scotland.
(a) Location of Loch Sween on the west coast of Scotland. (b) High scale map of intertidal zone at Linne Muirich.

Individual oysters were attached by their left valve to lithic greywacke rock (Figure 17) (coarse grained sandstone composed chiefly of quartz, feldspar, and rock fragments embedded in a clay rich matrix). For analysis of the contact zone between oyster shell and rock, two samples labelled RA1 and RA2 were prepared for analysis.

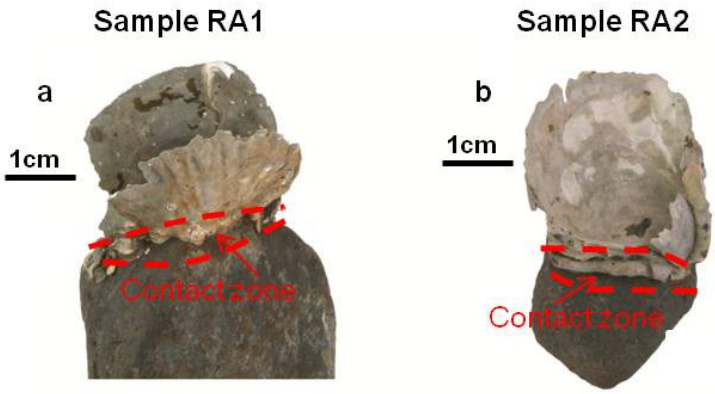

Figure 17. Samples of *C. gigas* attached to rock, collected from Linne Muirch, Loch Sween. (a) Sample RA1. (b) Sample RA2. In both samples the contact zone between shell and rock is highlighted by red dashed lines.

2.2 Sample preparation

2.2.1 Preparation of estuarine and marine samples

Samples were disarticulated and cleaned under running water to remove organic matter such as muscle fibres and other debris. Shells were then transferred to an ultrasonic bath and cleaned using deionised water. All samples were labelled and left to dry at room temperature.

Both right (RV) and left (LV) valves of all samples were photographed on both interior and exterior surfaces and were described in terms of shape, colour and ornamentation. From each valve three principle dimensions were measured using Vernier callipers. These dimensions are based on biometric indices described by Galtsoff (1964) and are shown in Figure 18. Measurements include, valve height (maximum measurement from the umbo to ventral margin) and valve length (maximum measurement from anterior-posterior margins parallel with hinge axis) (Galtsoff 1964). Valve thickness is measured as the maximum thickness from interior to exterior surface of a single valve (Figure 18).

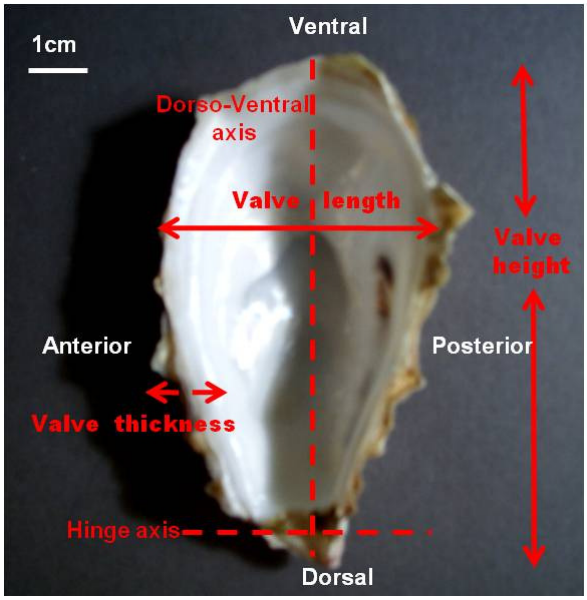

Figure 18. Representation of the three principle dimensions measured on all samples. Image shows the left valve of an estuarine sample where solid lines represent lines of measurement. Measurements were made using Vernier callipers on both valves of estuarine and marine samples. Dashed lines represent the position of the dorso-ventral axis and hinge axis (Stenzel 1971).

From the above measurements the Shell Thickness Index (STI), as defined by (Alzieu et al. 1986), was calculated for each sample (Equation 2).

$$STI = height\ right\ valve / thickness\ right\ valve \qquad \textbf{Equation 2}$$

A list of all samples analysed in this study together with valve dimensions are given in Appendix A.

2.2.2 Cross sections

Right and left valves of estuarine and marine samples were analysed in cross section. From each valve, a 1 cm wide section was cut along the dorsal-ventral axis, 0.5 cm anterior of the anterior edge of the adductor muscle scar using a slow speed Isomet saw (speed = 2400 rpm) (Figure 19).

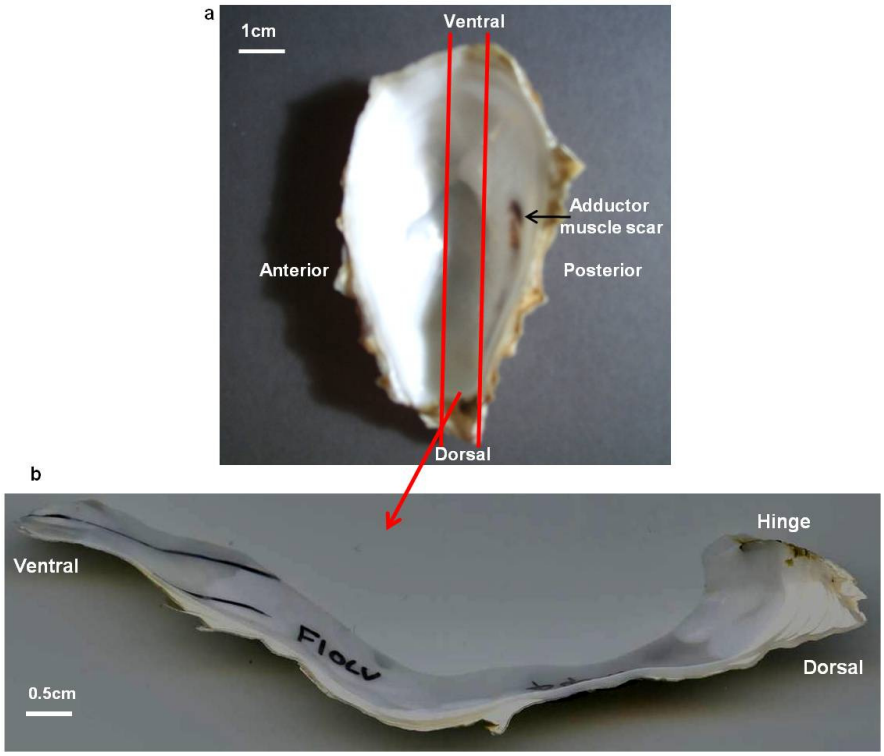

Figure 19. Preparation and position of valve cross sections.
Image (a) shows a typical left valve with solid red lines representing lines of section. (b) Image of resulting cross section revealing details of internal shell structure.

Sectioning in this way provides a continuous section from dorsal to ventral margin. Both valves of six estuarine and six marine oysters were prepared in this way. Of these, three from each sample set were analysed by optical microscopy and image analysis (detailed in sections 2.3.1); the remaining three were used for isotopic analysis (detailed in section 2.3.6).

2.2.3 Growth line analysis

Incremental growth lines provide a temporal frame on which geochemical analyses can be conducted (Jones 1983, Kirby et al. 1998, Ullmann et al. 2010, Fan et al. 2011). Following optical microscopy and image analysis the cross section, prepared as described above, of the left valve of marine sample U3 was prepared for growth line analysis.

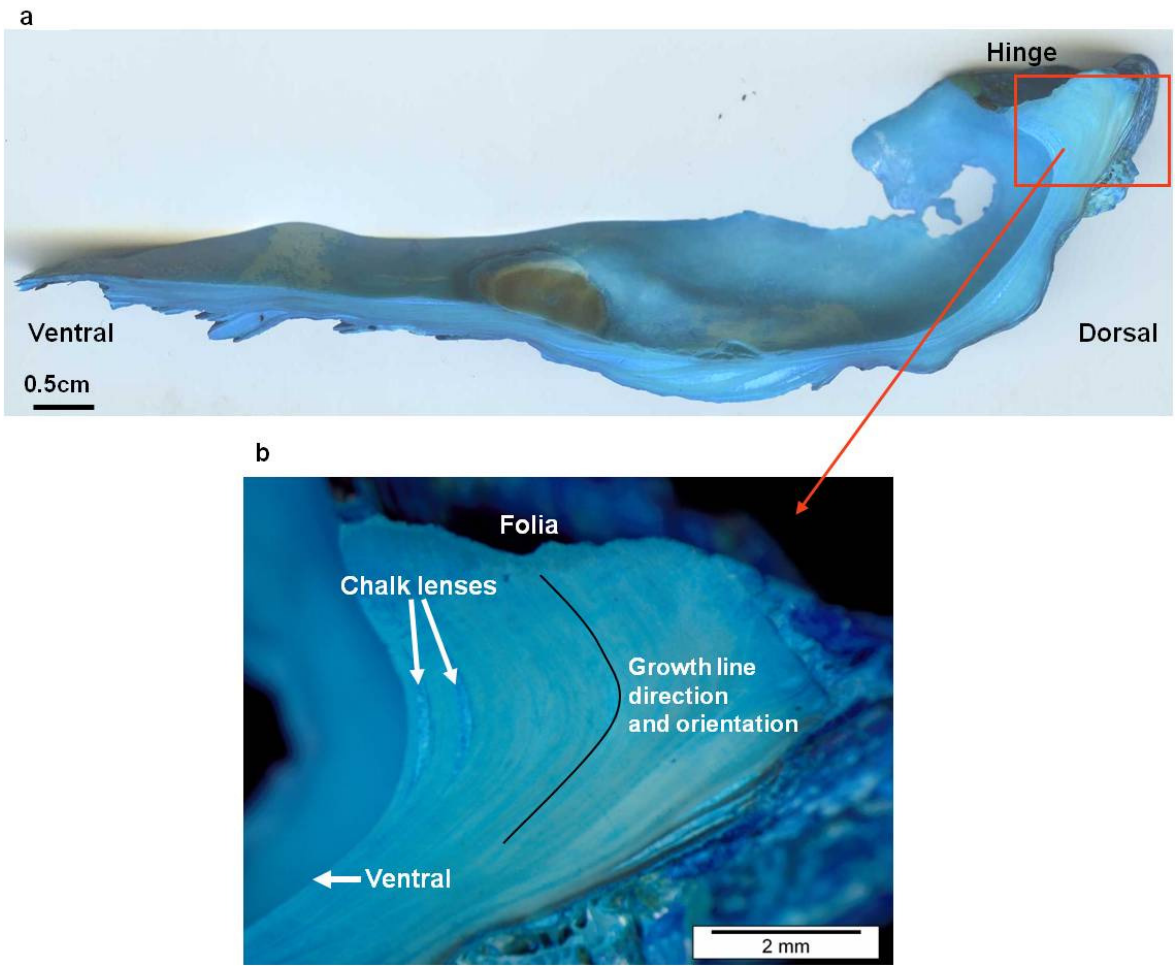

Figure 20. Treatment of valve cross section for analysis of incremental growth lines. (a) Photograph of the left valve cross section of marine sample U3 following treatment with Mutvei solution (Schöne et al. 2005). (b) High magnification optical microscopy image of the hinge region of cross section shown in (a) highlighting the position of growth lines within foliated calcite.

The valve cross section was treated with Mutvei solution, using methods described by Schöne et al. (2005), to highlight incremental growth bands (Figure 20a). In optical microscopy, growth bands can be observed as faint thin lines extending from the ligament surface to the shell exterior, perpendicular to the dorso-ventral axis (Figure 20b). Growth lines are approximately 0.2-0.5 mm apart in the foliated calcite but cannot be traced in the chalky lenses (Figure 20b). Although apparent in the hinge region, growth lines could not be traced in shell sections ventral of the umbo.

2.2.4 Fracture blocks

Fractured blocks of right and left valves of estuarine and marine samples were prepared for scanning electron microscopy (detailed in section 2.3.2). The hinge region of the oyster shell is morphologically complex (e.g. Carriker et al. 1980),

and so was prepared and analysed separately as discussed in section 2.2.7. The hinge region was removed by cutting parallel to the hinge axis at a ventral distance of approximately 0.5 cm from the hinge (Figure 21). A radial section was then cut from the remaining valve by cutting along the dorsal-ventral axis immediately adjacent to posterior and anterior sides of the muscle scar (Figure 21) to create a continuous section. All cuts were made using a slow speed Isomet saw (speed = 2400 rpm). Radial sections were then fractured at approximately 1 cm intervals to produce a series of fractured shell blocks labelled A-D from ventral to dorsal edge (Figure 21). Fractures were made either by hand or with carpenter's pincers (gripping pliers).

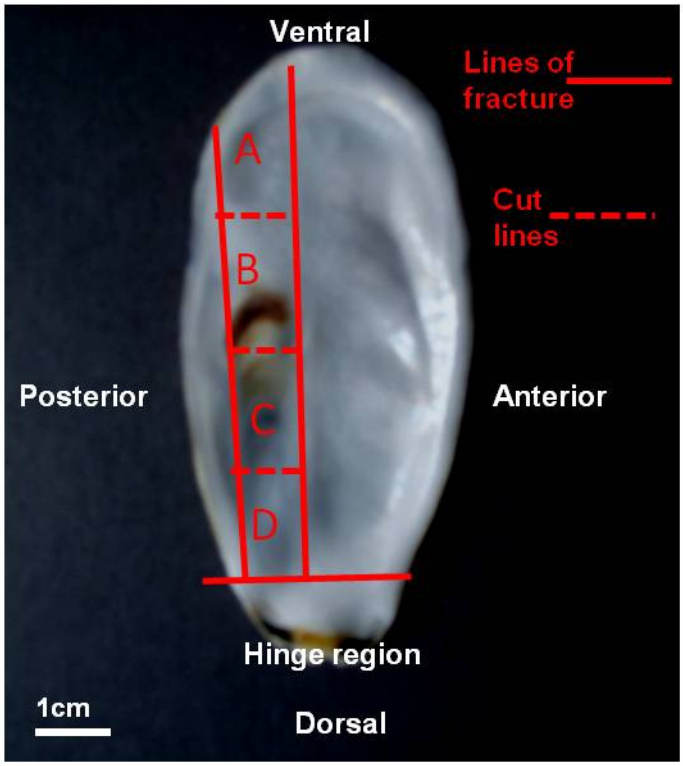

Figure 21. Preparation of fracture shell sections for analysis by scanning electron microscopy.
Image of a right valve showing the position of saw lines (solid) and fracture lines (dashed) creating individual fracture blocks along dorsal-ventral axis. Identical fracture blocks were created for left valves.

Each fracture block was glued to an aluminium stub. Samples were mounted with an orientation such that the samples were viewed in cross section on the ventral side of the fracture. Samples were then coated in gold using an Agar Gold Sputter Coater and gold was applied to each sample for a duration of 90 seconds.

Both right and left valves of one oyster from each sample set (samples F4 and U4) were prepared in this way. A further two marine samples (sample U5 and U7) were fractured in radial sections which contained cavities (see section 3.2.1) and mounted on aluminium stubs and coated as described above.

Fracture sections allow detailed observation of the microstructural and topographical arrangement of the valves. Both valves of the oyster are composed predominantly of foliated and chalky calcite (e.g. Carriker et al. 1980, Higuera-Ruiz and Elorza 2009). Where excess chalky material was present, some shell material was lost as the chalk crumbled. To overcome this problem, a second estuarine sample (sample F5) was prepared by the methods described above with the addition of a thin layer of epoxycure resin (5:1 resin:hardener) painted onto the interior and exterior surfaces of both valves prior to fracturing. Resin was left to cure for 24 hours before fracturing as described above. While this method did reduce the problem of 'crumbling', resin obscured the view of the outer surface of the prisms and the periostracum.

2.2.5 Resin blocks

The right and left valves of estuarine sample F6, and the left valve of marine sample U6 was prepared for crystallographic and chemical analysis as detailed in section 2.3.3 & 2.3.4. A radial section of the valve was isolated as described in section 2.2.4 and shown in Figure 21. The complete radial section was then embedded in epoxycure resin (5:1 resin:hardener) and left to set for 24 hours. The embedded valve section was then cut at approximately 1 cm intervals along the long axis to create a series of resin blocks labelled A-D from the ventral to dorsal margin, as shown in Figure 21. All cuts were made using a slow speed isomet saw (speed = 2400 rpm).

Crystallographic analysis by electron backscatter diffraction (EBSD) requires the sample surface to be completely free of topography (see section 2.3.4 for details). To achieve this, each resin block was polished through a series of grinding and polishing discs. All grinding and polishing stages were performed by hand. The sample surface is ground down using silicon carbine abrasive papers of decreasing grade, 320 (46 µm), 1200 (15 µm), and 4000 (< 5 µm). Resin blocks were subsequently polished using 1 µm and 0.3 µm alpha aluminium oxide, with

a final polish using 0.06 µm colloidal silica. Samples were then cleaned in an ultrasonic bath for 3 minutes and wiped with a methanol-soaked tissue to remove any polish residue.

Resin blocks were then mounted on aluminium stubs using silver dag or silver tape. All blocks were orientated for analysis of the anterior side of the section.

Carbonate materials are insulators and surface charging of specimens during EBSD analysis can reduce scan quality (e.g. Prior et al. 1999). A carbon coat of 2.5 nm is recognised as the optimal coat thickness when analysing biominerals (Pérez-Huerta and Cusack 2009). All resin blocks were coated with 2.5 nm of carbon prior to analysis. The thickness of the carbon coat was accurately controlled using a precision etching coating system (Model 682) by Gatan Inc. Following application of the carbon coat, silver paint was then applied to the edges of the resin block to provide a dispersive surface for electrons to further reduce charging.

Chalk lenses are composed of a network of fine calcite blades arranged around pore space (e.g. Higuera-Ruiz and Elorza 2009). The presence of empty cavities in the sample surface can reduce EBSD scan quality by producing shadows on the sample surface. After polishing, a single resin block containing multiple chalk lenses was painted with fresh resin and placed in a vacuum for three hours to allow resin to impregnate chalk pore space. The sample was then re-polished and carbon coated as described above.

A resin block of the left valves of both estuarine and marine samples were used for chemical analysis (detailed in section 2.3.3). Resin blocks of the right valve of estuarine sample F6 were used for EBSD analysis (detailed in section 2.3.4).

2.2.6 Thin sections

Thin sections of two fracture samples were subsequently prepared as thin sections to allow EBSD crystallographic analyses. These samples included a fracture shell section for analyses of the foliated structure, and a fracture section of attached sample AL1 to allow further analysis of the crystalline cement.

The fracture block was removed from the aluminium stub and coated with Epothin resin (3:1 resin: hardener) to provide support. Once cured, the resin-painted block was embedded in a mould with epoxycure resin (5:1 resin: hardener) in the desired orientation and left to cure for 24 hours. Once set, the surface of interest was ground down using silicon carbide abrasive paper of decreasing grades (P400, P800, P1500) to expose a flat sample surface. The sample was immersed in an ultra-sonic bath for 1 minute and allowed to dry before being mounted on a pre-ground glass slide. Samples were mounted with the exposed surface down, using a thin layer of Epothin Resin (3:1 resin: hardener) and placed under a spring press for 8 hours to allow the resin to set. Glass slides, with attached sample blocks, were mounted to a Buehler Petrothin thin sectioning system with integrated diamond blade and trimmed to a thickness of ~40 µm. Final grinding and polishing stages were performed by hand using silicon carbide abrasive paper of decreasing grades (P400, P800, P1500), followed by polishing cloths of 1 µm and 0.3 µm aluminium oxide and 0.06 µm colloidal silica. The final section thickness is ~30 µm.

Slides were mounted on aluminium stubs using silver paint and coated with carbon as described in section 2.2.5.

2.2.7 Hinge sections

The hinge region of the oyster shell is morphologically complex (Carriker et al. 1980) and was prepared and analysed separately from the rest of the shell. Both valves were fractured parallel to the hinge axis (Figure 22) by cutting into the shell from the shell exterior, at the hinge region, using a hand held hacksaw. A screwdriver was then inserted into this line of cut and twisted to induce shell fracture.

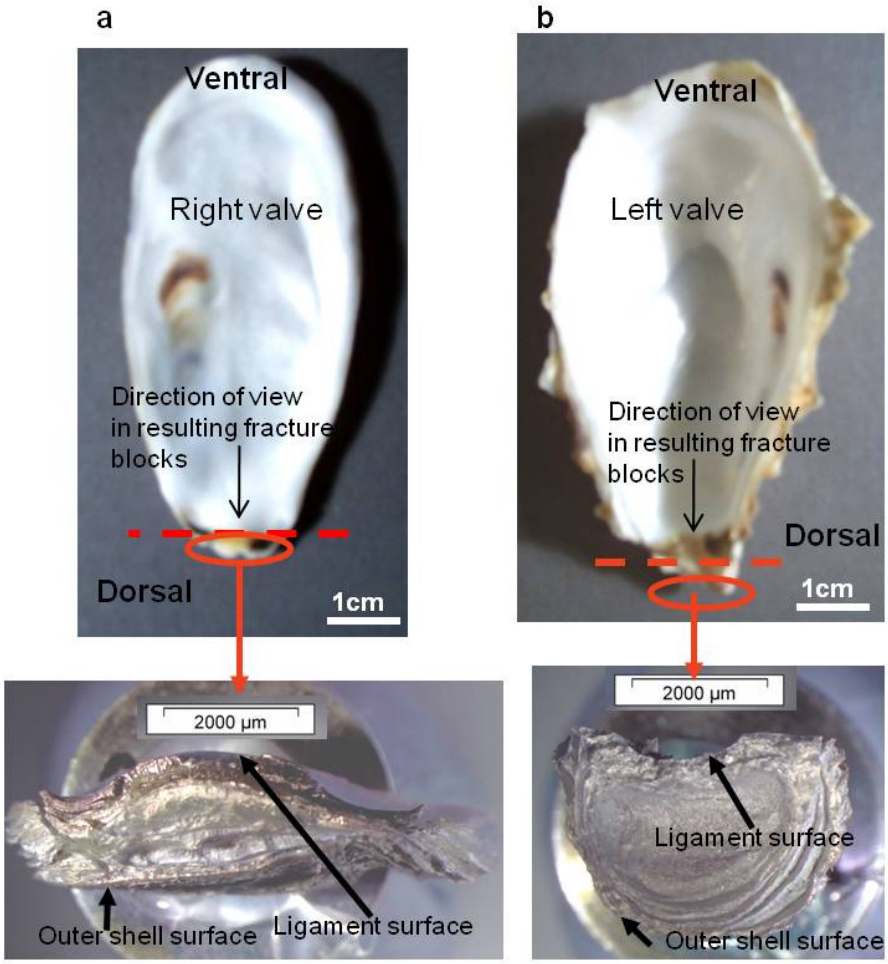

Figure 22. Preparation of valve hinge sections for analysis.
Top images show location of fracture line (dashed), bottom images show corresponding fracture block used for analysis as viewed from ventral to dorsal margin. For EBSD analysis resin blocks containing the hinge region were created by cutting, with a slow speed Isomet saw, along the dashed line shown above.

A total of three estuarine samples were prepared in this way (samples: F7, F11, and F12). Left and right valve hinge fracture blocks of sample F7 were immediately mounted on aluminium stubs using glue and coated in gold. Fractured hinge sections (Figure 22) of sample F11 were held in a 10% acetic acid solution for 15 minutes to allow partial decalcification of the hinge region. Hinge fractures of sample F12 were placed in a solution of 10% NaClO for two hours to allow partial removal of the organic components. Hinge sections from samples F11 and F12 were then mounted on aluminium stubs using glue and coated in gold and analysed by scanning electron microscopy (section 2.3.2).

EBSD analysis of the hinge region was carried out on sample F13. The hinge regions of both valves were isolated by cutting parallel to the hinge axis in the centre of the hinge region (Figure 22). Valve ventral to this line of cut was discarded. The remaining hinge section was treated for two hours in 10% NaClO

solution to partially remove organic material. Right and left valve hinge sections were then embedded in epoxycure resin (5:1 resin:hardener) and allowed to cure for 24 hours. Resin blocks were ground and polished (as described in section 2.2.5), mounted on aluminium stubs using silver dag and orientated with the shell exterior down, for viewing from ventral to dorsal margin. Resin blocks were then coated in carbon as described above.

2.2.8 Preparation of attached samples

Wild oysters cemented to shell and rock substrates were collected from the intertidal zone at La Baule, France and Loch Sween, Scotland respectively. All samples were attached by the left valve. Where right valves were present, valves were disarticulated and removed. Left valves attached to substrates were cleaned under running water to remove organic matter such as muscle fibres and other debris. Cemented valves were then transferred to an ultrasonic bath and cleaned with deionised water. All samples were labelled and left to dry at room temperature before being photographed.

2.2.8.1 Oyster-oyster attachment

In all samples, the contact zone between the two fused shells was isolated by removing excess shell material with a slow speed Isomet saw (speed=2400 rpm) (Figure 23).

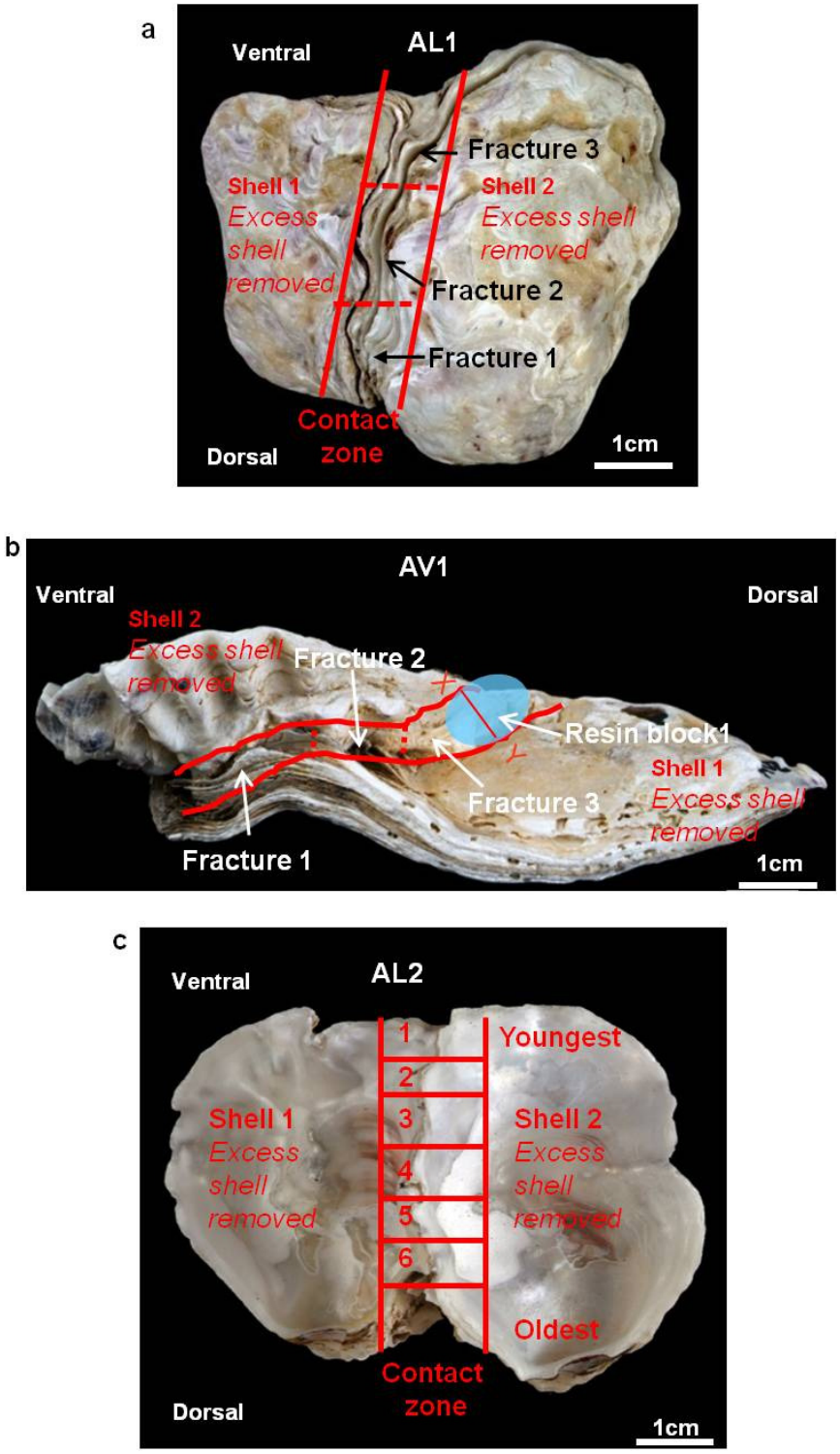

Figure 23. Preparation of samples of oyster-oyster attachment for analysis. (a-c) Preparation of samples AL1, AV1 and AL2 respectively, where solid lines represent lines of section, dashed lines represent position of fractures. The contact zone is the area between solid red lines. In (b) the blue circle represents the extent of the resin block which was then sub-sectioned by cutting along the line x-y. In (c) the entire contact zone was embedded in resin and sub-sectioned along the long axis to create a series of blocks labelled 1-6 along the ventral-dorsal axis.

The contact zone of sample AL1 was fractured at two points along the long axis of the contact to produce three fracture blocks (Figure 23a). Fracture blocks were mounted on aluminium stubs using glue and coated in gold for scanning

electron microscopy. The contact zone of sample AV1 was partially embedded in resin at the dorsal end of the contact (Figure 23b). Resin covered a section of approximately 2 cm along the contact zone. Resin was allowed to set for 24 hours. Following this, the resin block at the dorsal end of the sample was cut in half along the line x-y (Figure 23b) to provide a single resin block. The remaining section of the contact zone was fractured using carpenter's pincers at two points to produce three fracture surfaces (Figure 23b). Fractured sections were glued to an aluminium stub and coated in gold for scanning electron imaging analysis. The contact zone of sample AL2 was completely embedded in resin and left to cure for 24 hours. The resin block, containing the contact zone, was sectioned at approximately 1 cm intervals perpendicular to the long axis of the contact zone. Sectioning in this way produced a series of resin blocks from the youngest (ventral) to oldest (dorsal) parts of the contact (Figure 23c). All resin blocks from sample AL2 and the single resin block from AV1 were ground, polished and coated in carbon as described in section 2.2.5.

2.2.8.2 Oyster-rock attachment

The contact zone between oyster shell and rock was isolated by removing excess shell material with a slow speed isomet saw. Excess rock was removed using a Husqvarna TS 230F high speed saw (Figure 24).

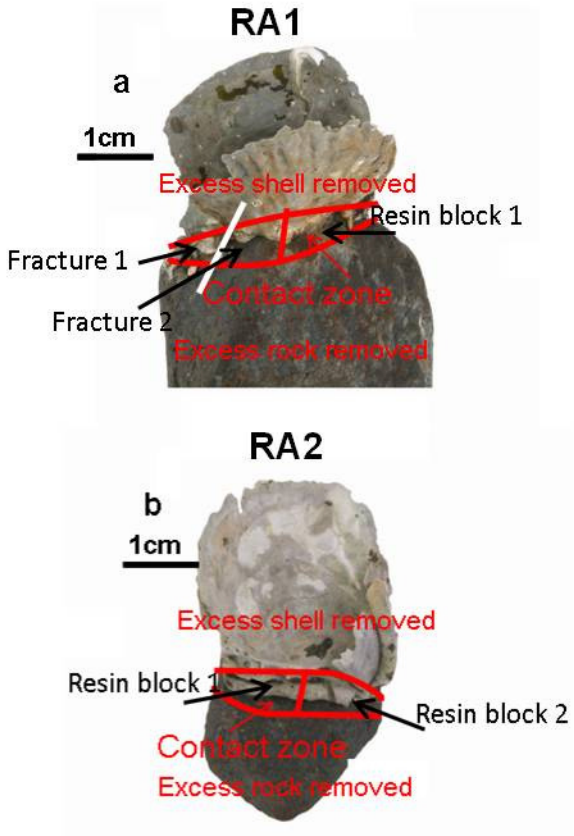

Figure 24. Preparation of samples of oyster-rock attachment.
The contact zone in both samples lies between the solid red lines. For both samples shell and rock adjacent to the contact zone was removed to leave an isolated contact between shell and rock. Sample RA1 (a) was fractured to produce a fracture block, the remaining contact was embedded in resin. The entire isolated contact of sample RA2 (b) was embedded in resin and sectioned perpendicular to the long axis of the contact to produce two resin blocks. Red solid lines represent saw lines, the white solid line represents the line of fracture.

Part of sample RA1 was fractured using pliers (Figure 24a) to produce two fracture surfaces which were glued to an aluminium stub and coated in gold for scanning electron microscopy. The remaining contact zone of sample RA1 was embedded in resin and prepared for crystallographic and chemical analysis by methods detailed in section 2.2.5. The entire contact zone of sample RA2 was embedded in epoxycure resin (5:1) and left to cure for 24 hours. The resin block of sample RA2 was cut in half perpendicular to the long axis of the contact zone using a slow speed isomet saw and polished through a series of grinding and polishing discs as described in section (2.2.5) and finally mounted on aluminium stubs using silver paint. Resin blocks from samples RA1 and RA2 were coated in carbon (as described in section 2.2.5) for crystallographic and chemical analysis. Resin blocks from sample RA2 were subsequently re-polished to remove the carbon coat for Raman spectroscopic analysis (detailed in section 2.3.5).

2.3 Analytical techniques

2.3.1 Image analysis using Image J

Quantification of valve composition and the volume of void space within chalk lenses was conducted by image analysis using Image J. Image J is a freely available Java based image processing programme. The programme is multi-functional and can be used to provide quantitative area measurements of complex objects. Area measurements are conducted by statistical pixel value analysis. Image J converts the image to greyscale and counts the number of pixels of different shades providing a total number of pixels in the image and the total number of any user defined pixel value (values of 0-255 where 0=black and 255=white). From this pixel quantification, the percentage area occupied by a certain pixel value can be calculated.

Image J version 1.43 was used in this study to provide quantitative analysis of valve composition and amount of void space present within chalk lenses.

Quantitative analysis of valve composition was carried out on cross sections of both valves of three estuarine (F1, F2,F3) and three marine (U1,U2,U3) samples for comparison. Cross sections of valves (described in 2.2.2) were prepared and digitally scanned. Chalky lenses can be observed in oyster shell sections as white porcelain areas, while the foliated layers are dull grey. To ensure that this subtle difference was correctly identified in Image J, all scan images were first traced in Adobe Illustrator CS2 and chalky lenses were coloured blue and foliated regions coloured light grey to highlight the different microstructures (Figure 25). These images were then converted to greyscale in Image J. Quantitative analysis of the cross section composition is used here to provide some indication of the composition of the whole valve.

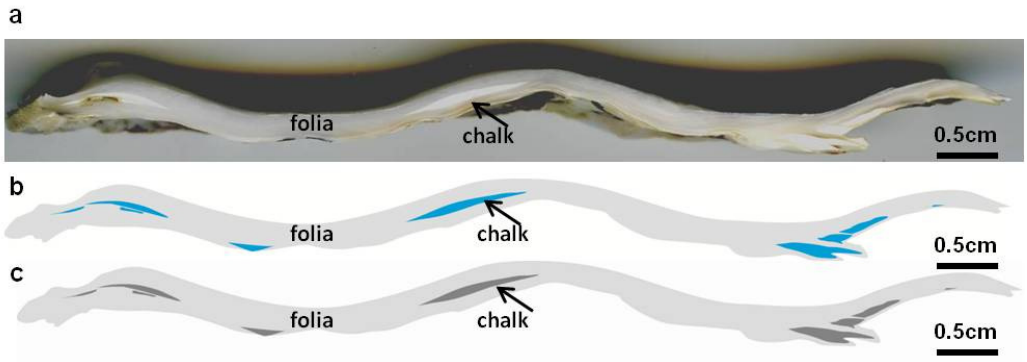

Figure 25. Quantification of valve composition by cross section image analysis using Image J.
Image analysis by Image J is carried out on valve cross sections (a) which are coloured to highlight the position of chalky and foliated calcite (b) where blue is chalk and grey is folia. This is then converted to greyscale for final image analysis (c). Image shows analysis of a right valve.

Image J was also used to provide quantitative analysis of the amount of void space present in chalky lenses. For this analysis, scanning electron micrographs were opened directly in Image J for pixel analysis. Mineralised areas appear as white or light grey while empty pores, enclosed by mineral blades, appear black allowing statistical pixel analysis to be conducted easily.

2.3.2 Scanning electron microscopy

Detailed microstructural, chemical and crystallographic analysis of all samples used in this study was carried out using a Zeiss Sigma field emission scanning electron microscope (SEM) and FEI Quanta 200F environmental SEM, at the University of Glasgow Imaging Spectroscopy and Analysis Centre (ISAAC). Both microscopes can operate in either high or low vacuum mode. Calcium carbonate, the main component of bivalve shells such as oysters, is an insulator and therefore the high vacuum (1.24 X 10^{-5} Torr) mode was selected for all SEM analysis in this study.

2.3.2.1 Secondary electron imaging

Secondary electron imaging (SE) was carried out using both Sigma and Quanta SEM units. An image is produced when beam electrons directed at the sample surface, interact with atoms of the sample causing the electrons present to be expelled. Expelled electrons are known as secondary electrons and are collected by the secondary electron detector within the SEM chamber. Secondary electron

imaging can provide high resolution images of rough surfaces, such as those of fractured shells, revealing topography and microstructural arrangement of the sample.

2.3.2.2 Backscattered electron imaging

Backscattered electron (BSE) imaging was carried out using both Sigma and Quanta SEM units using a backscattered electron detector. An image is produced when beam electrons strike a nucleus on the sample surface and are backscattered and collected by the backscatter electron detector from which an image is produced. Greyscale images are generated with minerals with highest mean atomic number producing the brightest areas as they produce the highest number of backscatter electrons. Therefore spatial variations in mean atomic number across the sample can be recognised through different shades of grey in the BSE image. BSE imaging was used throughout this study to obtain high resolution images of fractured and polished samples.

2.3.3 Energy dispersive spectroscopic (EDS) elemental analysis

Energy dispersive X-ray spectroscopy (EDS) is an extremely effective tool which is used in conjunction with secondary electron imaging to acquire quantitative and qualitative elemental analysis of samples. X-rays are produced when a beam of electrons is focused at the sample surface causing electrons within sample atoms to change energy states resulting in emission of an X-ray to restore the energy state. X-rays are detected by the EDS X-ray detector system and identified.

2.3.3.1 Quantitative analysis

Quantitative elemental analysis of samples was carried out by standardised analysis using a Sigma SEM with integrated Oxford Instruments and INCA microanalysis computer software. Prior to sample analysis instrumentation is standardised using Mac Microanalysis mineral reference block. Elements to be investigated are selected and appropriate standards, of known elemental composition, are analysed and the number of X-ray counts produced (response) standardised for each element. Peak optimization was carried out prior to

standardisation to ensure accuracy of response. A full list of elements analysed and corresponding reference standards and detection limits are given in Appendix B.

Sample analysis was carried out on polished, carbon-coated samples to ensure the optimum number of X-ray counts was produced. Sites of interest were selected on the sample surface and the electron beam scanned over a raster area of 7 µm by 5 µm. All analysis was carried out using 1 nanoamp power and a magnification of 40000. Acquisition time was 30 seconds and process time 5. For analysis of chalk structures spectra were collected from individual spot analysis, rather than raster areas, due to the fine nature of the calcite blades comprising the chalk. Spots are typically 1 µm diameter. Data are presented as elemental spectra (Figure 26a) and the quantity of each element present is presented numerically in weight% (Figure 26b). At each site of interest a minimum of five spectra were accumulated and the mean values reported.

a

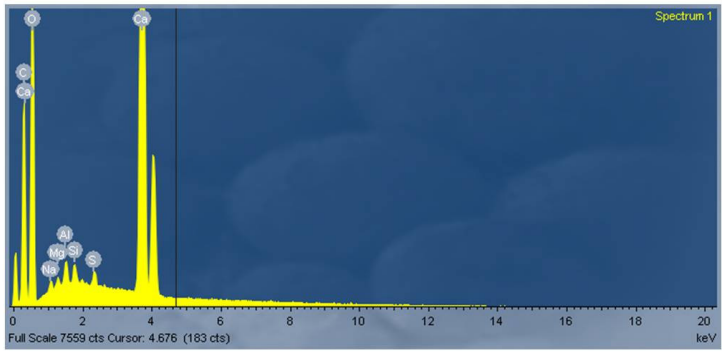

b

All spectra :

Position information : None Units : Millimeters

Spectrum label	O	Na	Mg	Al	Si	S	Ca	Mn	Fe
Spectrum 1	51.83	0.32	0.17	0.45	0.35	0.31	37.98	-0.02	0.08
Spectrum 2	57.65	0.35	0.24	0.31	0.72	0.26	37.42	0.00	0.02
Spectrum 3	60.80	0.38	0.18	0.82	1.56	0.27	36.33	-0.01	-0.01
Spectrum 4	53.23	0.34	0.15	0.42	1.25	0.27	35.60	0.00	0.02
Spectrum 5	47.42	0.36	0.13	0.06	0.18	0.25	36.69	-0.04	0.01

Statistic	O	Na	Mg	Al	Si	S	Ca	Mn	Fe
Mean	54.18	0.35	0.17	0.41	0.81	0.27	36.81	-0.02	0.02
Std. dev.	5.20	0.02	0.04	0.27	0.59	0.02	0.93	0.02	0.03
Max.	60.80	0.38	0.24	0.82	1.56	0.31	37.98	0.00	0.08
Min	47.42	0.32	0.13	0.06	0.18	0.25	35.60	-0.04	-0.0

Results type : Weight% Decimal places : 2

Figure 26. Representative example of energy dispersive spectroscopic (EDS) spot analysis data.
(a) Typical spectrum with elements automatically identified by EDS software. (b) Corresponding numerical readout showing quantitative analysis of elemental composition in weight%.

2.3.3.2 Qualitative spot analysis and elemental mapping

Spot analysis was carried out to provide a spectrum of the elemental composition of a given spot on the sample surface. The electron beam was directed at a user defined spot on the sample surface and the X-rays produced from a spot of 1 µm radius detected and identified by the X-ray detector. The response was not compared to a reference standard. Data are presented as elemental spectra with numerical readout (of similar style to that shown in Figure 26) providing semi-quantitative analysis of the elemental composition of the sample.

Elemental mapping was carried out to provide qualitative analysis of the spatial distribution of elements within a sample area. Individual elements are assigned a colour and the distribution shown for each element on an individual map. The intensity of the colour varies with the concentration of the particular element present (Figure 27).

Qualitative EDS analysis was carried out using a Sigma SEM with INCA software and Quanta SEM equipped with an EDS Pegasus 2000 X-ray detector system and Edax Genesis computer software.

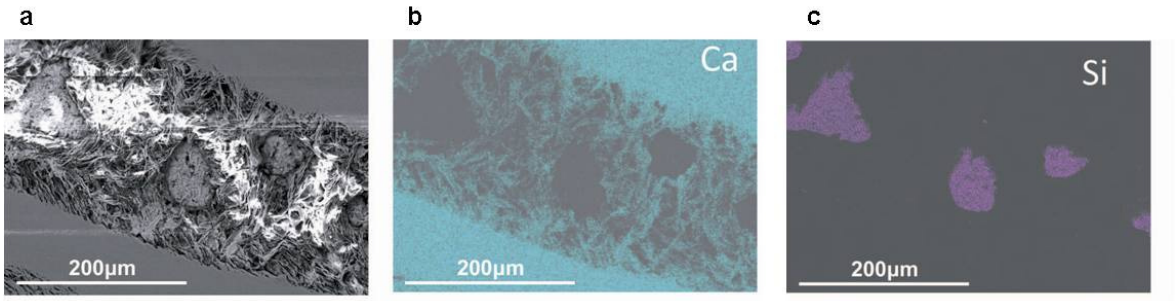

Figure 27. Representative example of electron dispersive spectroscopic (EDS) elemental mapping data.
A SEM image (a) is taken of the selected area and the elemental composition mapped by EDS analysis. The distribution of individual elements across the area is represented in individual maps where each element is assigned a unique colour. In the example above the distribution of calcium is shown in green (b) and the distribution of silica is shown in purple (c).

2.3.4 Electron backscatter diffraction (EBSD)

Electron backscatter diffraction (EBSD) is a sophisticated technique used to obtain high precision analysis of the crystallographic orientation and phase type of a sample. Since the pioneering work of Nishikawa and Kikuchi (1928a, b), the EBSD technique has been gradually refined resulting in the development of an automated, *in situ* analysis technique, (e.g. Alam et al. 1954, Venables and Harland 1973, Dingley and Randle 1992, Lassen 1996, Schwarzer 1997). Early application of automated EBSD analysis was predominantly in the field of metallurgy in the measurement of crystallographic texture in the context of material properties, and for rapid and reliable mapping of multiphase alloys (e.g. Dingley and Randle 1992, Field 1997). Recently, application of EBSD has expanded and has emerged as a powerful tool in the investigation and understanding of biominerals and the biomineralisation process (e.g. Griesshaber et al. 2005, Dalbeck and Cusack 2006, Cusack et al. 2007, England et al. 2007, Griesshaber et al. 2007, Pérez-Huerta et al. 2008a, Pérez-Huerta et al. 2008b, Checa et al. 2009, Pérez-Huerta and Cusack 2009, Freer et al. 2010, MacDonald et al. 2010, Okumura et al. 2010).

2.3.4.1 EBSD technique

EBSD is an SEM based surface analysis technique which requires the sample surface to be highly polished and completely free of topography. A polished crystalline sample is placed in the SEM chamber and the stage is tilted 70º relative to the electron beam (Figure 28). In the SEM chamber, an EBSD camera with a phosphor screen detects the backscattered electrons that have diffracted in the lattice planes near the sample surface.

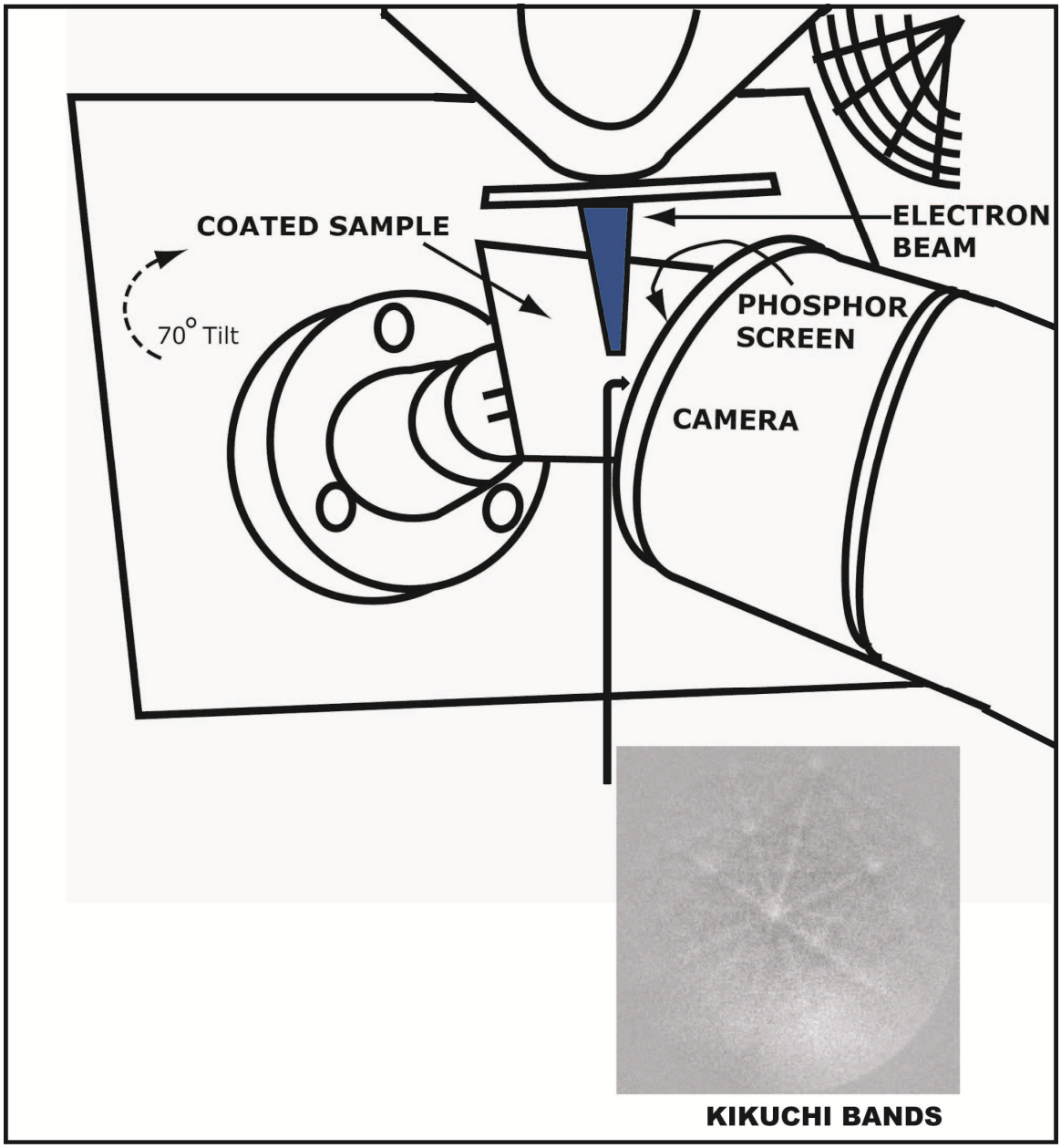

Figure 28. Details of SEM chamber setup for electron backscatter diffraction (EBSD) analysis.
A coated, polished sample is placed in the chamber and the stage is tilted to 70˚ relative to the electron beam. Beam electrons are directed at the tilted sample where they are diffracted by crystallographic planes in the sample and imaged using a phosphor screen and camera.

A beam of electrons, directed at the sample, interacts with the crystal lattice of the sample and is diffracted along crystal planes. Diffracted electrons form a pattern, known as a Kikuchi pattern, which is imaged by a phosphor screen and camera (Figure 28). The configuration of the Kikuchi bands is determined by crystallographic orientation and phase type. Phase files are preloaded before each scan allowing phase type to be identified by closest match based on Kikuchi band position. Thus EBSD enables identification of multiple phase types within a single sample (e.g. Cusack et al. 2007).

The electron beam is scanned across the sample surface to produce patterns for each point on the sample surface, constructing a map of crystallographic orientation and phase. The number of data points produced is dependent on the step size which must be smaller than the smallest crystal size to allow accurate detection of all crystals in a sample.

EBSD analysis in this study is conducted using a Quanta SEM equipped with EDAX OIM 2000 EBSD system with TSL OIM 5.2 data Collection software. All analysis is conducted using an operating voltage of 20 Kv and a spot size of 4 μm.

2.3.4.2 EBSD data analysis and representation

EBSD data in this study are interpreted and maps produced using OIM Analysis v5.3.1 software.

From the configuration of the Kikuchi patterns, EBSD analysis software assigns a solution to the crystal regarding phase type and crystal orientation. The confidence index (CI) of a data point is the reliability of the solution reached during the EBSD scan. The reliability of individual points of the scan can vary as a consequence of several factors including, inconsistency in the topography of the sample and the presence of organic material which can obscure the crystalline structure. The presence of dust particles on the sample surface may also obscure diffraction patterns resulting in a localised reduction in CI.

To ensure that only reliable data are displayed in final data sets, EBSD data collected in this study are subject to a two stage clean-up procedure. Firstly, grain confidence index (CI) standardization was applied with a grain tolerance angle of 5° and a minimum grain size of two pixels. Secondly, neighbour confidence index (CI) correlation was applied. This procedure assigns points of a CI ≤ a given value the orientation of neighbouring points. For each individual scan this was adjusted according to the average CI for the scan. Data were then partitioned so that only grains of CI ≥ a given value are displayed in the final data set. Again, the partition CI value was adjusted for each scan. This clean-up procedure ensures that only reliable data are presented in the final data set on which analysis and interpretation is based.

The final 'cleaned' data set can be viewed and analysed in a number of forms. The crystallographic orientation map represents the orientation of each crystal using a basic RGB colour scheme relative to the normal crystallographic direction. Crystallographic planes are colour-coded relative to the normal crystallographic direction using the colour key shown in Figure 29. Crystallographic orientation maps are produced for each EBSD scan with superimposed crystal models representing crystal orientation (Figure 29).

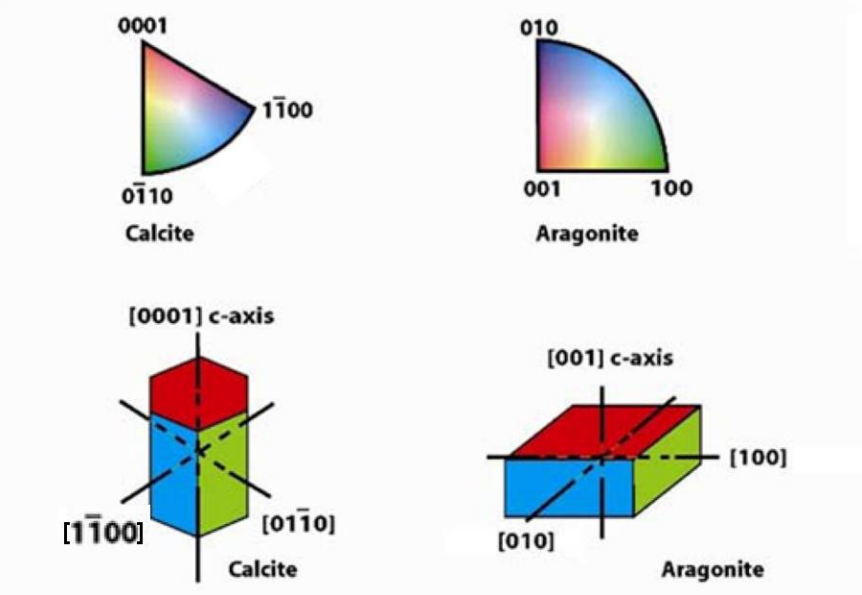

Figure 29. Crystallographic orientation colour keys for calcite and aragonite. Colour keys (top) are presented with reference to the normal direction. Corresponding wire frames (below) represent simplified crystal models showing the colour assigned to crystal planes. Figure from Paul Dalbeck PhD Thesis (2008).

Data are also viewed as pole figures which represent data in stereographic projection. Pole figures show the plot of a pole projected perpendicular to a crystal plane (Figure 30a). Projected poles plot as a single point on a hemispheric projection and so are viewed in 2-D (Figure 30b). Pole figures may represent any crystallographic plane and crystal orientation may be plotted with reference to the direction normal to the sample surface (normal direction ND), the direction parallel to the direction of sample title (Reference direction RD), or with reference to the transverse direction (TD=horizontally across the sample surface).

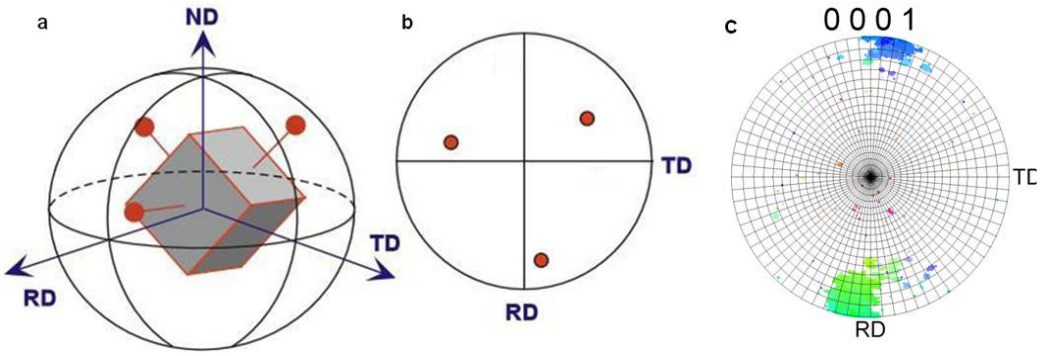

Figure 30. Representation of electron backscatter diffraction (EBSD) data as stereographic pole plots.
(a) Crystal model in 3D space showing projection of poles from crystal planes. Poles are projected and plotted in 2D hemispheric projection in normal projection (b). (a) & (b) are modified from OIM User's Manual (Mahway 2005). (c) Typical pole plot achieved from an EBSD scan, colours are based on orientation colour key shown in Figure 20.

All pole figures plotted in this study represent the {0001} crystal plane of calcite, or the {001} crystal plane of aragonite (therefore representing the crystallographic c-axis), with respect to ND. Points within the stereonet are colour coded using the colour key displayed in (Figure 29).

2.3.5 Raman spectroscopic analysis

Raman spectroscopy is a powerful technique used to identify the chemical structure of materials. It is based upon the fact that almost all light shone on a material will scatter with the same wavelength as the incident light (unmodified radiation or Rayleigh scattering) (Raman and Krishnan 1928). Where vibrations occur in the material, the incident light can undergo an energy shift resulting in a small amount of the incident light being scattered at a different wavelength (modified radiation). Modified scatter radiation was first detected by Raman (1928) and Raman and Krishnan (1928) and was termed Raman Scattering. Raman scattered light is emitted at wavelengths unique to the molecular bonds within the material being investigated, providing information on the chemical structure of the material.

Detection of Raman scattering requires a powerful source of radiation to excite the molecules in the sample. Throughout the 20th century, advances in the development of high powered lasers have facilitated the development of fully automated Raman spectroscopy allowing analysis of almost any material (e.g. Loudon 1963, Ferraro et al. 2003, Bernard et al. 2008). The application of

Raman spectroscopy in the understanding of carbonate structures has long been recognised with synthetic (Bischoff et al. 1983, Bischoff et al. 1985), inorganic (Perez and Martinez-Frias 2003, Edwards et al. 2005, Gunasekaran and Anbalagan 2007) and biogenic carbonates being investigated (Bischoff et al. 1983, Bischoff et al. 1985, Urmos et al. 1991, Lecuyer et al. 2004).

2.3.5.1 Raman spectroscopy technique

In this study, Raman spectroscopy was used to obtain detailed chemical analysis of oyster shell and the cement occupying the contact zone between shell and substrate. All Raman spectroscopic analyses were conducted using a Renishaw Invia Raman microscope equipped with Wire 3.2 Raman software.

A polished, uncoated, sample was placed in the microscope and the microscope focussed at a set magnification of between 5X -100X. A laser is directed at the sample surface and the Raman scattered light is detected by a charged coupled device (CCD) camera. This Raman scattered light is then split into component wavelengths to produce a spectrum. The wavelength of each Raman shift is characteristic of the molecular bonds within the material being investigated. The resulting spectrum can be compared to existing Raman spectra databases.

All Raman spectroscopic analyses in this study were carried out using a 514 nm edge green laser at 100% laser power. Calcite produces three characteristic Raman shifts at 280 cm^{-1}, 712 cm^{-1} and 1086 cm^{-1} (e.g. Bischoff et al. 1983, Bischoff et al. 1985, Urmos et al. 1991, Gillet et al. 1993). To enable detection in this region, spectra were obtained by static scan with a centre of 920 cm^{-1}. Between 10-100 accumulations were carried out per spectra to improve the signal to noise ratio.

2.3.5.2 Raman data analysis and representation

Raman spectroscopy data were processed and analysed using Wire 3.2 software with built-in Raman spectroscopy library.

Fluorescence present within samples causes additional light to be detected raising the background of the resulting spectrum. The baseline of each spectrum

was therefore subtracted to improve the fit and obtain a spectrum with a horizontal baseline allowing better comparison of the Raman shifts detected (Figure 31).

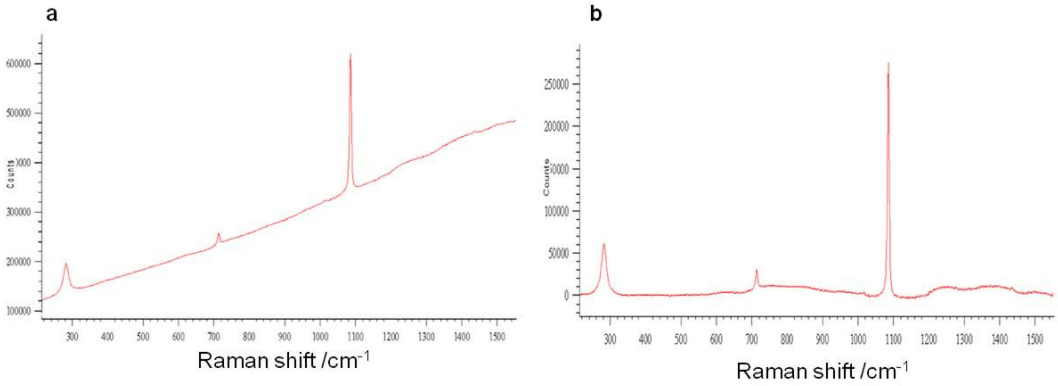

Figure 31. Analysis of Raman spectroscopic data using background subtract. (a) A typical raw Raman spectrum with raised background caused by fluorescence in the sample. (b) Spectrum is analysed with a horizontal baseline, following baseline subtract procedure.

2.3.6 Isotopic analysis

The carbon and oxygen isotope composition of estuarine and marine *C. gigas* samples was determined by stable isotope mass spectrometry at the Scottish Universities Research Centre (SUERC), East Kilbride. The $\delta^{18}O$ value of seawater from Loch Tuath was also determined.

2.3.6.1 Sample preparation for isotopic analysis

Cross sections of the left valves of three estuarine (F8, F9, F10) and three marine (U8, U8, U10) samples were prepared as described in section 2.2.2.

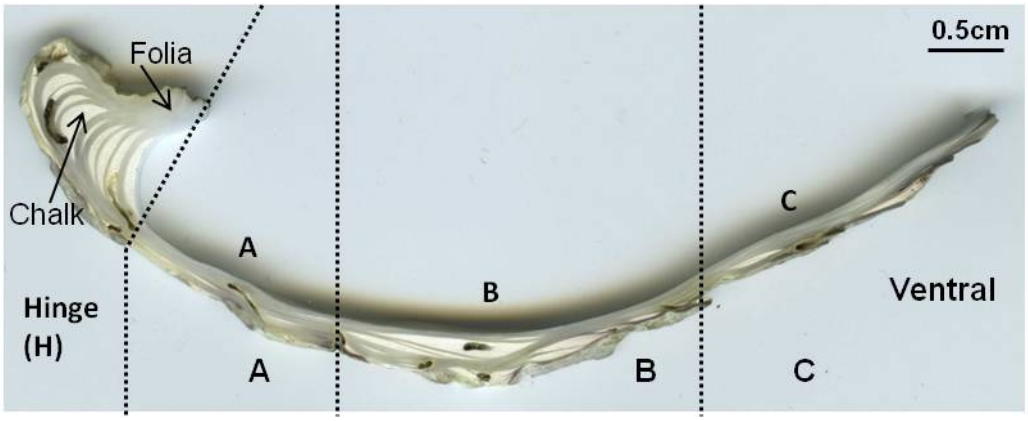

Figure 32. Preparation of samples for isotopic analysis.
Valve cross sections are prepared using methods detailed in section 2.2.2. Left valve cross sections are divided into sub-sections along the dorso-ventral axis labelled hinge (H), A,B,C from hinge to ventral margin. From each section 3 x 1 mg samples of foliated and chalky calcite were milled by micro-drilling.

Valve cross sections were divided into four areas along the height of the valve, labelled as Hinge, A, B and C (Figure 32). From each area, small samples of foliated and chalky shell material were milled under a binocular microscope using a low speed micro-drill with 0.5 mm drill bit. From each section, three 1 mg samples of folia and chalk were collected to allow triplicate analyses of both microstructures from each section. From each oyster shell, a total of 12 samples of folia and 12 samples of chalk were taken, giving a total of 24 samples per valve. A total of three oyster valves were analysed from estuarine and marine sample sets, giving a total of 72 analyses from each, comprising 36 chalk and 36 folia samples.

Powder samples were collected using vacuum suction into eppendorf tubes. Samples were then carefully transferred into glass buckets and weighed. Where valves were particularly thin, most notably in section C (Figure 32), material was scraped off using a scalpel or razor blade. This was necessary to prevent the valve from breaking and causing potential sample contamination. Scraped powder was collected on aluminium foil and transferred to glass buckets. All samples collected weighed 0.8-3.1 mg. Powdered samples were transferred to a Quarum Emitech K1050X solid state plasma asher to remove any organic matter from the samples. The oxygen plasma was set up under vacuum with 60 watt power and left to run for 18 hours to ensure complete loss of organics.

Many authors apply a sclerochronological strategy when sampling oyster shells for isotopic analysis. Growth lines can provide a temporal frame on which to

sample allowing a seasonal pattern of growth to be determined (e.g. Kirby et al. 1998, Surge et al. 2001, Surge et al. 2003, Ullmann et al. 2010, Fan et al. 2011). Growth bands identified in this study, by Mutvei solution staining (see section 2.2.3), are at a spatial resolution of 0.5 mm. A minimum of 1 mg of powder is required when using the Prism mass spectrometer facilities at SUERC. Single 0.5 mm holes drilled in the foliated and chalky calcite could not provide enough material for analysis and thus high spatial resolution sampling of growth lines could not be achieved during this study. As a result bulk sampling of folia and chalk individually at four sections throughout the height of the valve was carried out (Figure 32). It is acknowledged that this will result in 'temperature averaging' (e.g. Jones 1983) and seasonal variation will not be identified. However, deviations from equilibrium will be identified if the maximum and minimum $\delta^{18}O$ values fall outside the calculated equilibrium range (see section 2.3.6.4 for details).

2.3.6.2 Mass spectrometry

Isotopic analysis of shell carbonate was carried out using a VG ISOGAS Prism II mass spectrometer with integrated VG ISOCARB automated preparation system. Following similar methods of McCrea (1950), the carbon and oxygen isotope ratios of $CaCO_3$ samples is determined from analysis of CO_2 produced from the sample on reaction with 103% phosphoric acid (H_3PO_4) at 90ºC. Internal laboratory marble standards (MAB2) were incorporated into each batch of analyses to enable analytical precision to be monitored. Internal standards are calibrated in the International Atomic Agencies (IAEA) Carrera marble comparison standard IAE-CO-1. Reproducibility of MAB2 standards was better than 0.1‰. Raw data are corrected for isotopic fractionation between calcite and CO_2 using a fractionation factor of 7.904 (10^3 lnα) for the reaction with 103% H_3PO_4 at 90°C (Friedman and O'Neil 1977). Contributions from minor isotope combinations (e.g. ^{17}O) in CO_2 molecules are compensated for using the methods of Craig (1957). Carbon and oxygen isotope values are reported in standard delta (δ) calculated using Equation 3.

$$\delta^{18}O_{\text{sample-standard}} = \left(\frac{R_{\text{sample}}}{R_{\text{ref}}} - 1 \right) \times 10^3 \qquad \textbf{Equation 3}$$

Where R is the measured ratio of $^{13}C/^{12}C$ or $^{18}O/^{16}O$ of the sample and internal reference gas standard. Final delta values are reported with respect to the international standards, Vienna Pee Dee Beleminite (VPDB) and Standard Mean Ocean Water (SMOW) using Equation 4.

$$\delta_{X-B} = \delta_{X-A} + \delta_{A-B} + 0.001\delta_{X-A}\delta_{A-B} \qquad \textbf{Equation 4}$$

Where X is the sample gas, A is the internal reference gas and B is the international standard.

2.3.6.3 Oxygen isotope analysis of Loch Tuath seawater sample

A sample of seawater was collected at the time of oyster collection from Ulva Oyster Farm in Loch Tuath. Seawater was collected in a sterile plastic container, sealed and transferred to SUERC for isotopic analysis.

The oxygen isotope composition of the seawater was analysed using the CO_2 equilibration method (e.g. Cohn and Urey 1938, Craig 1957). A 1 ml sample of seawater was carefully measured and placed in a 12 ml exetainer tube. The remaining head space of the tube is flushed with helium prior to injection of 300 µl of CO_2 of known isotopic composition. Exetainer tubes are sealed and left for 24 hours to allow the samples and injected CO_2 to equilibrate. The isotopic composition of the resulting CO_2 is analysed using an AP2000 mass spectrometer with integrated Gilson auto-sampler. Internal gas standards are incorporated into the analysis batch to ensure accuracy. Internal standards are calibrated to SMOW and showed reproducibility of better than 0.1‰. The isotopic composition of seawater is reported in standard delta notation (δ) relative to SMOW.

2.3.6.4 Isotopic equilibrium calculations

The relationship between biogenic carbonates and the temperature of surrounding seawater was first expressed in the 'palaeotemperature scale' for biogenic carbonates pioneered by Epstein et al. (1953). Over the last five decades this has been built upon to allow for advances in analytical techniques (Anderson and Arthur 1983), and to include inorganic carbonates (O'Neil et al. 1969) and aragonite (Grossman and Ku 1986). A recent expression for the oxygen isotope fractionation between calcite and water, at low temperatures, was reported by Kim and O'Neil (1997) and is presented in Equation 5 below. The equation offered by Kim and O'Neil (1997) agrees with that of the updated (Epstein et al. 1953) expression, presented in Chacko et al. (2001) and is used throughout this study.

$$\delta^{18}O_{carb} - \delta^{18}O_{water} = 18.03(10^3/T) - 32.42 \qquad \textbf{Equation 5}$$

Where temperature (T) is in Kelvin and $\delta^{18}O_{carbonate}$ and $\delta^{18}O_{water}$ are with respect to SMOW. Using Equation 5, the range of $\delta^{18}O$ values for carbonate expected under equilibrium conditions was determined. For estuarine and marine sample sets actual seawater temperatures for Loch Fyne and Loch Tuath were substituted into Equation 5 to solve for the range of $\delta^{18}O_{carb}$ values expected under equilibrium conditions. Minimum and maximum annual temperatures were calculated for each site and used to determine the expected range of $\delta^{18}O_{carbonate}$ values expected for isotopic equilibrium. The $\delta^{18}O$ of the Loch Tuath waters was measured and reported with a value of -0.42‰. The $\delta^{18}O$ value for Loch Fyne waters was calculated from average measured salinity values using equation 1 (Austin and Inall 2002) and gave a value of -0.6‰ Calculated and measured $\delta^{18}O_{water}$ values are relative to SMOW.

Expected equilibrium values were converted from SMOW to VPDB scale using Equation 6, in Sharp (2006).

$$\delta^{18}O_{carb}SMOW = 1.03091(\delta^{18}O_{carb}VPDB) + 30.91 \qquad \textbf{Equation 6}$$

2.3.7 Statistical analysis

Statistical analysis of the data was carried out using Excel data analysis function.

2.3.7.1 Student T-test

The student T-test determines the significance of the difference between two population means. The T-test was used in this study to compare values relating to valve dimension and composition from estuarine and marine sample sets. All tests were carried using two tailed equal variance at 5% significance level.

Hypothesis

Null Hypothesis (H_0): There is no statistical difference between sample sets
Alternative hypothesis (H_1): There is a significant statistical difference between sample sets.

The T-test assigns a p value as a measure of the credibility of the null hypothesis (H_0). H_0 may be rejected in favour of H_1 where p=<0.05, i.e. H_0 is valid in <5% of cases.

2.3.7.2 Two way analysis of variance (ANOVA)

Where more than two sample groups are being compared, the T-test is not appropriate. ANOVA is used to compare the variability within and between sample groups. ANOVA was used in this study to determine the significance of inter-sample variability in $\delta^{18}O$/ $\delta^{13}C$ values for folia and chalk within estuarine and marine sample sets.

Hypothesis.

Null hypothesis (H_0): There is no statistical difference in $\delta^{18}O$ or $\delta^{13}C$ isotope composition of folia or chalk between individual samples (three samples) from a single (estuarine or marine) sample set.
Alternative hypothesis (H_1): There is a significant difference in $\delta^{18}O$ or $\delta^{13}C$ values from folia or chalk of different individuals from a single sample set.

A p value is assigned as a measure of the credibility of the null hypothesis (H_0). H_0 may be rejected in favour of H_1 where p=<0.05, i.e. H_0 is valid in <5% of cases.

2.3.7.3 Pearsons correlation coefficient

Pearsons correlation is a measure of the strength of a correlation between two variables. The correlation coefficient was used in this study to determine any significant correlation between values of $\delta^{18}O$ and $\delta^{13}C$ of folia and chalk from both estuarine and marine sample sets. The correlation coefficient is typically denoted by r, the significance of which is taken from Pearsons correlation coefficient table (Clarke and Cooke 2004, Table A5) in two tails at 5% significance level.

Hypothesis.

Null hypothesis (H_0): Values of $\delta^{18}O$ or $\delta^{13}C$ are not significantly correlated.
Alternative hypothesis (H_1): There is significant, positive or negative, correlation in $\delta^{18}O$ or $\delta^{13}C$ values from folia or chalk

Chapter 3. Microstructure, chemistry and crystallography of *Crassostrea gigas*

3.1 Introduction

Biological systems exhibit exquisite control over biomineral production determining mineral polymorphs and microstructural layering sequences (e.g. Weiner et al. 2000, Cusack et al. 2007, Cusack et al. 2008). The result is a robust biomineral structure designed to provide a function that facilitates the survival of the living organism. In addition to this biological control, the secretion and growth of biomineral structures is often closely related to the ambient environment (e.g. Lowenstam 1954, Neri et al. 1979, Checa et al. 2007b, Lartaud et al. 2010a, Lartaud et al. 2010b, Lartaud et al. 2010c). Marine organisms that secrete shells of calcium carbonate can record climatic conditions via proxies of seawater temperature such as $\delta^{18}O$ in their shell carbonate (e.g. Urey 1948, Epstein et al. 1953, Kirby et al. 1998, Ullmann et al. 2010). Often however, such proxies are influenced by both seawater temperature and biological processes making it difficult to isolate a valid temperature signal (e.g. Popp et al. 1986, McConnaughey 1989, Owen et al. 2002, Parkinson et al. 2005, Schöne 2008). The effect of biological processes on temperature proxies is further complicated by prevailing environmental conditions where variations in energy, predation, temperature and salinity can affect the growth rate and shell structure of marine organisms (e.g. Kirby 2000, Kirby 2001, Lartaud et al. 2010a, Lartaud et al. 2010c).

Analysis of shell microstructure, crystallography and chemistry provides valuable insights into the arrangement and growth of the shells of marine organisms. Such knowledge is invaluable in the interpretation of environmental proxies stored within the shell carbonate (e.g. Schöne 2008) and will also further our understanding of the efficient formation and design of biomineral structures.

Since their first appearance in the Triassic (Stenzel 1971), oysters have successfully expanded to occupy a range of habitats with global distribution.

Such success, which may be attributed to their unique shell structure, makes oysters potentially ideal candidates to study environmental change.

3.1.1 Oyster shell structure, previous work

The global distribution, geological longevity and economic importance of oysters have brought them to the forefront of many scientific studies since the earliest 20th century with pioneers in the field such as Gray (1833), Nelson (1924) and Orton et al. (1927).

Widescale investigations into the shell structure of the oyster have been made by several authors (e.g. Yonge 1960, Galtsoff 1964, Stenzel 1971, Carriker et al. 1980). These authors report that the shell of the oyster (Ostreidae) is composed of low magnesium calcite with aragonite restricted to the myostracum and hinge region. Both valves of the adult oyster shell are composed predominantly of foliated calcite which is bound on the outermost surface by prismatic calcite and is frequently interrupted by lenses of chalky calcite. These structures are summarised in Figure 33. The myostracum is composed of aragonite and extends dorsally from the adductor muscle scar to the umbo (Figure 33). This microstructural arrangement of the oyster shell classifies them in the foliated group of bivalves (Kobayashi and Samata 2006). However this simple classification does not identify the chalky calcite lenses which interrupt the foliated structure of most oyster shells (Carriker et al. 1980). Oyster shell structure can be further interrupted by chambers (e.g. Korringa 1951, Galtsoff 1964, Stenzel 1971, Higuera-Ruiz and Elorza 2009). Where present, chambers of varying size are sporadically distributed throughout the shell with varying frequency.

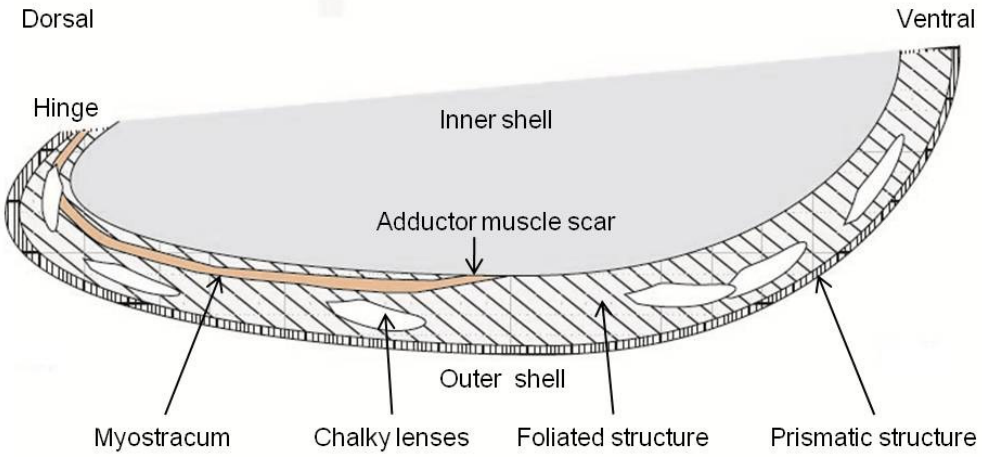

Figure 33. Oyster shell microstructure. Diagrammatic representation of the structural components of a typical shell of *C. gigas*.
Cartoon represents a typical shell of about 8cm in height that has been cut along the dorso-ventral axis.

The section of the oyster shell in Figure 33 does not include detail of the hinge and ligament. The hinge area and ligament of the oyster shell is morphologically complex with several microstructural subdivisions which are shown in Figure 34.

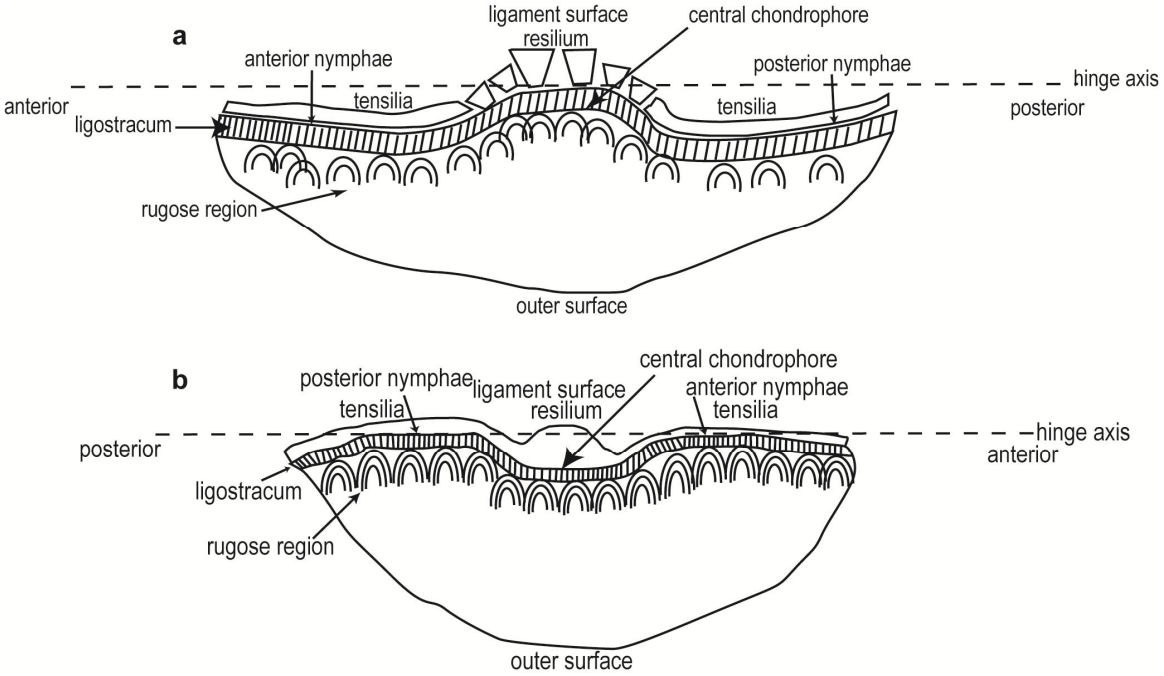

Figure 34. Schematic section of the hinge of the oyster.
(a) Schematic diagram of the hinge region of the right valve, viewed from ventral marign towards umbo. (b) Schematic diagram of the hinge region of the left valve, viewed from ventral margin towards the umbo. Diagrammatic representation of text in Carriker and Palmer (1979) and Carriker et al. (1980).

The ligament is a predominantly non-mineralised structure which may be divided into the central resilium which is flanked anteriorly and posteriorly by the tensilia (nymphae of other authors). The resilium is attached to the mineralised

shell at the chondrophore (resilifer, Stenzel 1971), which is bounded by the anterior and posterior nymphae (bourrelets, Stenzel 1971) to which the tensilia attach. A thin mineralised structure, termed the ligostracum, lies between the calcified shell and the organic ligament. The ligostracum acts to bind the ligament to the surface of the shell (Carriker and Palmer 1979, Carriker et al. 1980). Underlying the ligostracum, foliated calcite is folded to form a 'rugose region' (Carriker et al. 1980).

3.1.2 Effect of environment on oyster shell structure

Oysters (specifically those of genus *Crassostrea*) have adapted to survive in a wide range of environmental conditions (Troost 2010) and the effect that the external environment has on shell morphology and growth rate is significant (Palmer and Carriker 1979, Surge et al. 2001). Variation in shell shape and ornamentation is largely determined by the topography of the substrate on which the oyster is cemented (e.g. Lewy 1972, Harper 1992, Troost 2010). Growth rate, valve thickness and quantity of chalk are greatly affected by external environmental conditions such as temperature, salinity, energy and predation (e.g. Key et al. 1976, Palmer and Carriker 1979, Kirby 2000, Kirby 2001, Lartaud et al. 2010a, Lartaud et al. 2010c, Higuera-Ruiz and Elorza 2011). Palmer and Carriker (1979) report variation in valve thickness and density between oysters grown in three different environments. Palmer and Carriker (1979) attributed variation in valve density to the volume of chalk present, and found that valves were most dense (contained less chalk) in oysters grown in 'recycled cultural systems' compared with 'flow-through cultural systems' or natural estuarine environments. Rate of growth band deposition was also reported to be variable between environments (Palmer and Carriker 1979). Similarly,Lartaud et al. (2010c) report higher growth rates of *Crassostrea gigas* grown in exposed sites, compared with more protected sheltered areas. Valve thickness and chalk volume has also been reported to vary as a response to temperature, energy (Ruddy et al. 1975, Key et al. 1976, Higuera-Ruiz and Elorza 2011), salinity (Medcoff 1944) and predation (Kirby 2001). Okoshi et al. (1987) demonstrated that while the appearance of chambers is probably, to a large degree, genetically controlled, chambers often form as a response to changing environmental conditions. For example, recently Higuera-Ruiz and

Elorza (2011) demonstrated that the presence of fine sediment can induce chamber formation. The appearance of chambers has also been attributed to pollutants, such as tributyltin (TBT) in the water (e.g. Alzieu et al. 1986, Higuera-Ruiz and Elorza 2009). Increases in CO_2 have also been reported to have a negative effect on oyster shell growth rate, hardness and crack resistance (Beniash et al 2010).

3.1.3 Aims of this study

Many authors have demonstrated that estuarine and brackish water oysters are suitable for use in palaeoclimatic studies (e.g. Kirby et al. 1998, Kirby 2000, Surge et al. 2001, Surge et al. 2003, Fan et al. 2011). However, only Ullmann et al (2010) have considered the relationship between shell chemistry and the ambient environment from oysters inhabiting coastal marine environments. Since oyster shell growth rate and macrostructure can vary in response to prevailing environmental conditions (Kirby 2000, Kirby 2001, Lartaud et al. 2010b, Lartaud et al. 2010c), such a response may alter the isotopic signal of the shell by producing kinetic isotope fractionation.

This study aims to characterise the microstructure, chemistry and crystallography of both valves of the oyster, *C. gigas* from estuarine and marine environments. Specifically the study aims to gain a full understanding of shell structure of both estuarine and marine oysters to provide a context for subsequent isotopic analysis.

3.2 Results

3.2.1 Physical characteristics of shells of estuarine and marine oysters

Samples of *C. gigas* farmed in an estuarine environment at Loch Fyne, Scotland (samples F1 – F13) were collected for comparison with *C. gigas* farmed in an open marine environment off the Island of Ulva, Scotland (samples U1-U10). From each environment ten samples were analysed for comparison. A further

three estuarine samples were prepared for additional analysis of the hinge region.

All samples were collected alive and were three years old at the time of collection. Samples were disarticulated and prepared by methods described in section 2.2. From each sample, three principle dimensions of both valves were measured for comparison. These dimensions include, based on the biometric indices defined by Galstoff (1964), valve height (maximum measurement between umbo and ventral valve margin) and valve length (maximum measurement from anterior-posterior margins parallel with hinge axis). Valve thickness represents the maximum measurement from the interior to exterior surface of individual valves. The Shell Thickness Index (STI) (as defined by Alzieu et al. 1986) was calculated for each sample, where STI=height of right valve/thickness of right valve. Dimensions of all valves analysed in this study are presented in Appendix A.

For comparison, the average valve dimensions of ten marine and ten estuarine samples are shown in Table 1. There is no significant difference in valve height or length of estuarine and marine samples. However, both valves of marine oysters are more variable in all dimensions compared with estuarine oysters. The thickness of both right and left valves is significantly greater in marine specimens than estuarine specimens (T-test, p=0.01, p=0.001 for right and left valves respectively). Both sample sets are considered to be of 'normal' shell thickness, with an average STI >10 (Alzieu et al. 1986). In marine samples however, two oysters (samples U5 and U7) show abnormal thickening, with a STI of 5.9 and 8.6 respectively (Appendix A)

	Height		Length		Thickness		Thickness Index
	Right Valve	Left Valve	Right Valve	Left Valve	Right Valve	Left Valve	STI
Estuarine *C. gigas* Loch Fyne	7.65 ± 0.85	9.20 ± 0.97	4.12 ± 0.54	4.88 ± 0.92	0.36 ± 0.11	0.45 ± 0.19	23.7 ± 9.4
Marine *C. gigas* Ulva	7.73 ± 1.09	8.63 ± 1.23	4.53 ± 0.88	4.87 ± 0.93	0.57 ± 0.22	0.78 ± 0.20	15.7 ± 7.0

Table 1. Average valve dimensions of 10 specimens of *C. gigas* from estuarine and marine environments.

Estuarine samples are relatively uniform in terms of shell colour and ornamentation. Exterior surfaces of both valves are white or dark grey with

frequent purple pigmentation most notable at the ventral margin. Fine, irregularly spaced concentric lamellae are present on the external surface of some samples, most pronounced on left valves. Folds on the shell surface perpendicular to the ventral margin, antimarginal ribs (Checa and Jimenez-Jimenez 2003), are occasionally noticeable on the left valves but not on the right which are relatively smooth. The interior surfaces are smooth, white or light grey. No encrusting organisms were found on the exterior surface of any valve. However, at the umbonal region of the right and left valve of sample F2, two scars were identified, possibly from previous encrusting organisms.

Marine samples are more variable in shape, colour and ornamentation. The exterior surfaces of most marine valves are dull or dark grey with blotches of purple pigmentation randomly distributed across the height and length of the valve. Both right and left valves of most of the marine samples, have coarse lamination on the exterior shell surface. Lamellae are deep and irregularly spaced. Both valves of sample U3 are relatively smooth with no ornamentation. Antimarginal ribs are occasionally evident on the exterior surface of the left valves but not the right. Interior surfaces are dull grey, with some patches of darker material which appears as mud blisters trapped beneath the interior shell surface. Blister areas stand proud relative to the rest of the interior surface. The presence of mud blisters is characteristic of infestation from mud worms (e.g. Almeida et al. 1998, Royer et al. 2006, Chambon et al. 2007). Mud worms, such as Polydora and Polychaeta, accumulate mud which is then later covered by shell material (Royer et al. 2006, Chambon et al. 2007). The outer surfaces of both valves of all marine samples are heavily encrusted with barnacles, young oysters and tube worms.

3.2.2 Macrostructure of shells of estuarine and marine oysters

Shell macrostructure is used to describe all aspects of the shell structure that are visible by light microscopy.

From estuarine and marine environments, right and left valves of three oysters (estuarine samples F1, F2, F3 and marine samples U1, U2, U3) were sectioned along the dorsal-ventral axis, on anterior and posterior sides of the adductor

muscle scar, to create a continuous section along the full height of the valve (as described in section 2.2.2). These sections were observed by optical microscopy.

In cross section, both valves of estuarine samples are composed of dull opaque calcite with frequent white chalky lenses of varying size irregularly distributed throughout the valve height and thickness. Valves are complete with no cavities evident (Figure 35a).

Figure 35. Comparison of *C. gigas* from estuarine & marine environments. (a) Radial section of the right valve of *C. gigas* from an estuarine environment. (b) Radial section of the right valve of *C. gigas* from a marine environment.

Valves from the marine environment are composed of dull opaque calcite with occasional chalky lenses and frequent cavities. These cavities may be vacant or filled with sediment including sand grains and mud (Figure 35b). Spionid worms bore u-shaped hollows in the shell which are connected to the shell exterior (Zottoli and Carriker 1974). Boring worms induce the formation of blisters in the shell as shell material is secreted around the worm to isolate it (Royer et al. 2006). It is likely that cavities within the marine valves are related to the presence of Spionid worms. Most cavities are found within, or closely associated with chalky lenses. The outline shape of the cavities is also very similar to the shape of chalky deposits. In some marine samples however, mud blisters are not evident on the interior surface. In this instance cavities are present, but do not show internal u-shaped morphology and are not connected the valve exterior. It is considered that these cavities are not related to Spionid worms. Galtsoff (1964) differentiates between 'blisters' formed by the presence of worms and chambers which are defined as 'regular structural features'. Some empty cavities in marine samples in this study are related to the presence of Spionid

worms while others are not. These cavities are not however 'regular' and so the term 'chamber' is not applicable. The term 'cavity' is used throughout this study as a general term for any 'empty space' observed in the oyster shell structure.

3.2.3 Quantitative imaging analysis

The distribution and quantity of chalk, folia and cavities within oyster shells was analysed using the Image J image processing programme. The radial sections, described above, were digitally scanned and coloured to highlight chalky lenses, foliated calcite and cavities (see section 2.3.1 for details). These sections were analysed by Image J to determine quantitatively the area of each section occupied by chalk, folia and cavities. Results of section composition analysis are considered to be indicative of whole valve composition.

Figure 36 shows the percentage area of each valve occupied by chalk, folia and cavities from both sample sets. Cavities in marine samples, occupy on average 6.4 ± 8.8% and 1.2 ± 1.3% of total valve area of right and left valves respectively. Cavities were not present in any of the estuarine samples analysed in this study. The total valve area occupied by foliated calcite for the right valves is not significantly different between environments (75.2 ± 15.7% for estuarine samples and 82.8 ± 8.2% for marine samples). Comparison of the left valves however shows significantly more foliated calcite in the left valves of marine oysters when compared to estuarine samples (T-test, $p=0.03$) (Figure 36). This increase in folia corresponds to a decrease in valve area occupied by chalk in marine samples compared with estuarine. Both sample sets however show considerable variation in chalk volume.

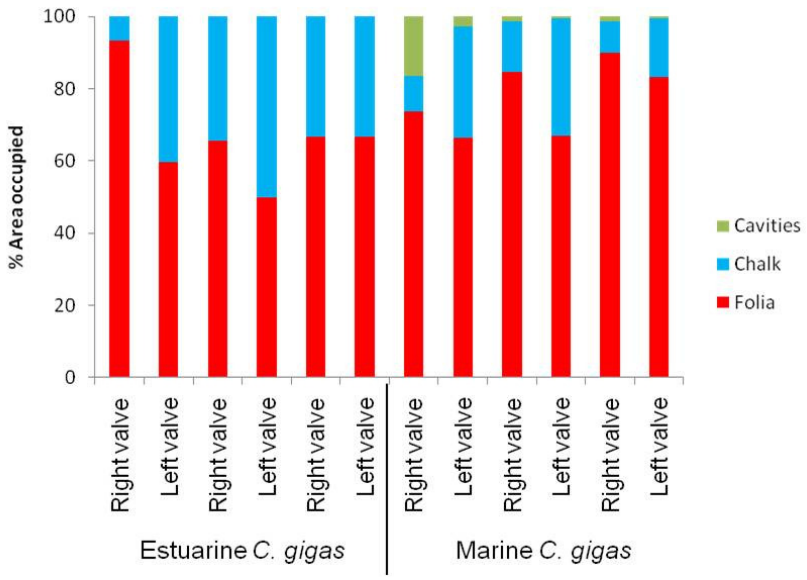

Figure 36. Comparison of quantities of chalk, folia and cavity distribution in cross sections of estuarine and marine specimens of *C. gigas*.

From both sample sets chalky calcite occupies significantly more area in the left valve than the right valve (T-test, p=0.04) (Figure 36). The right valve is composed of, on average, 17.8±12.7% chalky calcite compared to the left valve in which chalky calcite occupies, on average, 33.9±11.2% of the overall valve space. The total amount of chalk present is inconsistent between estuarine and marine samples. Estuarine samples contain an average of 24.8±15.8% and 41.3±8.4% chalk in the right and left valves respectively. In marine samples chalk occupies an average area of 10.8±2.9% in the right valve and 26.5±8.9% in the left valve. Marine samples contain less chalk than estuarine samples, however marine valves host cavities associated with chalky lenses. These cavities were never found in estuarine samples (Figure 35 & Figure 36).

3.2.4 Microstructure

While valve thickness, chalk volume and presence of cavities vary between estuarine and marine samples, overall ultrastructure and microstructural arrangement of the shells is constant between environments and so no distinction between environments is made during discussion of shell microstructures. Images presented of the internal shell structure represent the best images from both estuarine and marine sample sets.

With the exception of the hinge region, the microstructural arrangement of both right and left valves of *C. gigas* is broadly identical. Both valves are composed of four principle mineralised microstructures (e.g. Yonge 1960, Galtsoff 1964,

Stenzel 1971, Carriker et al. 1980) as summarised in Figure 33**.** These include calcite layers which are classified as the prismatic structure, foliated structure and chalky lenses. Aragonite is present at the myostracum. The hinge region of the oyster shell is composed of a complex network of calcite and aragonite crystals embedded within an organic framework. There are considerable differences in the hinge region of the right and left valves in terms of polymorph distribution, morphological arrangement and crystallographic orientation, and so the hinge region of right and left valves will be discussed separately.

3.2.4.1 Prisms

The prismatic layer of both valves consists of parallel, closely packed prisms of low Mg calcite (Galtsoff 1964, Stenzel 1971, Carriker et al. 1980, Checa et al. 2005, Checa et al. 2009). Prisms, as shown in Figure 37, are broadly hexagonal, orientated with the long axis of the prisms perpendicular to the outer shell surface.

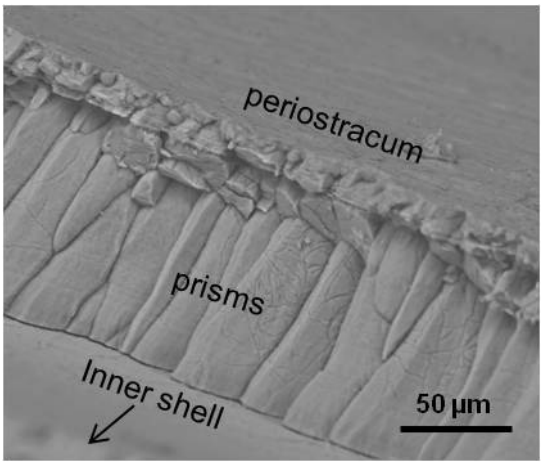

Figure 37. Backscattered electron SEM image of a fractured shell section revealing the prismatic layer.

Previous studies of the microstructure of *Crassostrea virginica,* identified calcite prisms as the outermost mineralised layer of both right and left valves (Galtsoff 1964, Carriker et al. 1980). However, for other species including *C. gigas* and *Ostrea edulis,* it is reported that the prismatic region is restricted to the right valve and does not appear in the left (Taylor et al. 1969, Checa et al. 2005). In the *C.gigas* samples analysed in this study, calcite prisms form the outermost mineralised layer of both valves. These prisms are, however, considerably less

conspicuous in the left when compared to the right (Carriker et al. 1980, Higuera-Ruiz and Elorza 2009).

Prisms of the right valve typically range from 100-190 µm in height and 10-37 µm in width (Figure 38a). Prism height and width becomes reduced in older shell parts, on the dorsal side of the adductor muscles scar, to 18-22 µm in height and 5-12 µm in width. Left valve prisms are consistently smaller and range from 11-31 µm in height and 9.5-17.7 µm in width. In some cases, the prisms of the left valve are not visible (Checa et al. 2005). Occasionally, prisms are overlain, to the exterior, by a significant layer of chalk (Figure 38b)

In the right valve individual prisms are stratified with a repetitive series of thin lines traversing the surface of the prisms perpendicular to the long axis and parallel - subparallel to the growth surface (Figure 38a). These thin lines are interrupted by thicker alternating light and dark bands (Figure 38c). Both forms of stratification show lateral continuity between prisms (Figure 38a & c) and are most prominent at the base of the prisms becoming less obvious, and occasionally absent, towards the external surface. This stratification is similar to that reported for the prismatic region of the right valve of *C. virginica* by Carriker et al. (1980). Carriker et al. (1980) reported bands corresponding to periods of winter growth cessation. Stratification of the prismatic region was also reported by Higuera-Ruiz and Elorza (2009) for *C. gigas* from the Bay of Biscay. In the present study, prisms of the left valve are homogenous and lack any stratification.

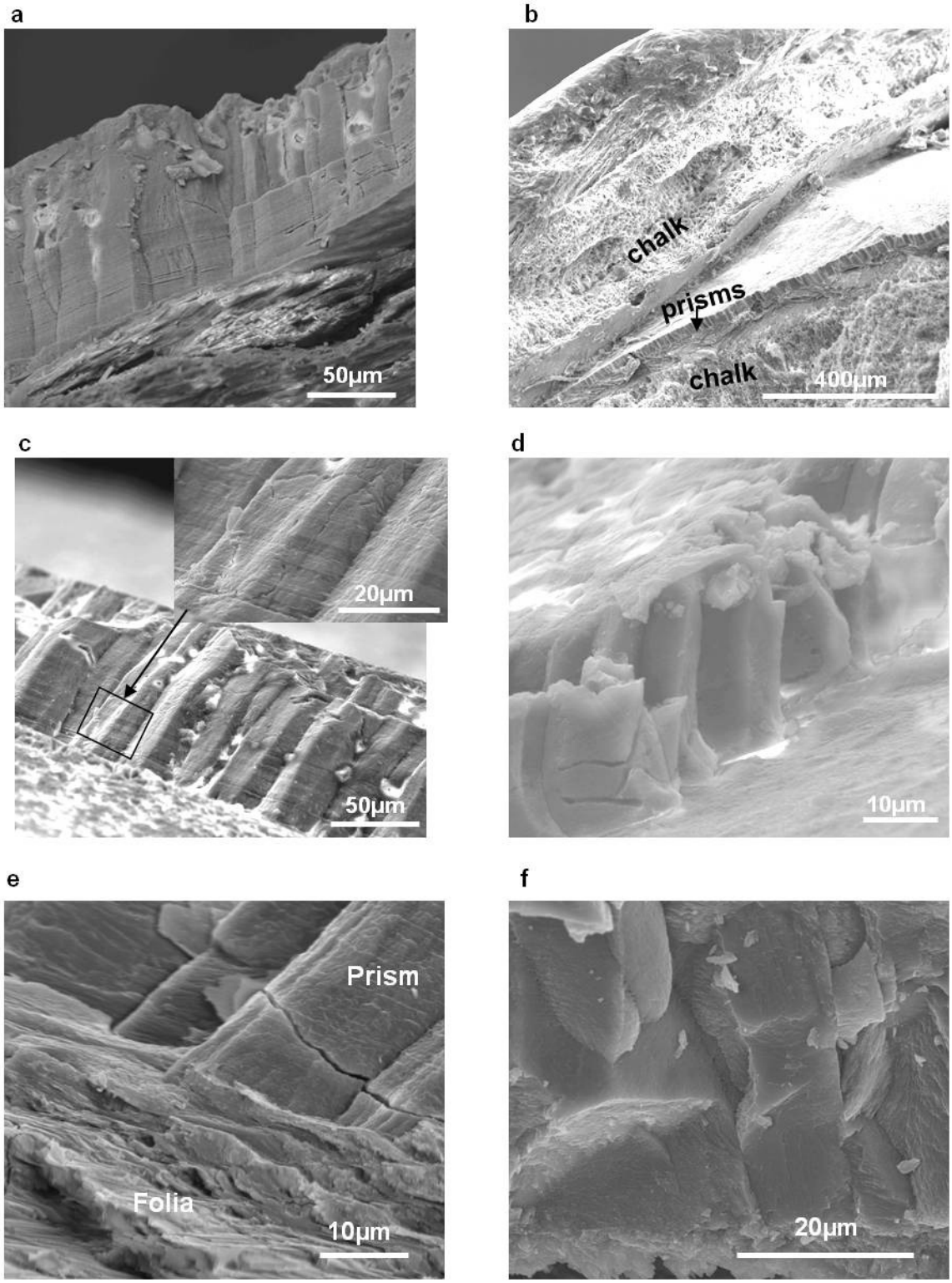

Figure 38. Secondary electron and mixed secondary and backscattered electron SEM images of fracture sections of right and left valves of *C. gigas* revealing details of the prismatic layer.
(a) Secondary electron and backscattered electron mixed SEM image of prisms of right valve with repetitive series of thin lines traversing the surface. (b) Secondary electron SEM image of prisms of the left valve with reduced height and obscured beneath a significant layer of chalk. (c) Secondary electron SEM image of right valve prisms showing alternating light and dark bands perpendicular to the long axis of the prisms and high magnification image of this banding stratification. (d) Secondary electron SEM image of organic sheaths with no mineral infill. (e) & (f) Internal foliated structure of prisms, images are secondary and backscattered electron mixed image and secondary electron image respectively.

A thick organic coating extends from the exterior surface of the prisms, between prisms toward the shell interior creating interprismatic organic walls (e.g. Stenzel 1971, Carriker et al. 1980, Checa et al. 2005, Higuera-Ruiz and Elorza 2009). Organic walls normally enclose the mineralised part of the prism, however occasionally organic walls are present with no mineral infill (Figure 38d). Empty organic envelopes have also been reported in *C. virginica* and O. *edulis* by Carriker et al. (1980) and Checa et al. (2005) respectively.

Fracture sections of the prismatic structure reveals that prisms of both valves are composite materials composed of individual lath shaped crystals (Figure 38e & f). This internal structure, reported previously by Esteban-Delgado et al. (2008) and Checa et al. (2009), is not apparent on polished sections or where the surface of the prisms is obscured by a thick organic layer.

In both valves, the base of the prismatic unit, as shown in Figure 39, is abruptly truncated at the interior margin by a homogenous, dominantly organic, transitional zone (Watabe and Wilbur 1961). This transition zone varies in thickness from 6–60 µm. Some small crystals, mainly disorganised laths, are visible within the transition zone (Figure 39). The structure of the transition zone observed in this study is very similar to that identified by Esteban-Delgado et al. (2008, Figure 3E). Towards the shell interior these laths become progressively organised eventually becoming aligned to form the underlying foliated structure (Figure 39).

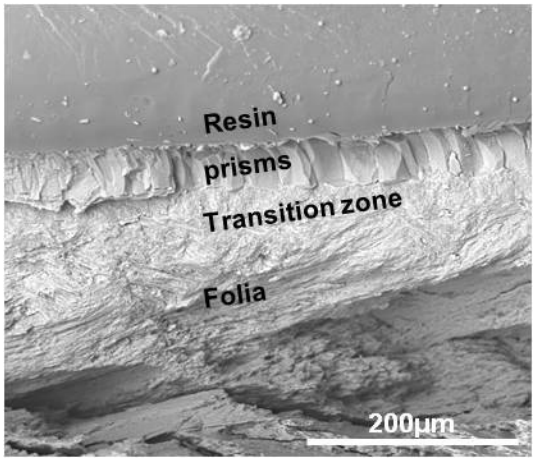

Figure 39. Backscattered electron SEM image of a fractured valve of *C. gigas* revealing the transition zone between prismatic region and foliated structure.
The nature of the transition zone is similar in both right and left valves.

3.2.4.2 Foliated structure

The bulk of both valves of *C.gigas* are composed of foliated calcite. This microstructure is composed of long, tabular laths of low Mg calcite orientated with the long axis of the lath parallel to the growth surface. Individual laths are joined laterally to form sheets, termed folia (Watabe and Wilbur 1961, Watabe 1965, Carriker et al. 1980, Runnegar 1984, Checa et al. 2007a). Sheets of folia are stacked vertically to form the foliated structure (Figure 40a & b). The nature of the foliated structure is similar in both valves.

Laths comprising a single sheet of folia are parallel or sub parallel, (Figure 40a & c) joined laterally and typically range from 0.9–3 µm wide and 0.1-0.6 µm thick. These dimensions appear to remain constant along the length of individual laths, however the full length of the long axis of individual laths could not be found. Intercrystalline organic material is much less conspicuous in the folia than in the overlying prismatic region, but is occasionally noticeable on fracture surfaces, occurring between sheets of folia and occasionally present at the boundaries between laths (Figure 40c).

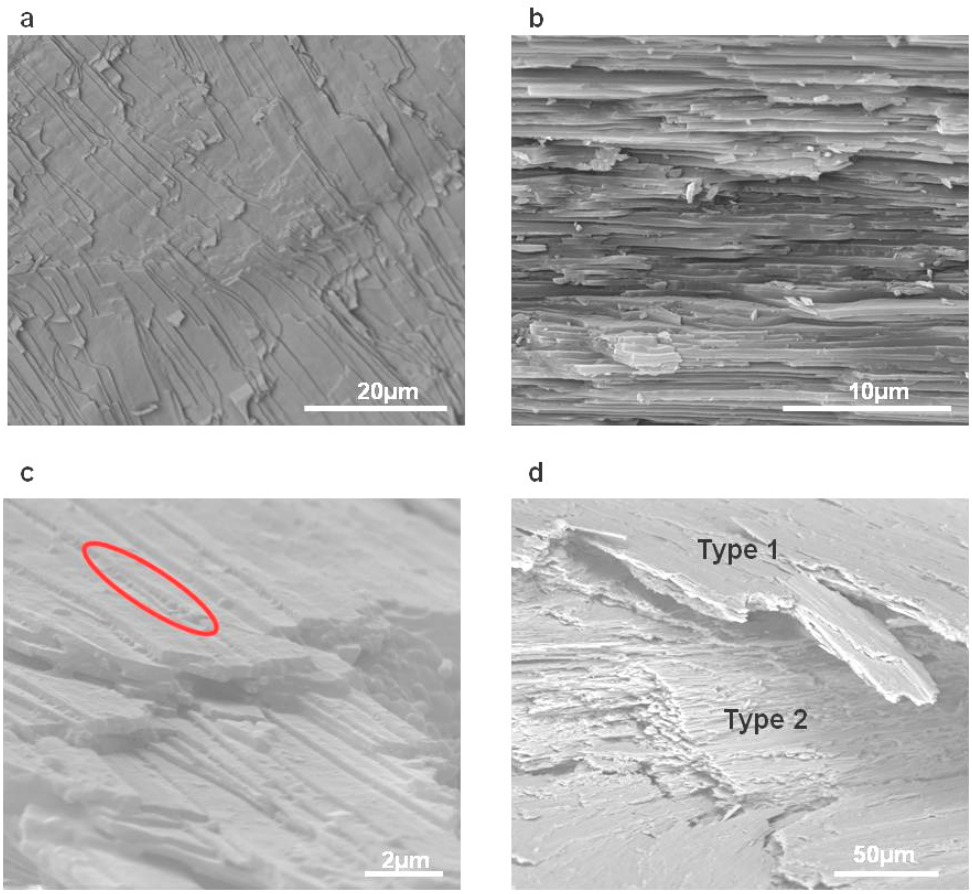

Figure 40. Secondary electron and backscattered electron SEM images of fractured valve sections of *C. gigas* revealing details of the foliated structure.
(a) Backscattered electron SEM plan view image of folia showing laths arranged laterally. (b) Secondary electron cross section SEM image of folia showing laths stacked vertically. (c) Secondary electron SEM image of organic matter covering surface of laths highlighted by red circle. (d) Backscattered electron SEM image showing clusters of laths of alternating orientation.

With the exception of areas near transition zones with neighbouring microstructures, sheets of laths are highly organised and exist as a series of clusters of alternating orientation (Figure 40d). Clusters of foliated sheets are referred to as having type 1 or type 2 orientation (Lee et al. 2008a). Using Alicona Mex 3D modelling software, the orientation of the two lath types was determined. A three dimensional model of clustered folia is displayed in Figure 41. Laths of type 1 orientation are orientated with the long axis of lath parallel with the dorso-ventral axis, while type 2 laths are parallel to each other, but orientated up to 45° to type 1. Both type 1 and type 2 laths are occasionally tilted with respect to the outer shell surface.

The foliated microstructure is frequently interrupted and occasionally dominated by lenses of chalky calcite deposits. The switch between the chalky and foliated microstructures may be extremely abrupt with no transition zone (Figure 45a),

gradual (Figure 45b & c) or marked with a thin transition zone comprising disorganised clusters of laths and organic matter (Figure 45d). The transition between the 2 microstructures is described fully in section 3.2.4.4.

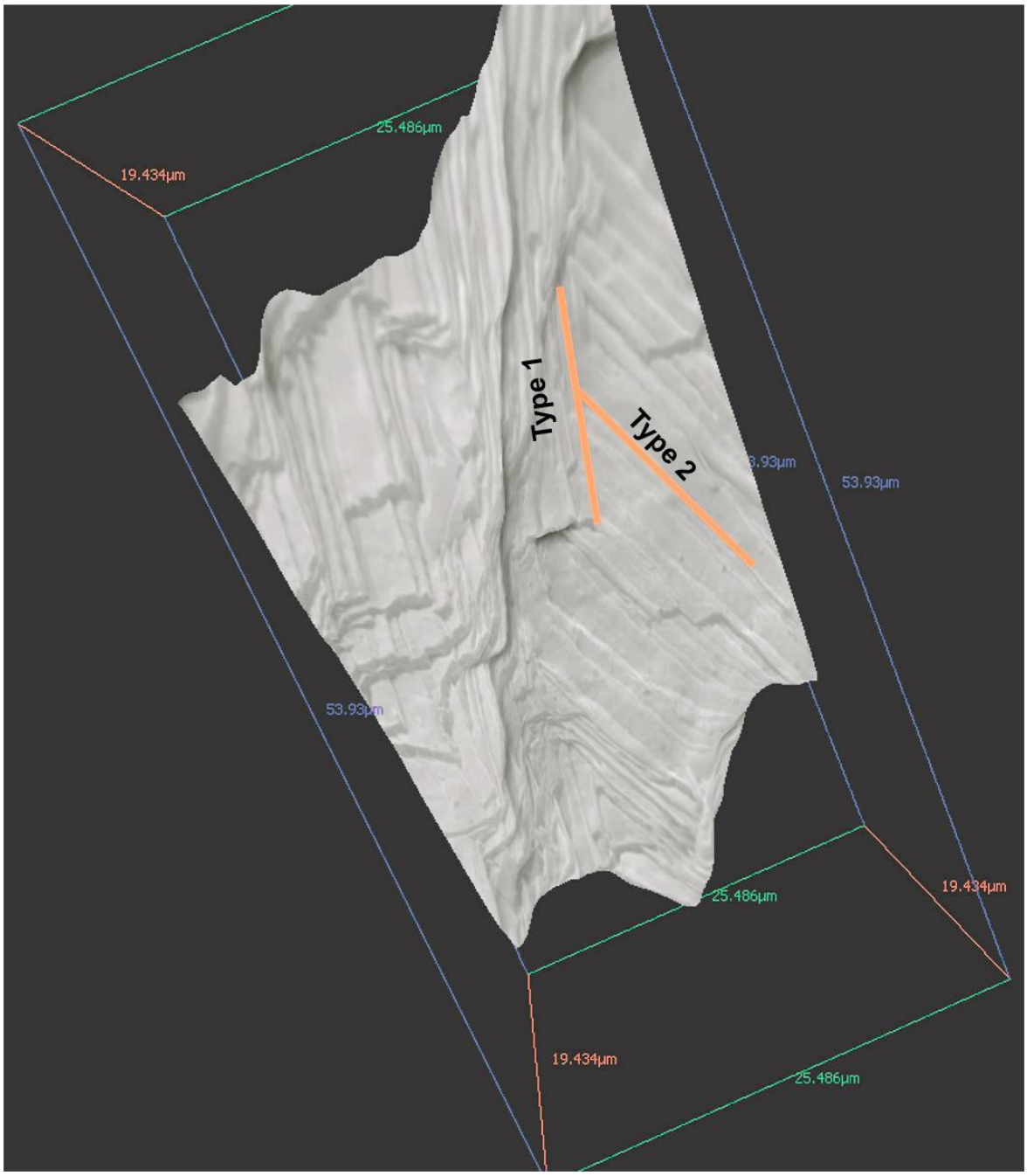

Figure 41. 3D model of foliated structure showing alternating lath orientation. Type 1 laths are orientated with long axis parallel to the dorso-ventral axis, type 2 laths are orientated 30-45° from type 1 axis.

3.2.4.3 Chalky lenses

Chalky lenses can be observed with the naked eye as soft, white areas of the shell (Figure 42). In marine samples, these are frequently found to host or be closely associated with cavities which can be filled with sediment (Figure 42). Cavities are not present in estuarine samples (Figure 35). Chalky deposits form discontinuous lenticular bodies of varying size and are considered to be normal components of the shell (Carriker et al. 1980). At the hinge region, chalk lenses can form as regularly spaced, parallel, crescent shaped lenses of varying size (Figure 42a). Ventral of the hinge region chalk lenses are irregularly distributed, most frequently within the body of the shell interrupting the foliated microstructure (Figure 42b). However, chalk lenses are occasionally found overlying the prismatic region (see section 3.2.4.1).

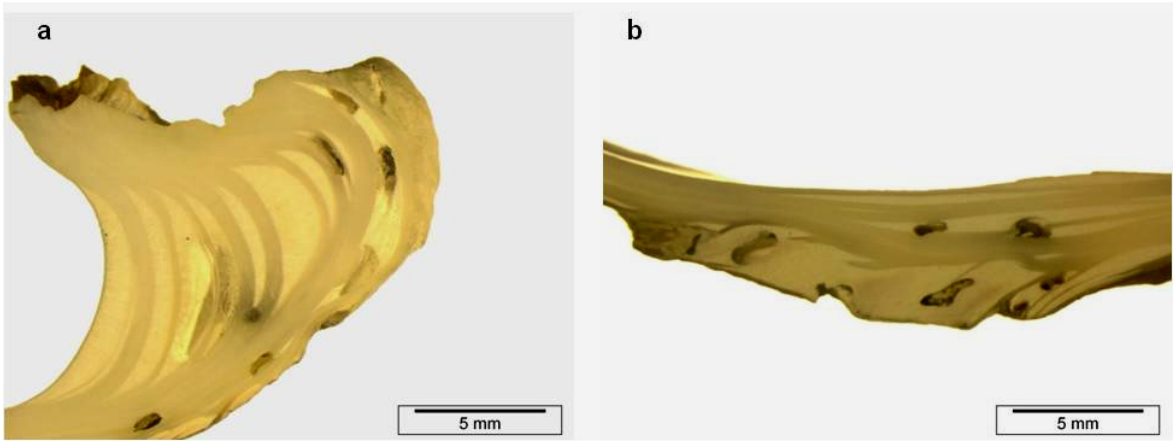

Figure 42. Optical microscopy images of radial shell sections revealing distribution and shape of chalky lenses.
(a) Chalk lenses at hinge region form regularly spaced crescent shaped lenses. (b) Ventral of the hinge, lenses are more irregular in distribution and shape. In all sections of the marine samples (pictured) cavities are closely associated with chalk lenses.

The positioning of chalky lenses within valves appears sporadic. However, significantly more chalk is present in the left valve compared with the right (see section 3.2.3 for discussion). On average, chalk occupies 17.8±12.7% in the right valve compared with 33.9±11.2% in the left valve. This difference in chalk volume between valves is evident in samples from both estuarine and marine environments, however the overall area occupied by chalk in marine samples is less than in estuarine shells (Figure 36).

Despite the difference in the volume of chalk between estuarine and marine samples the microstructure of the chalk is consistent between the two sample sets.

3.2.4.4 Chalk morphology

Chalky deposits comprise extremely thin, smooth, platy, calcite blades and sheets of various sizes. Within the microstructure it is possible to define a set of parallel main blades (Carriker et al. 1980, Higuera-Ruiz and Elorza 2009) predominantly orientated with the long axis of each blade perpendicular to the inner and outer surface of the valves, from which smaller leaf-like microstructures, termed 'leaflets' (Carriker et al. 1980) ('Spurs' of Margolis and Carver 1974) branch at varying angles (Figure 43).

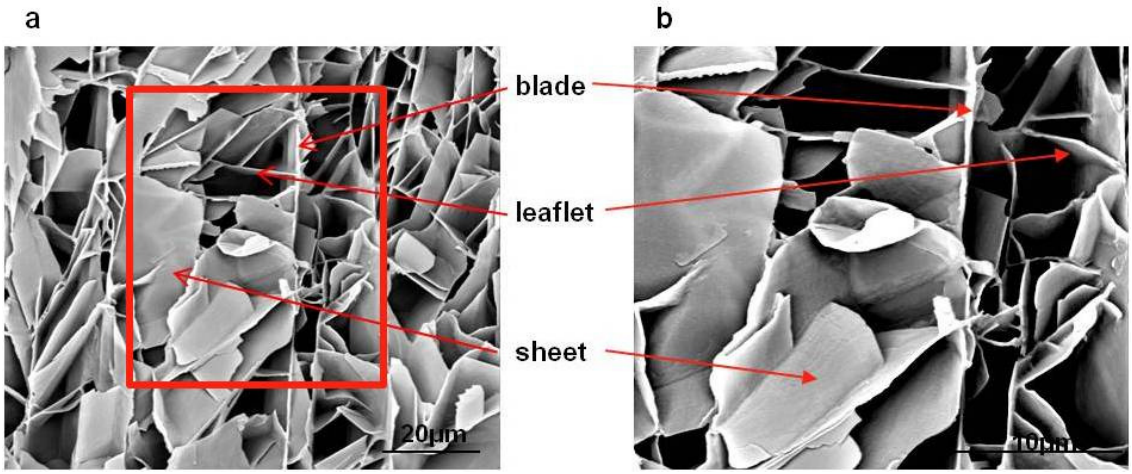

Figure 43. Backscattered electron SEM images of fractured section of the right valve revealing structural components of chalky lenses.
(a) Low magnification image of typical chalk lens. (b) High magnification image of area enclosed in red box in (a).

Leaflets interlock with each other, leaving a large amount of void space between them, which gives the chalk its characteristic porous structure. The distance between rows of blades is variable between valves and even within a single deposit resulting in varying amounts of void space. In addition, larger 'sheets' may be present between blades and leaflets covering the void spaces between blades (Figure 43). It is considered that sheets are in fact leaflets tilted so that the body of the leaflet is parallel with the main blades. Where these sheets are present, the amount of void space is reduced dramatically.

Chalk lenses present in the left valves are predominantly composed of blades and leaflets only, with few sheets visible (Figure 44a). Chalk lenses of the right valve however, predominately comprise all three components; blades, leaflets and sheets (Figure 44b).

Image J image analysis of SEM micrographs of chalk from both right and left valves was carried out to obtain quantitative analysis of the variation in amount of void space present within chalk lenses of right and left valves. A total of nine SEM micrographs of chalk from each valve were analysed. Chalk lenses in the left valve have significantly more void space than those in the right valves (T-test, $p=0.002$) (Figure 44c). Chalk lenses of the left valve have an average void space of $17.7 \pm 6.3\%$ compared with an average of $7.4 \pm 5.6\%$ in right valves. However, some lenses in the right valve lack calcite sheets and are composed of blades and leaflets only. Where sheets are absent the amount of void space can reach 14.6%. Calcite sheets are less common in left valves and so the amount of void space present in chalk lenses of the left valve is consistently $\geq 10\%$.

Little organic matter is visible within the chalky microstructure. This may be a consequence of the orientation of the blades and leaflets making it difficult to observe organic matter on their surfaces. Some organic matter is occasionally visible on the surface of chalk components, most frequently on chalk components at the chalk-folia interface (Figure 45c & d). Early studies using detailed chemical analysis, report a higher quantity of organics in the chalky lenses when compared with foliated parts (Korringa 1951, Weiner and Hood 1975).

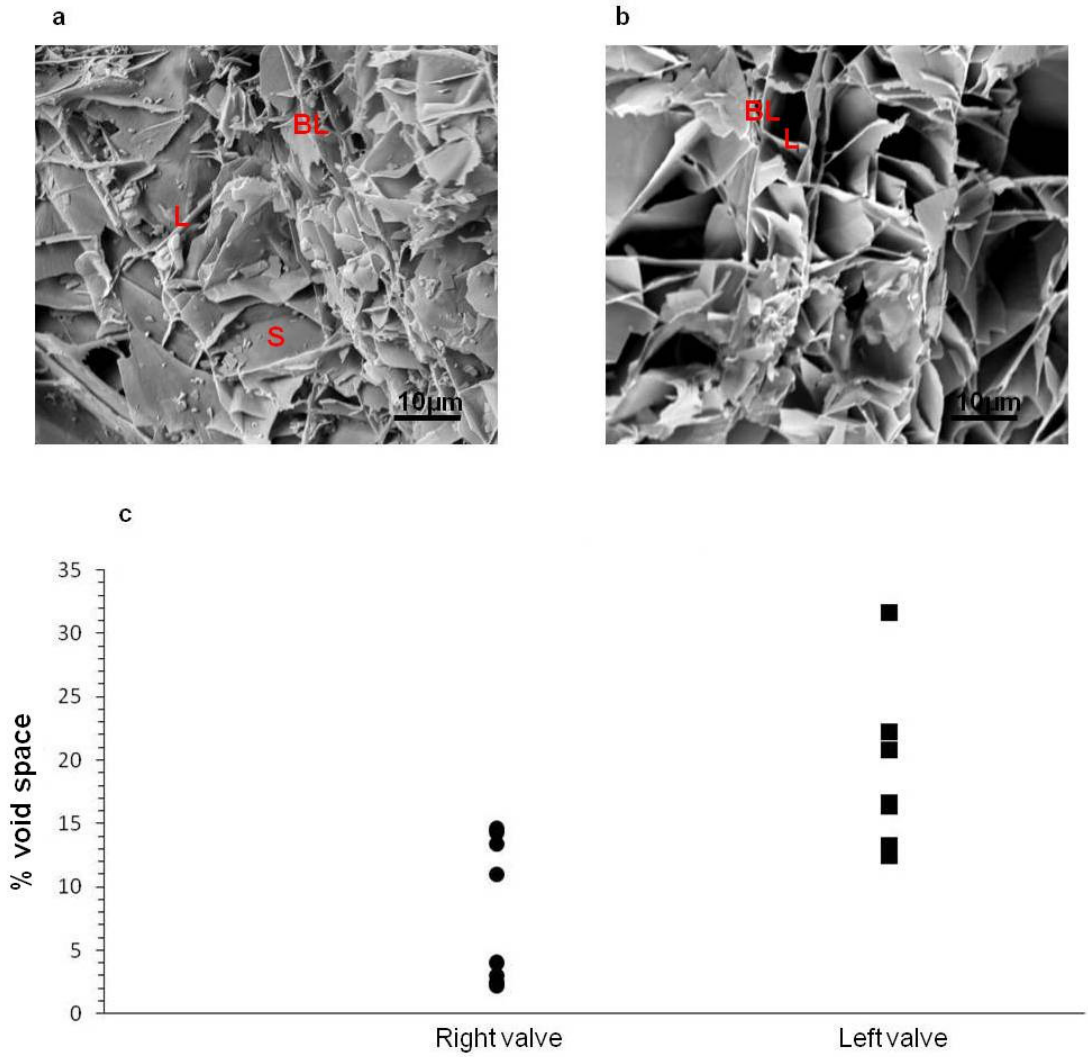

Figure 44. Comparison of the quantity of void space in the chalky lenses within right and left valves.
(a) Backscattered electron SEM image of chalk typical of right valve with blades, leaflets and sheets. (b) Secondary electron image of chalk typical of the left valve composed predominantly of blades and leaflets giving greater volume of void space than the right valve. Key: BL= blades, L= leaflets, S= sheets. (c) Comparison of the void space within chalk lenses of right and left valves determined using Image j.

The nature of the transition between chalk and folia is variable and the relationship between the two microstructures is complex. The transition between the two may be abrupt (Figure 45a), gradual (Figure 45b & c) or an intermediate transition zone may be present (Figure 45d). Where the transition is gradual there appears to be continuity between the laths of the folia and the blades and leaflets of the chalk (Figure 45b & c). The laths of the folia seem to continue into chalk lenses and provide a template for the leaflets. Interestingly, Lee et al. (2011) also suggest that the initial growth of chalk is dependant on the orientation of the folia. This continuity of lath orientation is evident at the boundary between the chalk and folia. However, continuity of lath orientation can only be traced for approximately 10 µm into the body of the chalk layer

where continuity is lost. This relationship between chalk blades and foliated laths is not evident where a transition zone is present between chalk and folia. This chalk-folia interface, similar to that present at the base of the prismatic structure, comprises tightly clustered, disorientated laths with abundant organic material which is visible extending from the transition zone into the chalk microstructure (Figure 45d). Occasionally, the boundary between chalk and folia is extremely abrupt with no visible transition zone or continuity between chalk blades and foliated laths (Figure 45a).

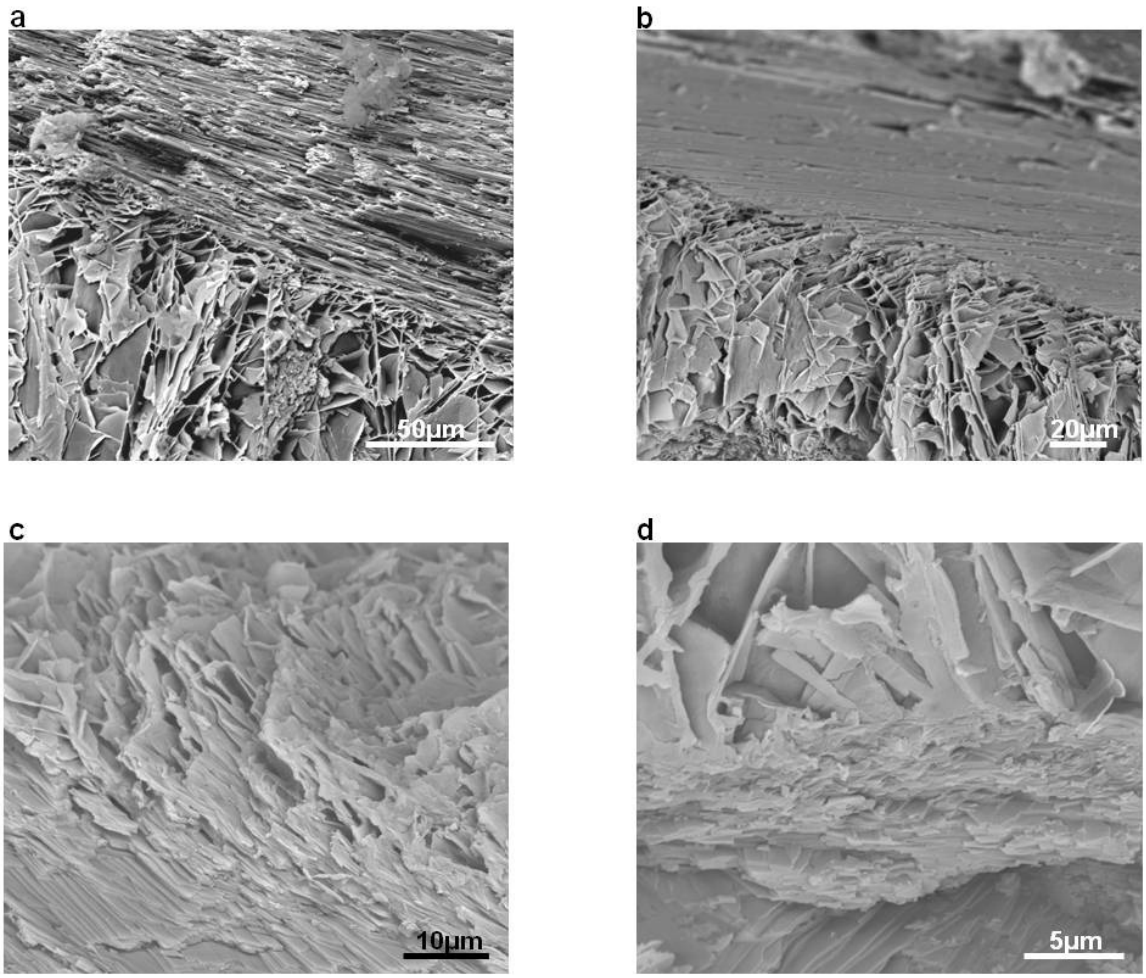

Figure 45. Backscattered electron and secondary and backscattered electron mixed SEM images of fractured sections of right and left valves revealing the interface between chalky and foliated microstructures.
(a) Secondary and backscattered electron mixed SEM image revealing an abrupt transition zone between folia and chalk. (b)&(c) Backscattered electron SEM images revealing a gradual transition between folia and chalk with some continuity in morphological lath orientation into chalk leaflets. (d) Backscattered electron SEM image of an organic-rich transition zone at boundary of the chalk and folia.

3.2.5 Myostracum

Both valves contain a myostracum extending from the adductor muscle to the umbo, where the myostracum is buried beneath younger deposits of folia and chalk. The myostracum comprises fine, needle-like, well developed aragonite prisms, orientated with the long axis of the prisms perpendicular to the inner shell surface (Figure 46a). As a unit, the myostracum is relatively uniform. Unit thickness measured across all samples range from 14-27 µm with little variation, usually in the order of 1-2 µm within a single sample. Where exposed on the inner shell surface, the myostracum is bound by a thin predominantly organic granular layer (Figure 46b). The exterior boundary with the foliated structure is marked by an organic-rich transition zone (Figure 46d) which has a granular fabric that is typically 4-11 µm thick, similar to that described by Lee and Choi (2007).

While calcite prisms of the prismatic region are composite structures composed internally of foliated laths (see section 3.2.4.1, Figure 38e & f), no internal structure could be identified in the aragonite prisms of the myostracum. Excess organic matter (Figure 46b-d) associated with the muscle attachment may have obscured the surface of the prisms making it difficult to identify any internal structure. It is possible that the aragonite prisms are also composite mesocrystal structures.

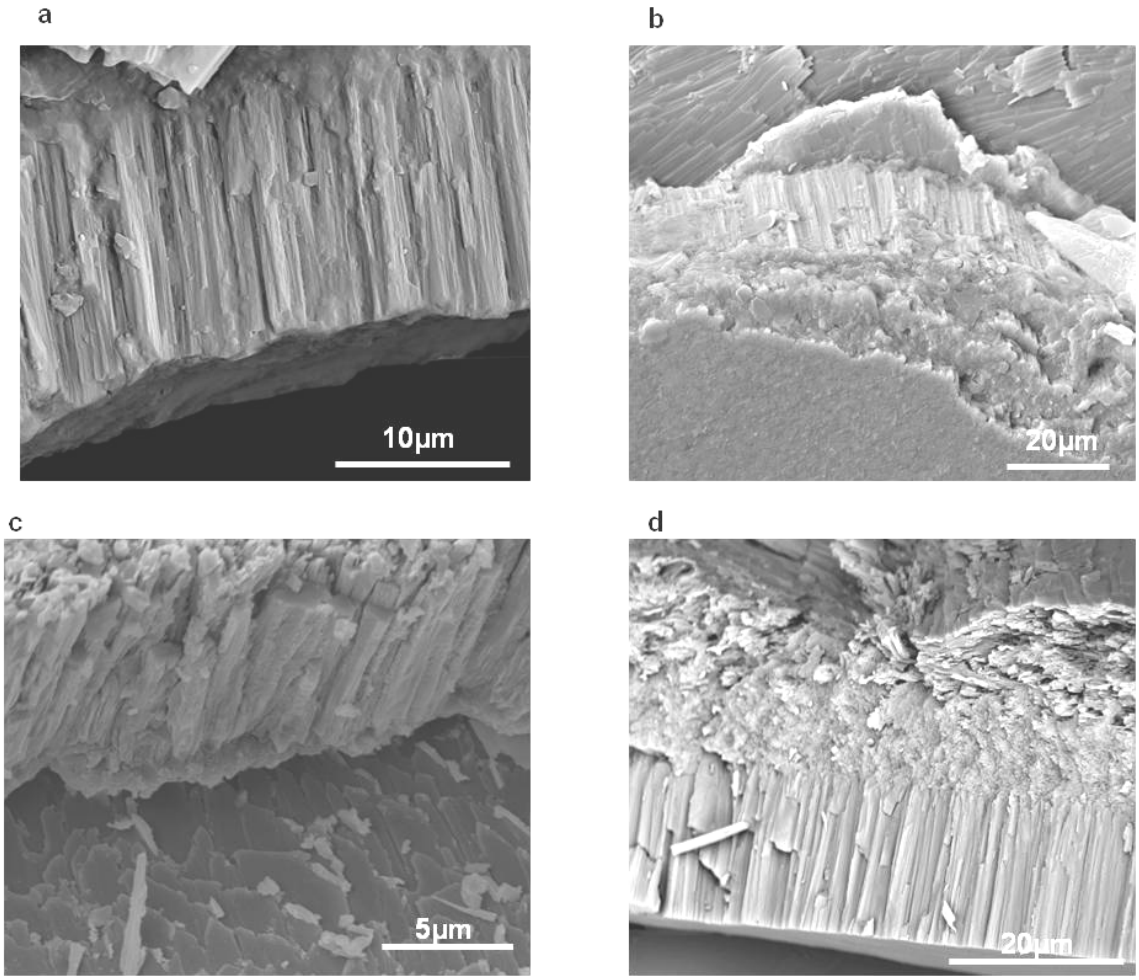

Figure 46. Secondary electron, backscattered electron and secondary and backscattered electron mixed SEM images of fracture shell sections revealing details of the myostracum. (a) Backscattered electron SEM image of aragonite needle-like prisms of myostracum. (b) Secondary and backscattered electron mixed plan view SEM image of the myostracum- view from internal shell surface showing organic matter on the interior surface of the myostracum. (c) Secondary electron SEM image of aragonite prisms with thick organic sheath. (d) Backscattered electron SEM image revealing the transition zone between myostracum and foliated structure.

3.2.6 Hinge region

The interface of the mineralised valve and the organic ligament (Figure 34) is extremely complex and can be obscured by abundant organic matter. To allow detailed observation of all structural components, the hinge region of right and left valves of four samples were each prepared in a different manner. These samples, summarised in Appendix A.1, include fracture sections of the hinge region of both valves viewed as fresh surfaces, partially decalcified surfaces (by acid etching) and fracture surfaces with organic material partially removed (by treatment with NaClO) (described in section 2.2.7). Polished sections of the hinge region of both valves were also prepared, following partial removal of organic material, for crystallographic analysis by EBSD.

At the ligament interface, both valves comprise a complex network of calcite and aragonite crystals of various morphologies with an extensive organic component. The mineralogical distribution and morphological types present at the ligament interface are not uniform between right and left valves and so each valve will be discussed separately.

3.2.6.1 Hinge region of the right valve

Topographically, the ligament interface of the right valve, comprises a central raised area (the chondrophore, Carriker et al. 1980), relative to which the anterior and posterior surfaces are depressed (Figure 47) (anterior and posterior nymphae (Carriker et al. 1980). At all shell parts two distinct microstructural layers can be identified as an exterior (toward valve exterior) foliated structure (Figure 47Figure 48a) and an interior (at ligament interface) prismatic region (Figure 47Figure 48b) (ligostracum, Carriker and Palmer 1979, Carriker et al. 1980).

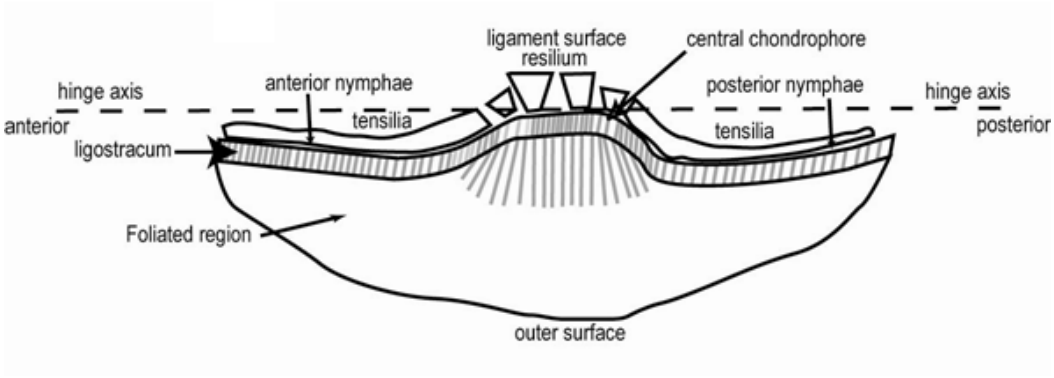

Figure 47. Diagrammatic representation of the hinge region of the right valve. Schematic section of the hinge region of the right valve viewed from ventral margin to umbo.

The prismatic ligostracum is composed of fine rectangular prisms orientated with the long axis of the prism perpendicular, or subperpendicular, to the overlying ligament and underlying folia (Figure 48b). The thickness of the layer can reach up to 200 µm at the centre, tapering towards the anterior and posterior where individual prism height is approximately 60 µm. The interior foliated layer comprises blades of calcite arranged laterally to form sheets (Figure 48a). Underlying the chondrophore surface, calcite blades are arranged with the long axis of the blades perpendicular to the ligament surface. Moving anteriorally and

posteriorally, blades become splayed with the long axis sub perpendicular to the ligament surface (Figure 47).

The ligostracum is responsible for attachment of the ligament to the shell (Carriker and Palmer 1979). The ligament is also divided into a central area (resilium, Carriker et al. 1980), and depressed anterior and posterior parts (tensilia, Carriker et al. 1980). The central part of the ligament is composed of two layers (Figure 48c). The interior layer (furthest from shell) comprises long slender prisms. Prisms are homogenous with alternating horizontal light and dark lines traversing the surface parallel to the hinge axis. These strata are laterally continuous between prisms (Figure 48d). These homogenous prisms are bound to the exterior by a series of parallel massive blocks, approximately 780 µm high and 800 µm wide (Figure 48c). These blocks are connected to the shell carbonate by the ligostracum. Individual blocks are composed of organic matter with bundles of mineralised fibres (Galtsoff 1964, Carriker et al. 1980). Fibres are arranged with the long axis normal to the shell surface (Figure 48e). Occasionally faint annulations are noticeable on the surface of individual blocks.

In contrast to the central part of the ligament, the posterior and anterior parts are smooth and homogenous and show no distinct stratification (Figure 48f). At the base of anterior and posterior parts, at the boundary with the ligostracum, fine fibres can be identified. It is considered that these are part of the ligostracum which have remained connected to the ligament on fracturing.

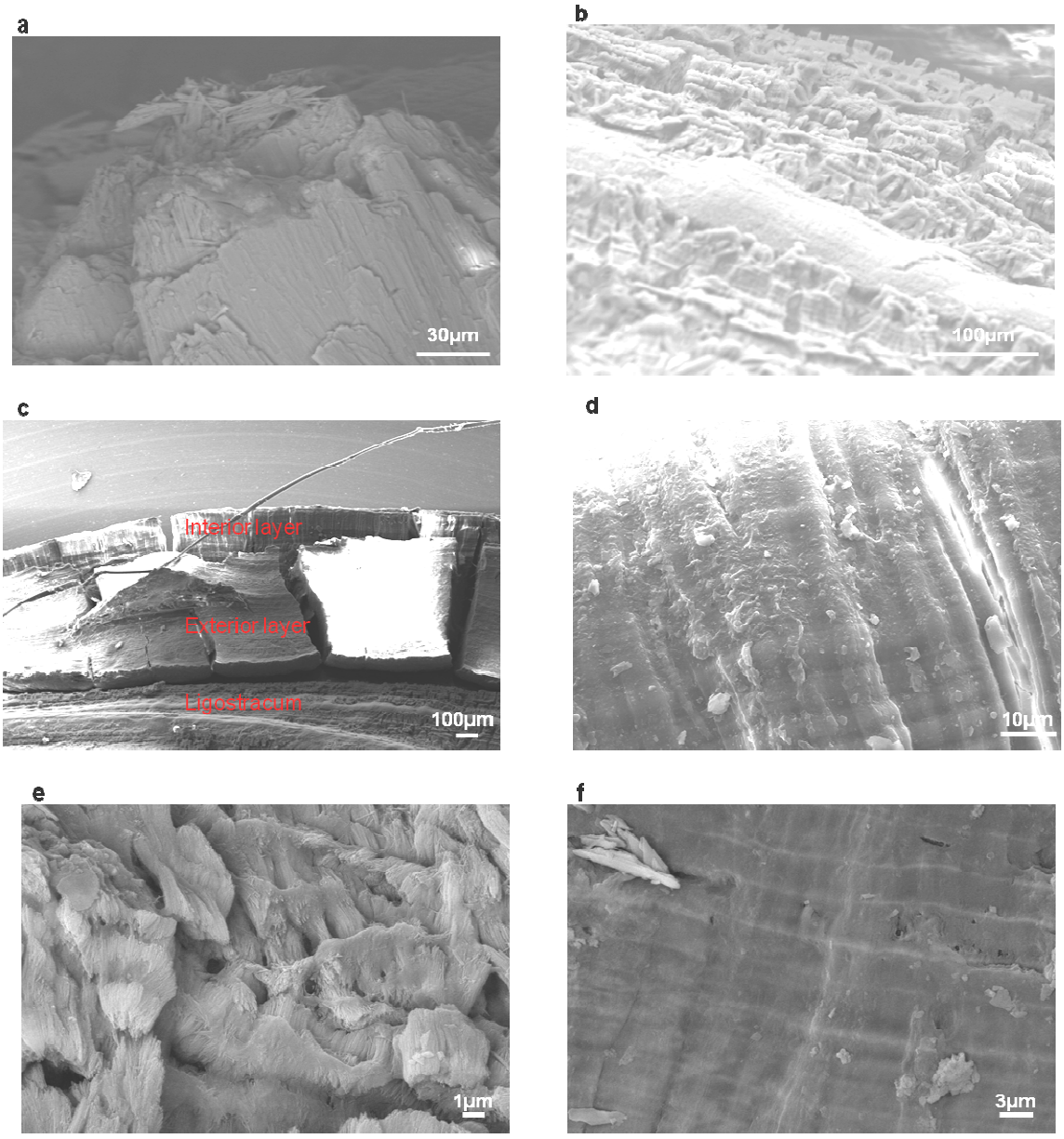

Figure 48. Secondary electron SEM images of fracture sections, treated with NaClO to partially remove organics, of the right valve hinge region, as viewed from ventral margin towards umbo.
(a) Foliated calcite underlying all parts of the shell-ligament interface. (b) Prismatic ligostracum binding ligament to shell carbonate. (c) Central part of the ligament showing interior and exterior layers and underlying ligostracum. (d) Homogenous surface of the interior layer of the central part of the ligament. (e) Surface of exterior layer of the central part of the ligament. (f) Homogenous surface of anterior and posterior parts of the ligament.

3.2.6.2 Hinge region of the left valve

Topographically, the ligament interface of the left valve is inverted relative to the right valve. The central part (chondrophore) is depressed relative to anterior and posterior surfaces (nymphae) which are raised (Figure 49). All parts are composed of an exterior foliated region which is heavily folded and termed 'rugose' (Carriker et al. 1980), and an interior prismatic region (ligostracum Carriker and Palmer (1979).

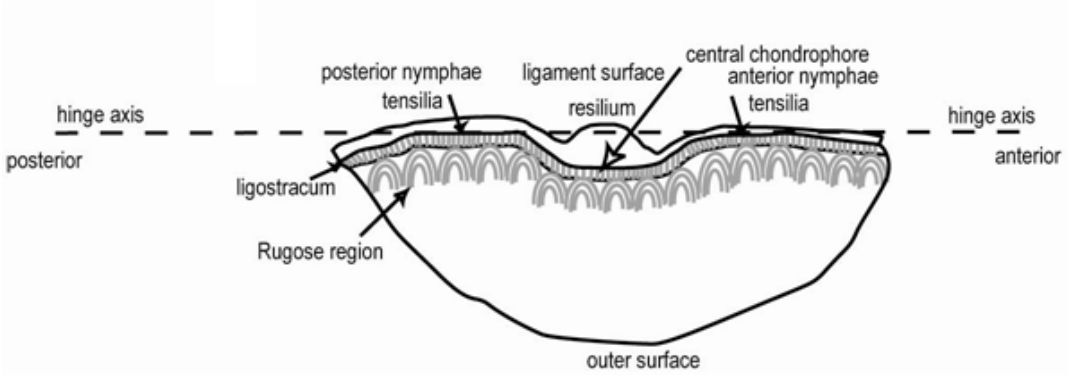

Figure 49. Diagrammatic representation of the hinge region of the left valve. Schematic section of the hinge region of the left valve viewed from ventral margin to umbo.

The exterior foliated region has a 'rugose' texture (Carriker et al. 1980), comprising laths arranged in varying orientation to form a series of adjacent elongate depressions (Figure 50a). Depressions are orientated with the long axis perpendicular to the ligament surface. Each depression is composed of a concentric series of laths clustering in the centre to form a narrow pit. Moving away from the ligament interface, towards the valve exterior, laths gradually become aligned eventually reaching a uniform arrangement, with the long axis of the lath perpendicular to the hinge axis and parallel to the growth front (Figure 50b).

The rugose foliated region is overlain by the ligostracum. The ligostracum comprises fine rectangular prisms, aligned with the long axis of the prism sub perpendicular to the overlying ligament and underlying rugose region. Where prisms meet the rugose region, prisms are arranged around the rugose texture of the folia (Figure 50c). The orientation of prisms in Figure 50c suggests that the ligostracum lies at an oblique angle to the underlying rugose region. Similarly, Carriker and Palmer (1979) noted that while the ligostracal prisms of the right valve were perpendicular to the underlying folia, those of the left valve were obliquely orientated. High magnification images (Figure 50d) of fractures of the ligostracum show that prisms are a complex of individual fine mineralised blades orientated with the long axis of the blades parallel with the long axis of the prism (Figure 50d).

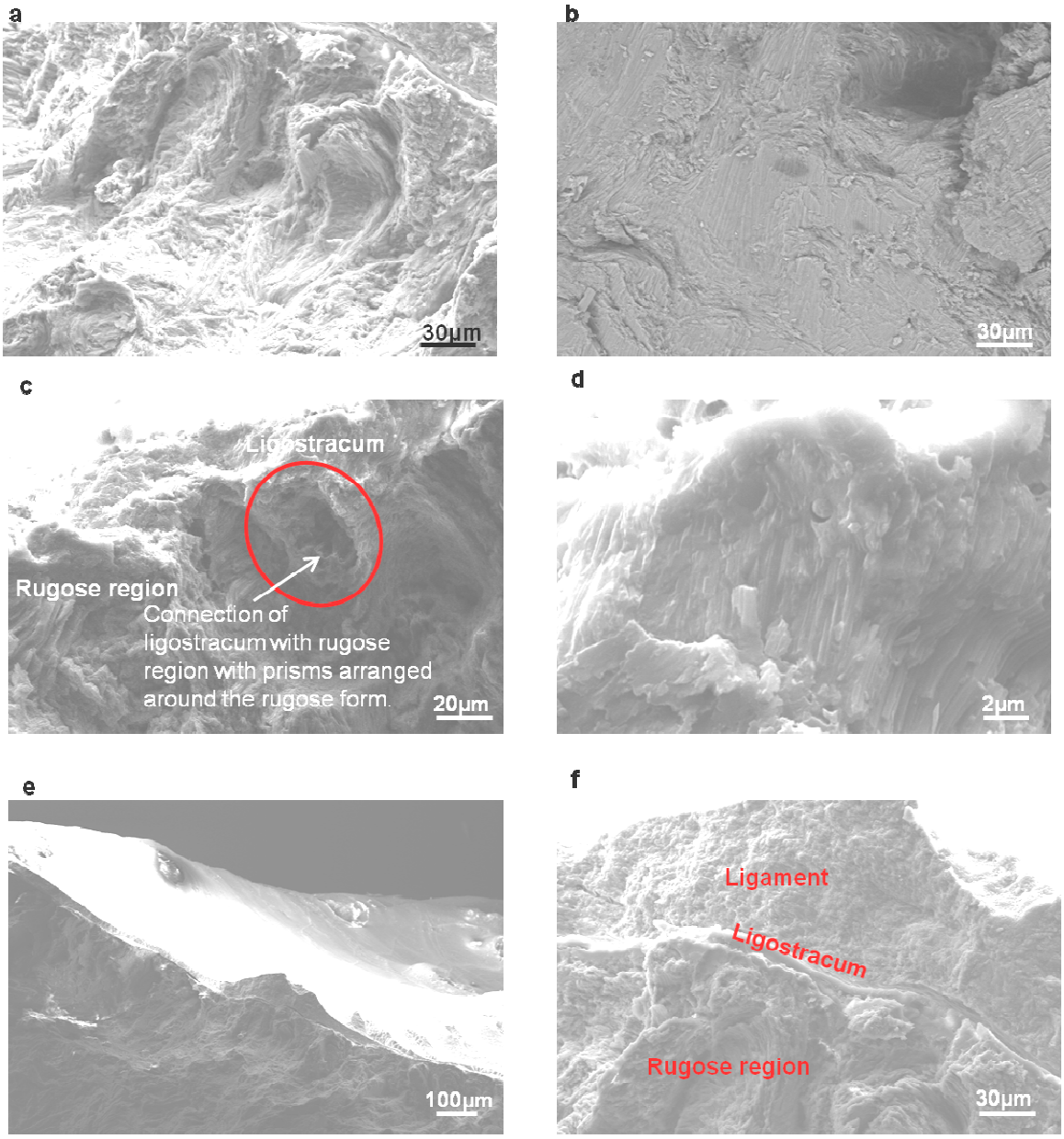

Figure 50. Secondary electron SEM images of fracture sections, treated with NaClO to partially remove organics, of the left valve hinge region. View from ventral margin towards umbo.
(a) Foliated calcite arranged to form a distinct rugose texture. (b) Foliated structure towards the shell exterior loses rugose texture and becomes regularly aligned. (c) Ligostracum connecting to rugose region. (d) High magnification image of the ligostracum revealing internal structure of fine blades. (e) Structure of ligament surface of the left valve. (f) Organic rich ligament lacks any noticeable crystalline structure.

As in the right valve, the ligostracum attaches the ligament to the shell (Carriker and Palmer 1979, Carriker et al 1980). At the centre, the ligament is 130 µm high tapering to 60 µm towards the anterior and posterior (Figure 50e). The ligament of the left valve is composed of an organic homogenous block which lacks stratification or mineralisation (Figure 50f).

3.2.7 SEM imaging analysis of cavities in marine samples

Marine samples containing sediment cavities were fractured and observed under the SEM in cross section and plan view.

Cavities are surrounded by dark organic material the surface of which is heavily indented (Figure 51a). These indents are spherical and exist as a network of shallow depressions and connecting walls (Figure 51b). Connecting walls stand proud of the spherical-depressions and occasionally show small crystals within them (Figure 51c). While most depressions are empty, they are frequently associated with grains of 50-100 μm long. These grains may have once occupied the depressions and have become dislodged, possibly during fracturing (Figure 51d). Grains are likely to be particles of sediment trapped within the organic network. The network of interconnecting walls surrounding the depressions is reminiscent of the blade and leaflet structures which surround the void space in chalk layers (Figure 51e). The interface between the organic network and surrounding foliated calcite is abrupt. Where laths of the folia meet the organic material surrounding the cavities, laths are terminated and the growth front of the lath takes the same concave morphology as the depressions within the organic network (Figure 51f).

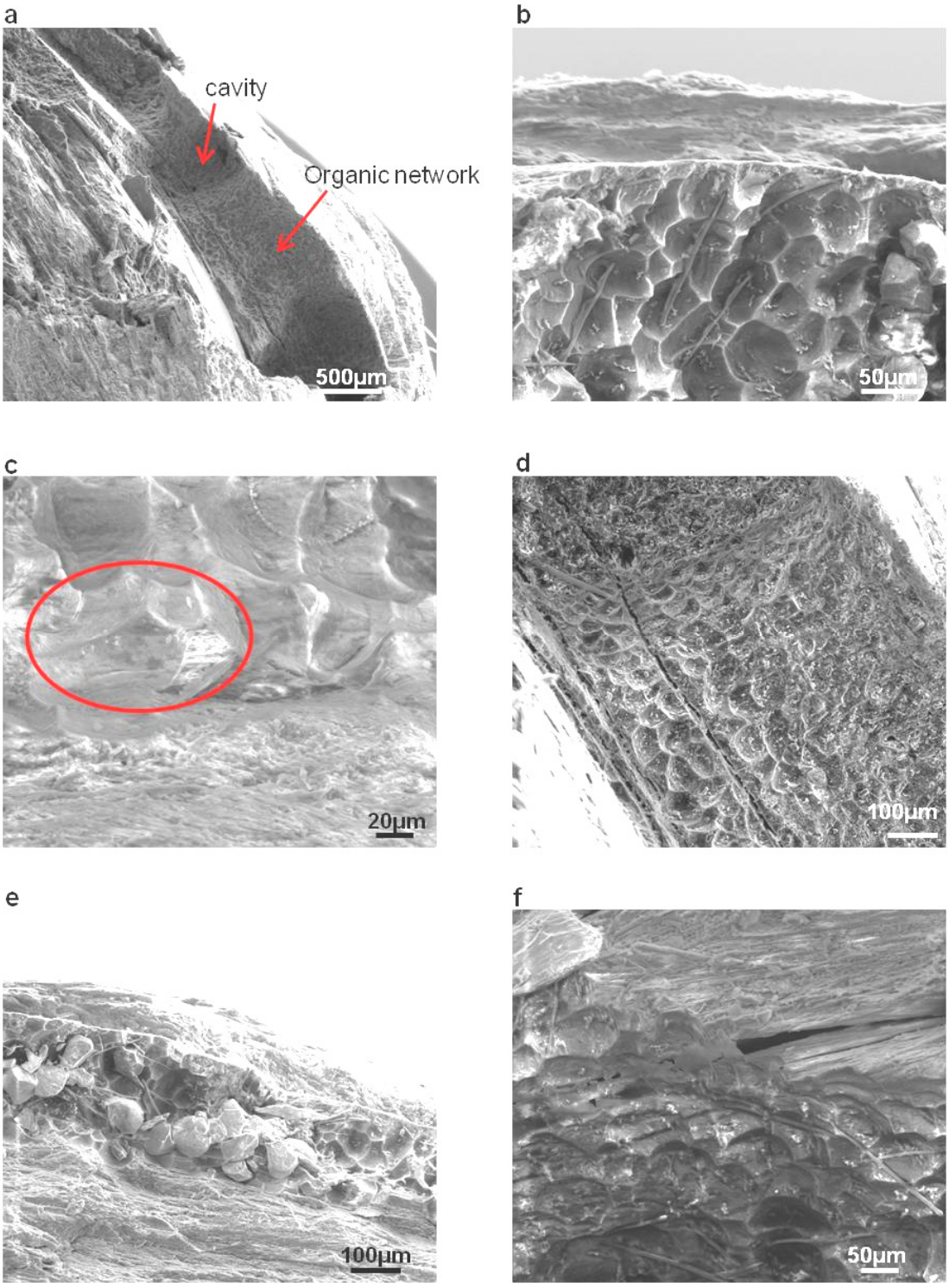

Figure 51. Secondary electron SEM images of cavities in marine specimens of *C. gigas*. (a) Cross section of cavities surrounded by dark organic rich walls. (b) Topography of organic matter surrounding cavities showing shallow depressions and connecting walls. (c) High magnification image of organic walls revealing faintly mineralised parts which are highlighted by a red circle. (d) Faintly mineralised connecting walls reminiscent of chalk blades and leaflets. (e) Sediment particles associated with organic network. (f) Laths of folia terminate and take the same concave topography as the organic matter.

3.3 Chemistry

3.3.1 Chemical variation throughout three calcite microstructures

Quantitative element analysis and qualitative element mapping was conducted using a Sigma SEM with Inca software (section 2.3.3). The chemical composition of the three calcite microstructures; prisms, folia and chalk, as well as the folia/chalk boundary was analysed at shell section A of the left valves of estuarine sample F6 and marine sample U6 (see sections 2.3.3.1 & 2.3.3.2 for details). In both samples each microstructure was analysed at three points and within each point five spectra were accumulated allowing the mean element composition to be calculated. The elemental constituents (weight%) of all microstructures are given in Table 2 (estuarine) and Table 3 (marine).

The elemental composition of prisms and folia is similar, within and between, estuarine and marine samples. $CaCO_3$ constitutes, on average, 98.09 ± 0.07 and 98.56 ± 0.4 weight% in estuarine and marine samples respectively (average value for prisms & folia). Sodium is consistent in both microstructures, however is more concentrated in the marine sample (average= 0.44 ± 0.08 weight%) than estuarine (average= 0.35 ± 0.03 weight%). In both estuarine and marine samples, sulphur is most concentrated in the folia, comprising on average 0.18 ± 0.05 weight% in marine sample and slightly higher in estuarine sample, (0.34 ± 0.05 weight%). In both estuarine and marine samples the weight% of sulphur increases towards the folia/chalk boundary, this increase is most pronounced in the marine sample. Sulphur was detected only occasionally in the prisms, most consistently so in the estuarine sample and, where detected, was in greater quantities than in folia (average 0.37 weight% estuarine, 0.41 weight% marine). Magnesium is occasionally present in the prismatic region of both samples but is entirely absent in folia and only occasionally present at the folia/chalk boundary. Towards the boundary with chalk, total $CaCO_3$ concentration decreases, most notably in the marine sample, while concentration of magnesium and sulphur increase.

The elemental composition of chalk is considerably more variable than other microstructures. Chalk blades are typically < 0.5 µm wide and so each spectrum

was collected by spot analysis, rather than raster area (section 2.3.3.1), to reduce the number of X-rays detected from surrounding void space. While this improved X-ray detection, spots are typically 1 µm radius and therefore detection of some X-rays produced from void space surrounding the chalk blades was inevitable. As a consequence conclusive quantification of the elemental composition of chalk blades is difficult. In both estuarine and marine samples the concentration of $CaCO_3$ of chalk is less, and more variable, than both prisms and folia, (average= 85.99 ± 10.2 weight% estuarine, 84.19 ± 12.5 weight% marine). Indeed, the concentration of calcium is notably reduced in chalk samples relative to other microstructures while carbon and oxygen, most notably in marine specimen, is slightly elevated. Similarly, Carriker et al. (1991) also noted a reduction in Ca in the chalk relative to folia, but an increase relative to the prisms. Magnesium, sulphur and sodium concentrations appear consistent in chalk lenses of both samples. In addition, in the marine specimen, chalk lenses consistently contain aluminium and silica which were not detected in estuarine chalk. Marine chalk lenses frequently contain foreign particles embedded within the chalk structure. Elemental maps of chalky lenses containing such particles are shown in Figure 52. These particles are not composed of calcium carbonate, have high silica, sodium, magnesium and oxygen composition and are therefore considered not to be normal constituents of the oyster shell. Contamination of chalk by polishing artefacts is possible. However, particles are up 100 µm across which is considerably greater than the grade of polish used (0.6 µm colloidal silica). It is considered that these particles are more likely to be grains of sand or sediment embedded within the chalk. Traces of sand throughout the chalk structure may cause contamination of the true elemental composition of the chalk carbonate and may account for the high values of trace elements detected within the chalk lenses. Similarly, Carriker et al. (1991) suggest that fluid trapped within the void space of the chalk may explain the high concentration of elements such as sodium, magnesium, chlorine and zinc in the chalk lenses. Sediment particles were not detected in chalk lenses of estuarine oysters.

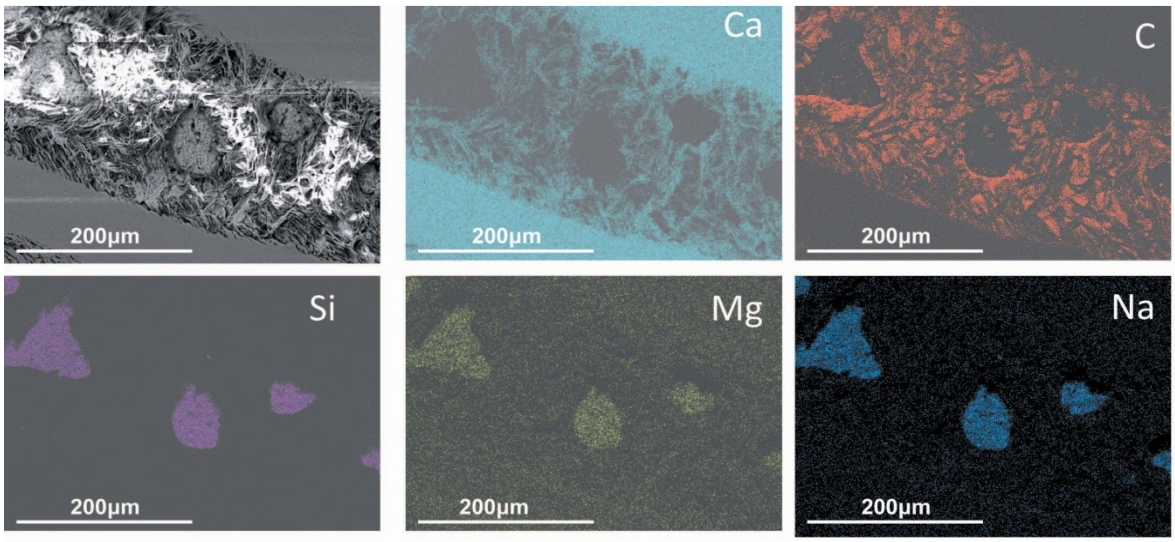

Figure 52. Elemental maps showing distribution of elements within a chalk lens. (a) Secondary electron image of polished shell section A of marine sample U6, containing chalk lenses. (b-f) Elemental distribution maps of Ca, C, Si, Mg, and Na respectively.

Estuarine	POI	C	O	Na	Mg	Al	Si	S	Ca	CaCO3
Prisms	1	19.91	49.75	0.34	DL	DL	DL	0.38	38.62	96.40
	2	19.21	52.43	0.30	0.92	DL	DL	0.35	39.58	98.83
	3	19.28	52.07	0.35	1.12	DL	DL	DL	39.61	98.91
Folia	1	19.47	51.52	0.38	DL	DL	DL	0.33	39.12	97.68
	2	19.49	51.24	0.38	DL	DL	DL	0.30	39.43	98.46
	3	19.30	52.35	0.37	DL	DL	DL	0.40	39.36	98.28
Folia/chalk boundary	1	18.06	50.24	0.25	0.14	DL	DL	0.48	39.84	99.48
	2	19.84	52.59	0.25	DL	DL	DL	0.48	38.64	96.48
	3	19.48	50.55	0.39	DL	DL	DL	0.27	39.32	98.18
Chalk	1	17.91	48.17	0.03	0.12	DL	0.20	0.28	29.72	74.21
	2	20.38	55.24	0.30	DL	DL	DL	0.26	36.61	91.42
	3	19.17	54.57	0.24	0.14	DL	DL	0.30	36.98	92.34

Table 2. Elemental composition of calcite microstructures of estuarine *C. gigas* as determined by quantitative EDS analysis.
Each microstructure was analysed as three points (POI= point of interest), and within each point five analyses were conducted. Values presented above are the average values calculated for each POI. All values are expressed as weight%. DL= below limit of detection.

Marine	POI	C	O	Na	Mg	Al	Si	S	Ca		$CaCO_3$
Prisms	1	19.50	51.95	0.52	DL	DL	DL	DL	39.79		99.36
	2	19.47	51.86	0.51	DL	DL	DL	DL	39.73		99.21
	3	19.75	52.62	0.32	0.41	DL	DL	0.41	39.22		97.93
Folia	1	19.06	50.78	0.48	DL	DL	DL	0.17	39.54		98.73
	2	19.14	51.00	0.47	DL	DL	DL	0.14	39.34		98.23
	3	18.91	50.37	0.35	DL	DL	DL	0.24	39.21		97.91
Folia/chalk boundary	1	18.35	48.88	0.22	0.16	DL	DL	0.38	38.83		96.96
	2	18.43	49.09	0.24	0.20	DL	DL	0.39	37.46		93.54
	3	17.69	47.12	0.31	0.08	DL	DL	0.23	37.85		94.51
Chalk	1	17.21	45.86	0.27	0.22	0.47	2.60	0.27	27.90		69.67
	2	20.72	55.20	0.35	0.23	0.44	0.80	0.32	36.44		90.99
	3	20.34	54.18	0.35	0.17	0.41	0.81	0.27	36.81		91.91

Table 3. Elemental composition of calcite microstructures of marine *C. gigas* as determined by quantitative EDS analysis.
Each microstructure was analysed at three points (POI= point of interest), and within each point five analyses were conducted. Values presented above are the average values calculated for each POI. All values are expressed as weight%. DL= below limit of detection.

3.4 Crystallography

The crystallographic orientation of each microstructural domain was analysed by electron backscatter diffraction (EBSD) at sections A, B and C on the right valve of estuarine sample F6 (section 2.2.5 & 2.3.4). Given the similarities in shell ultrastructure, microstructural arrangement and chemistry between estuarine and marine samples, it is considered that crystallographic analyses of estuarine sample would also be representative of the crystallography of marine oysters. For each microstructure the step size was adjusted to optimize diffraction intensity. The hinge region of the oyster is complex (Carriker and Palmer 1979, Carriker et al. 1980 also see section 3.2.6), and will be discussed separately.

3.4.1 Crystallography of the prisms

All scans of the prismatic region were carried out using a step size of 0.5 µm. Final data sets were partitioned through a two stage clean-up procedure so that only grains of confidence index (CI) ≥ 0.5 are displayed in the final data set. EBSD maps with superimposed crystal models show that within each prism the c-axis is orientated perpendicular to the outer and inner shell surfaces, parallel with the elongation of the prisms (Figure 53b). The corresponding pole figure (Figure 53c) representing the {0001} crystal plane of calcite, shows one single maxima perpendicular to the {0001} plane of calcite with lateral variation of up to 40°. Prisms in mid shell sections (blocks B & C detailed on Figure 21) have smaller lateral variation of no more than 25°.

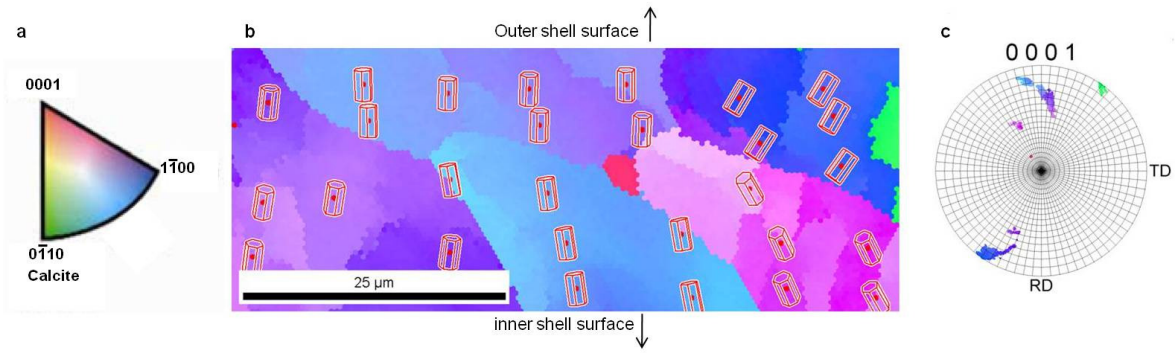

Figure 53. Typical EBSD crystallographic orientation map of prismatic structure. (a) Crystallographic orientation map colour key for calcite with reference to normal direction. (b) EBSD map of prismatic structure with superimposed crystal models in red, individual prisms are delineated by a single colour according to colour key (a). (c) Corresponding pole figure representing the {0001} plane of calcite.

Individual prisms (Figure 53b) display a single colour suggesting each prism behaves, crystallographically, as a single crystal. However, fracture sections reveal that each prism is a composite structure composed internally of individual laths (see section 3.2.4.1, Esteban-Delgado et al. 2008, Checa et al. 2009). Common orientation of these nano-particles may result in prisms diffracting as apparently monocrystalline materials (Checa et al. 2009). Several prisms, displayed in Figure 53b, show colour shading across prism surface, indicating slight rotation in c-axis alignment from different areas of a single prism. This confirms the composite internal structure of the prismatic region.

Neighbouring prisms show rotation around the c-axis, implying disorientation of a- and b- axes between prisms. Similarly, Checa et al. (2005) report adjacent prisms to be rotated around the direction of the c-axis, referring to the crystallographic texture as (0001) fiber texture or turbostratic disposition.

The crystallographic orientation of the prismatic region is consistent, with the c-axis perpendicular to the outer shell surface, throughout the height of the valve.

3.4.2 Crystallography of the foliated structure

To observe variation in crystallographic orientation between the foliated structure and the overlying prismatic region, both microstructures were analysed together from shell sections A and C using a spot size of 0.5 µm. To obtain high precision crystallographic analysis of individual folia, the foliated structure was analysed separately in section B using a step size of 0.1 µm. A fracture section containing type 1 and type 2 laths was prepared as a thin section for crystallographic analysis to observe any differences in crystallographic orientation between type 1 and type 2 laths. All final data sets for the foliated structure were partitioned through a two stage clean-up procedure so that only grains of confidence index (CI) ≥ 0.2 are displayed in the final data set.

The foliated structure shows c-axis crystallographic unity throughout the valve. EBSD maps with superimposed crystal models show that the orientation of the crystallographic c-axis, throughout the foliated structure is, perpendicular to the outer and inner shell surface. This mirrors that of the overlying prisms. Unlike the prisms however, the crystallographic c-axis is perpendicular, or sub-

perpendicular to the long axis of the laths (Figure 54a). Crystallographic orientation remains constant along the length of each lath. The pole figure representing the {0001} crystal plane of calcite shows one single maxima perpendicular to the {0001} plane of calcite with lateral variation of up to 35° (Figure 54b). The EBSD map shows superimposed crystal models orientated perpendicular, or sub perpendicular to the long axis of the lath. Similarly, Checa et al. (2007b) report c-axis orientation to be tilted back by 21-30° from the lath front.

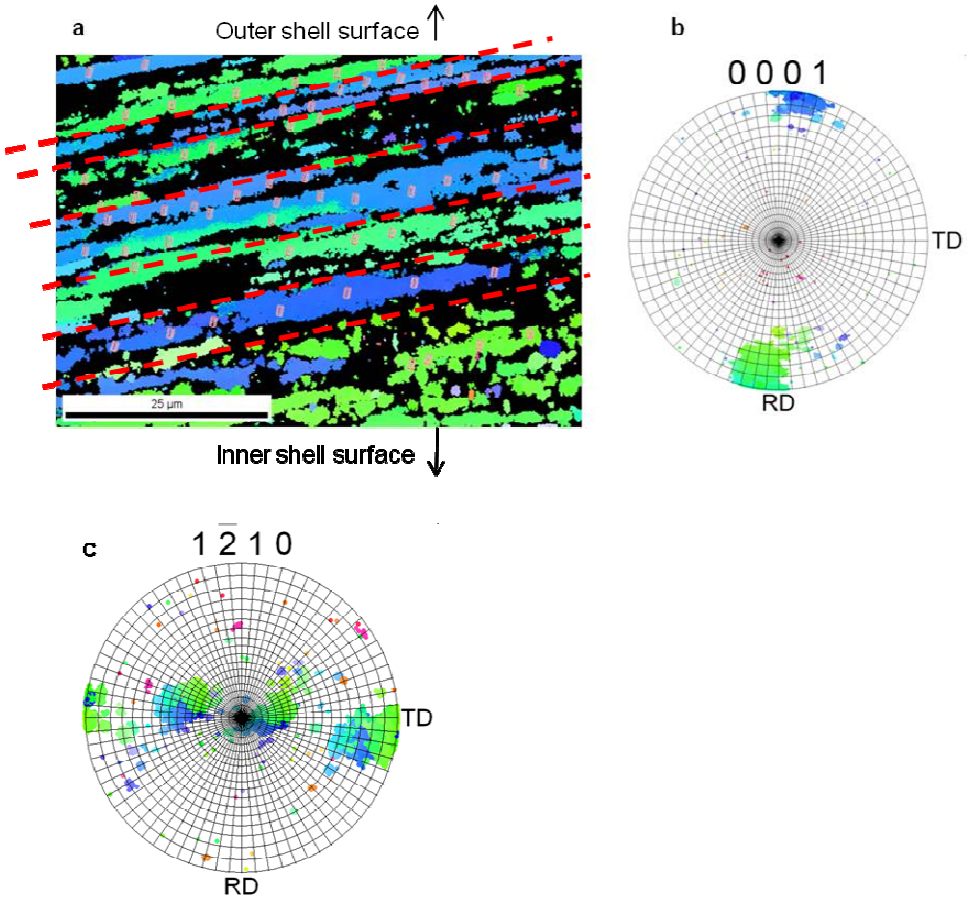

Figure 54. Typical EBSD crystallographic orientation map of foliated structure. (a) EBSD map of foliated structure with superimposed crystal models, colours according to colour key presented in Figure 53a. Dashed lines highlight alteration between type 1 and type 2 laths. (b) Corresponding pole figure representing the {0001} plane of calcite. (c) Pole figure representing the $\{1\bar{2}10\}$ plane of calcite.

The crystallographic c-axis across the foliated structure is orientated perpendicular, or slightly tilted, relative to the elongation of the lath. This confirms reports by earlier authors (e.g. Watabe 1965, Checa et al. 2007b, Lee et al. 2008b) that each lath must be composed of individual crystals of uniform orientation. Laths diffract as single crystals (as noted above and by Lee et al

2008b), and therefore the c-axis of each sub-unit must be identical. Individual laths comprise large numbers of nanogranules, each of which are separated by a continuous organic matrix (Lee et al. 2008b).

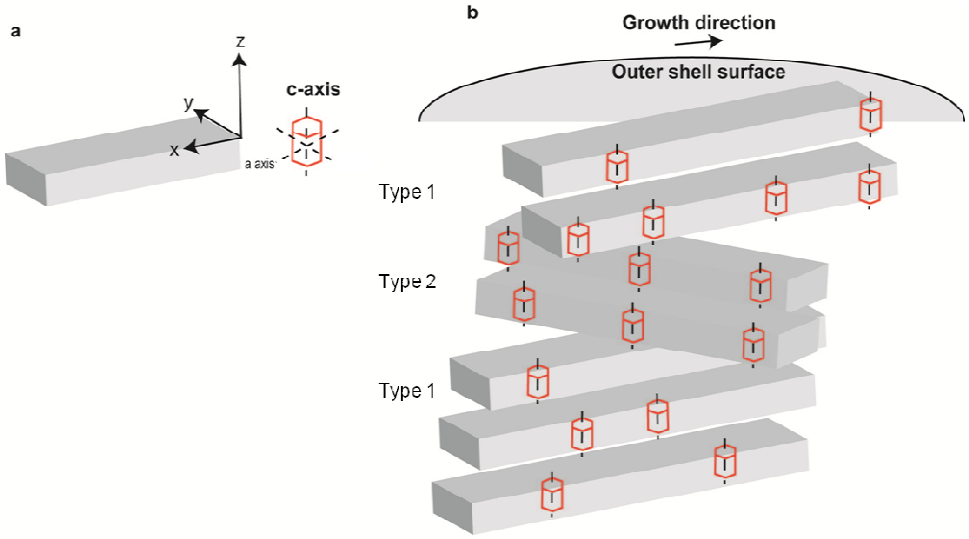

Figure 55. Schematic diagram of crystal orientation within laths of type 1 and type 2 orientation.
(a) Single lath showing morphological axis (x,y,z) and corresponding crystallographic axis.
(b) Model of type 1 and type 2 orientated laths and corresponding orientation of crystallographic c-axis.

C-axis orientation is consistent across the foliated structure demonstrating that the difference in orientation of type 1 and 2 laths is morphological, altering the in-plane orientation of the laths and crystallographic a-axis but not the orientation of the crystallographic c-axis (Figure 55b). The change in lath orientation is around the z-axis while the x and y axis remain constant, thus not affecting the crystallographic c-axis orientation (Figure 55b). The pole figure representing the $\{1\bar{2}10\}$ plane of calcite (Figure 54c) shows that variation in a-axis orientation between lath clusters (highlighted in Figure 54a) is 30-55°. This implies that the difference in morphological orientation between type 1 and type 2 laths is 30-55°.

Laths may be inclined relative to the outer shell surface, most notably under cupped shell parts. Where laths are inclined, c-axis also becomes tilted, as shown in Figure 56. This may explain the lateral variation, from perpendicular to the outer surface, in c-axis orientation (Figure 54b).

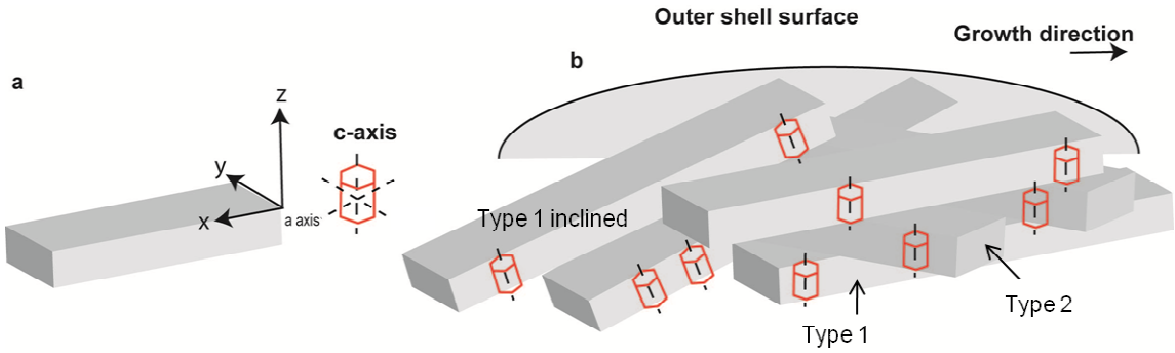

Figure 56. Schematic diagram of crystallographic orientation in foliated structure where laths are inclined relative to shell surface.
(a) Single lath showing morphological axis (x,y,z) and corresponding crystallographic axis.
(b) Model of folia showing c-axis orientation where laths of type 1 & 2 orientation are inclined relative to the growth surface.

3.4.3 Crystallography of chalky lenses

EBSD analysis is a surface analysis technique which requires a smooth, even surface, tilted to 70° to the electron beam to ensure accurate indexing of diffracted patterns (section 2.3.4.1). The surface of the chalky lenses is extremely uneven and porous, with many mineralised surfaces at different orientations. Chalky lenses are therefore not ideal for EBSD analysis. Polishing of samples prior to EBSD analysis is essential to create a smooth surface. However, the calcite of the chalky lenses is exceptionally fine and is easily destroyed during polishing. As a consequence, EBSD analysis with a reasonable confidence index (greater than 0.1 (Wright and Adams 1992)) is difficult to achieve on this material.

Several attempts at EBSD scans of chalky lenses were made. However, the confidence index of most was considered too poor to show accurate crystallographic orientation.

Higher confidence index is achieved where the calcite blades of the chalky lenses are closely aligned, with minimum void space. A single scan with an average confidence index of 0.08 was achieved and is shown in Figure 57b below. The scan was partitioned through a two stage clean-up procedure so that only grains of confidence index (CI) ≥ 0.1 are displayed in the final data set.

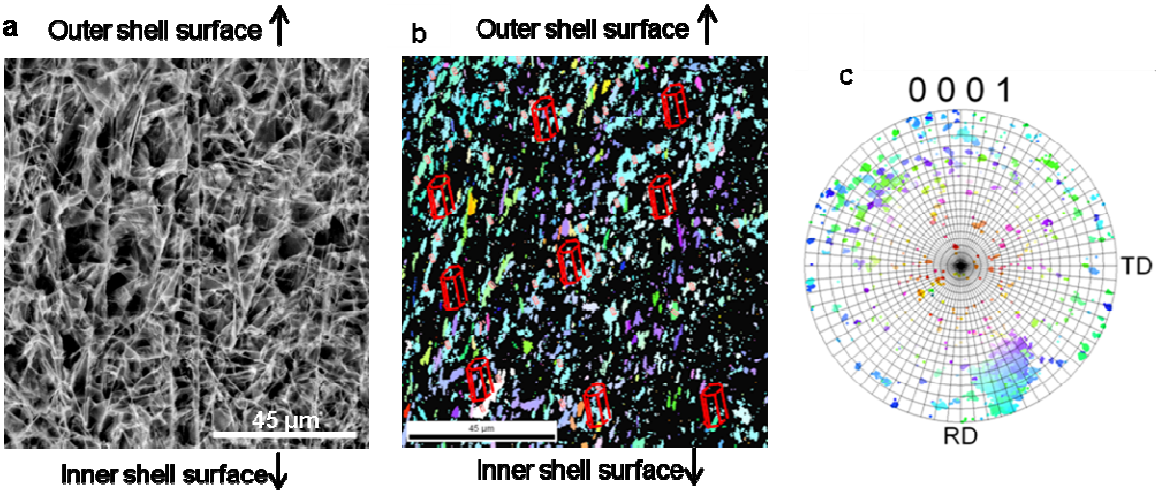

Figure 57. EBSD crystallographic orientation of chalk lenses.
(a) Secondary electron SEM image of scan area. (b) EBSD map of chalky structure with superimposed crystal models, according to the colour key presented in Figure 53a. (c) Corresponding pole figure representing the {0001} plane of calcite.

This scan is considered representative of the crystallographic orientation of the chalky lenses. Calcite crystals of the main blades are orientated, consistently with the folia and prisms, with the c-axis perpendicular to the inner and outer shell surface, and parallel with the long axis of the blades. The pole figure representing the {0001} crystal plane of calcite for the chalky lens (Figure 57c) shows a dominant cluster at 10-40° from perpendicular to the {0001} crystal plane. Scatter around this cluster shows some isolated crystals with irregular crystallographic orientation. The dominant cluster of crystals, orientated with c-axis near perpendicular to the outer and inner shell surface represents crystals of the main blades (Figure 57a). Isolated crystals of varying orientations correspond to those crystals between main blades, and are therefore considered to represent crystals of the interlocking calcite leaflets. Few crystals of the leaflets could be indexed with a sufficiently high confidence index (≥ 0.1) to be included in the final data set. Therefore, conclusive analysis of the crystallographic orientation of the leaflets is not possible. It is considered that, given the significant variation in morphological orientation of the leaflets, the crystallographic orientation may also be irregular.

Attempts were made to improve the quality of EBSD scans from chalky lenses. Impregnation of shell sections containing chalky lenses with resin prior to polishing was carried out to fill void space. However, due to the fine crystalline nature of the blades, calcite was lost on polishing before the resin was ground to an even surface. As a result, resin within the void space was left standing proud

relative to the calcite blades, which further increased surface topography and reduced the scan quality.

3.4.4 Myostracum

Crystallographic analysis of the myostracum was carried out directly behind the adductor muscle scar. The EBSD scan was carried out using a step size of 0.3 µm and data were cleaned through a two stage clean up procedure so that only grains with a confidence index of ≥ 0.1 are displayed in the final data set.

The EBSD map of the myostracum with superimposed crystal models shows that each prism of the myostracum is composed of aragonite orientated with the c-axis perpendicular to the outer and inner shell surfaces, parallel with the elongation of the prisms (Figure 58b). The corresponding pole figure representing the {001} crystal plane of aragonite (Figure 58c) shows a dominant orientation perpendicular to the {001} crystal plane of aragonite. Crystals are tightly clustered with maximum lateral variation of 27°.

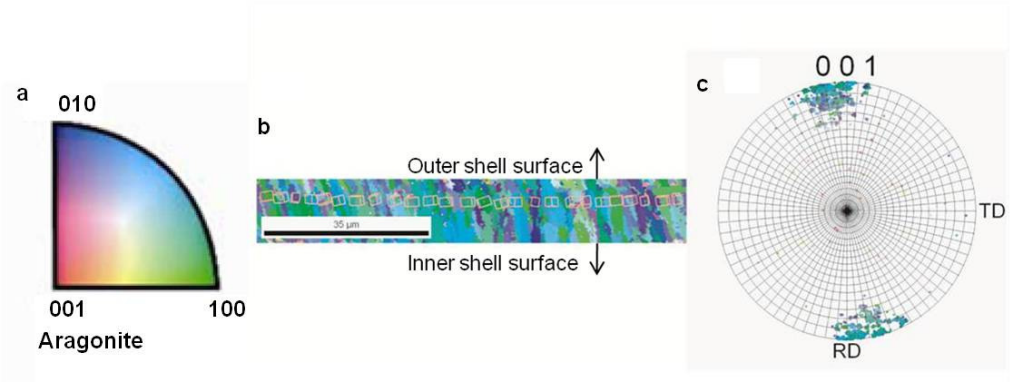

Figure 58. EBSD crystallographic orientation of the myostracum.
(a) Crystallographic orientation map colour key for aragonite with reference to normal direction. (b) EBSD map of myostracum with superimposed crystal models. (c) Corresponding pole figure representing the {001} plane of aragonite.

Individual prisms display a single colour in EBSD analysis indicating a monocrystalline composition. Adjacent prisms show systematic rotation around the c-axis exposing alternate {010} and {100} crystal planes.

3.4.5 Hinge region

The hinge region of the oyster contains a dense organic network that can reduce EBSD scan quality (section 2.3.4.2). To overcome this problem, the hinge region of both valves was treated with NaClO prior to preparation for EBSD analysis. This treatment allowed partial removal of organic components to increase diffraction intensity from mineralised parts.

All scans of the hinge region of both valves were carried out using a step size of 0.25 µm. Final data sets were partitioned through a two stage clean-up procedure so that only grains of confidence index (CI) ≥ 0.1 are displayed in the final data set.

Given the morphological differences between the hinge regions, right and left valves will be discussed separately. EBSD data from right and left valves are presented in Figure 59 and Figure 60 respectively. Polymorph type and crystallographic orientation for each microstructure of the hinge region of both valves is summarised in Figure 61.

All ligament parts of the left valve, and anterior and posterior parts of the right valve, are entirely organic and were lost during treatment with NaClO. The central part of the right valve ligament comprises bundles of mineralised fibres. Despite removal of organics, these fibres could not be indexed with a sufficiently high (> 0.1) confidence index to reveal accurate crystallographic orientation within the fibres.

3.4.5.1 Crystallography of the hinge region of the right valve

EBSD analysis of the hinge region of the right valve are displayed in Figure 59 and summarised in Figure 61.

All parts of the hinge region of the right valve are composed of foliated calcite overlain by ligostracal prisms (Figure 59c-e). Phase maps, shown in Figure 59i-k, show that prisms of the ligostracum are composed of calcite with randomly distributed aragonite, which is most dominant at the anterior nymphae surface. Where present, aragonite crystals are consistently orientated with c-axis

perpendicular to the hinge axis, parallel with the long axis of the prism (Figure 59f-h). Calcite crystals show varied orientation. At the central and posterior parts (Figure 59g & h), calcite crystals are orientated with c-axis parallel with the hinge axis, perpendicular to prism elongation. At the posterior, the calcite c-axis is slightly rotated towards the ventral margin (Figure 59h). At the anterior, calcite crystals are orientated consistent with the aragonite, with c-axis perpendicular to the hinge axis (Figure 59f).

The ligostracum of all hinge parts of the right valve is underlain by foliated calcite (Figure 59a). Calcite crystals of the folia are orientated with the c-axis perpendicular to lath elongation. Underlying the central chondrophore surface, laths are orientated with the long axis perpendicular to the hinge axis, hence aligning the c-axis parallel with hinge axis. Towards the anterior and posterior, laths splay out becoming sub-parallel to the sloping ligament surface (Figure 59f-h). C-axis orientation remains perpendicular to lath elongation.

At the posterior, a transition region, 30 µm thick, underlies the ligostracum. This region tapers to 5-10 µm close to the boundary with the chondrophore. The transition region is composed of calcite crystals orientated in a similar manner to those of the overlying ligostracum with c-axis parallel to ligament surface but rotated towards the ventral margin. Aragonite was not detected in this region.

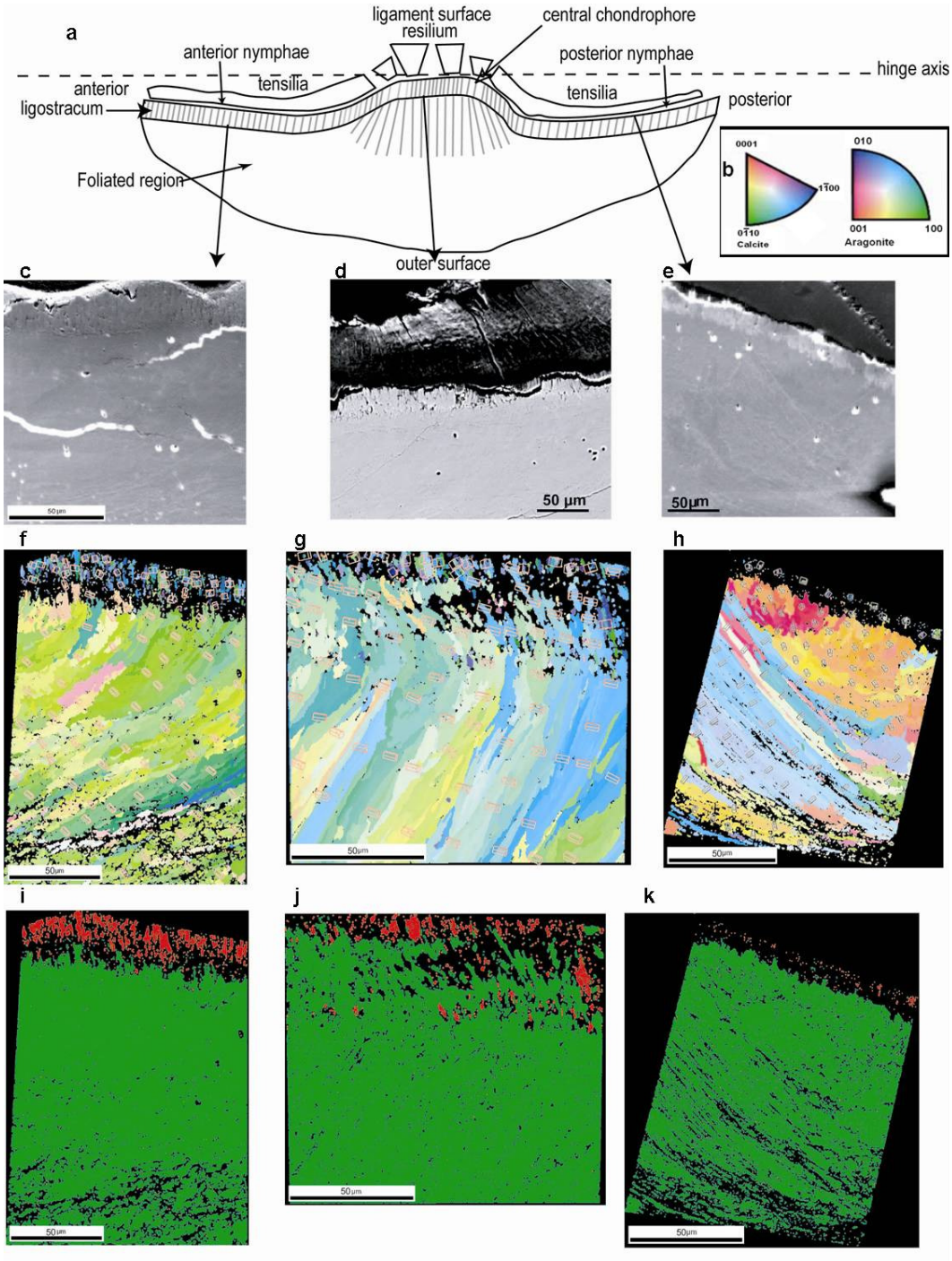

Figure 59. Crystallography of the structural components of the hinge region of the right valve.
(a) Diagrammatic representation of the hinge region of the right valve viewed from the ventral margin towards the umbo. (b) EBSD colour keys for calcite and aragonite. (c-e) Secondary electron SEM images showing scan areas of anterior nymphae, chondrophore and posterior nymphae surfaces respectively. (f-h). EBSD crystallographic orientation maps of anterior nymphae, chondrophore and posterior nymphae surfaces respectively with superimposed crystal models, with reference to the colour keys in (b). (i-k) Polymorph distribution maps of anterior nymphae, chondrophore and posterior nymphae respectively where green=calcite, red=aragonite.

3.4.5.2 Crystallography of the hinge region of the left valve

EBSD maps of all parts of the hinge region of the left valve are displayed in Figure 60 and summarised in Figure 61.

The ligostracum of the left valve is composed entirely of calcite with only very few single aragonite crystals (Figure 60i-k). At the centre the ligostracum is composed of two layers; an interior mineralised layer (in contact with the ligament) and outer organic rich layer with an underlying transition zone. At the interior layer of the ligostracum, in contact with the ligament, calcite crystals are orientated with the c-axis perpendicular to the ligament surface, with no significant aragonite component. Underlying the interior layer there is a thin layer (approximately 10 µm thick) which is depressed relative to the outer parts and underlying foliated region. This depressed region is composed of finely crystalline prisms that are likely to have been surrounded by a thick organic network which have been lost during treatment with NaClO. These prisms are composed of calcite with some interspersed aragonite.

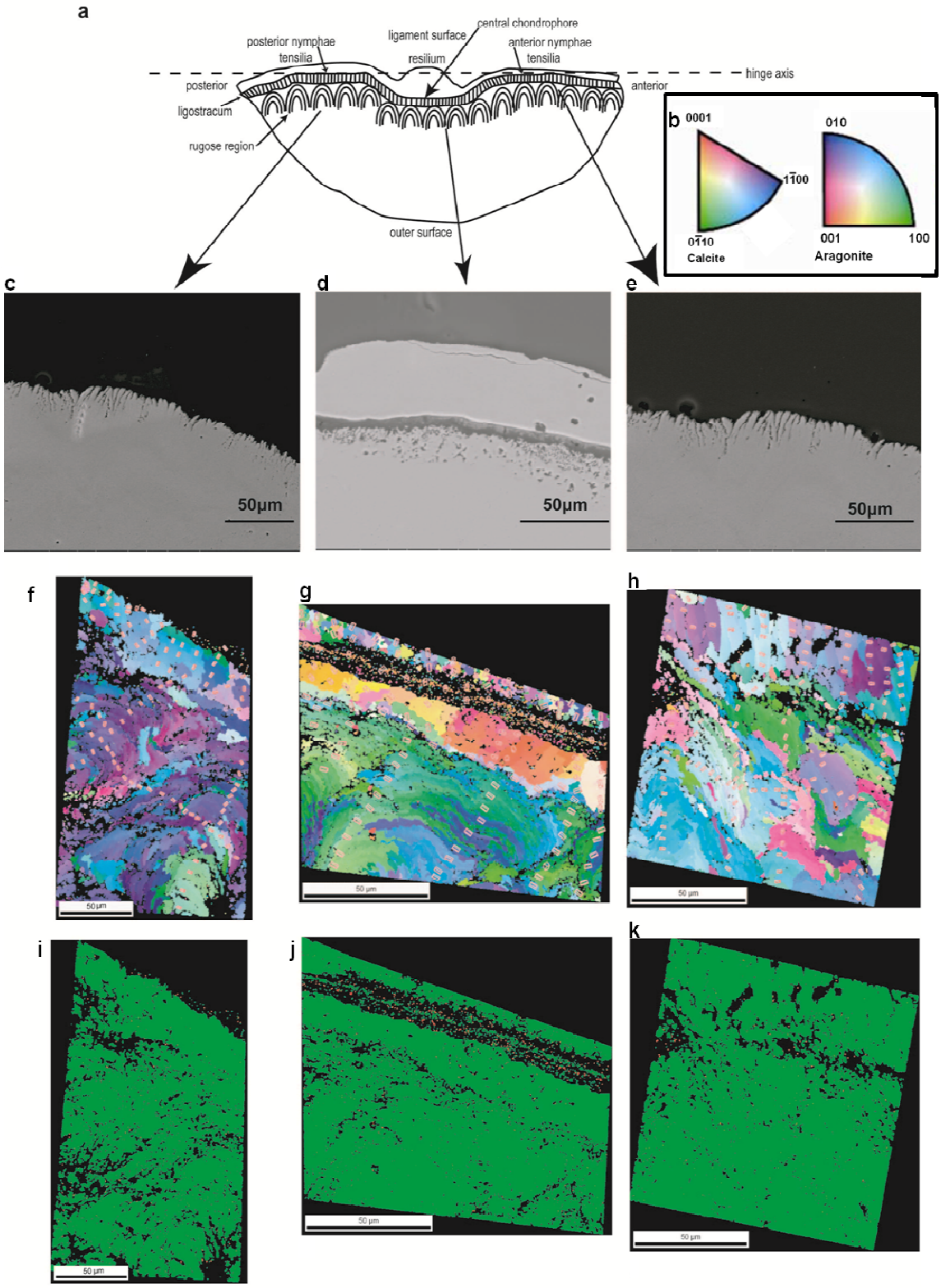

Figure 60. Crystallography of the structural components of the hinge region of the left valve. (a) Diagrammatic representation of the hinge region of the left valve viewed from the ventral margin towards the umbo. (b) EBSD colour keys of calcite and aragonite. (c-e) Secondary electron SEM images showing scan areas of posterior nymphae, chondrophore and anterior nymphae respectively. (f-h). EBSD crystallographic orientation maps of posterior nymphae, chondrophore and anterior nymphae respectively with superimposed crystal models, with reference to the colour keys in (b). (i-k) Polymorph distribution maps of posterior nymphae, chondrophore and anterior nymphae respectively where green=calcite, red=aragonite.

The ligostracum of the posterior nymphae is composed of calcite with two orientation types. Near the boundary with the chondrophore, the calcite c-axis is orientated perpendicular to the ligament surface. Moving away from this boundary, the c-axis rotates to near parallel with the ligament surface (Figure 60f). At the anterior, the ligostracum shows strong alignment of the calcite c-axis parallel with the ligament surface (Figure 60h).

The ligostracum of all parts of the hinge of the left valve is underlain by rugose folia (Carriker and Palmer 1979, Carriker et al. 1980). The rugose region is composed of laths of calcite folded around a series of elongate pits to create a corrugated texture (see section 3.2.6.2 & Figure 60f-h). The rugose region underlying all parts is composed of calcite orientated with the c-axis parallel to the ligament surface. The c-axis mirrors the topography of the ligament surface to remain parallel at all times, i.e. the c-axis is inclined at the posterior and anterior to follow the slope of the ligament surface, becoming horizontal at the centre (Figure 60e-g). Phase maps(Figure 60i-k) show the rugose region as being composed of calcite with no aragonite present.

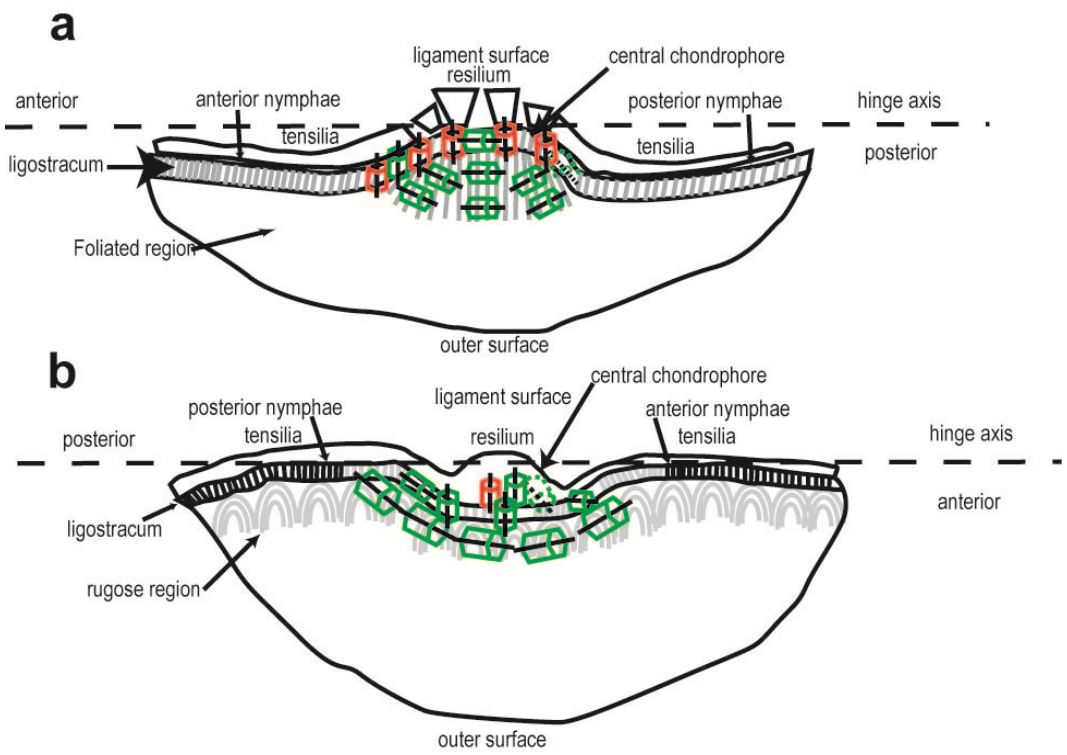

Figure 61. Summary of crystallography of the mineralised parts of the hinge.
(a) Summary of the crystallography of the hinge region of the right valve, schematic diagram of the hinge region, viewed from the ventral margin towards the umbo, with crystal orientation models. (b) Summary of the crystallography of the hinge region of the left valve, schematic diagram of the hinge region, viewed from the ventral margin towards the umbo, with crystal orientation models. Key: red crystal models =aragonite, green crystal models = calcite.

3.5 Discussion

3.5.1 Comparison of estuarine and marine Crassostrea gigas

Oyster shell growth rate, size and density vary as a response to external environmental conditions (e.g. Palmer and Carriker 1979, Cognie et al. 2006, Diederich 2006, Lartaud et al. 2010a, Lartaud et al. 2010c). Comparison of the oyster, *C. gigas*, from estuarine and marine environments, in this study, showed differences in shell macrostructure while the microstructural arrangement, and to a large extent chemistry, of the shells was similar. Both right and left valves of marine *C. gigas,* from Loch Tuath, were significantly thicker (T-test, $p=0.006$, $p<0.01$ for right and left valves respectively) than those of estuarine *C. gigas,* from Loch Fyne. Marine samples also contained cavities that were entirely absent in estuarine equivalents.

3.5.2 Cavities in marine C. gigas

Spionid worms (Spionidae) have worldwide distribution and are common inhabitants of the shells of many bivalves including oysters (e.g Royer et al. 2006) and clams (e.g. Riascos et al. 2008), as well as some gastropods such as abalone (Lleonart et al. 2003). Spionid worms, often termed blister or mudworms, bore U-shaped burrows in shells which are connected to the shell exterior and become filled with mud accumulated by the worm (Zottoli and Carriker 1974). Oysters respond to the irritation caused by the worm by secreting a thick organic membrane onto which normal shell growth continues creating a 'blister' containing the worm and mud (e.g. Almeida et al. 1996, Almeida et al. 1998, Royer et al. 2006, and references therein). It is likely that most cavities present in marine *C. gigas* in this study are related to infestation by Spionid worms. The blisters predominantly occur within, and are of a similar shape to, chalk lenses. Chalk deposits are porous and are considerably softer than surrounding folia. It is likely that worms preferentially attack chalky deposits excavating, in some cases, the entire lens structure. Isolation of the worm by secretion of an organic membrane and growth of folia around the blister hinders further movement of the worm. Within some cavities however, U-shaped internal structure cannot be identified, nor are the cavities connected to the shell exterior. SEM imaging of these cavities reveals that cavities are filled with sediment particles up to 100 μm long. It is considered that these sediment-filled cavities are not formed by Spionid worms. It has long been recognised that oysters may form empty chambers in their shell (e.g. Korringa 1951, Galtsoff 1964, Stenzel 1971, Higuera-Ruiz and Elorza 2009). Many authors have reported a correlation between chamber formation and high concentrations of inorganic material in the water column (Korringa 1951, Key et al. (1976), Higuera-Ruiz and Elorza 2011). Oysters grow around the particles by secreting an organic membrane, onto which folia develop, encasing the sediment in a chamber (Korringa 1951, Higuera-Ruiz and Elorza 2011). This mechanism is almost identical to that described by other authors for the isolation of Spionid worms (e.g. Almeida et al. 1996, Almeida et al. 1998, Royer et al. 2006, and references therein). Severe chambering has been attributed to anthropogenic factors such as contamination by tributyltin (TBT) (Alzieu et al. 1986, Minchin 2003, Higuera-Ruiz and Elorza 2009). Chambering in this study is not as extensive

as that normally associated with pollution, and TBT pollution is unlikely to be present Loch Tuath as it is not an active port or marina. It is considered that cavities in marine samples, not formed by Spionid worms are related to high sedimentation in the water of Loch Tuath. Indeed, elemental mapping of marine oyster shells reveals sediment particles incorporated in chalk lenses (Figure 52).

The structure and biochemical properties of the organic membrane in blisters have been intensively studied by Almeida et al. (1996, 1998). Almeida et al. suggested that the organic membrane in shell blisters is similar to the organic material of the prismatic region, and consider that the mantle epithelium can switch from folia to prism secretion in response to worm irritation. The structure of the organic material around sediment-filled cavities broadly resembles the chalky structure (Figure 51d). The organic material consists of a network of shallow depressions and connecting walls that, in places, show crystalline structure. While no biochemical studies were carried out on the organic membranes, the structure and positioning of the blisters suggests that the organic material, secreted to incorporate inorganic particles, may be similar to that of the chalk. Oysters frequently interrupt folia with chalky lenses (e.g. Carriker et al. 1980), and so it is considered that the secretion of chalk membranes in response to irritation could be possible. Individual biochemical analysis of organic membranes of blisters/chambers, chalk, folia and prisms would provide more information to help test this hypothesis.

3.5.3 Thick valves and reduction of chalk in marine C. gigas*.*

Both valves of marine *C. gigas* were significantly thicker than estuarine (T-test, p=0.01 and p=0.001 for right and left valves respectively). Thickening of valves may be related to the presence of cavities, or may form as an independent response to high incidence of predation and sedimentation and higher energy conditions in the marine environment (Kirby 2000, Kirby 2001). Marine valves were heavily encrusted with barnacles, tube worms and young oysters. Increasing valve thickness may be a response to such irritants and /or to provide density in high energy marine conditions.

Thick valves are often associated with a high chalk volume (e.g. Kirby 2000). In this study however, the thick valves of marine *C. gigas* contain, on average, less

chalk than thinner estuarine samples. Irritation by inorganic particles and worms may inhibit chalk development in marine samples. Alternatively, chalk may be induced in estuarine samples by fluctuating water conditions. Palmer and Carriker (1979) report more dense shells (containing less chalk), in oysters reared in 'recycle systems' compared with those from 'flow through systems' and natural estuaries. The recycle system used by Palmer and Carriker (1979) involves continued use of the same water, while in the flow through system the water is replaced every second day. Similarly natural estuaries generally have a high water turnover due to high volumes of freshwater runoff entering the system (e.g. Dame and Allen 1996, Surge et al. 2001, Sheldon and Alber 2006). Palmer and Carriker (1979) suggest that fluctuating, and lower calcium concentrations in recycle systems may induce the development of more rigid, relatively chalk-free, shells. In flow through and estuarine systems, with higher water turnover, and higher calcium concentrations, shells are chalkier (Palmer and Carriker 1979). Similarly in this study, it is in the estuarine system that oysters develop shells with highest chalk volume. High water turnover may be responsible for high volumes of chalk in estuarine oysters, possibly due to a rapid influx of new nutrients and increasing calcium concentrations from terrestrial runoff.

As a response to environmental conditions in the marine environment, including exposure to high sedimentation and predation from Spionid worms, *C. gigas* develops a thicker, more rigid shell. Cavities form to isolate irritants including worms and sediment within the shell. The lack of chalk in marine samples, compared with estuarine, is interesting. Marine samples may form a dominantly foliated shell to provide rigid support in the higher energy environment and to defer against predation. Alternatively, excess chalk may form in estuarine oysters as a consequence of constantly mixing marine and freshwaters causing influxes in calcium and nutrient concentrations.

3.5.4 Microstructure, crystallography and chemistry of C. gigas

In terms of the microstructural arrangement of the valves, estuarine and marine samples are indistinguishable. Both valves are identical in terms of microstructural arrangement and crystallographic orientation, with the

exception of the hinge region. Ventral of the umbo the oyster shell is composed predominantly of low Mg calcite in three forms, prismatic calcite, foliated calcite and chalky calcite. Aragonite is present only at the myostracum. These findings are in accordance with the works of previous authors for American oyster, *C. virginica*, the European oyster *O. edulis* as well as *C. gigas* (e.g. Galtsoff 1964, Stenzel 1971, Carriker et al. 1980, Kirby 2000, Higuera-Ruiz and Elorza 2009). The prismatic region constitutes the outermost mineralised structure of the oyster shell. Previous authors report conflicting results regarding the presence or absence of the prismatic region in the left valve (e.g. Checa et al. 2005). This study confirms the presence of the prismatic region as the outermost structure in both right and left valves of *C. gigas,* albeit shorter prisms in the left valve relative to the right.

Within each microstructure, the crystallographic orientation is the same, that is with c-axis orientated perpendicular to the inner and outer shell surface (maximum lateral variation of 45° occurring in the folia). The microstructure and crystallography throughout the oyster shell is summarised in Figure 62.

3.5.4.1 Functional morphology of oyster shell structure

The geological longevity and widespread distribution of the oyster suggests that the valves have successfully evolved to provide optimum protection to the organism while being adaptable to a range of environmental conditions.

Like many bivalves, the outermost mineralised shell layer of the oyster comprises calcite prisms. Calcite prisms are composite structures, composed internally of individual laths, encased in an organic sheath (Esteban-Delagdo et al. 2008, Checa et al. 2009, Okomuru et al. 2010). The crystallographic c-axis within, and between, individual prisms is the same with the c-axis orientated perpendicular to the shell surface and parallel to the elongation of the prism (Checa et al. 2005, Checa et al. 2009, MacDonald et al. 2010, Freer et al. 2010). Orientation of the c-axis parallel with prism elongation is advantageous in terms of growth (Checa et al. 2005) but may also enhance the material properties of the structure. Harper et al. (2009) proposed that this morphological - crystallographic relationship in the prismatic region of *E. navicula*, together with a high quantity of organic matrix, provides the shell with flexibility that

enhances the ability of the shell to withstand impact. Similarly, the prismatic region of the oyster has been noted to exhibit exceptional bending capacities (Checa et al. 2005, Checa et al. 2009). It is proposed that the presence of comparable characteristics in the prismatic region of *C. gigas* may serve a similar function in minimizing the effect of impact by adding flexibility to the shell structure. This flexible structure must therefore rely upon the rigidity of the internal shell for support.

The prismatic layer of both valves of *C. gigas* is bound to the interior by the foliated structure. This structure constitutes the bulk of both valves and is composed of elongate laths of calcite arranged laterally to form sheets. Individual laths are coated with a thin organic matrix (Lee et al. 2008b), however this organic material is much less conspicuous in the foliated structure when compared with the overlying prismatic region. This reduction in organic content may account for the reduced flexibility of this structure when compared to the prismatic structure (e.g. Taylor and Layman 1972). Taylor and Layman (1972) noted that although foliated calcite has a very low resistance to impact, the cracks generated were not able to penetrate the entire structure and formed only localised holes. This ability to prevent crack propagation was also noted by Lee et al (2008a) who attributed this feature to clustering of folia of different orientations. Lee et al (2008a) identify lath orientation to be 1 of 2 possible types where type 1 laths are orientated within 90° of a reference lath (taken as the top lath of the block of folia analysed) and type 2 are orientated at > 100° from the same reference. Clustering of lath orientations was also noted in this study. Supporting the observations by Lee et al (2008a), laths were found to be of two orientation types. Type 1 laths are orientated with long axis of the lath parallel or near parallel with the dorso-ventral axis, type 2 laths are orientated up to 45° from type 1 (Figure 55). It is also noted that the lath growth front may be inclined towards the outer shell surface (Figure 56). Despite variation in lath orientation, EBSD analysis reveals consistent orientation of the crystallographic c-axis, perpendicular to the outer and inner shell surfaces with lateral variation of up to 35°. This supports the work of Checa et al. (2007a), who report that there is only one possible c-axis orientation in the folia, where the c-axis is tilted 21-30º from the lath front. Uniformity in c-axis orientation illustrates that variation in lath orientation, between type 1 and type 2, must be

a morphological feature causing in-plane rotation of crystallographic a and b axis around a fixed c-axis (Figure 55). Where laths are inclined towards the shell exterior, most notably underlying curved shell parts, the c-axis is tilted relative to the shell surface (Figure 56).

Clustering of laths of variable morphological orientation enables the shell to inhibit crack propagation (Lee et al 2008a). Maintaining a uniform c-axis orientation, while changing the morphological orientation of the laths, may further enhance the shell properties. Schmahl et al. (2004) reports that, like the folia of the oyster, the secondary fibrous layer of the brachiopod (order Terebratulida) is composed of calcite fibres orientated parallel with the shell surface while the crystallographic c-axis is perpendicular to the shell surface. Calcite crystals preferentially cleave along the {104} plane and so by orientating the {0001} plane perpendicular to the outer shell surface, maximum distance is achieved between the plane of weakness in the calcite crystal (the {104} plane) and the potential fracture surface (Schmahl et al. 2004). This morphological-crystallographic arrangement in the terebratulide brachiopod, which is analogous to that of the foliated structure of the oyster, provides optimum resistance to fracture. Within the oyster shell folia, the crystallographic c-axis is orientated consistently with that of the prismatic structure, and therefore perpendicular with the outer shell surface and long axis of the laths. It is proposed that through this arrangement the shell maintains a degree of strength as a first line of defence against impact. Altering lath orientation may provide deflection in the event of cracking by inhibiting the progress of any cleavage failure through adjacent folia (Lee et al 2008a).

The foliated structure is frequently interrupted with lenses of chalky calcite. The function and sporadic appearance of the chalk lenses has long been of interest (e.g. Gray 1883, Orton 1927, Korringa 1951, Galtsoff 1964, Carriker et al. 1980). The left valves of *C. gigas*, from both estuarine and marine environments, contain significantly more chalk than the right valves. The left valves are deeply cupped relative to the flatter right, indicating, as suggested by Korringa (1951), that the chalk lenses act to 'smooth' the shell surface. However, despite similar valve shape, significantly less chalk is present in both valves of marine *C. gigas* when compared with estuarine. This difference in chalk volume between sample sets suggests that the appearance of chalk is, to some

degree, a response to environmental conditions. Salinity is variable between environments and is more stable in marine settings than in estuarine. However, Palmer and Carriker (1979) report differences in chalk volume between environments in which the salinity was constant. Estuarine samples are exposed to higher water turnover rates which may cause rapid influxes in nutrients which may encourage chalk development. Chalk occupies more space per unit volume than folia, and so may offer 'cheap padding' by requiring less energy, than folia, in its secretion (Korringa 1951, Galtsoff 1964, Stenzel 1971, Carriker et al. 1980). It is possible that this requirement for 'cheap padding' may come as a response to external environmental conditions, such as rapid fluctuations in nutrient content. The onset of chalk deposition can be sudden (Figure 45a), or gradual (Figure 45b-d), suggesting that the rate at which chalk is deposited can be controlled. This difference in rate of shift from folia to chalk deposition may reflect the rate of changing environmental conditions. The preference for a higher volume of more porous chalk in the left valve compared with right valve is interesting. Oysters invariably attach to a substrate by cementation of the left valve (e.g. Yonge 1960, Harper 1992). This difference in chalk volume amount of void space suggests that oysters preferentially secrete chalk in the left valve, possibly to preserve a dominantly foliated upper right valve to provide rigidity and protection.

Crystallographic analysis reveals that, within the main blades of the chalk, the c-axis is orientated, as in the folia and prisms, perpendicular to inner and outer shell surfaces, parallel with blade elongation. This morphological-crystallographic relationship, together with a higher quantity of organic material in the chalk (Korringa 1951, Weiner and Hood 1975), would give the chalk flexibility, further enhancing the ability of the shell to withstand impact. Similarly, Taylor and Layman (1972) suggest that the chalky lenses of the oyster serve a similar function to the holes incorporated into bone which act as 'crack stoppers' (Currey 1964). The mechanical properties of the chalk layer were recently investigated by Lee et al (2011) and the chalk layer is reported to be brittle, with low hardness yet is capable of absorbing shock helping to prevent crack propagation.

Although chalk may be deposited as a 'cheap' secretion in response to external environmental conditions, the crystallography of the chalk blades is precisely

controlled to ensure consistent c-axis orientation between folia and chalk. Chalk is likely to be more flexible than folia and is therefore preferentially secreted into the left valve to maintain rigidity in the exposed upper right valve.

3.5.4.1.1 Functional morphology of the hinge region of C. gigas

The hinge region of the oyster, summarised in Figure 59-61, is complex and variable between valves. The organic ligament attaches to the shell by a prismatic layer (ligostracum (Carriker and Palmer 1979)), which in the right valve comprises intertwined calcite and aragonite and in the left comprises only calcite. The ligostracum overlies the foliated structure which in the left valve is folded to create a rugose texture (Carriker et al. 1980).

First identified by Carriker and Palmer (1979), the ligostracum acts to bind the organic ligament to the mineralised shell. In this respect the ligostracum serves a similar function as the myostracum which binds the adductor muscle to the shell. Myostracum shell deposits are common to most bivalves and are invariably composed of aragonite (e.g. Kennedy et al. 1969). Carriker and Palmer (1979) identified both calcite and aragonite in the ligostracum of several oyster species. This study has confirmed, by EBSD analysis, the presence of both aragonite and calcite in the right valve ligostracum of *C. gigas*. The presence of both polymorphs in a single shell microstructure is unusual (e.g. Kennedy et al 1969). Polymorph selection is determined by shell matrix protein components which select and control the secretion of a single polymorph of $CaCO_3$ (Marin et al 2007). Carriker et al. (1980) suggest that oysters may switch polymorph in response to environmental or physiological stimuli. Salinity and temperature variation are shown not to affect the mineralogy of bivalve shell structures (e.g. Kennedy et al. 1969, Neri et al. 1979). Checa et al. (2007b) show that Mg-enriched waters can cause aragonite precipitation in calcite bivalves. Increases in Mg/Ca ratio of local seawater could cause aragonite deposition in the ligostracum. However, presumably increase in Mg/Ca ratio would lead to single aragonite horizons rather than intertwined aragonite and calcite. It is more likely that the presence of both polymorphs is a genetic characteristic. Aragonite may be deposited to reinforce, and add strength to, a calcite structure as a way of reducing the energy that would be required to secrete an entirely aragonite structure (Carter et al. 1998). The presence of aragonite in the right valve

ligostracum and not the left is curious and may suggest that the right valve is more directly involved in the function of the ligament.

Underlying the ligostracum of the left valve, the foliated calcite forms a rugose texture. Carriker et al. (1980) noted the presence of this layer and imply it is present in both valves. From SEM and EBSD analysis (Figure 59 & Figure 60), it is clear that the foliated calcite underlying the ligostracum in the left valve is rugose while in the right valve 'normal' folia is present. Few studies have focused on the mineralised parts of the oyster hinge and little is known of this structure. The folded nature of the rugose region suggests that it may act to absorb impact when the valves close, which in the lower valve may be more than in the upper.

3.6 Summary

C. gigas reared in an open marine environment develops a significantly thicker shell, containing cavities and less chalk than estuarine equivalents. Oysters in marine environments are likely to grow thick valves as a response to high energy conditions, increased predation and irritants. The increase in chalk volume in oysters from estuarine environments may be a response to higher water turnover in this environment. No other difference in valve size or structure was observed between estuarine and marine samples of *C. gigas*.

Both valves of oysters from estuarine and marine environments are composed of three distinct calcite microstructures recognised as the prismatic layer, foliated structure and chalky lenses. Aragonite is restricted to the myostracum and parts of the hinge region. Despite differences in morphology, each of these microstructures exhibits an identical crystallographic orientation, with c-axis orientated perpendicular to inner and outer shell surfaces. This microstructural and crystallographic arrangement of the oyster shell is summarised in Figure 62. It is proposed that crystallographic unity throughout the oyster shell may provide a degree of strength while morphological variation provides flexibility and crack deflection. These shell properties have enabled oysters to successfully adapt to and exploit a range of habitats by providing optimum protection, whilst being adaptable to changing environmental conditions.

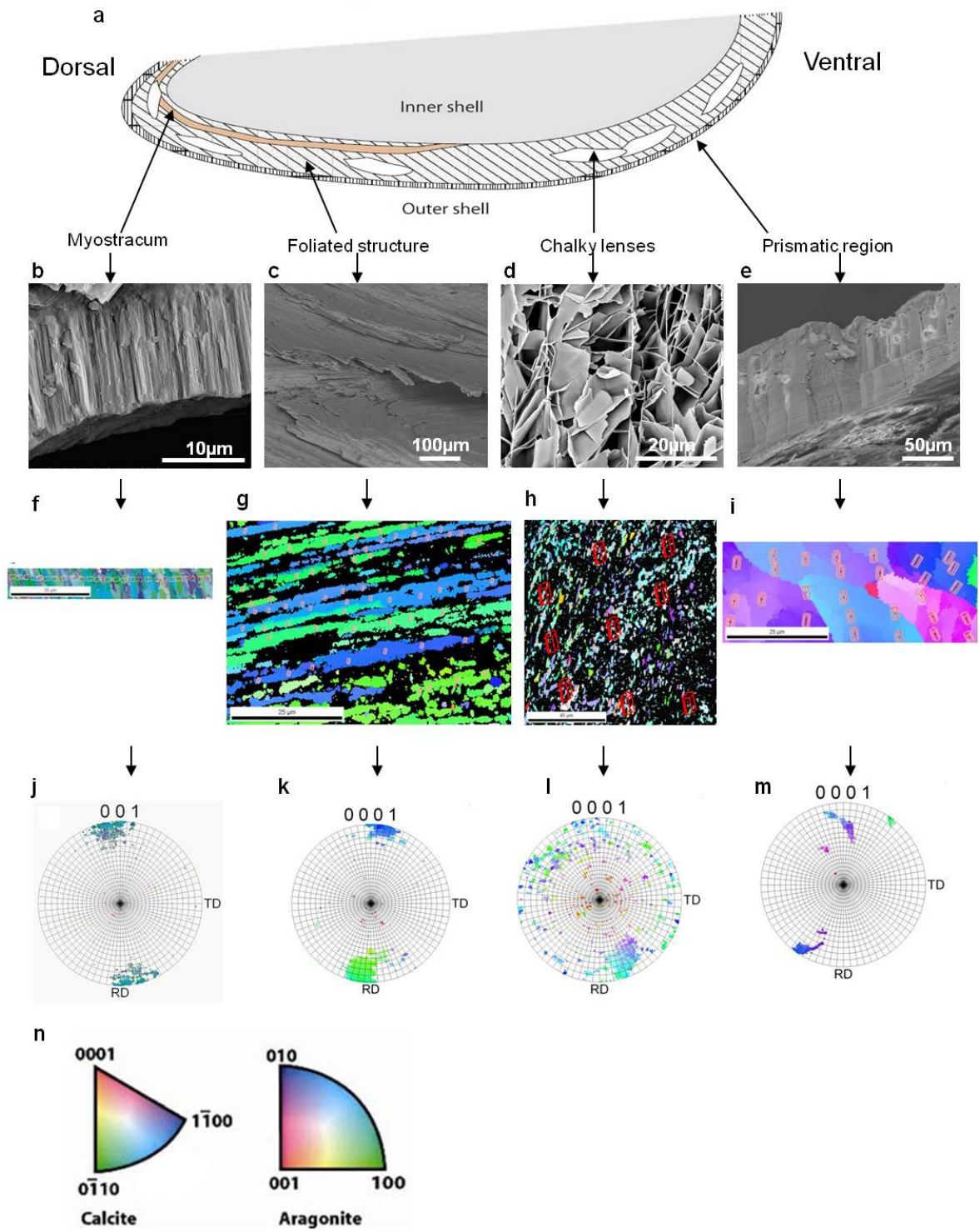

Figure 62. Summary diagram of the microstructure and crystallography of *C. gigas*.
(a) Schematic cross section of the shell of *C. gigas* showing structural components. (b-d) Backscattered electron SEM images of the myostracum, folia and chalk respectively. (e) Secondary and backscatter electron mixed SEM image of the prisms. (f–i) Electron backscattered diffraction maps with superimposed crystal models, showing crystallographic orientation for myostracum, folia, chalk and prismatic region respectively. Scale bars are 5 µm, 25 µm, 45 µm, 25 µm respectively. (j) Pole figure showing crystallographic orientation of aragonite crystals in myostracum in reference to {001} plane. (k-m) Pole figures showing crystallographic orientation of calcite crystals in reference to {0001} plane, for folia, chalk and prisms respectively. (n) Crystallographic orientation map colour key for calcite and aragonite with reference to normal direction

Chapter 4. Stable isotope composition of estuarine and marine *Crassostrea gigas*.

4.1 Introduction

The stable carbon and oxygen isotopic ratios of biogenic carbonates have long been recognised as potential archives of environmental change (e.g. Urey 1948, Epstein et al. 1953, Lowenstam 1961, Lecuyer et al. 2004, Parkinson et al. 2005, Fan et al. 2011). The $^{18}O/^{16}O$ and $^{13}C/^{12}C$ ratios of biogenic $CaCO_3$ are to a large extent a function of the temperature and isotopic ratios of the external environment. Where isotopic equilibrium exists between $CaCO_3$ and the ambient environment, a wealth of environmental information can be obtained such as temperature (e.g. Epstein et al 1951, Lowenstam 1961), salinity (e.g. Mook and Vogel 1968, Mook 1971) and marine productivity (e.g. Wang et al. 1995). However, the strict biological control exerted during the secretion of most biomineral structures can influence shell isotope ratios, complicating interpretation of the environmental signal (e.g. McConnaughey 1989, Auclair et al. 2003, Schöne 2008, Ford et al. 2010). Within a dynamic biological system, variables such as growth rate, respiration, metabolism and calcification can influence stable isotope compositions (e.g. Schöne 2008). This biological effect is further complicated as biological functions are themselves often influenced by prevailing environmental conditions (e.g. Putten et al. 2000, Schöne et al. 2003, Dahlhoff 2004, Gillikin et al. 2005, Lartaud et al. 2010c). For example, changes in metabolic rate as a response to stress may influence the amount of isotopically light metabolic carbon incorporated into parts of the $CaCO_3$ structure (e.g. Carpenter and Lohmann 1995, McConnaughey et al. 1997, Owen et al. 2002, Lartaud et al. 2010b). Understanding stable isotope proxies in the context of biomineralisation is therefore imperative prior to the application of biogenic carbonates as reliable environmental proxies.

4.1.1 The stable isotope signature of oyster shells - previous studies

It is widely accepted that environmental interpretation of stable isotope ratios from biogenic carbonates may be complicated by the biological or 'vital' effects of the organism. Following the influential study by Lowenstam (1961), much work has been conducted to assess the influence of vital effects in a range of phyla, using modern specimens grown in waters with known environmental parameters (e.g. Lecuyer et al. 2004, Parkinson et al. 2005, Ford et al. 2010).

The ubiquitous nature and gregarious habit of the oyster makes them potentially ideal proxies of environmental change. However, most modern oysters inhabit estuarine or brackish water environments, where fluctuating $^{18}O/^{16}O$ ratios in the water make it difficult to differentiate between the effects of temperature and biological function (e.g Gillikin et al. 2005, Brigaud et al. 2008, Ford et al. 2010). Kirby et al. (1998) carried out the first rigorous assessment of the stable isotope signature of the modern estuarine oyster *Crassostrea virginica*. Applying a sclerochronological approach, the authors sampled foliated calcite adjacent to external convex and concave growth bands to achieve a seasonal isotopic profile which corresponded to actual seasonal temperature variations. These data were added to by Surge et al. (2001, 2003) who demonstrated that both chalky and foliated microstructures at the hinge region of *C. virginica* are secreted in oxygen isotopic equilibrium with the ambient environment. Indeed, seasonal oxygen isotope profiles, accurately reflecting actual temperature variation, have been reported for the hinge region of the oyster by several authors (e.g. Surge et al. 2001, 2003, Lartaud et al. 2010b, Lartaud et al 2010c, Ulmann et al. 2010, Fan et al. 2011). However, where more than one oyster is sampled, interspecimen variation can be significant (Andrus and Crowe 2000, Surge et al. 2003, Lecuyer et al. 2004).

Interpretation of carbon isotope profiles are inherently more complicated than oxygen isotope profiles as they are influenced by dissolved inorganic carbon (DIC pool) and organic carbon from food sources (particulate organic matter (POM)) (e.g. Riera and Richard 1997, Gillikin et al. 2005, McConnaughey and Gillikin 2008, Lartaud 2010b). This is further complicated as POM enters the shell via

metabolic pathways and as such the proportion of metabolic carbon included in shell carbonate fluctuates with metabolic rate (Lartaud et al. 2010b). This has lead to some confusion regarding the interpretation of $\delta^{13}C$ profiles in oysters. Several authors report strong covariance between $\delta^{18}O$ and $\delta^{13}C$ (e.g. Surge et al. 2001, 2003, Lartaud et al. 2010b, Fan et al. 2011), and some authors have suggested that $\delta^{13}C$ may be used as a salinity proxy (Kirby et al. 1998, Surge et al. 2001). However, interspecimen variation with respect to $\delta^{13}C$ can be significant suggesting a strong biological influence on the $^{13}C/^{12}C$ ratios (Owen et al. 2002, Lecuyer et al. 2004). For example, Lartaud et al. (2010b) demonstrate that changing food supply can have significant influence on metabolism which in turn alters the proportion of $\delta^{13}C_{meta}$ in shell carbonate.

Growth lines provide a temporal frame for isotopic analysis allowing seasonal isotopic variations to be deduced (e.g. Kirby et al. 1998). Most authors have utilised the incremental growth lines of the oyster when analysing the stable isotope composition of the shell, sampling only foliated calcite from the hinge region (e.g. Wang et al. 1995, Kirby et al. 1998, Kirby 2000, Surge et al. 2001, 2003, Ullmann et al. 2010, Fan et al. 2011). As a result, little is known of the stable isotope composition ventral of the hinge region. Interestingly, Wisshak et al. (2009) compared $\delta^{18}O$ values obtained from hinge and ventral parts of the deep sea oyster *Neopycnodonte zibrowii sp* and reported that values of $\delta^{18}O$ from the hinge and ventral parts showed no correlation and were positively offset from equilibrium. Ecophenotypic variation is inherent in oysters (Surge et al. 2001) and, as a result, external growth lines are not always readily apparent (Surge et al. 2001, Lartaud et al. 2010a). For example the convex/concave bands of Kirby et al. (1998) could not be identified by Surge et al. (2001), yet Fan et al. (2011) correlate external concave bands to internal growth lines. Other authors define growth bands as adjacent translucent (folia) and white (chalky) layers of the hinge region (e.g. Andrus and Crowe 2000, Ullmann et al. 2010, Fan et al. 2011). Some oysters contain no, or very little, chalk at the hinge region making it impossible to identify such growth bands. Lartaud et al. (2010a) identified internal growth increments by cathodoluminescence resulting from manganese incorporation in living oysters. However, this is only suitable where Mn has been deliberately increased during oyster growth to enable sufficient incorporation for detection by this technique. Growth line sampling is further

limited in cases where the hinge region is too small to provide sufficient material for analysis (e.g. Surge et al. 2001, Brigaud et al. 2008).

Most studies concerning oyster stable isotopes have been limited to the hinge region of estuarine oysters (Kirby et al. 1998, Surge et al. 2001, 2003). Oysters are euryhaline bivalves, surviving in a wide range of salinities (Yonge 1960, Stenzel 1971) and while most modern examples are common to estuaries, many are descendants of fully marine ancestors (Kirby 2000, 2001). The effect of external environmental conditions is prominent in oysters (Troost 2010) affecting growth rate (Lartaud et al. 2010a, Lartaud et al. 2010b, Lartaud et al. 2010c), shell density (Palmer and Carriker 1979, Kirby 2000) and shell thickness (Palmer and Carriker 1979, Kirby 2000). However, few authors have considered the influence of the external environment on the stable isotope ratios of shell carbonate. Oysters inhabiting open marine habitats are often exposed to harsher environmental conditions including increased predation and sedimentation and, as a result, are often associated with higher growth rates (Kirby 2000, 2001, Lartaud et al 2010c) and thicker, more chalky shells than their estuarine relatives (Kirby 2000, 2001). Recently Ullmann et al. (2010) considered the stable isotope composition of modern oysters from a marine environment. The authors analysed the hinge folia of a single oyster and report a seasonal isotopic profile that reflects actual environmental conditions.

Over the last decade much work has been conducted to understand the stable isotope profile of oysters. It is generally accepted that folia from the hinge region of estuarine oysters is in isotopic equilibrium with respect to $\delta^{18}O$ (e.g. Kirby et al. 1998, Surge et al. 2001). Further work is required to understand the $\delta^{13}C$ signature of the oyster and to investigate the $\delta^{18}O/\delta^{13}C$ composition of valve parts ventral of the hinge. The influence of environment on stable isotope ratios of oyster shells should be investigated to further assess the suitability of marine oysters as proxies of environmental change. Interspecimen variation in oysters can be significant (Andrus and Crowe 2000, Lecuyer et al. 2004), and therefore, to provide a thorough analysis of oysters from any environment, several individuals should be analysed.

4.1.2 Aims of this study

This study aims to investigate the stable carbon and oxygen isotopic composition of the oyster *Crassostrea gigas*. A profile of $\delta^{18}O$ and $\delta^{13}C$ from hinge to ventral margin will be compared for foliated and chalk microstructures. Stable isotope profiles will be compiled from oysters farmed in an estuarine environment in Loch Fyne and compared with isotope profiles from marine oysters farmed in Loch Tuath, Island of Ulva (see section 2.1 for details). This will enable the effect of environment on shell stable isotope profiles to be determined. This approach will provide further understanding of oyster biomineralisation systems and the response of oysters to changing environmental conditions. A detailed assessment of the isotopic signature of marine oysters will inform the reliability of marine oysters as environmental proxies.

4.2 Results

The stable carbon and oxygen and isotopic composition of three estuarine and three marine oysters was investigated in this study. For each oyster, cross sections of the left valves were produced by methods detailed in section 2.2.2. Each valve was subsequently divided into four sections of approximately equal size from hinge to ventral margin – sections hinge (H), A, B, C (Figure 63).

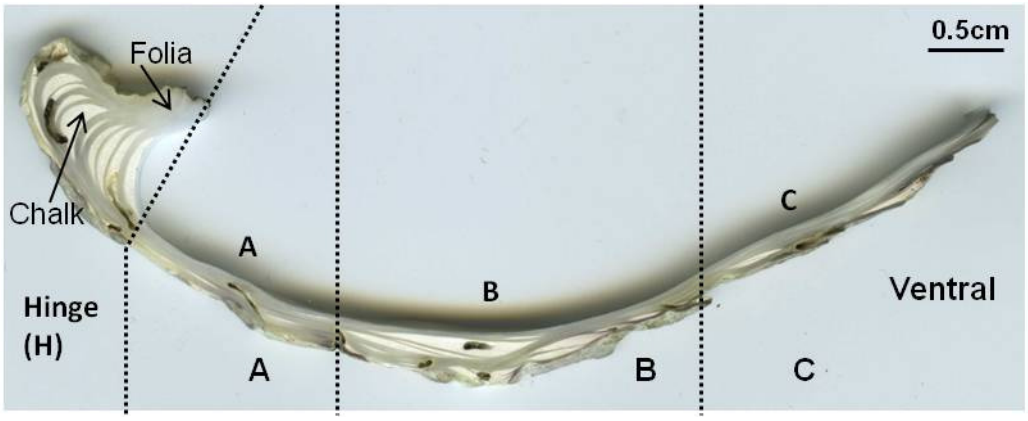

Figure 63. Valve division from hinge to ventral margin for isotopic analysis.
Left valves of three estuarine and three marine oysters were subdivided into four sections, of approximately equal size, from hinge to ventral margin. From each valve section 3 X 1 mg samples of chalk and, 3 X 1 mg samples of folia were sampled for isotopic analysis.

From each section, a minimum of 3 mg of folia and 3 mg of chalky calcite were milled and separated into three separate 1 mg samples to allow replicate analysis. This sampling strategy provided, from each valve, 12 folia and 12 chalk

samples. Three estuarine and three marine valves were sampled in this way, providing a total of 36 folia and 36 chalk samples from each environment. The outermost mineralised layer of the oyster shell comprises prismatic calcite (see section 3.2.4.1 and references therein). Prisms are typically < 200µm in height and could not be identified during micromilling and were therefore not sampled for isotopic analysis.

Results from estuarine and marine sample sets are presented individually on cross plots of $\delta^{18}O$ versus $\delta^{13}C$, discussed separately and then compared. A full account of all isotopic analyses is provided in Appendix C.

4.2.1 Carbon and oxygen isotope composition of estuarine C. gigas.

The left valves of estuarine samples, F8, F9 and F10 were analysed in order to ascertain the oxygen and carbon isotope composition of both foliated (folia) and chalky calcite throughout the height (from H to C) of the valve (see sections 2.3.6 & 4.2). During analyses by mass spectrometry, two samples of chalk and one sample of folia failed to provide a result. All analyses of the isotopic composition of chalky calcite from estuarine samples are therefore based on the analyses of 34 chalk samples, and analyses of foliated calcite is based on 35 folia samples.

Isotopic results obtained from all valve sections are presented in Figure 64 where replicate samples are shown individually. Values obtained from all valve sections for $\delta^{18}O$ range from -2.28‰ to 0.39‰, while $\delta^{13}C$ values exhibit a much smaller range from -1.29‰ to 0.36‰. Values for $\delta^{18}O$ and $\delta^{13}C$ are not significantly correlated (correlation coefficient, r=-0.10, n=69). Variation in isotopic values obtained from individual oysters for $\delta^{18}O$ is not significant. There is significant interspecimen variation with respect to $\delta^{13}C$ of the folia (ANOVA, p=0.005). However, $\delta^{13}C$ of chalk from individual oysters is not significantly different.

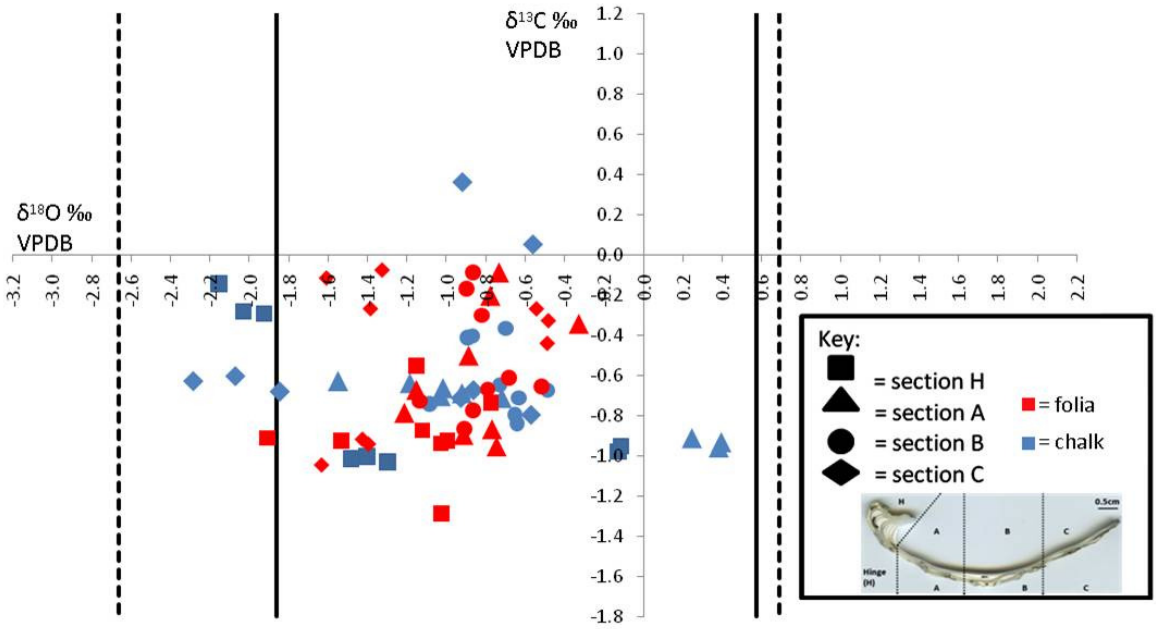

Figure 64. $\delta^{18}O$ – $\delta^{13}C$ cross plot of all isotopic data obtained for estuarine *C. gigas*. Each data point represents a single 1 mg sample of foliated or chalky calcite, where red=folia, blue=chalk. Solid lines represent maximum and minimum values of $\delta^{18}O$ expected under equilibrium conditions, based on an average $\delta^{18}O_{water}$ value of -0.6‰. Dashed lines represent maximum and minimum values of $\delta^{18}O_{carbonate}$ expected for equilibrium allowing for the actual range in $\delta^{18}O_{water}$ values.

There is no statistical difference in values obtained from folia and chalk for either $\delta^{18}O$ (T-test, p=0.95) or $\delta^{13}C$ (T-test, p=0.51). However, chalk samples exhibit the greatest range in values for both isotopes. Indeed, the maximum overall range for $\delta^{18}O$ of -2.28‰ to 0.39‰ reflects maximum and minimum values of chalk samples. Folia samples exhibit a much smaller range of $\delta^{18}O$ from -1.91‰ to -0.33‰, yet the average $\delta^{18}O$ values for both folia and chalk are similar, -0.99‰ and -0.96‰ respectively. Chalk also shows the greatest range in $\delta^{13}C$ values, ranging from -1.11‰ to 0.36‰, while for folia $\delta^{13}C$ values range from -1.29‰ to -0.07‰. The cross plot of $\delta^{18}O$ and $\delta^{13}C$ in Figure 64 reveals chalk to be most variable with respect to $\delta^{18}O$ (standard deviation σ=0.7‰) while $\delta^{13}C$ values are relatively stable (σ=0.3‰). The opposite is true for the folia for which values of $\delta^{13}C$ and $\delta^{18}O$ exhibit a similar degree of variability (σ=0.3‰ for both $\delta^{13}C$ and $\delta^{18}O$). Variability between chalk and folia for $\delta^{18}O$ and $\delta^{13}C$ is not significant (ANOVA, p=0.79 and p=0.51 for $\delta^{18}O$ and $\delta^{13}C$ respectively). Both microstructures show a weak trend of increasing $\delta^{13}C$ values from valve section H to C. However, through-valve patterns of $\delta^{18}O$ are variable between valve sections and follow no common trends.

Maximum and minimum values of $\delta^{18}O$ expected for carbonates secreted in isotopic equilibrium with Loch Fyne waters were calculated using the oxygen isotope fractionation expression of Kim and O'Neil (1997) shown in Equation 5 (section 2.3.6.4). Given the average $\delta^{18}O_{water}$ value for Loch Fyne of -0.6‰ (see section 2.3.6.4 for details), and known water temperature range of 6.3ºC to 17.6ºC, values of $\delta^{18}O$, for carbonates secreted in isotopic equilibrium, are expected to range from -1.86‰ to 0.57‰ (Figure 64). All folia samples lie within the expected equilibrium range with the exception of one (hinge sample of sample F8). The greater range in chalk $\delta^{18}O$ values sees five chalk samples fall outside the expected range for isotopic equilibrium at an average $\delta^{18}O_{water}$ value of -0.6‰. Salinity in Loch Fyne frequently fluctuates from 20 to 36 in response to fresh water runoff (discussed in section 2.1.1). Allowing for the actual salinity range (20-36) and corresponding range of $\delta^{18}O_{water}$ of -2.4‰ to 0.48‰ (section 2.1.1), $\delta^{18}O_{carbonate}$ values for equilibrium could range from -2.66‰ to 0.69‰, therefore encompassing all values of $\delta^{18}O$ obtained from folia and chalk samples.

Figure 65 shows a cross plot for $\delta^{18}O$ versus $\delta^{13}C$ where each data point represents the mean value of replicate samples from each valve, and error bars show the standard deviation (σ) for each group of replicates (replicate group=three folia or three chalk samples from a given valve section). Discrepancy within each group of replicates ranges from σ=0.02‰ to 0.22‰ for $\delta^{13}C$ and σ=0.01‰ to 0.47‰ for $\delta^{18}O$. Mean values of folia from all valve sections fall within the expected range for isotopic equilibrium. All mean chalk values also fall within the equilibrium range allowing for variable $\delta^{18}O_{water}$ values.

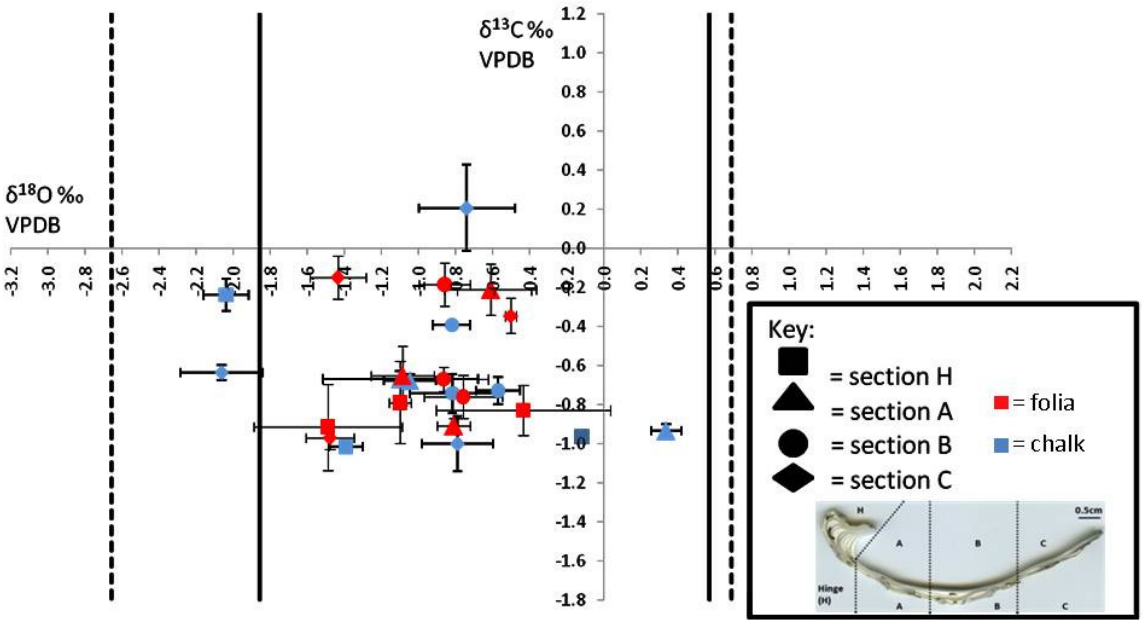

Figure 65. $\delta^{18}O$ – $\delta^{13}C$ cross plot of the mean values of replicate samples for estuarine *C. gigas*.
Each data point represents the average value of three replicate samples from one individual specimen with error bars showing standard deviation (σ) between replicates. Red=folia, blue=chalk. Solid lines represent maximum and minimum values of $\delta^{18}O$ expected under equilibrium conditions. Dashed lines represent maximum and minimum values of $\delta^{18}O_{carbonate}$ expected for equilibrium allowing for the actual range in $\delta^{18}O_{water}$ values.

Mean values of folia from shell sections A and B are almost indistinguishable with respect to both $\delta^{18}O$ (T-test, p=0.95) and $\delta^{13}C$ (T-test, p=0.73) and predominantly lie between values obtained from valve sections H and C for both $\delta^{18}O$ and $\delta^{13}C$. Mean $\delta^{18}O$ values of chalk from sections A & B are also similar (T-test, p=0.59) while values of $\delta^{13}C$ are slightly more varied, but are not significantly different (T-test, p=0.08). Mean chalk $\delta^{18}O$ and $\delta^{13}C$ values from valve sections A & B also, with the exception of one, lie between isotope values obtained from sections H and C. Two of the three valves sampled show a progressive increase in $\delta^{13}C$ values from section H to section C. This trend is consistent for both microstructures. In the third valve (F9) the opposite trend is observed in both folia and chalk, with progressive decrease in $\delta^{13}C$ values from section H-C. Patterns in $\delta^{18}O$ throughout the height of the valve are different for chalk and folia samples and are not consistent between individual valves. However, the lightest values of $\delta^{18}O$ are observed from shell sections H or C, and sections A & B exhibit similar values.

Patterns of $\delta^{18}O$ and $\delta^{13}C$ throughout valve height are more easily observed when removing the individual effect of sampling from valves of three individual oysters. In Figure 66 individual data points represent the mean value of folia or

chalk for each valve section from all valves analysed, so each point represents the mean of nine replicate folia or chalk samples.

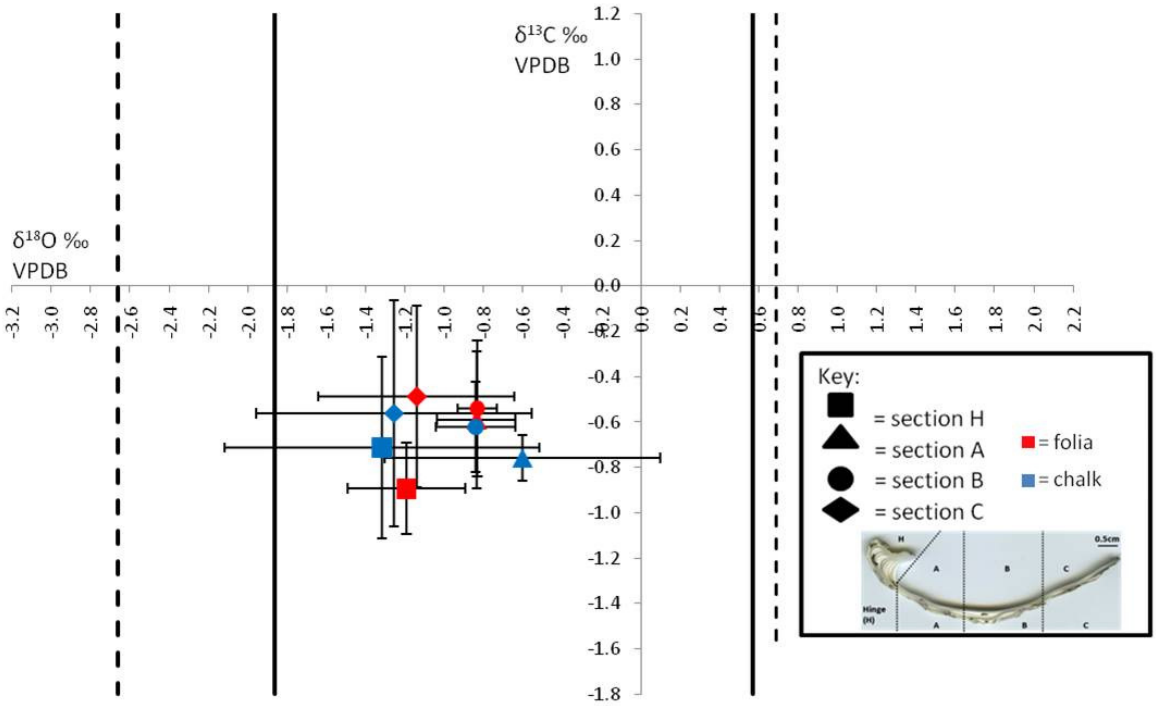

Figure 66. $\delta^{18}O$ – $\delta^{13}C$ cross plot of the mean isotope values obtained from estuarine *C. gigas,* where any individual effect has been removed.
Each data point represents the average value of nine replicate samples, (the average value for chalk or folia samples for each valve section from all oysters analysed) with error bars showing interspecimen standard deviation (σ). Red=folia, blue=chalk. Solid lines represent maximum and minimum values of $\delta^{18}O$ expected under equilibrium conditions. Dashed lines represent maximum and minimum values of $\delta^{18}O_{carbonate}$ expected for equilibrium allowing for the actual range in $\delta^{18}O_{water}$ values.

While mean folia and chalk values for both $\delta^{18}O$ and $\delta^{13}C$ from all valve sections are extremely similar (T-test, p=0.95 ($\delta^{18}O$), p=0.74 ($\delta^{13}C$)), some consistent trends are observed. For both folia and chalk, mean values of $\delta^{13}C$ become progressively, although not significantly, heavier from valve sections H-C. Lightest values of $\delta^{18}O$ for folia and chalk represent section H, with samples from section C being second lightest for both microstructures. $\delta^{18}O$ values from section A & B are coincident and are slightly heavier in $\delta^{18}O$ than values of H and C.

4.2.2 Carbon and oxygen isotope composition of marine C. gigas.

The oxygen and carbon isotope composition of marine *C. gigas* was determined by isotopic analyses of the left valves of marine samples, U8, U9 and U10. Samples of folia and chalk were analysed from each valve section using an

identical sampling strategy as described for estuarine samples (detailed in section 4.2). A total of 36 chalk and 36 folia samples from marine valves were successfully analysed by mass spectrometry at SUERC.

Isotopic values obtained from all valve sections are presented in Figure 67 where replicate samples are shown individually. Values for $\delta^{18}O$ range from -2.80‰ to 1.46‰, while $\delta^{13}C$ range from -1.54‰ to 0.65‰. Values of $\delta^{18}O$ or $\delta^{13}C$ show significant positive correlation (correlation coefficient, r=0.69 n=72). Covariance between $\delta^{18}O$ and $\delta^{13}C$ is significant for both folia (correlation coefficient, r=0.75, n=36), and chalk (correlation coefficient, r=0.69, n=36) samples. Variation in isotopic values obtained from individual oysters is not significant for either $\delta^{18}O$ or $\delta^{13}C$ (ANOVA, p=0.9 $\delta^{18}O$, p=0.1 $\delta^{13}C$), although through-valve trends in $\delta^{18}O$ and $\delta^{13}C$ are not consistent between individual valves.

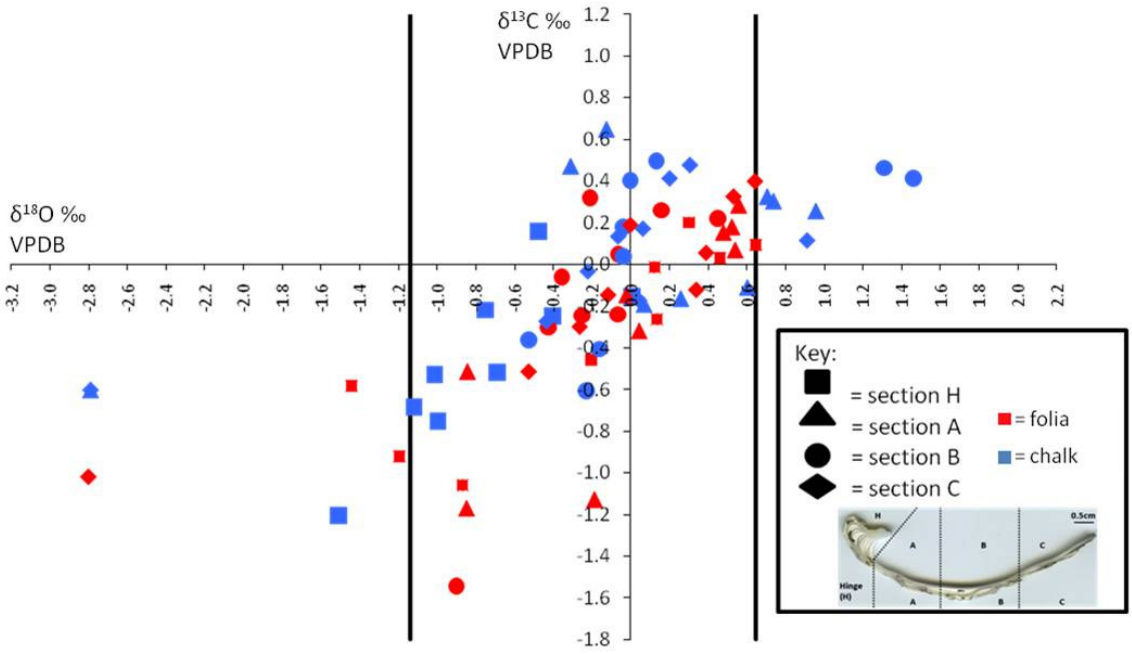

Figure 67. $\delta^{18}O$ – $\delta^{13}C$ cross plot of all isotopic data obtained for marine *C. gigas*. Each data point represents a single 1 mg sample of foliated or chalky calcite, where red=folia, blue=chalk. Solid lines represent maximum and minimum values of $\delta^{18}O$ expected under equilibrium conditions.

There is no statistical difference between folia and chalk for either $\delta^{18}O$ (T-test, p=0.82) or $\delta^{13}C$ (T-test, p=0.14), however the range in isotopic values obtained from the two microstructures is distinct. At the negative end, the lowest values for folia and chalk are very similar for $\delta^{18}O$ (-2.80‰ and -2.79‰ respectively), however the maximum $\delta^{18}O$ value for folia is 0.65‰, while for chalk the

maximum is 1.46‰. Average $\delta^{18}O$ values for folia and chalk are very similar (-0.15‰ and -0.19‰ respectively). Conversely, folia samples have the greatest range in $\delta^{13}C$ from -1.54‰ to 0.40‰ with an average of -0.23‰, while chalk $\delta^{13}C$ values average -0.07‰ from a range of -1.21‰ to -0.65‰.

The $\delta^{13}C$ and $\delta^{18}O$ composition of waters at the site of oyster growth in Loch Tuath was measured during this study as 2.3‰ and -0.42‰ respectively (section 2.1.2). Taking $\delta^{18}O_{water}$ = -0.42‰, together known maximum and minimum annual water temperatures, the expected range of $\delta^{18}O_{carbonate}$ for equilibrium was calculated (using Equation 5, section 2.3.6.4) and reported a range of -1.14‰ to 0.64‰. The majority of $\delta^{18}O$ values obtained from folia samples fall within the calculated range for isotopic equilibrium (Figure 67). A single sample of hinge folia from each of the valves U8 and U10 are light relative to isotopic equilibrium by 0.34‰ and 0.06‰ respectively. A single folia sample from valve section C of sample U9 is considerably light in $\delta^{18}O$ relative to equilibrium values. A quarter of all chalk samples analysed exhibit values of $\delta^{18}O$ that lie outside of those expected from equilibrium. From all valve sections, at least one chalk sample displays values of $\delta^{18}O$ that fall outside of the maximum and minimum values for equilibrium. The expected range for oxygen isotopic equilibrium, displayed in Figure 67-Figure 69, is based on a static $\delta^{18}O_{water}$ value of -0.42‰. The effect of possible salinity fluctuation on the expected $\delta^{18}O_{carbonate}$ equilibrium range is discussed in section 4.3.4.2. Expected values of $\delta^{13}C_{shell}$ for equilibrium were calculated using a ^{13}C equilibrium fractionation, for calcite relative to HCO_3^-, of +1‰ (Romanek et al. 1992), providing predicted $\delta^{13}C_{shell}$ values, for equilibrium, of 3.3‰. All values of folia and chalk are light with respect to $\delta^{13}C$.

The mean value for replicate samples is presented in Figure 68 where error bars show the standard deviation (σ) for each group of replicates (replicate group=three folia or three chalk samples from a given valve section). For $\delta^{18}O$, σ ranges from 0.04‰ to 1.88‰, and for $\delta^{13}C$ σ=0.04 to 0.92‰.

All mean values of folia fall within the expected range for isotopic equilibrium. The majority of mean chalk values also fall within the equilibrium range with the exception of three samples. All outlying samples of chalk represent valve U10 and include chalk samples from valve sections H, A and B. While the majority of

mean chalk values lie within the equilibrium range, the uncertainties associated with these data points frequently extend outside of equilibrium bands.

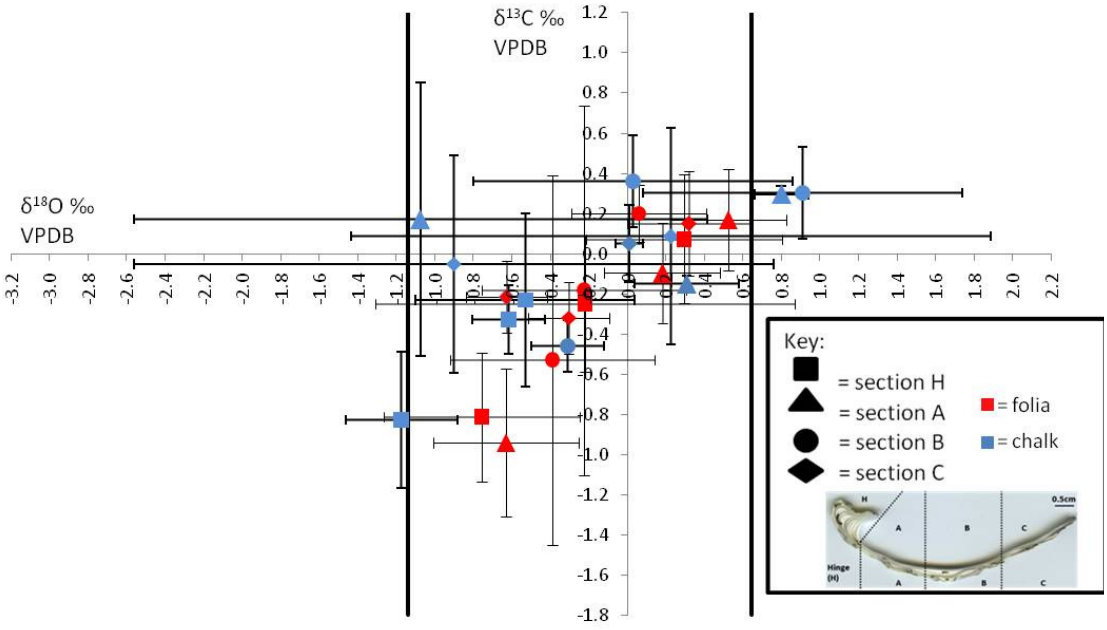

Figure 68. $\delta^{18}O$ – $\delta^{13}C$ cross plot of the mean values of replicate samples for marine *C. gigas*.
Each data point represents the average value of three replicate samples from one individual specimen with error bars showing standard deviation (σ) between replicates. Red=folia, blue=chalk. Solid lines represent maximum and minimum values of $\delta^{18}O$ expected under equilibrium conditions.

Individual valves display different patterns of $\delta^{18}O$ and $\delta^{13}C$ from valve sections H to C with no common trend present between individual valves.

The average $\delta^{18}O$ and $\delta^{13}C$ values from all valves was calculated for each valve section (H-C) to remove the natural variation present between individual samples and is presented in Figure 69. The cross plot in Figure 69 enables better observation of the variation in $\delta^{18}O$ and $\delta^{13}C$ throughout the height of the valve.

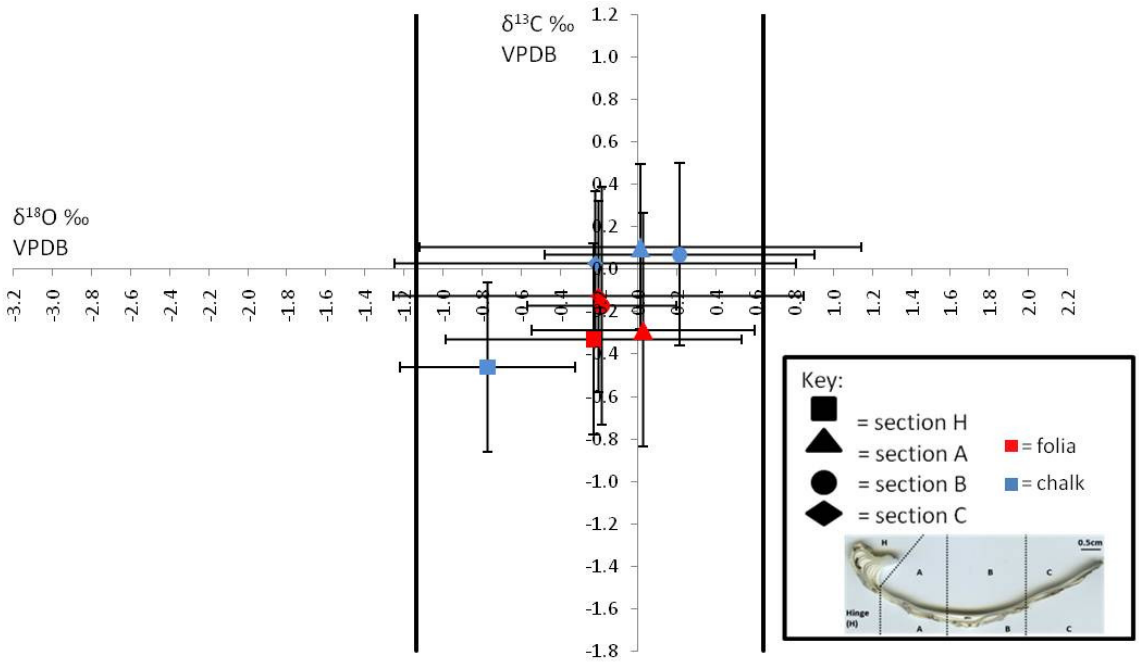

Figure 69. $\delta^{18}O$ – $\delta^{13}C$ cross plot of the mean isotope values obtained from marine *C. gigas,* where any individual effect has been removed.
Each data point represents the average value of nine replicate samples, (the average value for chalk or folia samples for each valve section from all oysters analysed) with error bars showing interspecimen standard deviation (σ). Red=folia, blue=chalk. Solid lines represent maximum and minimum values of $\delta^{18}O$ expected under equilibrium conditions.

Mean $\delta^{13}C$ values of folia become progressively, although not significantly, heavier from valve sections H-C. The lightest $\delta^{13}C$ values of chalk are in the hinge region. However, values of $\delta^{13}C$ from sections A, B and C are similar with the mean value from section C falling 0.8‰ lighter than section A. Chalk samples from valve sections A-C are significantly heavier than those of folia from the same valve sections (T-test, p=0.008). However, the $\delta^{13}C$ value of chalk from the hinge region (H) is lighter than that from hinge folia. The hinge region displays the lightest $\delta^{18}O$ folia and chalk values, followed by section C. Values of $\delta^{18}O$ from sections A & B are similar for both folia and chalk. Mean values of $\delta^{18}O$ and $\delta^{13}C$ from all valve sections are not significantly different for folia or chalk (T-test, p=0.6 ($\delta^{18}O$), p=0.3 ($\delta^{13}C$)) and show considerable overlap.

4.2.3 Comparison of the carbon and oxygen isotope signature of estuarine and marine C. gigas.

All isotopic results obtained from estuarine and marine oysters are presented in Figure 70 where all replicate samples from both data sets are shown individually. As there is no significant difference in values of $\delta^{18}O$ or $\delta^{13}C$

obtained from foliated or chalky calcite in either data set, microstructures are not differentiated in Figure 70. Oysters grown in an estuarine environment in Loch Fyne exhibit a 2.67‰ range in $\delta^{18}O$ composition (ranging -2.28‰ to 0.39‰), while marine oysters from Loch Tuath exhibit a range of 4.26‰ for $\delta^{18}O$ (ranging -2.80‰ to 1.46‰). Marine oysters also exhibit the greatest range in $\delta^{13}C$ from -1.54‰ to 0.65‰, while the $\delta^{13}C$ composition of estuarine oysters ranges from -1.29‰ to 0.36‰. Indeed, isotopic data obtained from marine oysters is significantly more variable with respect both $\delta^{18}O$ and $\delta^{13}C$ when compared to estuarine equivalents (ANOVA, p=<0.0001 for both $\delta^{18}O$ and $\delta^{13}C$).

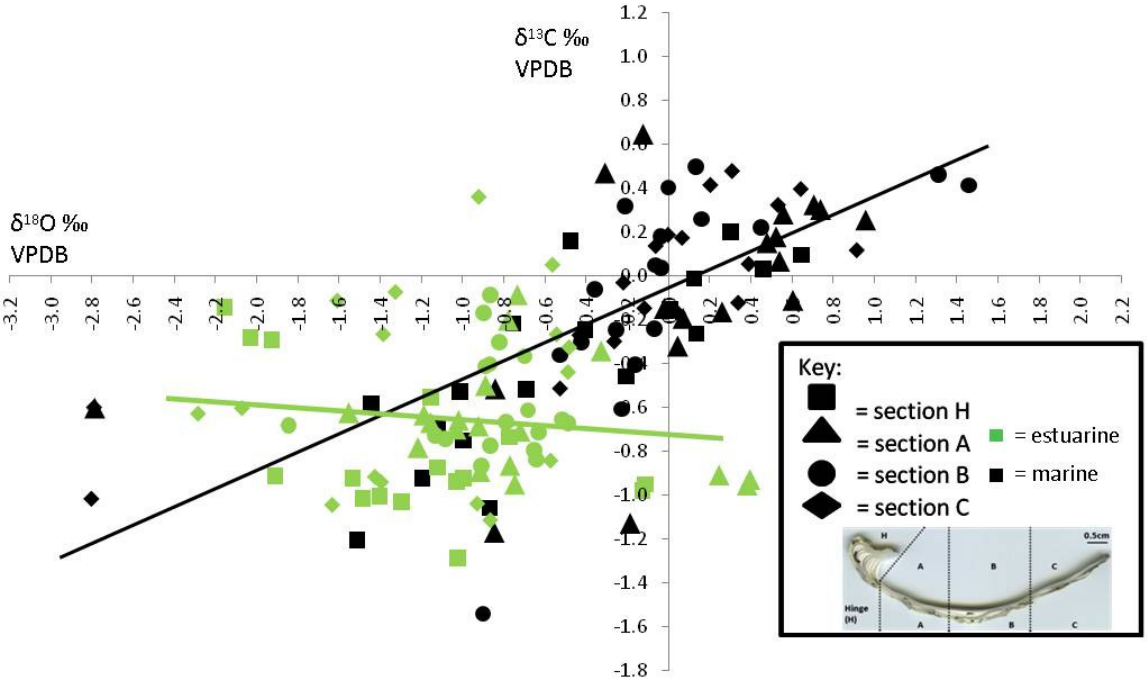

Figure 70. $\delta^{18}O$ – $\delta^{13}C$ cross plot of all estuarine and marine isotopic data for comparison. Each data point represents a single 1 mg sample of foliated or chalky calcite. Green=estuarine samples with corresponding green trend line, Black=marine samples with corresponding black trend line.

The cross plot presented in Figure 70 shows distinct differentiation in the isotopic results obtained from estuarine and marine samples. The majority of marine data points plot within the first (top right) and third (bottom left) quadrants of the cross plot with a positive sloping trend line reflecting the strong positive correlation between $\delta^{18}O$ and $\delta^{13}C$ values of marine data (correlation coefficient, r=0.69 n=72). Conversely, estuarine data is concentrated within the third quadrant and shows no correlation in $\delta^{18}O$ and $\delta^{13}C$ values (correlation coefficient, r=-0.10 n=69). As a result, the corresponding trend line for estuarine data is near horizontal. Marine samples have significantly

heavier values of $\delta^{18}O$ and $\delta^{13}C$ than those of estuarine samples (T-test, p=<0.001 for $\delta^{18}O$ and $\delta^{13}C$).

Within both estuarine and marine environments there is no significant difference in isotopic data obtained from folia and chalk microstructures. However, from both environments, chalk samples exhibit the greatest range in $\delta^{18}O$ values. Conversely, in marine samples folia exhibit the greatest range in $\delta^{13}C$ and in estuarine samples $\delta^{13}C_{folia}$ show significant interspecimen variation which is not apparent in chalk samples. Interspecimen variation is not apparent in the marine data set for either $\delta^{13}C$ or $\delta^{18}O$.

The cross plot presented in Figure 71 shows, for estuarine and marine data sets, the average values for folia and chalk at each valve section (H-C). Each data point represents the average of nine samples of folia or chalk at a given valve section (three replicate samples from three individual oysters).

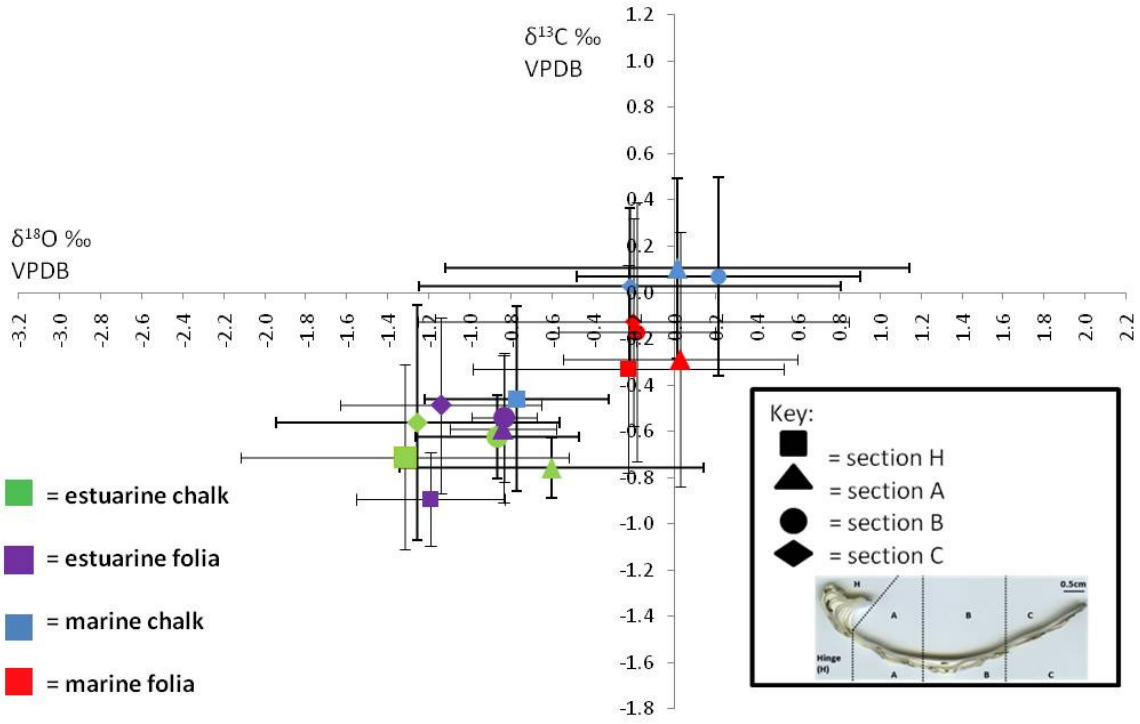

Figure 71. $\delta^{18}O$ – $\delta^{13}C$ cross plot of all estuarine and marine isotopic data for comparison, removing individual effects.
Each data point represents the mean of nine replicate samples and error bars represent the standard deviation (σ) for group of replicates (i.e. variation within nine samples of folia or chalk (three replicate samples from three individual specimens). Colours are green= estuarine chalk, purple = estuarine folia, blue= marine chalk, red= marine folia.

When plotted together (Figure 71), average values from the two data sets show little overlap. Marine values are most concentrated around the origin while estuarine data points plot well within the third quadrant of the cross plot. The exception to this is the chalk sample from the hinge region of marine oysters which overlap with estuarine folia from section B. Standard deviations associated with both data sets cause considerable overlap between results. Error bars associated with marine data are significantly higher than those associated with estuarine data (T-test, p=0.002).

Trends in $\delta^{13}C$ and $\delta^{18}O$ from valve sections H to C for estuarine and marine data sets are shown in Figure 72. Values of $\delta^{18}O$ and $\delta^{13}C$ for folia and chalk shown in Figure 72 represent the average of nine samples, as plotted in Figure 71.

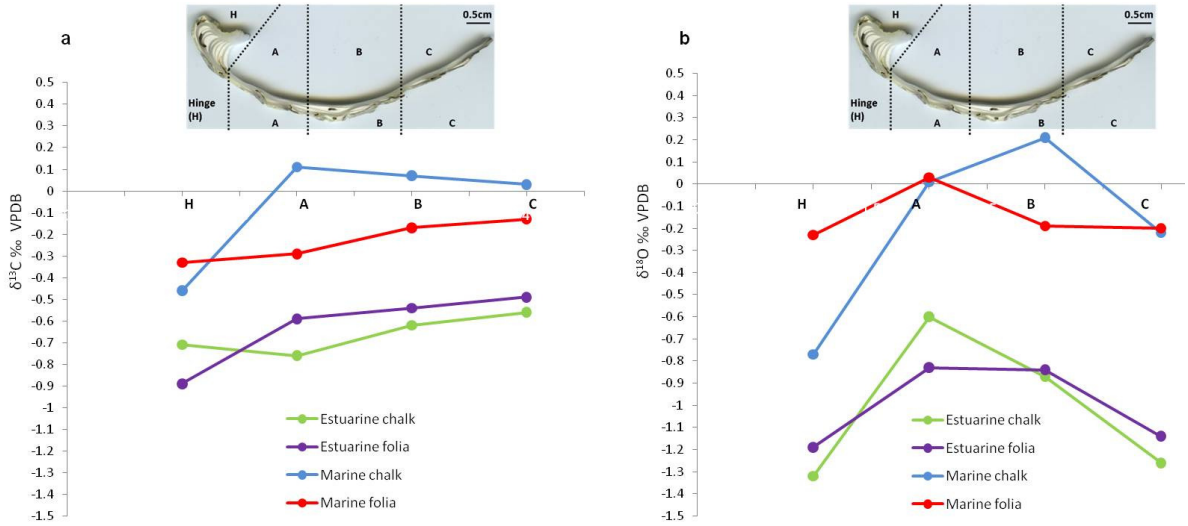

Figure 72. Profile of $\delta^{13}C$ and $\delta^{18}O$ throughout the height of the oyster valve. (a) Variation of $\delta^{13}C$ from valve sections H-C. (b) Variation of $\delta^{18}O$ from valve sections H-C. In both (a) and (b), green=estuarine chalk, pruple=estuarine folia, blue=marine chalk, red=marine folia.

A similar trend for $\delta^{13}C$ is observed throughout the height of the valves from both estuarine and marine environments. Samples from both environments show a trend of increasing $\delta^{13}C$ values from the hinge (H) to section C at the ventral margin. This trend equates to a gradual increase of $\delta^{13}C$ with increasing age of the oyster. The exception to this trend is the marine chalk samples in which the lightest $\delta^{13}C$ values correspond to the hinge region while the heaviest values of $\delta^{13}C$ correspond to section A. However, values of $\delta^{13}C$ from sections A, B and C are similar. Through-valve trends in $\delta^{18}O$ are not consistent between environments. Similar trends exist within the estuarine data set between folia

and chalk samples in which $\delta^{18}O$ is lightest in section H becoming heavier in sections A & B, and lighter towards section C. Within the marine data set $\delta^{18}O$ values of both folia and chalk are lightest from the hinge region, trends in $\delta^{18}O$ ventral of the hinge region are variable between microstructures. Both marine folia and marine chalk however have similar values for section C.

4.3 Discussion

4.3.1 Stable isotope composition of C. gigas

In agreement with previous authors (e.g. Surge et al. 2001, Ullmann et al. 2010, Fan et al. 2011), there is no significant difference in stable isotopic composition for folia or chalky microstructures. This similarity in isotopic composition is true of folia and chalk present at the hinge and in ventral valve parts (sections A, B, C in this study). However, despite similar mean values of $\delta^{18}O$ and $\delta^{13}C$, the range and patterns of isotopic values exhibited by folia and chalk are distinct. In both estuarine and marine data sets chalk exhibits a greater range in $\delta^{18}O$ compared with folia. In both data sets chalk samples are most variable with respect to $\delta^{18}O$ relative to $\delta^{13}C$. On the other hand, in marine samples, folia exhibit the greatest range for $\delta^{13}C$. In addition, within the estuarine data set folia samples exhibit a significant degree of interspecimen variability in $\delta^{13}C$, while chalk $\delta^{13}C$ values of individual oysters are similar.

The $^{13}C/^{12}C$ ratio of biogenic carbonate is controlled by the $^{13}C/^{12}C$ ratio in the extrapallial cavity (e.g. Schöne 2008, Lartaud et al. 2010b), which itself is contributed to by both the ambient dissolved inorganic carbon (DIC) pool and respired CO_2 (e.g. Butler et al. 2011). In the absence of a metabolic contribution, $\delta^{13}C_{carbonate}$ will reflect $\delta^{13}C$ of the ambient environment and may be used as a proxy of DIC (e.g. Mook and Vogel 1968, Wang et al. 1995, Surge et al. 2001, McConnaughey and Gillikin 2008). Several authors have reported oyster shell $\delta^{13}C$ to be primarily controlled by isotopic ratios of the external environment and may be considered as a DIC proxy (e.g. Wang et al. 1995, Kirby et al. 1998, Surge at al. 2001, 2003, Fan et al. 2011). However, where several oysters have been sampled, interspecimen variation in relative $\delta^{13}C$ values can be significant, suggesting that metabolic carbon (C_{meta}) can influence shell

$^{13}C/^{12}C$ ratios (e.g. Andrus and Crowe 2000, Lecuyer et al. 2004). In fact, Lartaud et al. (2010b) demonstrate that C_{meta} can account for up to 69% of oyster shell $\delta^{13}C$ and this proportion of metabolic carbon varies as a function of metabolic rate. Significant interspecimen variation in $\delta^{13}C$ has been identified in this study for estuarine folia (ANOVA, p=0.005). Lack of consistency in $\delta^{13}C$ between oysters suggests that $\delta^{13}C$ in the foliated structure is not controlled by a common variable but that it is influenced by metabolic effects of the individual organism. Fluctuations in $\delta^{13}C_{folia}$ values are likely to reflect changes in metabolic rate and/or changes in food source. For example, Riera and Richard (1997) noted that changes in estuarine particulate organic matter (POM), as a response to terrestrial runoff, were reflected in soft tissue $\delta^{13}C$ of *C. gigas*. Data regarding the DIC pool and POM content of Loch Fyne waters are not available and therefore it is not possible to speculate further as to the influence of food source/supply on these particular estuarine oysters. Contrasting with folia, variability in $\delta^{13}C$ of chalk samples is not significant between individual estuarine oysters, suggesting $\delta^{13}C_{chalk}$ is controlled predominantly by a common isotope signal and is not affected by metabolic carbon to the same extent as folia. Interestingly, interspecimen variation in $\delta^{13}C$ between marine oysters is not significant for either chalk or folia, signifying a possible loss of metabolic regulation in the marine environment, including during the secretion of folia (discussed in section 4.3.3). However, marine $\delta^{13}C_{shell}$ values are still considerably lighter than predicted equilibrium values (described in section 4.2.2), suggesting that some metabolic carbon is still included in shell secretion. It is noted that while there is no significant difference in $\delta^{13}C$ between marine folia and chalk, average $\delta^{13}C_{folia}$ is 0.16‰ lighter than $\delta^{13}C_{chalk}$, possibly due to a greater input of isotopically light metabolic carbon into folia. The lesser input of metabolic carbon to chalk, relative to folia, in estuarine and marine data sets may reflect a lower metabolic rate during secretion of chalk and prioritisation of metabolic carbon to folia.

In both data sets, $\delta^{18}O$ values are comparable between individual oysters, for folia and chalk, confirming that temperature and salinity are the dominant influences on shell $\delta^{18}O$ (e.g. Kirby et al. 1998, Surge et al. 2001, 2003, Lartaud et al. 2010c, Ullmann et al. 2010, Fan et al. 2011). From both environments, chalk samples exhibit a greater $\delta^{18}O$ range than folia. Indeed the narrow range

of $\delta^{18}O_{folia}$ together with more variable $\delta^{13}C$ values, suggests that secretion of folia requires specific environmental conditions and considerable metabolic regulation. Conversely, the greater range in $\delta^{18}O_{chalk,}$ relative to folia, indicates that chalk may be secreted across a broader range of environmental conditions, while $\delta^{13}C_{chalk}$ show little influence of metabolism on chalk secretion. It is widely acknowledged that bivalve metabolism decreases during periods of adverse environmental conditions (e.g. Schöne 2008) including when food availability is reduced (Lartaud et al 2010b). In oysters, deviation from optimum environmental conditions, outside of the margins required for folia production, may cause the oyster to default to chalk secretion which requires less metabolic regulation in its production.

In estuarine samples, chalk exhibits the most negative $\delta^{18}O$ values, yet still within predicted equilibrium values, suggesting that chalk is preferentially secreted during times of highest temperatures and/or low salinity causing reduced $\delta^{18}O_{water}$. In marine samples however, folia and chalk exhibit very similar values at the negative $\delta^{18}O$ excursion. Salinity in the marine environment is relatively stable compared with estuaries and is unlikely to be significantly diluted by terrestrial runoff (section 2.1.2). Therefore lowest $\delta^{18}O_{carbonate}$ values from marine samples are likely to reflect warm water temperatures and not low $\delta^{18}O_{water}$ values. Corresponding negative values of $\delta^{18}O$ between marine folia and chalk samples suggests both microstructures may be secreted during warm periods. Disparity between negative $\delta^{18}O_{folia}$ and $\delta^{18}O_{chalk}$ in estuarine samples is therefore more likely to be caused by fluctuating $\delta^{18}O_{water}$, whereby chalk is preferentially secreted during periods of reduced salinity. In both marine and estuarine data sets, chalk also exhibit the most positive values of $\delta^{18}O$. Interestingly, Wang et al. (1995) note that chalk isotope values are not as positive as folia and suggest that chalk is not secreted during the coldest months. Patterns of $\delta^{13}C$ and $\delta^{18}O$ in this study suggest that chalk is preferentially secreted during periods of high salinity or low temperature, possibly as a consequence of reduced metabolism. Indeed, reduced metabolism and growth rate, including growth cessation, at low temperatures has been reported by several authors (Wang et al. 1995, Kirby et al. 1998, Hickson et al. 1999, Surge et al. 2003, Elliot et al. 2003, Chavaud et al. 2005, Schöne 2008, Lartaud et al. 2010c, Ullmann et al. 2010).

4.3.2 Through-valve stable isotope trends

There is a subtle increase in $\delta^{13}C$ values of folia and chalk from hinge (section H) to ventral valve parts (section C) (Figure 72). In marine molluscs $\delta^{13}C$ values commonly decrease through ontogeny as metabolic rate increases relative to gradually decreasing growth rate (e.g. Gillikin et al. 2005, McConnaughey and Gillikin 2008, Butler et al. 2011). The opposite trend is observed in this study whereby $\delta^{13}C$ values slightly increase with increasing age of the oyster. A similar trend was observed by Gillikin et al. (2005) for some specimens of *Saxidomus giganteus* suggesting a general model of increasing metabolic influence with ontogeny may not be applicable to all bivalves. The lack of data regarding $\delta^{13}C_{water}$ of Loch Fyne makes it difficult to speculate as to whether the subtle increase of $\delta^{13}C$ through the valves (from H-C) reflects changes in metabolic rate or temporal changes in food source (e.g. Riera and Richard 1997). However, similar trends in both folia and chalk suggest that any changes in food source and/or metabolic rate affect both microstructures to the same extent. Through-valve patterns of $\delta^{18}O$ are not common to both estuarine and marine datasets. In estuarine samples $\delta^{18}O_{folia}$ and $\delta^{18}O_{chalk}$ show a close correlation in overall pattern and do not covary with $\delta^{13}C$. Changes in salinity as a response to terrestrial runoff, are likely to affect both oxygen and carbon isotopes by the introduction of isotopically light terrestrial material (depleted relative to ^{13}C and ^{18}O) to the system. Uncoupling of oxygen and carbon throughout the valves in estuarine samples, which are in oxygen isotopic equilibrium with the ambient environment, further confirms the inclusion of considerable metabolic carbon during shell secretion.

4.3.3 Effect of environment on shell isotope signature.

Marine oysters are characterised by $\delta^{13}C$ and $\delta^{18}O$ values that are significantly heavier than those of estuarine oysters (Figure 70-72). The $\delta^{18}O$ of all oyster shells used in this study, as for most molluscs, is controlled by temperature and $\delta^{18}O$ composition of surrounding water, with negligible input from 'vital effects' (Lecuyer et al. 2004, McConnaughey and Gilikin 2008). The higher $\delta^{18}O$ values of marine oysters accurately reflects the colder, more saline water of Loch Tuath compared with Loch Fyne. Carbon isotopes are complicated by the influences of

both DIC and organic carbon (e.g. Butler et al. 2011). The ^{13}C depleted compositions of estuarine oysters, relative to marine, are likely to result from the mixing of isotopically light terrestrial matter in estuarine water and a greater influence of metabolic carbon in estuarine shell secretion. Inter-species variability in $\delta^{13}C$ values of marine oysters is low signifying a negligible influence of metabolic carbon on shell $\delta^{13}C$. Indeed, marine oysters exhibit covarying trends of $\delta^{13}C$ and $\delta^{18}O$, in oxygen isotope equilibrium, suggesting that both isotopes are influenced predominantly by external environmental factors (Kirby et al. 1998, Surge et al. 2001). However, $\delta^{13}C_{shell}$ values are considerably lighter than predicted equilibrium values suggesting that at least some metabolic carbon is incorporated in shell carbonate. Kirby et al. (1998) and Surge et al. (2001) report that while $\delta^{13}C_{shell}$ patterns follow general trends of DIC, there is some input from metabolic carbon, which may vary seasonally. Further, Lartaud et al. (2010b) demonstrate that the proportion of metabolic carbon incorporated into shell carbonate can vary, usually as a response to changes in metabolism. The proportions of $^{13}C_{meta}$ and $^{13}C_{DIC}$ incorporated into marine oyster shells is unknown, however the lack of interspecimen variation in $\delta^{13}C$ suggests that DIC is the main source of carbon, with a relatively small input of $^{13}C_{meta}$. In estuarine oysters, certainly for folia secretion, incorporation of metabolic carbon can be considerable. The loss of metabolic influence in marine oyster shell secretion is interesting. Marine oysters used in this study were infested with Spionid worms (probably *Polydora* s.p), which may be regarded as a parasite of the oyster (Chambon et al. 2007). Parasite infestation causes oysters to hyperventilate due to oxidative stress, which may also influence the metabolism of digestion (Chambon et al. 2007) and general productivity of the oyster, including reducing body (meat) size and weight (Royer et al. 2006). Such stresses may alter the metabolic prioritisation of the oyster, possibly to enhance soft tissue function, leaving less metabolic carbon available for shell secretion.

4.3.4 Isotopic equilibrium and implications for palaeoclimatic studies.

4.3.4.1 Estuarine oysters

In agreement with previous authors (e.g. Kirby et al. 1998, Surge et al. 2001, 2003, Fan et al. 2011), this study has shown that both folia and chalk of estuarine oysters are secreted in oxygen isotopic equilibrium with the ambient environment. It has also demonstrated that isotopic equilibrium remains throughout the valve from hinge to ventral margin.

Using the isotopic temperature equation of Kim & O'Neil (1997), an isotopic temperature range for Loch Fyne water was calculated, based on average $\delta^{18}O_{water}$ = -0.6‰. The plot in Figure 73 shows the mean temperatures calculated from all folia and chalk samples individually with error bars showing the distribution around the mean. Comparison is made with actual water temperatures measured in-situ at Loch Fyne Oyster Farm which range from 6.3˚C to 17.6˚C, with an average of 11.6˚C. Folia samples produce calculated temperatures which range from 10.4˚C to 17.8˚C with an average of 13.4˚C. Average temperatures calculated from chalk samples range from 7.1˚C to 19.6˚C with an average of 13.4˚C.

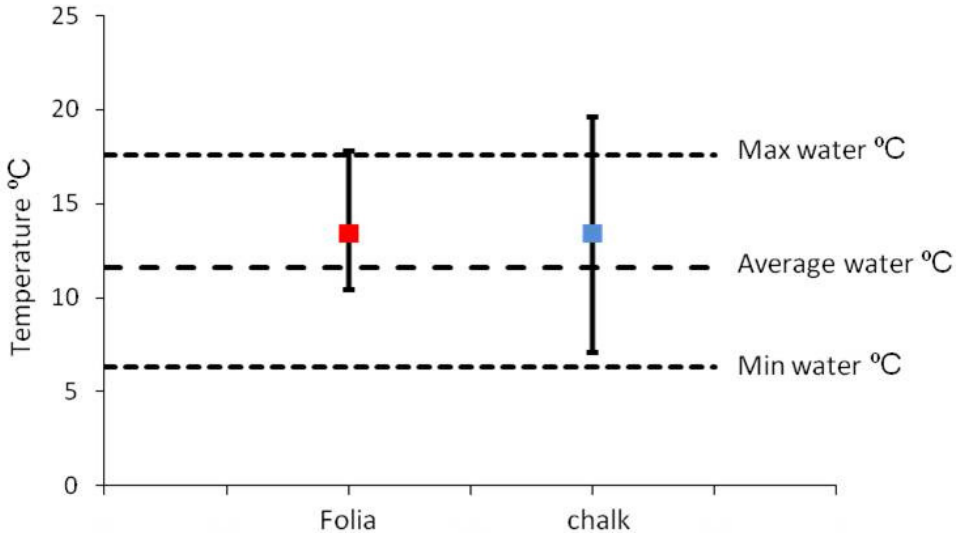

Figure 73. Plot of the mean and range in isotopic temperatures calculated from $\delta^{18}O$ values of all estuarine analyses from folia and chalk microstructures.
Dashed lines represent maximum, minimum and average annual water temperatures measured at Loch Fyne Oyster Farm for comparison with the temperature range calculated from $\delta^{18}O$ of folia (red) and chalk (blue) shell microstructures.

Temperatures from both microstructures predominantly reflect actual water temperatures. The maximum calculated temperature of chalk is 2˚C higher than the actual maximum temperature. This may be expected since these temperatures are based on an average $\delta^{18}O_{water}$ value. Decreases in salinity and therefore $\delta^{18}O_{water}$ will lower the resulting $\delta^{18}O_{carbonate}$, which if unaccounted for will lead to an overestimation of temperature (e.g. Kirby et al. 1998, Gillikin et al. 2005). As demonstrated in Figures 64-66, chalk values require the full range of salinity to be considered before isotopic equilibrium can be confirmed, and accurate temperatures calculated. This therefore limits the use of $\delta^{18}O$ from estuarine oysters as temperature proxies to studies where salinity variation is known. This is especially true when considering $\delta^{18}O$ values of chalky shell material as chalk is apparently secreted across a greater range of environmental conditions (discussed in section 4.3.1).

Surge et al. (2001) suggested that corresponding oyster $\delta^{13}C_{carbonate}$ values are secreted in carbon isotopic equilibrium with ambient DIC pool and so could be used as a salinity proxy. In this study, significant interspecimen variation with respect to $\delta^{13}C$ indicates that the primary source of $\delta^{13}C_{carbonate}$ is metabolic (McConnaughey 1989, Rahimpour-Bonab et al. 1997, McConnaughey and Gillikin 2008). Therefore, in agreement with Lecuyer et al. (2004) it is considered that $\delta^{13}C$ should not be used as a salinity proxy. Kirby et al. (1998) suggested that salinity variation could be estimated from known winter and summer growth cessation temperatures and maximum and minimum $\delta^{18}O_{carbonate}$ values, by substituting these values into the isotope temperature equation to solve for $\delta^{18}O_{water}$. However, this method requires knowledge of growth cessation temperatures, for which there are many conflicting reports. For example, Kirby et al. (1998) report lowest temperature for oyster growth to be 10˚C, while Ullmann et al. (2010) report winter growth cessation at 6˚C and Lartaud et al (2010c) report continuous growth below 6˚C. In addition, results of the present study suggest that chalk can be secreted at lower temperatures than folia which would further complicate determination of growth cessation. Furthermore, Fan et al. (2011) suggest that growth breaks are related to spawning related shocks rather than temperature or storm effects. It is therefore considered that an independent salinity proxy is required before estuarine oysters can be accurately used to obtain ancient water temperatures.

4.3.4.2 Marine oysters

In agreement with studies of estuarine oysters, Ullmann et al. (2010) report that marine oysters precipitate foliated and chalky calcite in oxygen isotope equilibrium with the ambient environment. This hypothesis is, to a large extent, confirmed by the present study. The majority of all marine folia and chalk samples fall within the expected range for oxygen isotope equilibrium. Most outlying values are likely to reflect changes in $\delta^{18}O_{water}$ as a result of salinity fluctuation. The calculated range for $\delta^{18}O_{carbonate}$ in isotopic equilibrium with seawater is based on known maximum and minimum seawater temperatures and a single $\delta^{18}O_{water}$ measurement of -0.42‰, which corresponds to a salinity value of 31 (section 2.1.2). Continuous salinity records for Loch Tuath are not available. It is likely that salinity at the site would fluctuate slightly in response to changing precipitation rates, especially at shallow depths (oysters were grown at a high tide depth of 4 m). Given the location and exposure of the oyster farm to open marine waters, and lack of freshwater input, it is considered that during dry months salinity could frequently reach 35, a value typical of marine waters in the Sound of Tiree (Figure 12) (Data from the Scottish Association of Marine Science, Tiree Passage Mooring). Likewise, rainfall can dilute surface waters, reducing salinity and $\delta^{18}O_{water}$, the effects of which can extend to 8 m depth in Scottish sea lochs (Stirling and Okumus 1995). However, the extent of salinity reduction is variable and site specific. For example, in Loch Fyne, salinity may be reduced by 16 (from 36 to 20) during periods of heavy rainfall and high flooding (see section 2.1.1 for details), yet a maximum salinity reduction of nine is reported by Tett and Wallis (1978) for Loch Crenan. Loch Tuath is more open and has a considerably lower annual volume freshwater runoff than both the above Lochs (section 2.1 and Edwards & Sharples 1986). It is considered therefore that salinity reduction in Loch Tuath, in response to precipitation and runoff, would not be greater than nine, and so a speculative salinity range of 35 to 26 is considered for Loch Tuath. Allowing for this salinity range (arguably more realistic than a static value), expected $\delta^{18}O_{carbonate}$ values expected for equilibrium were recalculated and are presented in Figure 74. All folia and chalk $\delta^{18}O$ values, with the exception of three, lie within the recalculated equilibrium range, and are therefore considered to reflect ambient environmental conditions.

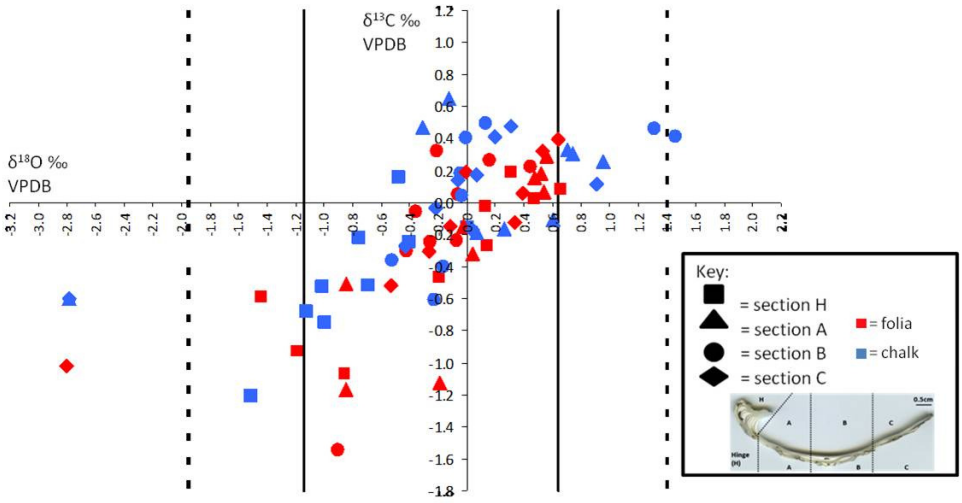

Figure 74. $\delta^{18}O$ – $\delta^{13}C$ cross plot of all isotopic data obtained for marine *C. gigas*. Each data point represents a single 1 mg sample of foliated or chalky calcite, where red=folia, blue=chalk. Solid lines represent maximum and minimum values of $\delta^{18}O$ expected under equilibrium conditions, based on measured $\delta^{18}O_{water}$ = -0.42‰. Dashed lines represent maximum and minimum values of $\delta^{18}O_{carbonate}$ expected for equilibrium allowing for a speculative salinity range of 35 – 26 ($\delta^{18}O_{water}$= 0.3 to -1.32‰).

Outlying values (Figure 74) are isotopically light relative to equilibrium by 0.9‰, which cannot be accounted for by salinity fluctuation. Sample contamination during preparation for isotopic analysis is possible, especially when handling fine calcite powders. However, the three outlying values represent samples from two oysters prepared separately, yet the samples exhibit similar $\delta^{18}O$ values. It is considered that isotopic values obtained from these samples represent true deviation from isotopic equilibrium. Disassociation of $\delta^{18}O_{carbonate}$ and the ambient environment normally results from kinetic isotope fractionation during calcification (e.g. McConnaughey 1989, McConnaughey and Gillikin 2008). Kinetic isotope effects are relatively rare in molluscs, possibly due to slow precipitation rates and low pH at the calcification site (e.g. McConnaughey et al. 1997, Zeebe 1999, Auclair et al. 2003, McConnaughey and Gillikin 2008). Marine oysters analysed in this study were infested with parasite Spionid worms which induce the formation of blisters in the shell as the oyster responds by rapidly secreting a new shell layer to isolate the worm (e.g. Zottoli and Carriker 1974, Royer et al. 2006, Chambon et al. 2007). Sediment-filled cavities were also present in most marine oyster samples. Rapid secretion of new shell layers to repair the shell and to isolate irritants such as worms or sediment particles, may not occur under the same physiological controls as normal shell material which may lead to kinetic isotope fractionation. Incorporation of such material in isotopic analysis is possible and may account for isotopic values that fall outside of equilibrium.

Inclusion of this material may also account for the high degree of variability within replicate groups of marine samples. Further isotopic analysis of blister and cavity areas or sites of shell repair would be required to confirm this hypothesis.

Water temperatures were calculated from marine $\delta^{18}O_{carbonate}$ values (using Equation 5 (Kim & O'Neil 1997)) and are presented in Figure 75. The plot in Figure 75 shows the mean temperatures calculated from all folia and chalk samples (excluding outlying values of possible kinetic origin), based on a measured $\delta^{18}O_{water}$ value of -0.42‰, and error bars show distribution around the mean. Comparison is made with actual water temperatures measured in Loch Tuath which range from 6.5˚C to 14.7˚C, with an average of 10.6˚C. Folia samples produce calculated temperatures which range from 6.7˚C to 16.4˚C with an average of 10.4˚C. Average temperatures calculated from chalk samples range from 3.1˚C to 16.7˚C with an average of 10.6˚C. Temperatures calculated from samples where kinetic fractionation is likely are plotted separately (Figure 75). Where kinetic effects are likely to have occurred, resulting isotope temperatures are nearly 10˚C higher than the maximum recorded temperature.

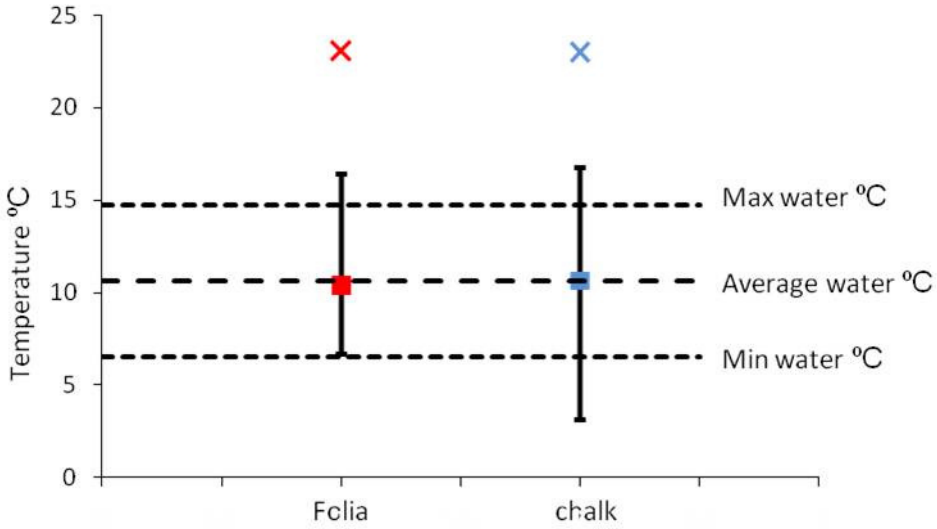

Figure 75. Plot of the mean and range in isotopic temperatures calculated from $\delta^{18}O$ values of all marine analyses from folia and chalk microstructures.
Dashed lines represent maximum, minimum and average annual water temperatures measured in Loch Tuath for comparison with the temperature range calculated from $\delta^{18}O$ of folia (red) and chalk (blue) microstructures. Crosses represent temperatures obtained from samples where kinetic isotope fractionation is likely to have occurred.

Mean calculated temperatures of folia (10.4˚C) and chalk (10.6˚C) correspond well with actual average temperature of 10.6˚C. The offset of 3˚C at the lowest

temperature of chalk, and of 2˚C at the highest temperature of folia and chalk probably result from salinity fluctuation, which is not accounted for when calculating temperatures using a static $\delta^{18}O_{water}$ value. This further highlights the need for a robust salinity proxy for use in conjunction with shell $\delta^{18}O$ values. Two chalk samples and one folia sample from the marine data set exhibit $\delta^{18}O$ values that lie considerably outside of the expected equilibrium range. These data points produce extrapolated temperatures of 23.1˚C. This considerable overestimation of temperature cannot be accounted for by salinity fluctuations and indicates that oysters containing numerous cavities and/or blisters and areas of shell repair should be avoided for stable isotope analysis.

Values of $\delta^{13}C$ and $\delta^{18}O$ of marine oysters exhibit a strong positive correlation, which has, in the past, been attributed to carbon and oxygen isotope equilibrium (e.g. Kirby et al. 1998, Surge et al. 2001). However, all values of $\delta^{13}C_{carbonate}$ obtained in this study are considerably lighter than $\delta^{13}C_{water}$ values measured for Loch Tuath. This negative offset from equilibrium suggests that some metabolic carbon is present in the shell. The use of shell $\delta^{13}C$ as proxies of salinity and phytoplanktonic blooms (e.g. Wang et al. 1995, Surge et al. 2001) would therefore be difficult as metabolic and DIC influences would first have to be separated, which may be further complicated as the amount of metabolic carbon may fluctuate with changes in metabolic rate (Lartaud et al. 2010b).

4.4 Summary

There is no significant difference in stable isotope values of folia and chalk microstructures of *C. gigas* (e.g. Surge et al. 2001). However distinct trends and patterns in isotopic values obtained from the two microstructures offers new insights into the biomineralisation regime controlling the secretion of, and alternation between, folia and chalk. Secretion of folia requires specific environmental conditions and considerable metabolic input for secretion. Chalk is apparently secreted across a greater range of environmental conditions, with less metabolic regulation. Deviation from optimal environmental conditions, for example during periods of reduced salinity and/or cold or warm temperatures, may reduce metabolism causing the oyster to default from folia to chalk secretion. While folia and chalk isotope trends hold true for both estuarine and

marine oysters, the overall metabolic input in marine samples is less, possibly as a consequence of metabolic prioritisation in response to parasite infestation. As a consequence marine samples exhibit strong covariance between carbon and oxygen isotopes while metabolic regulation in estuarine oysters, notably in folia samples, results in an uncoupling of $\delta^{13}C$ and $\delta^{18}O$.

This study has confirmed that folia and chalk microstructures in the hinge region of marine and estuarine oysters are secreted in oxygen isotope equilibrium with the ambient environment (e.g. Kirby et al. 1998, Surge et al. 2001, 2003, Ullmann et al. 2010, Fan et al. 2011), and has extended this to include calcite shell material ventral of the hinge. The use of oysters as palaeotemperature proxies is however limited to areas where detailed salinity data is available. This is especially true when considering the use of chalky calcite in temperature determinations, as this structure is apparently secreted across a large salinity range, which if unaccounted for could lead to erroneous temperature estimations. Care should be taken when using oysters which are infested with parasites such as Spionid worms, or which contain sediment-filled cavities. Shell layers secreted to isolate such irritants may not be subject to the same level of physiological control as surrounding shell layers. This less controlled precipitation may lead to kinetic isotope fractionation during calcification. Incorporation of metabolic carbon in shell carbonate complicates the use of shell $\delta^{13}C$ as proxies of DIC, as DIC and metabolic components would have to be isolated which is further complicated by changes in metabolic rate (Lartaud et al. 2010b). In addition the proportion of metabolic carbon included in the shell varies between folia and chalk microstructures, whereby metabolic influence is more apparent in folia than chalk.

Chapter 5. Attachment of oysters to natural substrata

5.1 Introduction

Many marine and freshwater organisms possess the ability to attach to natural and synthetic materials with varying degrees of strength and permanence (e.g. Kauffmann 1971, Stanley 1972, Yonge 1979, Smith 2002, Bromely and Heinberg 2006). This remarkable ability to achieve adhesion while submerged in seawater has intrigued researchers for many decades (Nelson 1924, Coe 1932, Cranfield 1973a,b,c, 1974, 1975, Yonge 1979, Waite 1983, Pearce and LaBarbera 2009, Burkett et al. 2010). This concept of submerged adhesion is currently beyond the scope of modern synthetic adhesives. An array of strategies are deployed by organisms to secure attachment, including muscular suckers, organic 'glue', byssal threads and crystalline cement (Bromely and Heinberg 2006). Through adhesion, organisms can create extensive bed and reef structures within which unique environments are created, which are, in themselves essential marine ecosystems (Jackson 2001, Burkett et al. 2010). In addition, many attaching organisms adhere to man-made surfaces such as ship hulls causing damage and reducing effectiveness. As a consequence, these so-called 'fouling' organisms have become the focus of many scientific studies exploring the development of anti-fouling surfaces (e.g. Weigemann 2004). Further, organic adhesives, specifically the organic glue of the barnacle (Balanidae) and the byssal threads of the common blue mussel (*Mytilus edulis*) have been widely investigated, with respect to synthetic mimics, and are generally well understood (e.g. Waite 1983, Mascolo and Waite 1986, Kamino et al. 2000, Waite 2002, Kamino 2008). However, many bivalves, and a few gastropods (e.g. Vermetidae, Schiaparelli et al. 2003), attach by way of mineralised cement (Kauffmann 1971, Yonge 1979, Harper 1991, 1992). The crystalline nature of the contact between the cementing organism and the substrate can create difficulties in defining this attachment strategy (Harper 1992). As a result, the materials and methods deployed by such organisms to achieve cementation are unclear.

Oysters are among the most common and well known cementing bivalves (e.g. Yonge 1960, 1979, Harper 1992, Yamaguchi 1993). The ability of oysters to adhere tightly, and usually permanently, to a variety of substrates, makes them particularly attractive in the study of the cementation attachment strategy.

5.1.1 Cementation of oysters and other bivalves - previous studies

Oyster aquaculture is of considerable global economic importance (Beaumont et al. 2006, Lartaud et al. 2010a). Understanding the attachment strategy of oysters has been fundamental in optimising oyster farming techniques, as oyster spat must be separated from substrates prior to the onset of cementation (Yonge 1979). As such, extensive studies, most notably by Cranfield (1973a,b,c, 1974, 1975), have focussed on the settlement of oyster larvae. Cranfield reported that oyster larvae settle by way of the foot and shortly become byssally attached. Once settled, the foot is withdrawn, the byssal attachment lost, and the mantle margins become active, marking the onset of the cementation process (Cranfield 1973b,c, 1974). During initial settlement, a similar sequence of behaviours may occur in other cementing groups, however the timing and extent to which the foot is withdrawn varies between families (Yonge 1979). Interestingly, Yonge (1979) speculated that, following initial settlement, all cementing adult bivalves become fully cemented by a common method. However, while there is a general acceptance that the cement involved is composed of crystalline $CaCO_3$ (e.g. Kauffmann 1971, Yonge 1979), an understanding of the cementation strategy has remained largely unclear.

Harper (1992, 1997) provided the first detailed accounts of the nature of the $CaCO_3$ cement responsible for adhesion in adult oysters which provided new insights into the cementation mechanism. Harper (1992) reported the cement as extra-periostracal, resembling the morphology of inorganic marine cement, with an elemental composition indistinguishable from the oyster shell. From this detailed analysis, Harper (1992) suggested that the cement is likely to have formed from the same extrapallial (EP) fluid as the shell and proposed a model of cementation whereby the oyster adheres by leakage of EP fluid through the periostracum. This EP fluid then crystallises to form $CaCO_3$ cement (Harper 1992,

1997). Conversely, crystalline cement was not identified by Yamaguchi (1993) who proposed that attachment occurs by modification of the outer prismatic layer. However, cement similar to that identified by Harper (1992) was later identified as a main constituent of oyster attachment in both fossil (Todd 1993) and recent forms (Harper 1997).

Reports of oyster attachment instigated the study of cementation in other mature bivalves (e.g. Harper & Morton 2000, Morton & Harper 2001) from which some common themes emerged. For example, most studies report the cement responsible for adhesion as extra-periostracal (Braithwaite et al. 2000, Harper and Morton 2000, Morton and Harper 2001). However, few studies report the cement involved to be completely crystalline. Indeed, Harper and Morton (2000) report that cementation in *Myochama anomioides* (Stutchbury) involves an organic adhesive that lacks any crystalline structure. Organic adhesives have also been reported for the freshwater bivalve, *Posostrea anomioides* (Corbiculidae) (Bogan and Bouchet 1998). Bogan and Bouchet (1998) note the attachment of *P. anomioides* to the substrate is easily broken, and is therefore unlikely to involve any crystalline cement. Interestingly, Braithwaite et al. (2000) report the involvement of both an organic 'mucus' adhesive and crystalline cement in the attachment of sand grains to the outer shell surface of some infaunal bivalves. Similarly, Morton and Harper (2001) identify both organic and crystalline material in the attachment of *Cleidothaurus albidus* (Lamarck 1819). Previous studies have reported oyster cement as crystalline describing only the mineralised component (e.g. Harper 1992, 1997, Todd 1993). Recently however, Burkett et al. (2010) reported a high organic content in oyster adhesives and describe the cement as an organic matrix of cross linked proteins with a high inorganic content.

Detailed accounts of the nature of the adhesives, organic and/or crystalline, involved in bivalve cementation have been provided by many authors (Harper 1992, 1997, Todd 1993, Harper and Morton 2000, Braithwate et al. 2000, Morton and Harper 2001, Burkett et al. 2010). However, the source of such adhesives is not well understood. While many authors suggest that the organic component is likely to be a secretion from the mantle (e.g. Prezant 1979, Yonge 1979, Morton 1987, Braithwaite et al. 2000, Morton and Harper 2001), the source of the crystalline component is less clear. Harper (1992, 1997) suggests that cement

crystallises from EP fluid leaked through the periostracum, yet Morton and Harper (2001) note that the periostracum is not porous and suggest that cement nucleates on the organic component secreted from the mantle. Similarly, Braithwaite et al. (2000) propose that initial attachment of sand grains to infaunal bivalves (*Granicorium & Samarangia*) occurs via secretion of an organic 'mucus' adhesive from the mantle, which induces the formation of inorganic cement by direct precipitation of $CaCO_3$ from seawater. Present day surface seawater is six times saturated with respect to calcite and four times saturated with respect to aragonite (e.g. Morse and Mackenzie 1990). Inorganic carbonate cementation is often associated with organic components. Indeed, organic substances are often responsible for driving the formation of inorganic cement (Bathurst 1975, Tucker and Wright 1990). Interestingly, similarities between the cement involved in bivalve adhesion and inorganic diagenetic cements have been noted by several authors (Harper 1992, 1997, Morton and Harper 2001) and Burkett et al. (2010) describe oyster cement as an 'organic-inorganic hybrid'. However, the possible role of seawater and the relationship between organic components and inorganic marine cements in bivalve cementation have not been fully explored.

Much work has been conducted over the past decades to understand the methods by which bivalves cement to external substrates. It is generally accepted that, where present, the crystalline material involved in attachment is $CaCO_3$ (Kauffmann 1971, Harper 1992, 1997). Further work is required to understand the formation and nucleation of the cement and the role of organic adhesives in cementation. The possible influence of inorganic precipitation from seawater should also be investigated.

5.1.2 Aims of this study

This study aims to understand the methods by which oysters (*Crassostrea gigas*) cement to hard substrates. Characterisation, in terms of ultrastructure, crystallography and chemistry, of the contact zone between oyster shell and both inorganic (rock) and biological (other oyster shells) substrates will inform of the range of materials involved in oyster cementation. Progressive sampling of the contact zone from youngest to oldest parts (from ventral-dorsal margin) will

provide a temporal frame for analysis. This approach will provide new insights into the stages and methods leading to cementation. Any effect that cementation may have on shell ultrastructure will also be explored.

5.2 Results

Fused pairs of *C. gigas* specimens were collected from the intertidal zone at La Baule, France (section 2.1.3.1). These samples included two pairs of oysters fused laterally (sample AL1 and AL2, Figure 76a & b respectively) and one pair of oysters fused vertically (sample AV1, Figure 76c). Individual samples of *C. gigas* attached to rock were collected from the intertidal zone at Loch Sween, Scotland (section 2.1.3.2) (sample RA1 and RA2, Figure 76d & e respectively). A list and brief description of all cemented samples analysed in this study is provided in Appendix A.2.

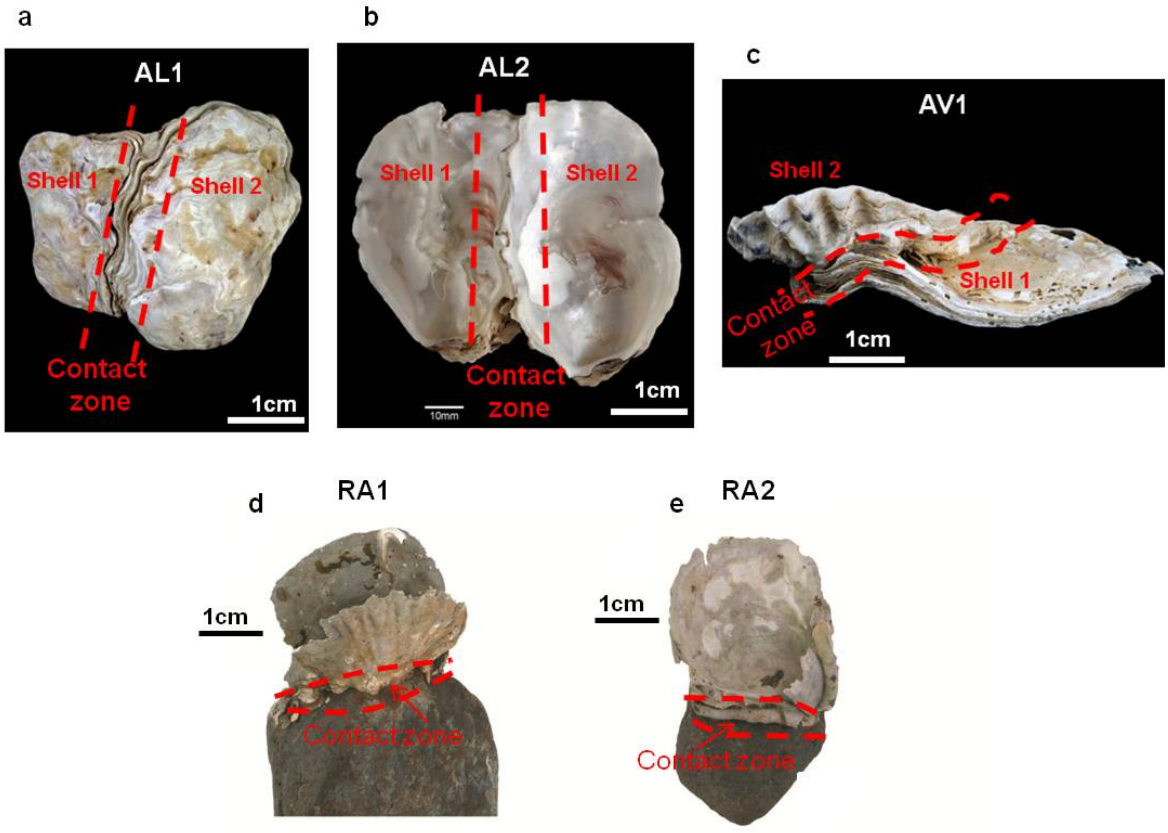

Figure 76. Samples of cemented oysters analysed in this study.
(a) & (b) Samples AL1 & AL2 respectively, both comprising two oyster shell fused laterally. (c) Sample AV1 comprising two oyster shells attached vertically where the left valve of shell 2 is attached to the right valve of shell 1. (d) & (e) Samples of *C. gigas* attached by the left valve to rock. Dashed lines highlight the contact zone between fused shells or between shell and rock.

For samples AL1, AV1, and RA1, a selection of rough fracture surfaces and polished blocks were produced of the contact zone as detailed in section 2.2.8. The contact zone of sample AL2 was isolated and sectioned progressively from ventral-dorsal margin (as described in section 2.2.8.1), producing six sub-samples labelled one to six from ventral to dorsal margin (Figure 79).

5.2.1 Ultrastructure of the contact zone

Through SEM analysis, two distinct materials were identified as the primary constituents of the contact zone, namely crystalline cement and organic 'glue'. Cement and glue may be present together or individually with the relative proportions of cement and glue variable between and within individual samples.

Crystalline cement was identified in parts of the contact zone of all samples analysed in this study. The thickness of the cement mirrors the topography of the substrate ranging from 10 µm to 1 mm. Where well formed, the cement is coarsely crystalline with a variety of crystal forms present including rectangular crystals arranged in radiating clusters as well as closely aligned fibres which form dense mats (Figure 77a & b). Crystals within the cement lack any common morphological orientation or obvious growth direction. Similarly, Harper (1992) reports that the cement is composed of radiating spherulites growing from all bounding walls of the contact zone. Where less well developed, cement is less coarse and is composed of fine acicular or fibrous calcite with a 'spongy' texture. The cement is often host to a variety of other organisms including diatoms (Figure 77c & d).

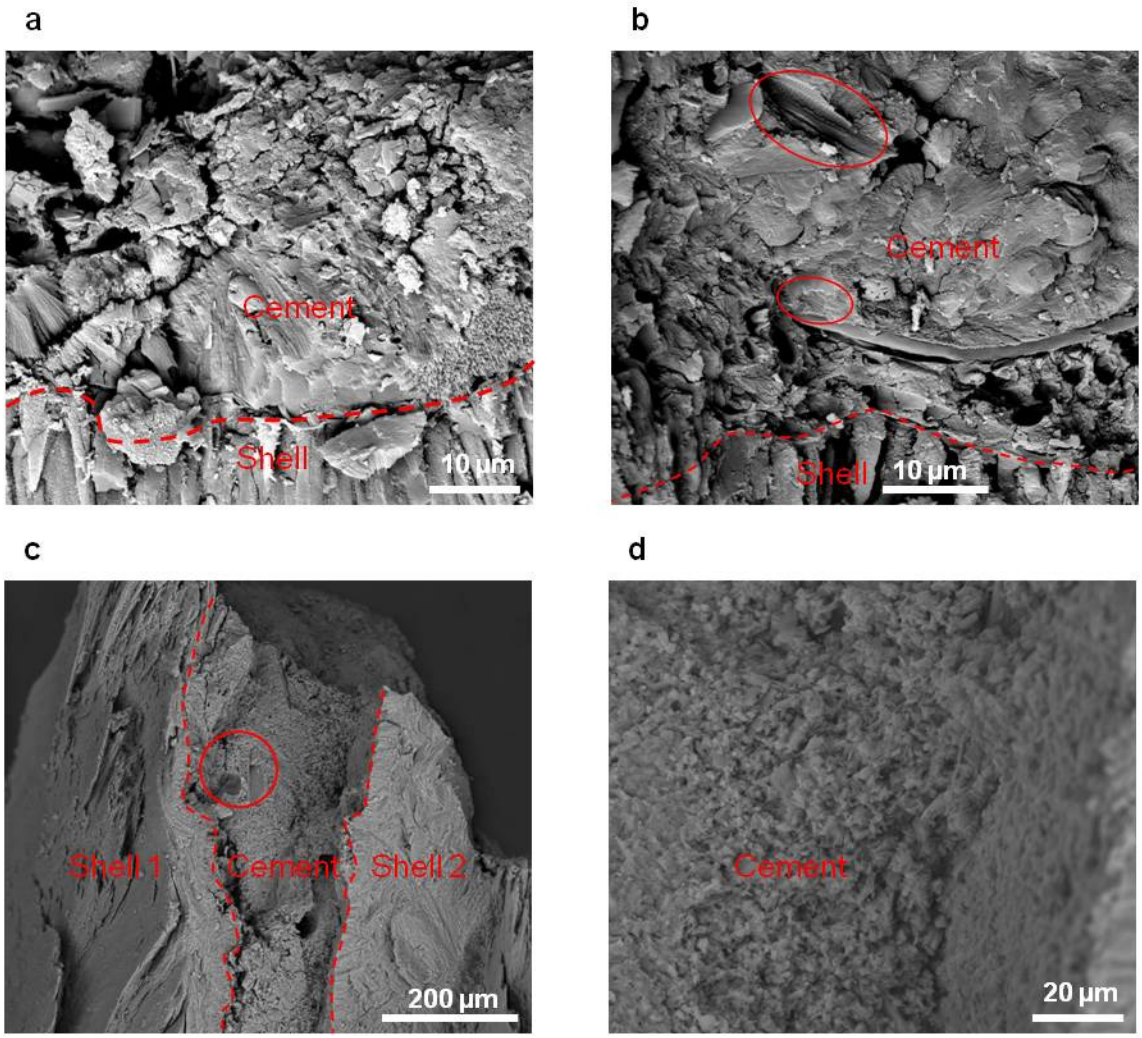

Figure 77. Backscattered electron SEM images revealing details of the crystalline cement present between oyster shell and substrate.
(a) & (b) Well developed cement with a variety of crystal forms present between oyster shell and rock. (c) Less coarse, 'spongy' cement between two laterally attached oyster shells, and (d) high magnification image of 'spongy' cement. Red dashed line indicates the assumed position of the periostracum, and red circle highlights the position of foreign organisms.

The cement identified in this study is similar to that previously identified in oyster attachment by Harper (1992, figure 3-5, 1997, figure 1). However, Harper (1992, Figure 6) notes a resemblance between the cement occupying the extreme ventral margin of the contact zone and the chalky deposits of the oyster shell. None of the cement identified in this study resembled chalky deposits observed in shells. Chalky shell deposits are composed of a distinct structure of blades and leaflets arranged to form a series of empty compartments or void space (see section 3.2.4.3). The cement identified in this study lacks any distinct structure or orientation and contains no visible empty space.

Large areas of the contact zone, most notably in samples of shell-shell attachment, are occupied by a smooth, amorphous material which has been termed 'organic glue' (Figure 78). The relationship of the organic glue and crystalline cement is variable and organic glue may be present as the sole constituent of the contact zone (Figure 78a) or coincident with crystalline cement (Figure 78b). Like the cement, the thickness of the organic glue varies with the topography of the substrate. Where shell and substrate are in close contact glue may be < 4 µm thick. Alternatively, where there is significant topography glue can reach ~400 µm thick (Figure 78c).

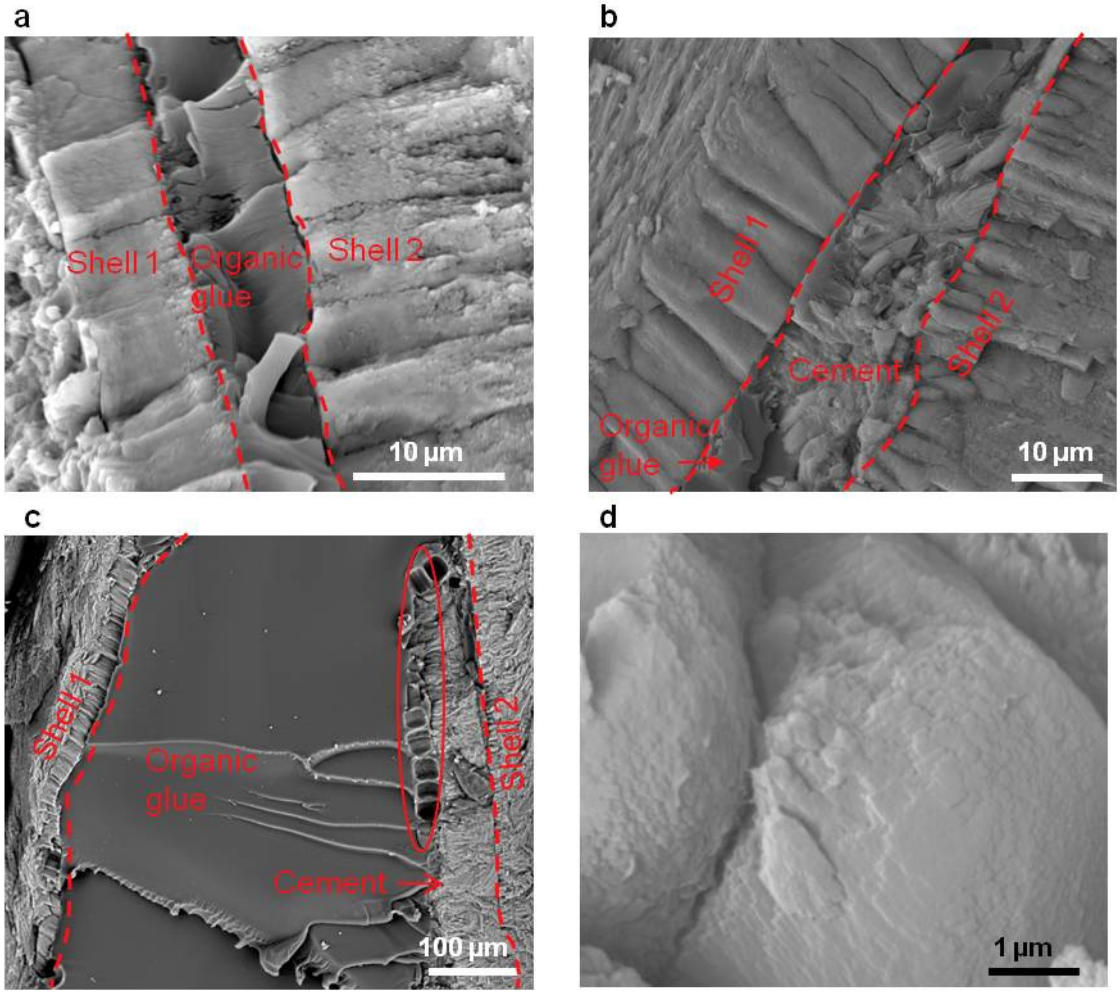

Figure 78. Backscattered electron SEM images revealing details of the organic glue present between oyster shell and substrate.
(a)-(c) Organic glue present between two laterally fused oyster shells where in (a) glue is homogonous with no crystalline component, (b) Organic glue with cement present within or on the surface of the glue. (c) Extensive organic glue present in the contact zone with cement present adjacent to the outer surface of shell 2, and coralline algae (highlighted by red circle). (d) High magnification image of raised areas on the surface of the organic glue, present between oyster shell and rock, revealing internal crystalline structure suggestive of crystals nucleating on the surface of the glue. Red dashed line indicates the assumed position of the periostracum, and red circle highlights the position of foreign organisms.

Organic glue is dark, homogenous, lacks any crystalline structure and is occasionally associated with organisms such as coralline algae (Figure 78c). Frequently, organic glue is associated with small crystals and 'patches' of cement that are erratically distributed within, or on, the organic glue (Figure 78b). Crystals are fine, bladed and lack any common orientation. In samples AV1 and RA1 the surface of the organic glue, surrounding individual crystals is often raised in circular 'bulges' which range in diameter from 2-20 µm. At high magnification it is clear that each 'bulge' is composed of fine mineralised blades, or laths (Figure 78d). It is likely that these 'bulges' represent early nucleation of crystals on the organic component.

5.2.1.1 Temporal distribution of materials

The relationship between the organic glue and crystalline cement is complicated and the quantity of each component varies between samples. To gain further understanding of the association between the two materials sample AL2 was prepared in such a way that the youngest, mid and oldest parts of the contact zone could be compared (Figure 79).

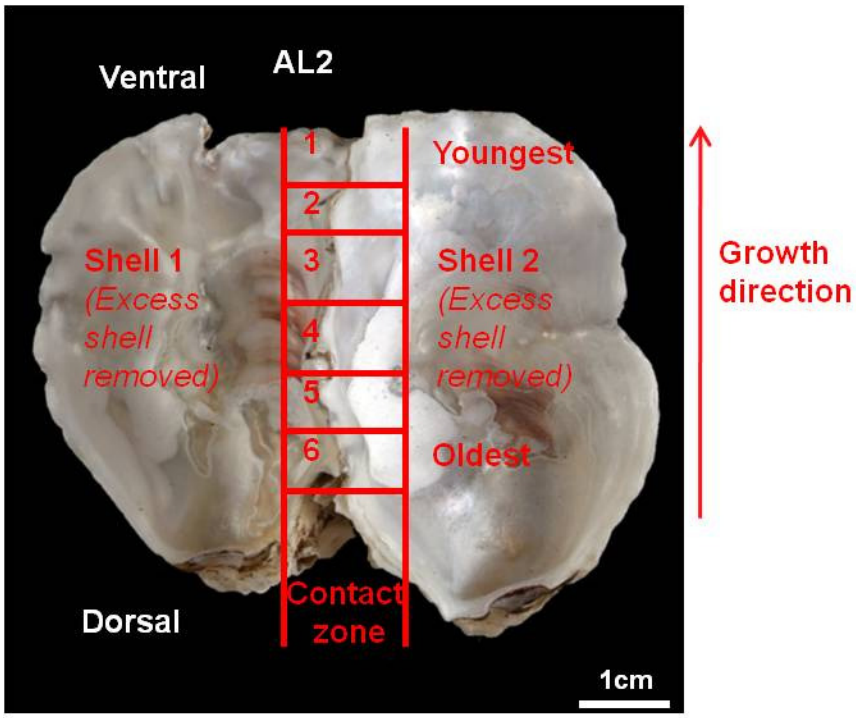

Figure 79. Temporal sectioning of the contact zone between two laterally attached oyster shells (sample AL2).
The contact zone between the shells was isolated (detailed in section 2.2.8.1) and the contact zone sectioned at approximately 1 cm intervals to produce a series of 1 cm blocks

from the youngest (1) to the oldest (6) parts of the contact.

In the youngest parts, sections one and two (Figure 79) the contact between shells is dominated mainly by organic material with very few micro crystals visible (Figure 80b). The relative proportions of organic glue and cement change towards mid sections of the contact zone (sections three and four, Figure 80c), where relative to section five, the volume of organic glue visible decreases whilst the volume of crystalline material increases. Indeed, in mid-sections the contact zone is composed of organic glue with fine crystals frequently visible within, or on, the surface of the glue (Figure 80c). These crystals include both fine individual acicular crystals and a few patches of cement. This gradual loss of organic material and increase in crystalline cement continues towards the oldest parts of the contact, and in dorsal sections (sections one and two, Figure 80d) crystalline material dominates and organic glue is rarely visible (Figure 80d).

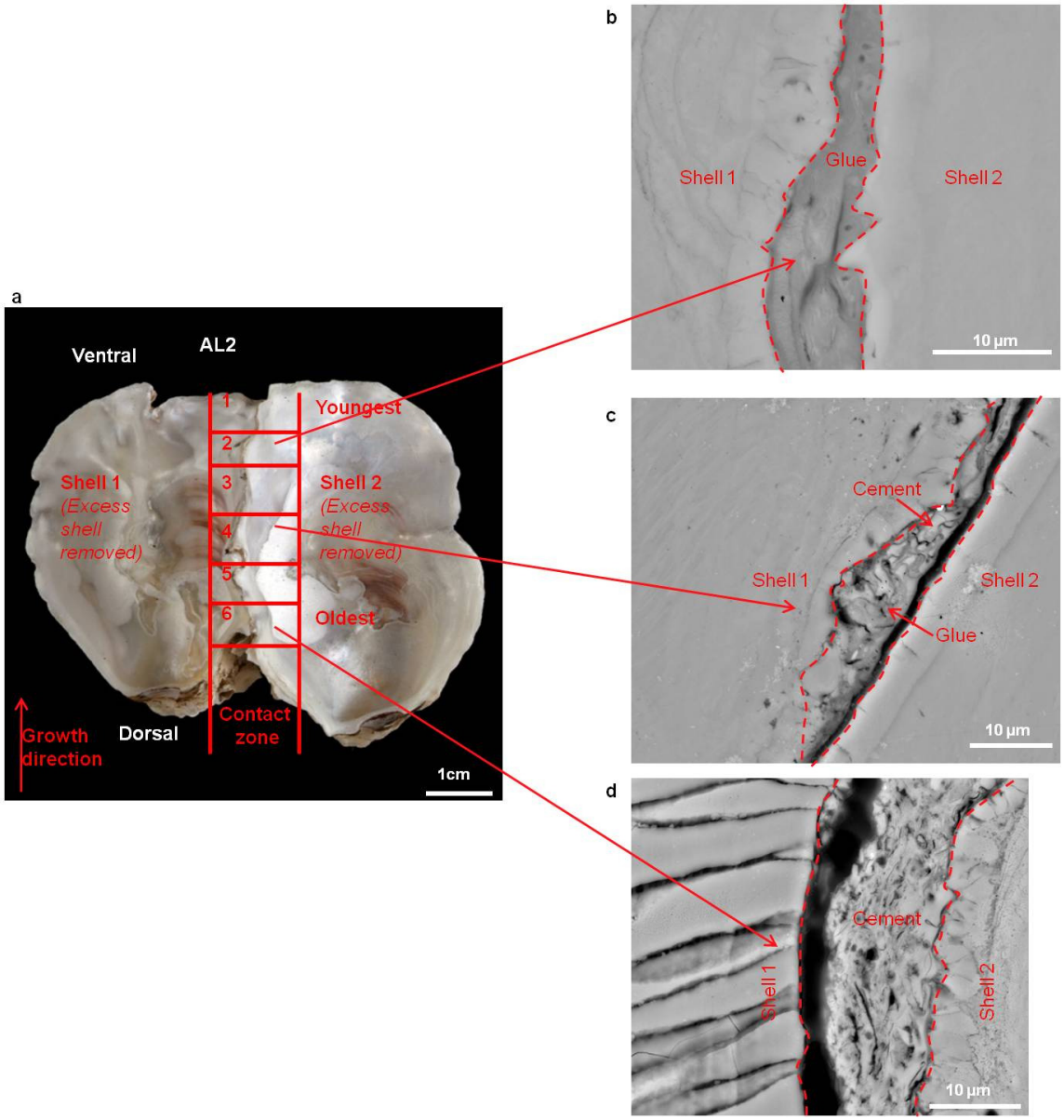

Figure 80. Backscattered electron SEM images revealing details of the contract zone progressively from ventral (youngest) to dorsal (oldest) sections.
(a) Sample of two laterally attached oyster shells showing details of sectioning from youngest (1) to oldest (6) parts. (b) The contact zone at section 2 showing contact to be occupied by organic glue with no significant crystalline material visible. (c) The contact zone at section 4 showing contact to be occupied by organic glue with some crystalline component. (d) The contact zone at section 6 revealing details of crystalline cement, with no significant organic component. Red dashed line on b-d represents the outermost edge of both shells and the presumed position of the periostracum.

5.2.2 Chemistry of the contact zone

The elemental composition of the materials occupying the contact zone was determined by energy dispersive spectroscopic (EDS) elemental analysis.

Qualitative elemental mapping of the contact zone of all samples was carried out using a FEI Quanta 200FEG SEM with EDAX Genesis software. Maps were

produced across shell, contact and substrate for the following elements: C, O, Mg, S, Ca. Typical maps are presented in Figure 81.

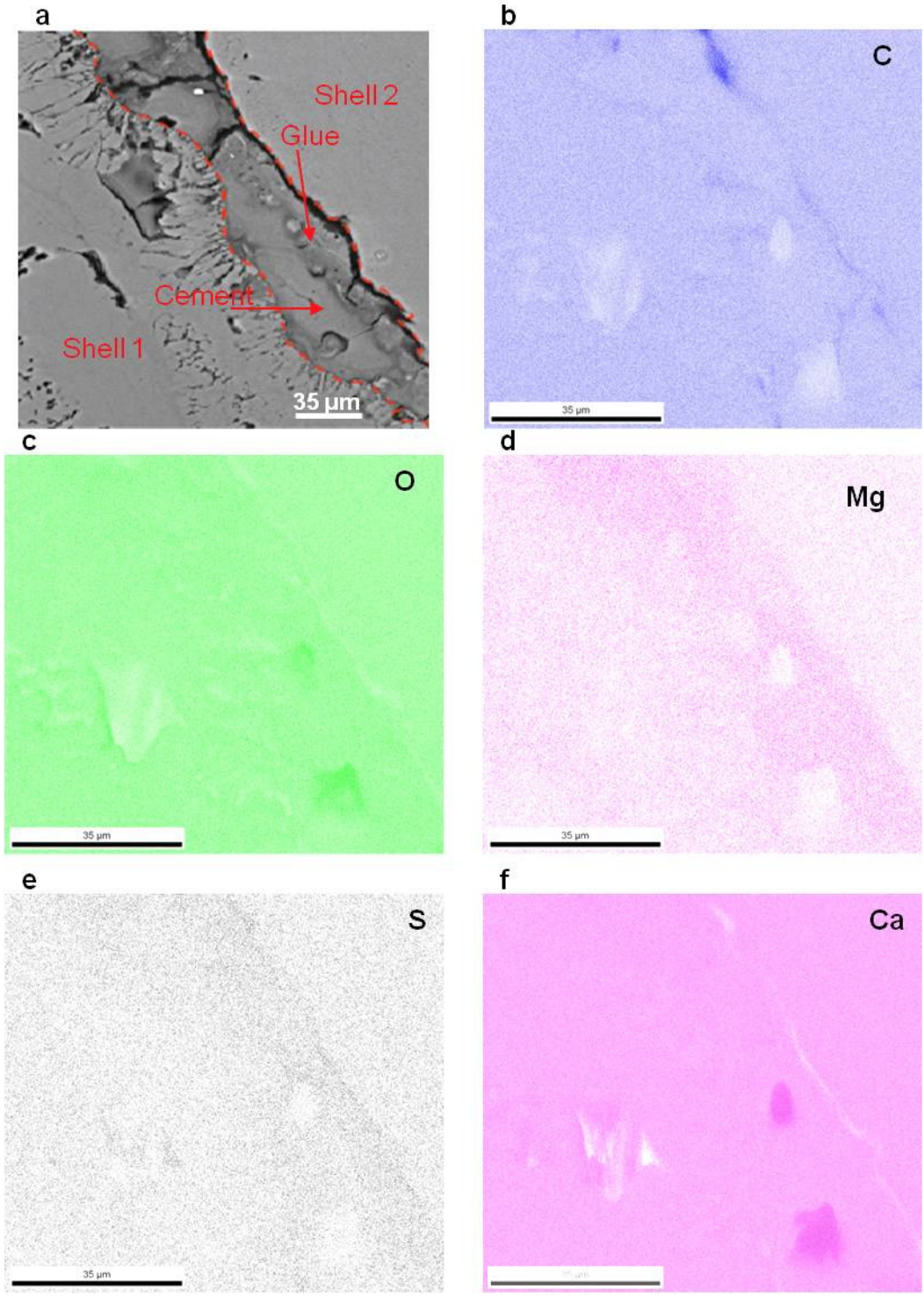

Figure 81. Elemental distribution maps of shell-shell contact zone.
(a) Backscattered electron SEM image showing shell-shell contact zone of two laterally attached oyster shells (AL2). (b)–(f) Elemental distribution maps of C, O, Mg, S, and Ca respectively where more intense colour equates to higher elemental concentration.

Distribution of calcium, carbon and oxygen is relatively uniform between adhering shells and across the contact zone, confirming the cement to be $CaCO_3$.

Concentration of carbon (Figure 81b) and sulphur (Figure 81e) is elevated at the outer surface of shell 2, corresponding to the area of organic glue (Figure 81a), and becoming gradually less intense towards more crystalline parts at the centre of the contact zone. Calcium concentration is not altered across the contact zone, which suggests that the organic glue does contain some crystalline component. Similarly, Harper & Morton (2000) noted that calcium is present in the organic adhesive of *M. anomioides* and is therefore likely to contain some of the crystalline component. The apparent fall in calcium concentration immediately adjacent to shell 2 is likely to be related to the gap between the shell and contact zone. This 'gap' is considered to be an artefact of polishing. The magnesium distribution map (Figure 81d) clearly shows a higher magnesium concentration in the crystalline parts of the contact zone when compared to the adjacent shells.

To accurately determine the quantity of magnesium in both the oyster shell carbonate and the carbonate cement of the contact zone, quantitative EDS analysis was carried out using a Zeiss Sigma FEG SEM with INCA software. The $CaCO_3$ and $MgCO_3$ composition of shell folia and contact zone cement was determined for sample RA2. Sample RA2 was selected for quantitative analysis as SEM observations showed that the cement of this sample is well formed with little organic material visible. Choosing this sample reduces interference of organic material with standardised elemental analysis as a suitable standard for organic matter is not available. Oyster shell folia and contact zone cement were analysed at three points and within each point a total of five spectra were accumulated allowing the mean elemental composition to be calculated. The total $CaCO_3$ and $MgCO_3$ present in shell and cement are presented in Table 4.

Structure	wt% Ca	wt% Mg	wt% $CaCO_3$	wt% $MgCO_3$	Mole% $CaCO_3$	Mole% $MgCO_3$
Shell folia	39.02	0.14	99.50	0.50	99.41	0.61
Shell folia	38.45	0.23	98.94	0.82	98.81	1.01
Shell folia	38.62	0.19	99.32	0.68	99.23	0.82
Cement	31.5	1.8	92.65	7.35	91.41	8.63
Cement	31.5	1.5	93.80	6.20	92.70	7.31
Cement	31.5	1.6	93.41	6.59	92.31	7.72

Table 4. Quantitative EDS analysis: comparison of $CaCO_3$ and $MgCO_3$ composition of shell and cement.
Elemental analysis carried out by standardised EDS analysis. Shell folia and cement were analysed at three areas and within each area five analyses were conducted. Values presented above are the average values calculated for each area.

The contact zone cement contains significantly more $MgCO_3$ than shell folia (T test, p=<0.01). The $MgCO_3$ component of the cement ranges from 7.3-8.6 mole% and is therefore high Mg calcite (Burton and Walter 1987). Conversely, the $MgCO_3$ component of the shell is typically 0.1-1 mole% and is more in line with low Mg calcite, as previously reported for oyster shell carbonate (e.g. Carriker et al. 1980).

5.2.2.1 Raman spectroscopic analysis

Both valves of the oyster are composed predominantly of low Mg calcite and localised aragonite (section 3.1.1 and references therein). The results of both qualitative and quantitative EDS analysis show that magnesium is considerably more concentrated in the cement than adjacent shells. Raman spectroscopy was used to inform of the calcite lattice structure of shell and cement to confirm the presence of magnesium in the cement as part of the calcite lattice. Sample RA2 was also used for this analysis.

Calcite exhibits three fundamental Raman shifts at 280, 712 and 1086 cm^{-1} (Bischoff et al. 1983, Urmos et al. 1991, Gillet et al. 1993, Perez and Martinez-Frias 2003, Lecuyer et al. 2004). A change in magnesium concentration within the calcite lattice can be detected by analysis of the full width half maximum (FWHM) of each of these Raman shifts. Substitution of calcium with magnesium causes distortion of the calcite lattice (e.g. Bischoff et al. 1983, 1985). This distortion can be detected by an increase in the FWHM of the fundamental Raman shifts (Urmos et al. 1991, Lecuyer et al. 2004).

Raman spectroscopy was carried out on nine points in both the shell folia and crystalline cement of the contact zone. Both folia and cement display each of the three prominent calcite shifts at 280, 712 and 1086 cm^{-1}. A plot of the average FWHM for each shift for both shell and cement is displayed in Figure 82. All three Raman shifts for the cement display a considerably higher FWHM when compared to the same Raman shift for the shell. In some cases the FWHM for the cement is almost double the line width of the corresponding shift in the shell.

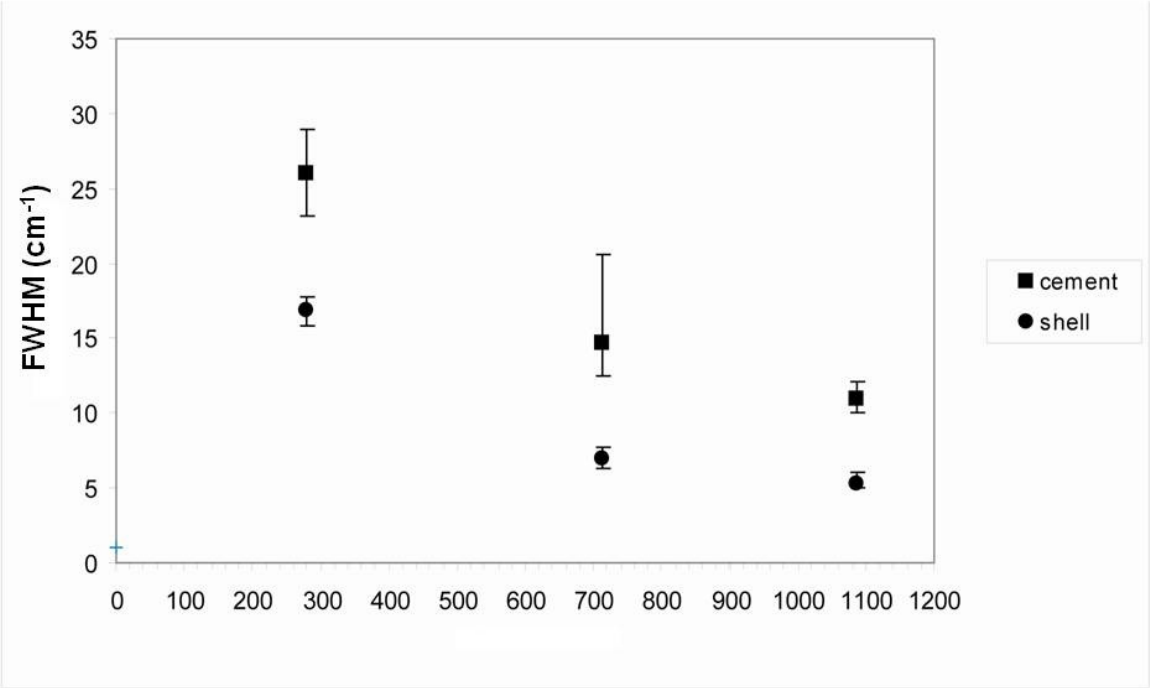

Figure 82. Raman spectroscopic analysis of shell folia and contact zone cement. Plot of the full width half maximum (FWHM) for each of the three characteristic Raman shifts of calcite at 280 cm^{-1}, 712 cm^{-1} and 1086 cm^{-1} for the shell and cement. Each point represents the average FWHM value gathered for each of the nine shell and cement samples. Error bars represent the maximum and minimum FWHM measured for each band.

5.2.3 Crystallography of crystalline cement

Electron backscatter diffraction (EBSD) crystallographic analysis was carried out to determine the crystallographic orientation of the cement occupying the contact zone.

EBSD analysis requires a flat topography-free surface. In samples of shell-shell attachment an even surface from which strong diffraction patterns could be detected was achieved. During polishing of resin blocks from samples of rock attachments (samples RA1 and RA2) the difference in material properties between shell carbonate, cement, and rock caused the rock to stand proud

against the shell. This created a shadow across the contact zone preventing the detection of diffraction patterns from the cement. For this reason EBSD analysis was carried out on a sample of shell-shell attachment only.

Given the high quantity of crystalline material present, EBSD analysis was carried out on sample AL2 section six (Figure 80d). EBSD scans were completed laterally across the contact zone. Data was cleaned through a two stage clean up procedure so only grains of confidence index of > 0.1 are displayed in the final data set. The resulting EBSD map with superimposed crystal models and corresponding pole figures are displayed in Figure 83.

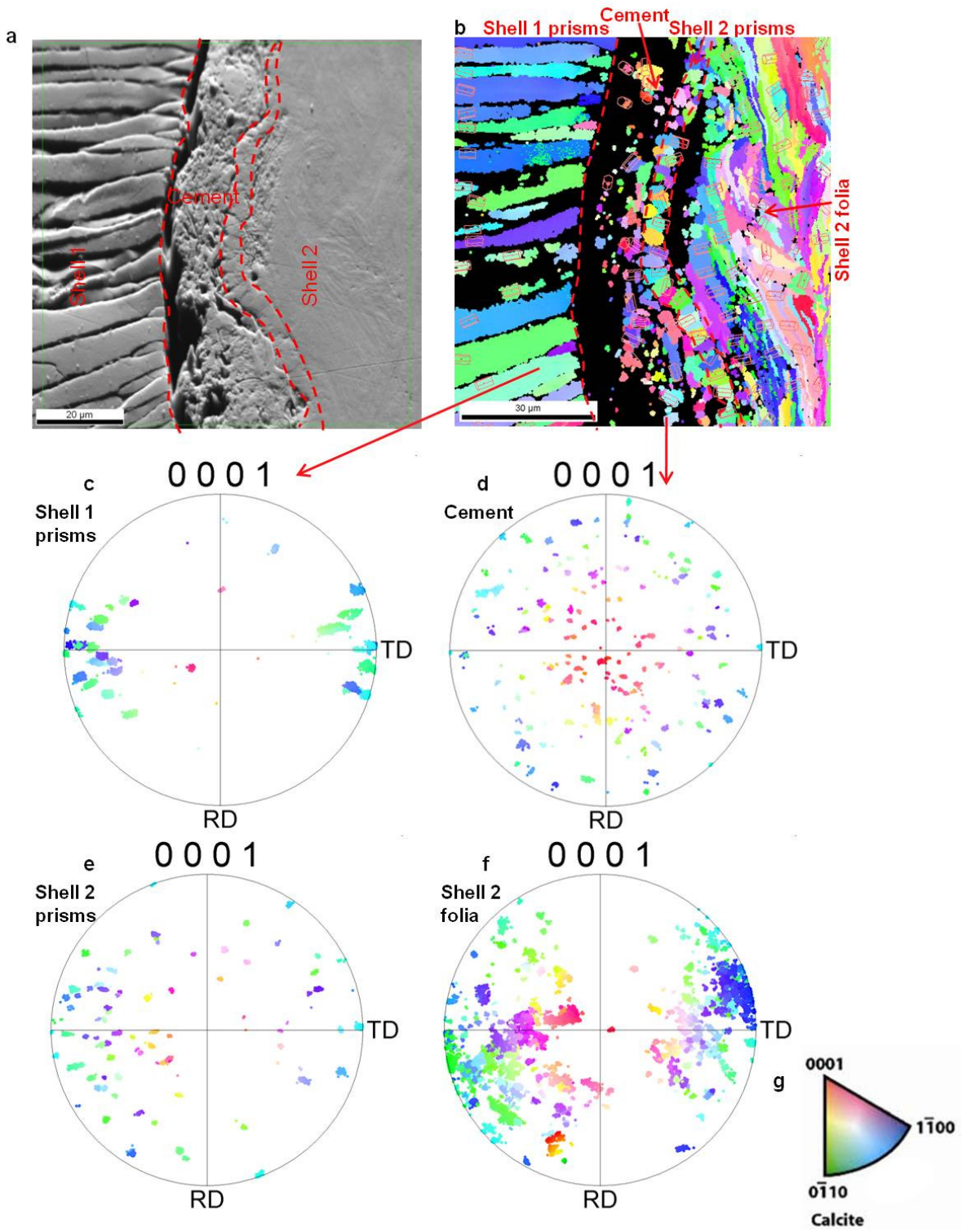

Figure 83. EBSD analysis across the contact zone of two laterally attached oyster shells. (a) Backscattered electron SEM image detailing scan area. (b) EBSD crystallographic orientation map with superimposed crystal models showing crystallographic orientation. Red dashed line represents boundaries between outer-edge of the prisms of shell 1 and shell 2 (the presumed position of the periostracum) and the boundary between prisms and folia of shell 2. (c)–(f) Pole figures representing the crystallographic orientation of shell 1 prisms, cement, shell 2 prisms and shell 2 folia respectively. (g) Crystallographic orientation map colour key for calcite with reference to normal direction.

In the prismatic region of both shell 1 and shell 2, the calcite c-axis is consistently orientated perpendicular to the inner and outer shell surface,

parallel with elongation of the prisms. This is consistent with crystallographic orientation of non–cemented oysters (e.g. section 3.4.1). Pole figures plotted for the prismatic region of shell 1 and 2 (representing the {0001} crystal plane of calcite) show dominant c-axis orientation perpendicular to the {0001} plane of calcite with maximum lateral variation of up to 46˚ occurring in the more weakly aligned prisms of shell 2 (Figure 83c & e). EBSD analysis confirms the cement to be composed of calcite. The calcite crystals of the cement lack any common orientation, and when plotted as a pole figure (Figure 83d), relative to the {0001} plane of calcite, the cement displays almost 360˚ variation in c-axis orientation. The folia of shell 2 are also aligned with the c-axis and perpendicular to the outer shell surface with a maximum variation of 42˚.

5.2.4 Effect of cementation on shell structure

Yamaguchi (1993) investigated the shell structure of attached oyster shells and reported modification of the prismatic region during cementation to a 'ridge and furrow' structure. This structure was not identified in any samples analysed in this study. Indeed, cementation had no major effect on shell structure. In all samples studied, shell morphology and microstructural arrangement is typical of that previously reported for unattached oyster shells (e.g. Chapter 3, Galtsoff 1964, Stenzel 1971, Carriker et al. 1980). The bulk of both valves is composed of foliated calcite which is frequently interrupted by lenses of chalky calcite. Both right and left valves are bound on the outer surface by calcite prisms.

In samples of laterally fused shells (AL1 and AL2, Figure 76), identification of the substrate shell is complicated. However, in both samples AL1 and AL2 the height of the prismatic region of shell 1 is considerably greater than in shell 2 (Figure 84). The prisms of shell 1, adjacent to the contact zone, are typically 30-40 µm high, while the prisms of shell 2, at the contact zone, are typically 7-10 µm high (Figure 84b). The reduction in prism height of shell 2 occurs only on the anterior side of the valve immediately adjacent to the contact zone with shell 1. The prismatic region at the posterior margin is not reduced, with prisms ranging in height from 35-40 µm (Figure 84c), a height typical for this microstructure on the left valve (section 3.2.4.1). The prismatic region of shell 1 is not reduced in

height at any point. This may suggest that shell 1 acted as a substrate to which shell 2 became attached.

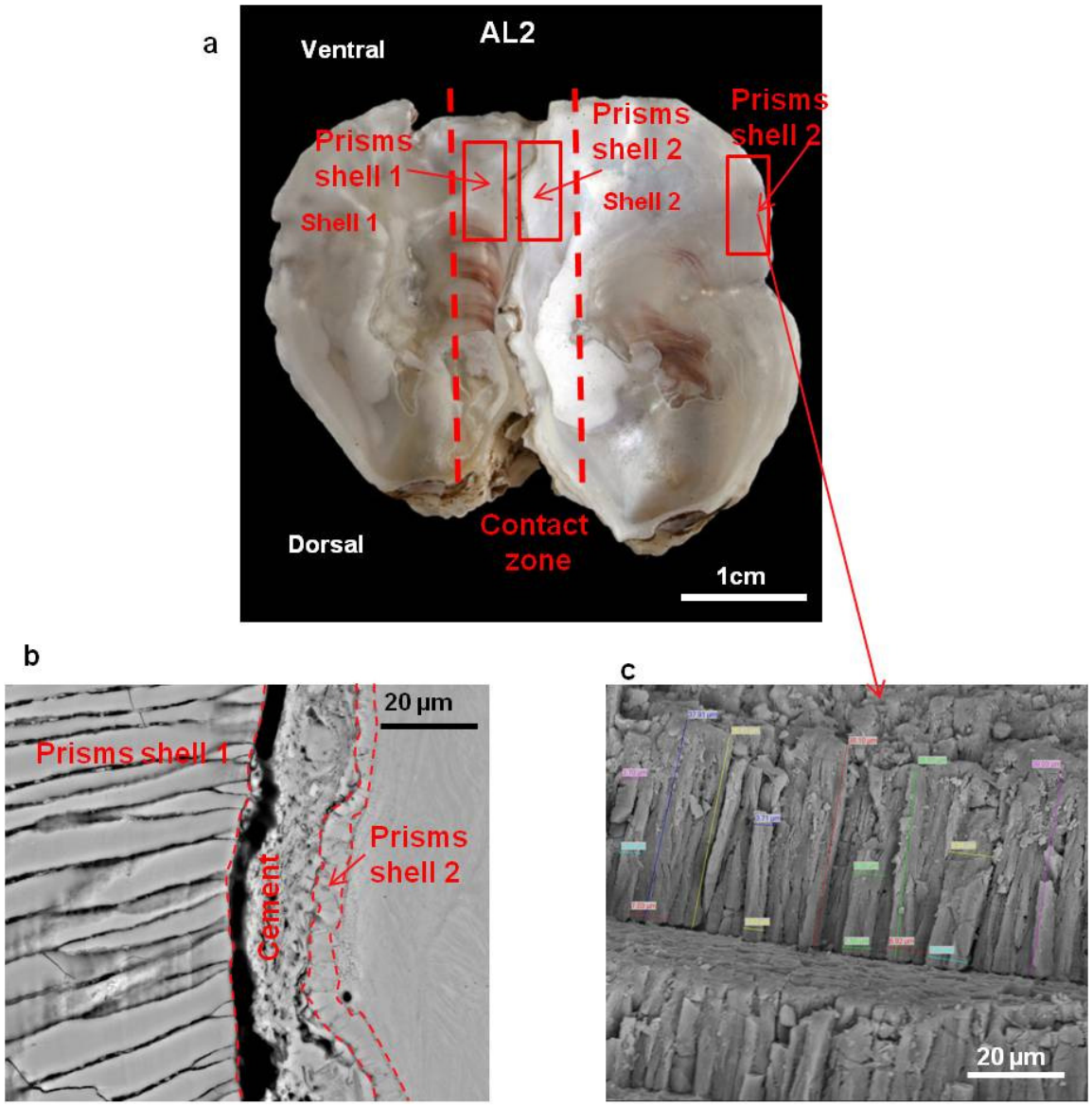

Figure 84. Effect of cementation on shell structure.
(a) Sample AL2 with red boxes denoting the position of the prismatic region adjacent to the contact zone on shell 1 and shell 2, and the prismatic region on shell 2 not in contact with the attachment site. (b) Backscattered electron SEM image of polished section showing the size of prisms of shell 1 relative to the reduced prisms of shell 2. (c) Secondary electron and backscattered electron mixed SEM image of rough surface showing height of the prisms of shell 2 at valve parts not in contact with the attachment.

Identification of the substrate shell in the vertically attached sample (AV1, Figure 76c) is easier. Oysters attach by cementation of the left valve, the right valve is never involved in cementation under natural conditions (e.g. Yonge 1979, Harper 1992, Yamaguchi 1993). It is clear in sample AV1 that the upper shell (shell 2) is attached by the left valve to the right valve of the lower shell (shell 1), confirming shell 1 as the substrate shell (Figure 76). Differences in prism height between shells in this sample are likely to reflect the normal

differences in prism height expected between right and left valves (see section 3.2.4.1 for details).

Previous reports detailing the attachment mechanism of oysters suggest some involvement of the periostracum (Harper 1992, 1997). The oyster shell periostracum is extremely thin and is readily lost on older shell parts as a result of erosion (e.g. Carriker et al. 1980). The periostracum could not be identified in any samples during this analysis. It is certain that the periostracum is present on the outer shell surface of all samples, however it could not be identified as samples were viewed in cross section rather than in plan view. In addition, the periostracum is likely to have been obscured by the presence of organic glue from which the periostracum could not be differentiated.

5.3 Discussion

Oysters adhere by cementation of the left valve to a hard substrate (e.g. Yonge 1960, 1979, Harper 1992, 1997) and for the most part cementation has little effect on shell structure. A reduction in prism height in the cementing left valve, relative to the right, is common in oysters (e.g. Carriker et al. 1980) as well as in other cementing bivalves such as *M. anomoides* (Harper and Morton 2000), and has been confirmed in this study (section 3.2.4.1). A further reduction in prism height is noted locally within the left valve at valve parts directly in contact with the attachment site. This localised reduction in prism height may simply be the result of erosion by the substrate or a result of metabolic control. It is possible that at valve parts adjacent to the attachment site, metabolic efficiency curtails the development of full prisms where they are not essential for the strength and flexibility of the shell.

5.3.1 Method of attachment

Previous studies, notably by Harper (1992, 1997), report crystalline cement ($CaCO_3$) as the adhesive responsible for oyster attachment, while recently Burkett et al. (2010) identified an organic adhesive as the primary constituent of the contact zone between fused oyster shells. This study has identified both crystalline cement and ‘organic glue’ adhesives in oyster attachment, and their

presence appears independent of substrate type (rock or shell substrate). Cement and glue were identified in all samples in varying proportions, both together and individually. Progressive sampling from youngest to oldest parts of the contact zone reveals the relationship between cement and glue as temporally controlled. The youngest part of the contact zone (Figure 80b) is predominantly occupied by organic glue while towards the oldest parts, crystalline cement becomes dominant (Figure 80d). This relationship, together with the presence of early nucleating crystals (Figure 78d), suggests that organic glue is initially secreted onto which, over time, crystals precipitate, eventually leading to the formation of crystalline cement. It is suggested that the secretion of the initial organic glue acts to smooth the substrate bringing shell and substrate close enough to bind (De Bruyne 1962, Harper 1992, 1997). Secretion of the organic glue would also provide a stable substrate for crystallogenesis to occur. Indeed, crystal nucleation on an original organic 'mucus', resulting in cementation, has been reported in *C. albidus* (Harper and Morton 2000) and for the infaunal bivalves *Granicorium* and *Samarangia* (Brathwaite et al. 2000). The relationship between the volume of crystalline cement and organic glue present in oyster attachment suggests that cementation of the organic glue is occurring as the oyster grows.

Both the organic glue and crystalline cement is, in places, associated with small organisms including diatoms and coralline algae suggesting that the original organic glue is secreted outside of the periostracum (e.g. Harper 1992, 1997, Harper and Morton 2000, Morton and Harper 2001). Once secreted, the glue becomes mineralised by precipitation of $CaCO_3$. As noted by Harper (1992, 1997), the morphology of the crystalline cement is almost indistinguishable from diagenetic marine cements and is similar to that reported for other cementing bivalves such as *C. albidus* (Morton and Harper 2001). The nature of the crystal forms within the cement and lack of common orientation, are features commonly associated with marine cements and are unlike any regulated microstructure normally found within the oyster shell. The oyster shell is a well ordered biological structure comprising four distinct microstructures, each composed of low Mg calcite and each with an identical c-axis orientation (section 3.6, Figure 62). On the other hand, the cement is composed of high Mg calcite crystals with no distinct order or growth pattern and random c-axis

orientation. Secretion of shell parts and attachment materials under biological control results in the formation of biomineral structures which are well ordered in terms of morphology and crystallography (Weiner et al. 2000, Cusack et al 2007, Cusack et al. 2008). For example, the calcified byssus of *Anomia s.p*, which is secreted under direct biological control, comprises highly organised crystals in an organic matrix (Eltzholtz and Birkedal 2009). Harper (1992, 1997) suggested that the cement involved in oyster attachment forms from the same EP fluid responsible for shell secretion. However, this study has identified discrepancies between the cement and shell in terms of morphology, chemistry and crystallography which strongly suggests that the cement is devoid of the biological control that is so apparent in the formation of the shell microstructures. The cement is composed of disordered crystals of high Mg calcite which are features more in line with inorganic marine cements. Indeed, in marine waters at temperatures between 5-25˚C, calcite with $MgCO_3$ content of 8±1 mole% is preferentially precipitated (Burton and Walter 1987). Samples analysed in this study were collected from waters which fall within this temperature range. Subsequent EDS and Raman spectroscopic analysis revealed that the cement has a $MgCO_3$ content which falls within the latter range (Table 4). It is therefore apposite to suggest that the cement is formed outwith the biological control experienced by shell biomineralisation processes and is the result of inorganic precipitation.

5.3.2 Marine cementation

The morphology, chemistry and crystallography of the cement present between oyster shells and substrates strongly suggests, as has been proposed for other cementing forms, that the cement is formed by inorganic precipitation (e.g. Morton and Harper 2001, Braithwaite et al 2000). Surface seawater is six times saturated with respect to calcite and four times saturated with respect to aragonite (Morse and Mackenzie 1990), despite this marine cementation is not a common occurrence. For marine cements to form a number of concomitant environmental parameters must be present. For example, a stable substrate must be present in an area with little exposure to mechanical abrasion, seawaters must be supersaturated and water exchange rates must be high (Tucker and Wright 1990). Cementation is often catalysed by the presence of

organic matter including biofilms, mucus and microbes which provide a nucleating surface on which precipitation can begin (Mitterer 1971, Bathurst 1975, Tucker and Wright 1990, Braithwaite et al. 2000, Hillgartner et al. 2001). Oysters, of genus *Crassostrea*, adhere tightly to intertidal zone substrates creating a narrow zone of attachment (usually < 1 mm) in which abrasion would presumably be minimised, yet seawater would constantly be replaced by tidal action. The micro environment created between oyster shell and substrate would be an ideal milieu for marine cementation to occur. In addition, the organic glue identified in this study would provide an ideal substrate for precipitation. Indeed, the surface of parts of the organic glue shows evidence of early crystal nucleation (Figure 78d, Figure 80c) and temporal sampling reveals that cement forms progressively following secretion of the organic component. Marine cementation can occur on rapid timescales (Friedman 1998) causing mineralisation of the organic glue soon after secretion. Once initiated, crystallisation will continue inorganically resulting in the progressive cementation of the entire organic substrate. Similarly, Harper and Morton (2000) and Morton and Harper (2001) report organic cement with a crystalline component, possibly early forming crystals, in the attachment of *M. anomioides* and *C. albidus* respectively. Braithwaite et al. (2000) demonstrate that polysaccharide biofilms induce crystallogenesis by lowering activation energy and attracting Ca^{2+} and CO_3^{2-} ions from seawater. Whilst the biochemical composition of the organic glue identified in this study is unknown (discussed in section 5.3.4 below), the secretion of the organic glue is likely to provide the oyster with initial adhesion and stability and induces the formation of $CaCO_3$ cement by inorganic precipitation from seawater.

5.3.3 Source of organic glue

The source of the organic glue is intriguing. Early works suggests some involvement of the periostracum in the cementation process (e.g.Yonge 1979). The cross sectional view of all samples taken in this study made it impossible to identify the periostracum and, as such, no comment can be made as to its role in attachment. However, it is noted that the periostracum in oysters is inherently thin (< 0.5 µm e.g. Todd 1993) and given the extent of the organic glue, which in places can reach up to 400 µm thick, it is considered unlikely that

the periostracum could be directly involved. Further, the presence of diatoms and coralline algae within the glue is evidence of the extra-periostracal nature of the material. Until recently, most work has focussed on the formation of the crystalline cement. Burkett et al. (2010) provide a detailed account of the organic component, however make no reference to the source of the material. Harper (1992, 1997) suggested that cement is formed by leakage of EP fluid through the periostracum. While this is possible, it would require the periostracum to be porous, a feature for which there is little evidence (Morton and Harper 2001). Larval oysters adhere by secretion of mucopolysaccharide from the foot, which is then withdrawn and the inner mantle fold becomes active and continues to secrete a similar substance (Cranfield 1973a, b, c, 1974, 1975). Given the involvement of the mantle in the early stages of oyster settlement, it is perhaps more likely that this involvement continues as the oyster matures, and may provide a source of the organic glue. Indeed, the mantle has been offered as a possible source of organic adhesives in a number of cementing bivalves (e.g. Braithwaite et al. 2000, Harper and Morton 2000). A pallial gland which could be responsible for the secretion of cement has been identified in the mantle of some specimens of *C. albidus* (Morton and Harper 2001). Such glands, if present in other cementing bivalves such as the oyster, would certainly provide a plausible source of the organic glue. Further studies should focus on the structure of the oyster mantle and the source of the organic glue.

5.3.4 Composition of organic glue

Detailed analysis of the composition of the organic glue is beyond the scope of this study. However, it is recognised that understanding the composition of the organic glue is fundamental to understanding the cementation strategy. Burkett et al. (2010) provide the first detailed accounts of the organic adhesive involved in oyster attachment reporting a composition of crossed-linked organic material with an elevated protein content and high inorganic component. Specifically, the organic material is reported to be composed of cross-linked phosphorylated proteins, which are also common to other organic adhesives such as the byssal threads of the mussel and organic glue of the barnacle (Burkett et al. 2010).

Previous studies have investigated the organic adhesives of the mussel and barnacle with respect to making synthetic mimics, upon which some common themes as well as critical compositional differences have been reported. Byssal threads are complex, consisting of four distinct portions, namely plaque, thread, stem and coating each with a unique chemical composition (Mascolo and Waite 1986, Weigemann 2004, Kamino 2008). The threads of some species, such as *Mytilus edulis* display a nonlinear protein gradient along the length of the thread bringing about differences in strength and flexibility required by different portions of the thread (Mascolo and Waite 1986). This complex arrangement contrasts with the relative simplicity of other organic adhesives such as the organic glue (proteinacous cement of Kamino 2008) of the barnacle (Balanidae). The barnacle glue is secreted from the cement gland in the basal portion of the barnacle as a homogenous adhesive layer of compositional uniformity (Kamino et al. 2000, Kamino 2008). The organic glue of the oyster is likely to be of similar homogenous composition as the barnacle glue. However, key compositional differences must be present which enable the barnacle glue to remain non-mineralised while the organic adhesive of the oyster rapidly becomes crystallised by inorganic precipitation from seawater. For example, Burkett et al. (2010) note that the oyster cement contains about ten times less water than barnacle cement, and is described as dominantly inorganic cement compared with the organic hydrated glue of the barnacle and mussel. Khandeparker and Anil (2007) compare the entirely organic cement of Balanid barnacles to the cement of the Cthamalid barnacles which, once secreted, hardens and becomes surrounded by calcite. The authors report that in the secretion of the organic cement, the cement passes through a series of intracellular canals before reaching the cement duct which is lined with chitin. On the other hand, in the Cthamalid barnacles, the calcareous cement passes directly to the cement ducts which are not lined with chitin (Khandeparker and Anil 2007). In addition, Khandeparker and Anil (2007) suggest that the presence of anionic groups in the matrix proteins may serve as nucleating sites for calcification, which may not be absent in non-calcareous forms. It should also be considered that key calcite-inhibiting protein groups may be missing in calcareous adhesives, such as the organic glue of the oyster, but are present in other organic adhesives such as the Balanidae. For example, Politi et al. (2007) demonstrate that aspartic acid-rich proteins inhibit the uncontrolled crystallisation of amorphous $CaCO_3$ during

biomineralisation in the prismatic shell layer. It is considered however that the organic substrate associated with crystal nucleation in the cement may not be of the same structural framework as the organic matrix of the shell. Mollusc shell layers form from interaction of an amorphous calcium carbonate (ACC) precursor with aspartic acid rich proteins of the organic matrix within a highly structured framework of chitin (Addadi et al. 2006). This framework binds CO_3^{2-} and Ca^{2+} to fixed positions inducing epitaxial growth resulting in the growth of highly organised specialised structures. However, structure and organisation is lacking in the cement suggesting that the original organic structural framework may not be present to induce epitaxial growth. Organic matter is frequently associated with microbes which can induce $CaCO_3$ precipitation as a by-product of biological activity (e.g. Lowenstam and Weiner 1989, Morse and MacKenzie 1990, Marin et al. 2007, Braithwaite et al. 2000). Microbes induce $CaCO_3$ precipitation by increasing local pH (by removal of CO_2) and increasing CO_3^{2-} alkalinity through CO_2 degassing and ammonia production (Wang et al. , Hillgartner et al. 2001). In addition, microbes accumulate extra-cellular polysaccharide which increases the available Ca^{2+}-binding macromolecules (Wang et al. 2010). Microbially induced $CaCO_3$ precipitation normally results in mineralised structures that lack any distinct organisation or structure (e.g. Lowenstam and Weiner 1989, Marin et al. 2007, Braithwaite et al. 2000). Microbes may play some part in the cementation of oysters, and possibly other bivalves. Indeed, Braithwaite et al. (2000) demonstrated that the infaunal bivalve *Granicorium* is closely associated with abundant microbial communities which are likely to act as a precursor to cementation.

Detailed biochemical analysis of the composition of the oyster organic adhesive is required to enable comparison with non-mineralised adhesives such as that of Balanidae. This would not only provide a conclusive account of the cementation strategy but would also further inform of the proteins involved in inhibiting and enabling calcification. Furthermore, the possible role of microbes in oyster cementation should be considered possibly through extraction and sequencing of DNA and RNA from the organic component.

5.4 Summary

Cementation of oysters (*C. gigas*) is a two stage process involving biological and inorganic processes which are summarised in Figure 85. Following initial settlement (as described by Cranfield 1973a, b, c, 1974, 1975), oysters secrete an organic adhesive to the outer surface of the periostracum and substrate surface. It is likely that this secretion comes via the glands of the mantle, however further work is required to identify suitable glands in the oyster mantle. This organic film acts to smooth the substrate bringing shell and substrate close enough for initial adhesion to arise. In addition, the organic glue provides a stable substrate in an ideal environment for precipitation from seawater to occur (Figure 85a & b). Crystallisation begins soon after secretion of the organic glue and continues inorganically as the oyster grows, forming a thick, high Mg calcite cement (Figure 85c-f). Oysters do not control or secrete the crystalline cement as previously thought. Instead, oysters secrete an organic film onto which crystals precipitate at random from seawater. Crystallisation of the organic glue would increase the strength and shear resistance of the adhesive, much in the same way as aggregate is added to synthetic cements to increase durability. It is possible that oysters and other cementing bivalves, have evolved to deliberately induce inorganic cementation to provide a secure attachment at little metabolic expense. Further work is required to further establish the source and composition of the organic glue.

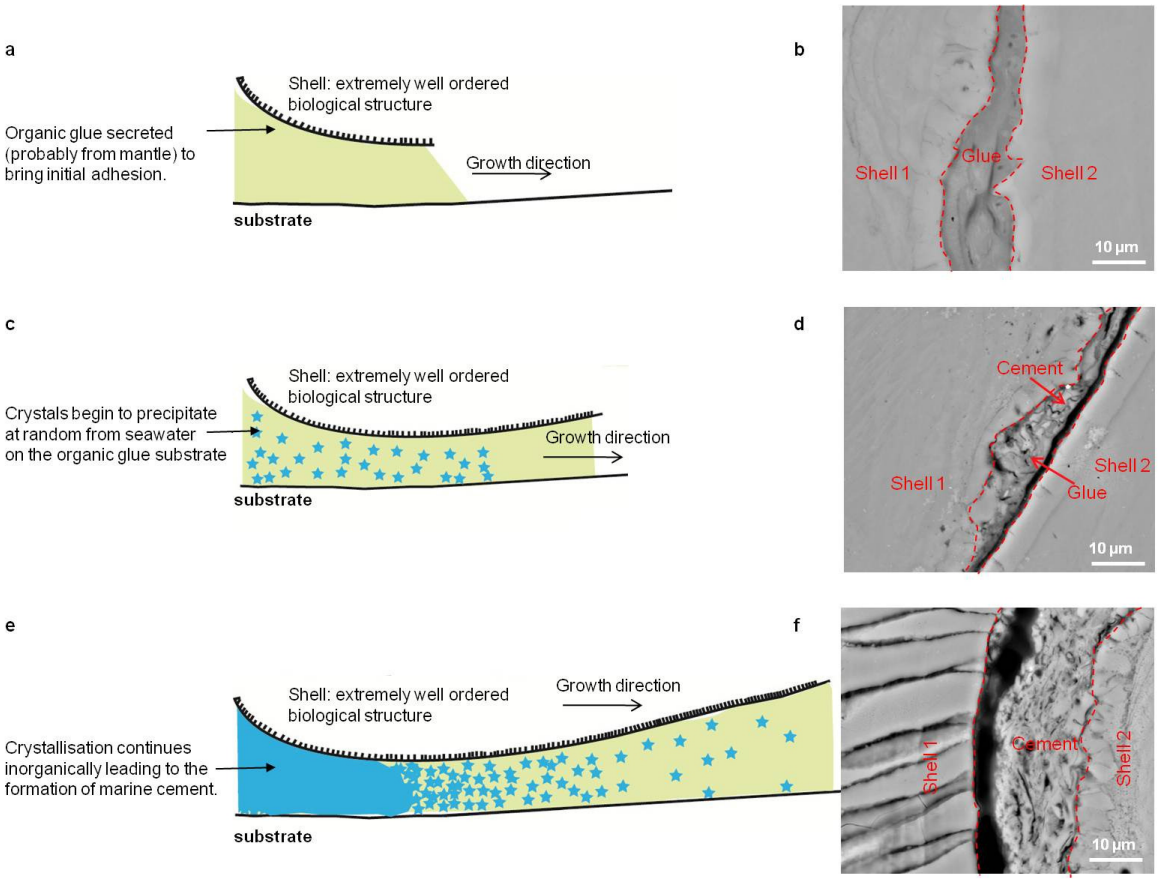

Figure 85. Schematic diagram detailing the biological and inorganic processes leading to cementation in *C. gigas*.
(a) Early stage of settlement during which time organic glue is secreted, probably from the mantle, to initiate adhesion with the substrate. (b) Backscattered electron SEM image revealing details of the contact zone during the early stages of attachment, where the contact is occupied entirely with organic glue. (c) As oyster grows, organic glue continues to be secreted and inorganic precipitation begins on older parts with the appearance of early nucleating crystals. (d) Backscattered electron SEM image revealing details of the contact zone during early cementation. (e) As oyster matures, cementation continues inorganically forming an entirely crystalline cement at oldest parts and causing progressive mineralisation of youngest parts. (f) Backscattered electron SEM image revealing details of the oldest parts of the contact zone in which cementation has resulted in complete mineralisation of the contact and loss of the original organic glue.

Chapter 6. Conclusions and discussion

6.1 Aims of this project

Oysters are amongst the most successful bivalves in terms of distribution and geological longevity and, in particular, *C. gigas* has the ability to adapt to survive in a wide range of environmental conditions (Troost 2010). The adaptability and robust nature of the species make them particularly attractive in terms of stable isotope ($\delta^{18}O$, $\delta^{13}C$) environmental proxies. Understanding oyster shell microstructure and isotopic composition, and the response of shell characteristics to changing environmental conditions, will inform the reliability of oysters as climate proxies and will contribute to our understanding of biomineralisation and biomineral function.

This study was undertaken to characterise the microstructure, crystallography and stable isotope signature of the Pacific oyster, *Crassostrea gigas* from estuarine and marine environments in order to assess the extent to which environment influences shell structure and isotope composition.

Oyster shell structure has been investigated at a macro and micro-structural level through examination of the physical shell attributes and scanning electron microscopy (SEM) imaging. The crystallography of individual shell microstructures has been characterised through electron backscatter diffraction (EBSD), offering new insights to the functional morphology of the shell and its components. This detailed analysis provided a context for subsequent isotopic analysis. The stable isotope composition of the dominant shell microstructures (folia and chalk) was determined by stable isotope mass spectrometry. Isotopic analysis was carried out to inform firstly of the reliability of individual shell components as temperature proxies, and secondly to explore further the isotopic difference between foliated and chalky shell microstructures.

The cemented habit of oysters provides an example of underwater adhesion however the processes and materials involved in oyster cementation have remained largely unclear. This project also investigated the methods by which oysters adhere to hard substrates. A range of SEM techniques, including imaging,

EBSD and energy dispersive spectroscopy (EDS) as well as Raman spectroscopy were carried out to characterise the contact zone between shell and substrate and a new model for the mechanism by which oysters cement has been proposed.

The following chapter summarises the main findings of this study in the context of biomineralisation and explores opportunities for future work. For a complete discussion and summary of the individual components of this study the reader is referred to Chapters 3, 4 and 5.

6.1.1 Crassostrea gigas *samples and environments*

Specimens of *C. gigas* from an estuarine environment were collected from a commercial oyster farm in Loch Fyne and were compared to specimens farmed in a marine environment in Loch Tuath, Island of Ulva. All specimens were grown by tressel and bag techniques and were three years old at the time of collection. Estuarine samples were periodically exposed during low tides and were subject to fluctuating salinity and a wide temperature range. Marine specimens were grown under more stable conditions in terms of salinity, a smaller temperature range and were rarely exposed at low tide.

Samples of cemented pairs of oyster shells were collected from La Baule, France and samples of oysters cemented to rock were collected from Loch Sween, Scotland. These samples allowed analysis of the contact zone between oyster shells and both biological and inorganic substrates, from which interpretation of the attachment mechanism of the oyster were made.

6.2 Shell structure and stable isotope composition of *C. gigas*

Detailed examination of the microstructure, chemistry, crystallography and stable isotope composition of estuarine and marine *C. gigas* is given in Chapters 3 and 4. The effect of environment on these shell characteristics is discussed in both chapters and summarised in section 6.2.1 below.

The oyster shell is composed of two asymmetrical valves both with identical microstructural arrangement and crystallographic orientation, with the exception of the hinge region. The hinge region is complex comprising a thin prismatic ligostracum overlying foliated calcite, which in the right valve is folded to form a rugose texture. Crystallographic orientation and polymorph distributions within the hinge region vary between valves as summarised in Figure 61. Ventral of the hinge region, both valves are composed predominately of low Mg calcite in three forms, prisms, folia and chalk, with aragonite restricted to the myostracum. Despite differences in morphology, the crystallography of each microstructure is the same, with the crystallographic c-axis orientated perpendicular to the outer shell surface. It is considered that this morphological-crystallographic relationship provides the shell with both strength and flexibility providing the optimum protection to the living organism. Indeed, oysters are amongst the most successful bivalves in terms of geological longevity and distribution, which is undoubtedly attributable to their shell structure. Interestingly, Carter (1990) reports the evolutionary history of oysters suggesting a transition from an originally nacreous shell to a predominantly calcitic, foliated structure. This transition, also discussed in Marquez-Aliaga et al. (2005) and Checa et al. (2006), is curious given that nacre is by far the most robust shell structure in terms of tensile strength (Taylor and Layman 1972, Jackson et al. 1988, Checa and Rodríguez-Navarro 2005), whilst folia is by far the weakest (Taylor and Layman 1972). Despite the replacement of nacre with a seemingly weaker alternative, exquisite biological control has maintained an efficient shell with high crack resistance (Taylor and Layman 1972, Lee et al. 2008a). This control facilitates the formation of a shell composed of a series of morphologically distinct layers to provide flexibility, whilst maintaining crystallographic unity throughout to provide strength. Together these properties may promote the crack resistance of the oyster shell.

Oysters also have the ability to alter their shell structure by interrupting the dominant foliated structure with discontinuous lenses of chalky calcite. The transition between these morphologically distinct microstructures may be abrupt, yet the crystallographic orientation remains constant between the two structures. In addition, oxygen isotopic analysis reveals no significant difference in the isotopic composition of folia and chalk, suggesting that the secretion of

chalk is a controlled biological process. Carbon isotope analysis however, suggests that the amount of metabolic carbon incorporated into chalk lenses is less than for folia. Indeed, folia $\delta^{13}C$ patterns show significant interspecimen variation in estuarine samples, suggesting considerable metabolic influence. On the other hand, chalk $\delta^{13}C$ patterns are devoid of interspecimen variation suggesting a common environmental control on $\delta^{13}C$ composition. Many authors have postulated that chalk is formed as a means of providing 'cheap padding', as chalk fills more area per unit volume than an equal volume of folia (Korringa 1951, Galtsoff 1964, Stenzel 1971, Carriker et al. 1980, Lee et al. 2011). This hypothesis is, to a large extent, supported by the apparent reduction in metabolic carbon between folia and chalk. Control of crystallographic orientation however, suggests that the secretion of chalk is a deliberate response to some stimulus. Lee et al. (2011) also consider chalk to be a deliberate and controlled shell secretion. In this study chalk was identified in places overlying the prismatic region at the outer shell surface suggesting oysters have the ability to 'switch' to chalk secretion at any time. This study has also found that estuarine *C. gigas* contains significantly more chalk than marine equivalents. Similarly, Palmer and Carriker (1979) demonstrated that the volume of chalk present in the oyster shell varied between environments. These studies point strongly towards external environmental conditions, possibly salinity or nutrient fluxes, as the main stimulants for chalk secretion.

6.2.1 Effect of environment on shell structure and stable isotope composition

The shell structure and stable isotope composition of estuarine and marine *C. gigas* were compared in order to assess the influence of environment on oyster shell characteristics. Differences between sample sets were predominantly macrostructural with marine samples exhibiting significantly thicker, yet less chalky valves than estuarine samples. In terms of stable isotopes, marine samples exhibited heavier values of both $\delta^{18}O$ and $\delta^{13}C$ than estuarine samples which may be expected given the lack of isotopically light terrestrial material and higher salinity in this environment. Interestingly, in marine samples $\delta^{18}O$ and $\delta^{13}C$ show a strong positive correlation and are devoid of interspecimen variation. In estuarine samples however, $\delta^{18}O$ and $\delta^{13}C$ show no obvious

correlation and $\delta^{13}C$ values show significant interspecimen variation in folia samples.

Oysters are euryhaline bivalves, with wide distribution and long geological history, making them potentially ideal candidates for palaeoenvironmental studies. Until recently however (Ullmann et al. 2010), only estuarine oysters had been rigorously assessed in terms of isotopic equilibrium (Kirby et al. 1998, Surge et al. 2001, 2003). This study has confirmed that estuarine and, to a large extent, marine oysters (*C. gigas*) secrete shells of low Mg-calcite in oxygen isotope equilibrium with the ambient environment. Marine oysters used in this study contained cavities filled with sediment and U-shaped burrows associated with Spionid worm infestation. Oysters isolate irritants by secretion of an organic membrane onto which folia grow thereby containing the irritant. Isotopic analysis suggests that shell layers produced to contain irritants including sediment particles (e.g. Higuera-Ruiz and Elorza 2011) and parasite worms (e.g. Royer et al. 2006), may not be secreted under the same physiological controls as surrounding shell layers and are therefore more likely to have undergone kinetic isotope fractionation during calcification. This study has shown that additional shell material, secreted to isolate irritants, is isotopically light, particularly with respect to $\delta^{18}O$, and so, if incorporated during isotopic analysis, will result in erroneously high estimations of seawater temperature. Similar cavities and larger 'chambers' have been reported from oysters from a range of environments (e.g. Almeida et al. 1998, Higuera-Ruiz and Elorza 2009) and therefore their appearance is not unique to the marine environment. As a caution, oysters containing cavities should be avoided in palaeoenvironmental studies.

Both valves of marine oyster shells contain significantly less chalk, yet are significantly thicker than estuarine equivalents. It is considered that marine oysters may produce thicker shells as a means of protection in response to higher energy conditions and infestation.

6.2.1.1 Appearance of chalky lenses.

This study has shown that the quantity of chalk present is not constant and varies between environments. Specifically, this study has shown that the amount

of chalk present is significantly higher in estuarine than marine oysters. Marine oysters in this study were infested with Spionid worms, which were found to preferentially burrow in chalk lenses. It may be that, when infested, the oyster produces a folia-dominated shell in order to minimise the movement of the worm. Palmer and Carriker (1979) however, show a variation in chalk volume in oysters grown in different environments where natural estuarine systems and 'flow-through cultural systems' produce more chalk than 'recycle cultural systems'. This suggests that environmental conditions may be the main determinant in chalk formation. Additionally, in this current study both estuarine and marine samples of chalk exhibited a greater range in $\delta^{18}O$ values than folia, yet most chalk $\delta^{18}O$ values still lay within the bounds of equilibrium with the ambient water. This pattern strongly suggests that chalk is secreted over a greater range of environmental conditions than folia. Secretion of folia may require more specific environmental conditions and considerable metabolic input. Deviation from these optimum environmental conditions is likely to result in chalk deposition. Environmental conditions have long been recognised as influential factors in biomineralisation (e.g. Lowenstam and Weiner 1989). For example, changes in water temperature have been reported to affect the amount of mineral deposited, polymorph type and skeletal growth rate (Lowenstam and Weiner 1989 and references therein). Results of this study suggest that environmental conditions, probably increased salinity fluctuation and/or nutrient influxes from terrestrial runoff in the estuarine environment, may induce chalk formation. Indeed, increased shell porosity in response to changes in salinity and nutrient levels have been reported for some species of foraminifera (Bijima et al. 1990) and the clam *Tridacna gigas* respectively (Belda et al. 1993).

The biomineralisation regime of the oyster enables the formation of a shell with high crack resistance that is metabolically efficient in its production and adaptable to changing environmental conditions. These traits have presumably enhanced and catalysed the expansion and diversification of the order Ostreidae since the Triassic.

6.3 Attachment mechanism of oysters

Oysters live permanently attached by cementation of the left valve to a hard substrate (e.g. Yonge 1960, Harper 1992, 1997). This study has examined the contact zone between oyster shells and inorganic (rock) and biological (other oyster shell) substrates and a new model for oyster cementation has been proposed (Chapter 5). This study has shown that oyster cementation is a two-stage process involving both organic and inorganic processes. Oysters initially adhere by secretion of an organic substance, probably from glands of the mantle, which induces subsequent cementation by inorganic precipitation from seawater. The morphology and chemistry of the resulting cement confirms that cementation is occurring without the biological control of the organism. Indeed, the high Mg-calcite composition of the cement is likely to be a function of prevailing environmental conditions and the mineralogy of the cement may change at different latitudes and temperatures. For example, aragonite cements are more likely to be precipitated in warmer waters than calcite (e.g Burton and Walter 1987). Oyster cementation is therefore an example of biologically induced mineralisation, rather than biologically controlled mineralisation which is responsible for shell formation (Lowenstam and Weiner 1989). Biologically induced mineralisation is widely reported in the marine environment in the formation of stromatolites (e.g. Pope et al. 2000), and beach-rocks (e.g. Webb et al. 1999). Interestingly, biologically induced and biologically controlled mineralisation processes are often closely associated. For example, Lowenstam et al. (1984) described the formation of the Nautilus shell as involving both biologically induced and organic matrix mediated mineralisation as well as intermediary processes. Most biologically induced mineral structures are associated with microbial action where crystallisation occurs as a by-product of respiration. This process has attracted much attention recently in the stabilisation and remediation of building stones (e.g. Rodriguez-Navarro et al. 2003) and cement-based materials (e.g. Qian et al. 2010) and in the prevention of pollutant migration in aquifers (e.g. Mitchell and Ferris 2006). The possible involvement of microbes in oyster cementation should be considered in future studies.

The close association of organic and inorganic processes in mineralisation are often overlooked and this study has demonstrated that uncontrolled inorganic crystallisation is responsible for cementation in oysters. Yonge (1979) considered that a single method of cementation may be present in all cementing bivalves. Certainly organic and partly mineralised attachments, similar to those reported in this study have been reported for other cementing bivalves including *M. anomoides* (Harper and Morton 2000) and *C. albidus* (Morton and Harper 2001). Inorganic cementation has also been identified in the infaunal bivalves *Granicorium* and *Samarangia* in the attachment of sand grains to the outer shell surface (Braithwaite et al. 2000). It is possible that biologically induced cementation is common to most cementing bivalve forms, however further investigation would be required to verify this hypothesis.

6.4 Future work

6.4.1 Shell structure and stable isotope composition

The oyster shell is a composite biomineral structure composed predominantly of low Mg-calcite in three forms; prisms, folia and chalk. This study provides evidence that the appearance of chalk may be a function of external environmental conditions. Future work should examine oysters from a wider range of environments, including those from deeper waters (8-10 m), and which are free of Spionid worm infestation, to asses further the relationship between chalk appearance and environment.

This study confirms that both folia and chalk from estuarine and marine oysters are secreted largely in isotopic equilibrium with the ambient environment. Future isotope studies of oyster shells should include a detailed study of the isotopic composition of seawater at the sample site, specifically the $\delta^{13}C$ composition of the dissolved inorganic carbon pool. This would enable a more detailed assessment of the quantity of metabolic carbon incorporated in individual shell layers.

A comprehensive biochemical and proteomic study of the organic matrix of all calcite microstructures, prisms, folia and chalk, and the hinge region structures

as well as the organic walls surrounding cavities would provide further insights into the unique biomineralisation system of the oyster.

6.4.2 Cementation of bivalves

This study has provided evidence that oysters achieve cementation via a two stage process involving both organic and inorganic methods. Stable carbon and oxygen isotope analysis of the crystalline cement of the contact zone could provide conclusive analysis of the inorganic source of the cement. Such analysis could not be achieved in this study as the quantity of cement present was too small to be accurately sampled by the micro-milling technique available. Stable isotope examination of the cement by ion microprobe analysis would enable confirmation of the source of the cement. Examination of cements associated with oysters from warm water environments could identify differences in the chemical composition of the cement and could inform further the control that the environment and biological processes has on cement formation.

This study has confirmed the involvement of organic adhesives in oyster cementation. Biochemical analysis of the organic glue is required to provide a conclusive understanding of the cementation process. This would also enable comparisons to be made with other organic adhesives such as the byssal thread of the mussel and organic glue of the barnacle. Such comparison would inform the biochemical constituents responsible for facilitating cementation which would have implications for biomineralisation research and in the study of marine adhesives with respect to synthetic replicas. The possible role of microbial action in cementation could be examined via RNA and DNA analysis of the organic glue. The source of the organic glue also needs to be identified. Detailed examination of the mantle of the adult oyster may identify glands involved in the attachment process.

Yonge (1979) considered that most cementing bivalves cement by a common method. Widescale investigation of the contact zone of other cementing species is required to validate this hypothesis.

Appendix A

A.1 List of samples and valve dimensions

Sample	Environment	Analysis	Shell Dimensions						
			Right Valve				Left Valve		
			Height (cm)	Length (cm)	Width (cm)	Shell Thickness Index	Height (cm)	Length (cm)	Width (cm)
F1	Estuarine - Loch Fyne	Optical microscopy & Image J	8.5	4.1	0.4	21.25	10.1	4.7	0.5
F2	Estuarine - Loch Fyne	Optical microscopy & Image J	7.7	4.2	0.4	19.25	9.1	4.8	0.2
F3	Estuarine - Loch Fyne	Optical microscopy & Image J	8.1	4.1	0.5	16.20	9.1	4.8	0.3
F4	Estuarine - Loch Fyne	SEM imaging of fracture sections	8.1	3.8	0.4	20.25	9.4	4.3	0.8
F5	Estuarine - Loch Fyne	SEM imaging of fracture sections with resin coat	6	3.4	0.4	15.00	7.4	3.6	0.7
F6	Estuarine - Loch Fyne	Left valve - EDS chemical analysis Right valve - EBSD crystallographic analysis	6.4	3.2	0.3	21.33	7.8	3.7	0.4
F7	Estuarine - Loch Fyne	SEM imaging of hinge fracture	7.3	4.8	0.5	14.60	9.3	6.3	0.5
F8	Estuarine - Loch Fyne	Isotopic analysis	7.9	4.8	0.3	26.33	9.9	6.1	0.3
F9	Estuarine - Loch Fyne	Isotopic analysis	7.9	4.2	0.2	39.50	9.3	4.8	0.3

F10	Estuarine - Loch Fyne	Isotopic analysis	8.6	4.6	0.2	43.00	10.6	5.7	0.5
F11	Estuarine - Loch Fyne	SEM imaging of hinge fracture section - partially decalcified with 10% acetic acid.	6.9	3.2	0.3	23.00	8.7	4	0.3
F12	Estuarine - Loch Fyne	SEM imaging of hinge fracture section - treated with 10% NaClO.	6.7	2.9	0.2	33.50	8.6	3.8	0.3
F13	Estuarine - Loch Fyne	EBSD of structural components of hinge	5.3	3.2	0.2	26.50	6.7	3.6	0.3
U1	Marine - Loch Tuath	Optical microscopy & Image J	8.4	5.3	0.5	16.80	8.7	5.5	1.1
U2	Marine - Loch Tuath	Optical microscopy & Image J	8.9	6.7	0.4	22.25	9.4	5.1	0.6
U3	Marine - Loch Tuath	Optical microscopy & Image J. Left valve treated with Mutvei solution for growth line analysis	7.4	4.3	0.5	14.80	7.5	4.2	0.6
U4	Marine - Loch Tuath	SEM imaging of fracture sections	7.9	4.2	0.4	19.75	9.1	5.1	0.7
U5	Marine - Loch Tuath	SEM imaging of fracture sections	6.5	3.7	1.1	5.91	7.2	4.5	1.1
U6	Marine - Loch Tuath	EDS Chemical analysis	7	4.2	0.6	11.67	8.6	4.4	0.8
U7	Marine - Loch Tuath	SEM imaging of fracture sections	6	4.5	0.7	8.57	6.5	3.3	0.8
U8	Marine - Loch Tuath	Isotopic analysis	7.2	4.3	0.6	12.00	9	5.7	0.7
U9	Marine - Loch Tuath	Isotopic analysis	9.4	4.4	0.3	31.33	10.5	6.6	0.5
U10	Marine - Loch Tuath	Isotopic analysis	8.6	3.7	0.6	14.33	9.8	4.3	0.9

A.2 Cemented Samples

Cemented Samples			
Sample	**Location**	**Description**	**Analysis**
AL1	La Baule, NW France	Two oysters attached laterally. Shell 2 is attached on the anterior side of the left valve to the posterior side of the left valve of shell 1. Valves are fused tightly along margins from dorsal-ventral.	SEM imaging
AV1	La Baule, NW France	Two oysters attached vertically. The upper oyster (shell 2) is cemented by the outer surface of the left valve to the outer surface of the right valve of the lower oyster (shell 1). Oysters are tightly fused. Shell 2 is cemented from the dorsal margin, ventral until 0.5 cm ventral of the adductor muscle scar where connection with shell 1 is lost.	SEM imaging of fracture surfaces. Chemical & crystallographic analysis of resin block by EDS & EBSD respectively.
AL2	La Baule, NW France	Two oysters attached laterally. Shell 2 is attached on the anterior side of the left valve to the posterior side of the left valve of shell 1. Valves are fused tightly along margins from dorsal-ventral.	Crystallographic & chemical analysis by EBSD & EDS respectively.
RA1	Loch Sween, Scotland	Single oyster cemented to rock substrate. Left valve is cemented on the outer surface to lithic greywacke rock. Oyster is tightly cemented from dorsal margin ventral approximately 3 cm. Ventral of this connection with substrate is lost.	SEM imaging of fracture surfaces. Chemical & crystallographic analysis of resin block by EDS & EBSD respectively.
RA2	Loch Sween, Scotland	Single oyster cemented to rock substrate. Left valve is cemented on the outer surface to lithic greywacke rock. Oyster is tightly cemented from dorsal margin ventral approximately 3 cm. Ventral of this connection with substrate is lost. Tube worms are cemented around the contact zone	Quantitative chemical analysis by EDS. Raman spectroscopic analysis

Appendix B Energy dispersive spectroscopic (EDS) standardised analysis: List of standards

Element	Standard		Detection Limit weight %
Calcium	Calcite	$CaCO_3$	0.11 ± 0.28
Oxygen	Calcite	$CaCO_3$	0.42 ± 1.20
Carbon	Calculated by stoichiometry		
Sulphur	Pyrite	FeS_2	0.07 ± 0.14
Sodium	Jadite	$NaAlSi_2O_6$	0.08 ± 0.75
Iron	Pyrite	FeS_2	0.27 ± 0.71
Silica	Jadite	$NaAlSi_2O_6$	0.06 ± 0.26
Magnesium	Periclase	MgO	0.06 ± 0.09
Aluminium	Jadite	$NaAlSi_2O_6$	0.06 ± 0.56
Manganese	Rhodonite	$MnSiO_3$	0.27 ± 0.82
Strontium	Celestite	$SrSO_4$	0.12 ± 0.25

Appendix C Stable isotope results

Environment	Sample	Microstructure	Section	Sample number	$\delta^{13}C$ VPDB (‰)	$\delta^{18}O$ VPDB (‰)	$\delta^{18}O$ SMOW (‰)
Standard	mab2c,1.037				2.37	-2.49	28.35
Standard	mab2c,0.917				2.45	-2.35	28.48
Estuarine: Loch Fyne	F8	Chalk	Hinge	1	-0.98	-0.13	30.78
	F8	Chalk	Hinge	2	-0.95	-0.11	30.79
	F8	Chalk	A	1	-0.96	0.38	31.30
	F8	Chalk	A	2	-0.91	0.24	31.16
	F8	Chalk	A	3	-0.93	0.39	31.32
	F8	Chalk	B	1	-0.65	-0.73	30.16
	F8	Chalk	B	2	-0.74	-1.08	29.79
	F8	Chalk	B	3	-0.84	-0.64	30.25
	F8	Chalk	C	1	-0.68	-1.84	29.01
	F8	Chalk	C	2	-0.60	-2.07	28.78
	F8	Chalk	C	3	-0.63	-2.28	28.56
Standard	MAB				2.47	-2.34	28.50
Standard	MAB				2.46	-2.41	28.43
Standard	MAB				2.48	-2.33	28.50
Estuarine: Loch Fyne	F8	Folia	Hinge	1	-0.91	-1.91	28.94
	F8	Folia	Hinge	2	-0.92	-1.53	29.33
	F8	Folia	Hinge	3	-1.29	-1.03	29.85
	F8	Folia	A	1	-0.21	-0.78	30.11
	F8	Folia	A	2	-0.09	-0.73	30.15

Estuarine: Loch Fyne	F8	Folia	A	3	-0.34	-0.33	30.57
	F8	Folia	B	1	-0.61	-0.68	30.21
	F8	Folia	B	2	-0.67	-0.79	30.10
	F8	Folia	B	3	-0.73	-1.13	29.74
	F8	Folia	C	1	-0.11	-1.61	29.25
	F8	Folia	C	2	-0.27	-1.38	29.48
	F8	Folia	C	3	-0.07	-1.32	29.54
Standard	MAB				2.51	-2.46	28.37
Standard	MAB				2.52	-2.43	28.40
Estuarine: Loch Fyne	F9	Chalk	Hinge	1	-0.14	-2.16	28.69
	F9	Chalk	Hinge	2	-0.29	-1.93	28.93
	F9	Chalk	Hinge	3	-0.28	-2.03	28.82
	F9	Chalk	A	1	-0.63	-1.55	29.31
	F9	Chalk	A	2	-0.66	-1.02	29.86
	F9	Chalk	A	3	-0.71	-0.72	30.17
	F9	Chalk	B	1	-0.80	-0.65	30.24
	F9	Chalk	B	2	-0.71	-0.63	30.26
	F9	Chalk	B	3	-0.67	-0.49	30.41
	F9	Chalk	C	1	-0.84	-0.57	30.32
	F9	Chalk	C	2	-1.04	-0.93	29.95
	F9	Chalk	C	3	-1.11	-0.86	30.02
Standard	MAB				2.47	-2.46	28.37
Standard	MAB				2.48	-2.41	28.43
Estuarine: Loch Fyne	F9	Folia	Hinge	1	-0.55	-1.15	29.72
	F9	Folia	Hinge	2	-0.87	-1.12	29.75
	F9	Folia	Hinge	3	-0.94	-1.03	29.85

	F9	Folia	A	1	-0.95	-0.75	30.14
Estuarine: Loch Fyne	F9	Folia	A	2	-0.90	-0.91	29.97
	F9	Folia	A	3	-0.87	-0.77	30.12
	F9	Folia	B	1	-0.77	-0.86	30.02
	F9	Folia	B	2	-0.65	-0.52	30.38
	F9	Folia	B	3	-0.87	-0.91	29.97
	F9	Folia	C	1	-0.92	-1.42	29.44
	F9	Folia	C	2	-1.04	-1.63	29.23
	F9	Folia	C	3	-0.94	-1.39	29.47
Standard	MAB				2.47	-2.34	28.50
Standard	MAB				2.46	-2.41	28.43
Estuarine: Loch Fyne	F10	Chalk	Hinge	1	-1.02	-1.48	29.38
	F10	Chalk	Hinge	2	-1.03	-1.30	29.57
	F10	Chalk	Hinge	3	-1.00	-1.40	29.46
	F10	Chalk	A	1	-0.70	-1.03	29.85
	F10	Chalk	A	2	-0.69	-0.92	29.96
	F10	Chalk	A	3	-0.64	-1.19	29.69
	F10	Chalk	B	1	-0.41	-0.89	29.99
	F10	Chalk	B	2	-0.37	-0.70	30.19
	F10	Chalk	B	3	-0.40	-0.87	30.01
	F10	Chalk	C	1	0.36	-0.92	29.96
	F10	Chalk	C	2	0.05	-0.56	30.33
Standard	MAB				2.37	-2.49	28.35
Standard	MAB				2.52	-2.43	28.40
Estuarine: Loch Fyne	F10	Folia	Hinge	1	-0.92	-1.00	29.88
	F10	Folia	Hinge	2	-0.74	-0.77	30.11

	F10	Folia	A	1	-0.79	-1.22	29.66
	F10	Folia	A	2	-0.50	-0.89	29.99
Estuarine: Loch Fyne	F10	Folia	A	3	-0.67	-1.15	29.72
	F10	Folia	B	1	-0.09	-0.86	30.02
	F10	Folia	B	2	-0.17	-0.90	29.98
	F10	Folia	B	3	-0.30	-0.82	30.06
	F10	Folia	C	1	-0.44	-0.49	30.41
	F10	Folia	C	2	-0.33	-0.48	30.41
	F10	Folia	C	3	-0.27	-0.54	30.35
standard	MAB				2.41	-2.40	28.43
standard	MAB				2.45	-2.55	28.28
Marine: Loch Tuath	U8	Chalk	Hinge	1	0.16	-0.48	30.42
	U8	Chalk	Hinge	2	-0.69	-1.12	29.76
	U8	Chalk	Hinge	3	-0.15	0.01	30.92
	U8	Chalk	A	1	-0.11	0.60	31.53
	U8	Chalk	A	2	-0.19	0.07	30.98
	U8	Chalk	A	3	-0.16	0.26	31.18
	U8	Chalk	B	1	-0.36	-0.53	30.37
	U8	Chalk	B	2	-0.41	-0.16	30.74
	U8	Chalk	B	3	-0.61	-0.23	30.67
	U8	Chalk	C	1	0.14	-0.06	30.84
	U8	Chalk	C	2	-0.17	0.04	30.96
	U8	Chalk	C	3	0.17	0.06	30.98
standard	MAB				2.45	-2.47	28.36
standard	MAB				2.55	-2.37	28.47
Marine: Loch Tuath	U8	Folia	Hinge	1	-0.58	-1.44	29.42
	U8	Folia	Hinge	2	0.09	0.65	31.58

	U8	Folia	Hinge	3	-0.26	0.14	31.05
	U8	Folia	A	1	-1.13	-0.19	30.72
Marine: Loch Tuath	U8	Folia	A	2	-1.17	-0.85	30.04
	U8	Folia	A	3	-0.51	-0.84	30.04
	U8	Folia	B	1	0.22	0.45	31.37
	U8	Folia	B	2	0.32	-0.21	30.69
	U8	Folia	B	3	0.05	-0.06	30.84
	U8	Folia	C	1	0.19	0.00	30.91
	U8	Folia	C	2	0.40	0.64	31.57
	U8	Folia	C	3	-0.12	0.34	31.26
standard	MAB				2.41	-2.44	28.40
standard	MAB				2.47	-2.46	28.38
Marine: Loch Tuath	U9	Chalk	Hinge	1	-0.52	-0.69	30.20
	U9	Chalk	Hinge	2	-0.25	-0.40	30.49
	U9	Chalk	Hinge	3	-0.22	-0.75	30.13
	U9	Chalk	A	1	0.65	-0.13	30.78
	U9	Chalk	A	2	-0.60	-2.79	28.04
	U9	Chalk	A	3	0.47	-0.31	30.59
	U9	Chalk	B	1	0.50	0.13	31.05
	U9	Chalk	B	2	0.40	0.00	30.91
	U9	Chalk	B	3	0.18	-0.04	30.87
	U9	Chalk	C	1	0.42	0.20	31.12
	U9	Chalk	C	2	-0.27	-0.43	30.46
	U9	Chalk	C	3	0.12	0.91	31.85
standard	MAB				2.58	-2.32	28.52
standard	MAB				2.60	-2.15	28.69
Marine: Loch	U9	Folia	Hinge	1	0.20	0.30	31.22

Tuath	U9	Folia	Hinge	2	-0.01	0.12	31.04
	U9	Folia	Hinge	3	0.03	0.46	31.38
Marine: Loch Tuath	U9	Folia	A	1	0.15	0.48	31.40
	U9	Folia	A	2	0.07	0.54	31.46
	U9	Folia	A	3	0.28	0.56	31.48
	U9	Folia	B	1	-0.24	-0.07	30.84
	U9	Folia	B	2	-0.06	-0.36	30.54
	U9	Folia	B	3	-0.25	-0.25	30.65
	U9	Folia	C	1	-1.02	-2.80	28.02
	U9	Folia	C	2	0.32	0.53	31.46
	U9	Folia	C	3	0.05	0.39	31.31
standard	MAB				2.50	-2.18	28.66
standard	MAB				2.50	-2.53	28.31
Marine: Loch Tuath	U10	Chalk	Hinge	1	-1.21	-1.51	29.35
	U10	Chalk	Hinge	2	-0.53	-1.01	29.87
	U10	Chalk	Hinge	3	-0.75	-0.99	29.88
	U10	Chalk	A	1	0.33	0.70	31.64
	U10	Chalk	A	2	0.30	0.74	31.67
	U10	Chalk	A	3	0.26	0.96	31.90
	U10	Chalk	B	1	0.41	1.46	32.41
	U10	Chalk	B	2	0.46	1.31	32.26
	U10	Chalk	B	3	0.04	-0.04	30.87
	U10	Chalk	C	1	-0.03	-0.22	30.68
	U10	Chalk	C	2	-0.60	-2.79	28.04
	U10	Chalk	C	3	0.48	0.31	31.23
standard	MAB				2.59	-2.32	28.51
standard	MAB				2.55	-2.37	28.47

Marine: Loch Tuath	U10	Folia	Hinge	1	-0.92	-1.20	29.68
	U10	Folia	Hinge	2	-1.06	-0.87	30.01
	U10	Folia	Hinge	3	-0.46	-0.20	30.70
Marine: Loch Tuath	U10	Folia	A	1	-0.15	-0.02	30.89
	U10	Folia	A	2	-0.32	0.04	30.95
	U10	Folia	A	3	0.18	0.52	31.45
	U10	Folia	B	1	-1.54	-0.90	29.98
	U10	Folia	B	2	0.26	0.16	31.07
	U10	Folia	B	3	-0.30	-0.42	30.47
	U10	Folia	C	1	-0.30	-0.26	30.64
	U10	Folia	C	2	-0.51	-0.53	30.37
	U10	Folia	C	3	-0.15	-0.12	30.79
standard	MAB				2.41	-2.44	28.40
standard	MAB				2.50	-2.18	28.66

List of References

Addadi, L., Joester, D., Nudelman, F. & Weiner, S. 2006. Mollusk shell formation: A source of new concepts for understanding biomineralization processes. Chemistry – A European Journal, 12, 980.

Aharon, P. 1991. Recorders of reef environment histories: stable isotopes in corals, giant clams, and calcareous algae. Coral Reefs, 10, 71.

Alam, M. N., Blackman, M. & Pashley, D. W. 1954. High-angle kikuchi patterns. Proceedings of the Royal Society of London Series a-Mathematical and Physical Sciences, 221, 224.

Almeida, M. J., Machado, J., Moura, G., Azevedo, M. & Coimbra, J. 1998. Temporal and local variations in biochemical composition of *Crassostrea gigas* shells. Journal of Sea Research, 40, 233.

Almeida, M. J., Moura, G., Machado, J., Coimbra, J., Vilarinho, L., Ribeiro, C. & Soares-da-Silva, P. 1996. Amino acid and metal content of *Crassostrea gigas* shell infested by *Polydora sp*. in the prismatic layer insoluble matrix and blister membrane. Aquatic Living Resources, 9, 179.

Alzieu, C. L., Sanjuan, J., Deltreil, J. P. & Borel, M. 1986. Tin contamination in Arcachon Bay: Effects on oyster shell anomalies. Marine Pollution Bulletin, 17, 494.

Anderson, T. F. & Arthur, M. A. 1983. Stable isotopes of oxygen and carbon and their application to sedimentologic and paleoenvironmental problems. *In:* Arthur, M. A., Anderson, T. F., Kaplan, I. R., Veizer, J. & Land, L. S. (eds.) *Stable Isotopes in Sedimentary Geology, SEPM Short Course Notes.* Society of Economic Paleontologists and Mineralologists, Tulsa, Oklahoma.

Andrus, C. F. T. & Crowe, D. E. 2000. Geochemical analysis of *Crassostrea virginica* as a method to determine season of capture. Journal of Archaeological Science, 27, 33.

Auclair, A. C., Joachimski, M. M. & Lécuyer, C. 2003. Deciphering kinetic, metabolic and environmental controls on stable isotope fractionations between seawater and the shell of *Terebratalia transversa* (Brachiopoda). Chemical Geology, 202, 59.

Austin, W. E. N. & Inall, M. E. 2002. Deep-water renewal in a Scottish fjord: temperature, salinity and oxygen isotopes. Polar Research, 21, 251.

Bathurst, R. G. C. 1975. *Carbonate Cements and their Diagenesis.* Elsevier Scientific Publishing Company.

Beaumont, A., Truebano-Garcia, M., Hönig, S. & Low, P. 2006. Genetics of Scottish populations of the native oyster, *Ostrea edulis*: gene flow, human intervention and conservation. Aquatic Living Resources, 19, 389.

Belda, C. A., Cuff, C. & Yellowlees, D. 1993. Modification of shell formation in the giant clam *Tridacna gigas* at elevated nutrient levels in sea water. Marine Biology, 117, 251.

Beniash, E., Ivanina, A., Lieb, N. S., Kurochkin, I. & Sokolova, I. M. 2010. Elevated level of carbon dioxide affects metabolism and shell formation in oysters *Crassostrea virginica*. Marine Ecology Progress Series, 419, 95.

Bernard, S., Beyssac, O. & Benzerara, K. 2008. Raman mapping using advanced line-scanning systems: Geological applications. Applied Spectroscopy, 62, 1180.

Bijima, J., Faber, W. W. J. & Hemleben, C. 1990. Temperature and salinity limits for growth and survival of some planktonic foraminifers in laboratory cultures. Journal of Foraminiferal Research, 20, 95.

Bischoff, W. D., Bishop, F. C. & Mackenzie, F. T. 1983. Biogenically produced magnesian calcite inhomogeneities in chemical and physical - properties comparison with synthetic phases. American Mineralogist, 68, 1183.

Bischoff, W. D., Sharma, S. K. & Mackenzie, F. T. 1985. Carbonate ion disorder in synthetic and biogenic magnesian calcites - A Raman spectral study. American Mineralogist, 70, 581.

Bogan, A. & Bouchet, P. 1998. Cementation in the freshwater bivalve family Corbiculidae (Mollusca : Bivalvia): a new genus and species from Lake Poso, Indonesia. Hydrobiologia, 389, 131.

Bøggild, O. B. 1930. The shell structure of the mollusks. Kgl Danske Vidensk Selbsk Skrifter, Naturvidensk Math, 2, 235.

Braithwaite, C. J. R., Taylor, J. D. & Glover, E. A. 2000. Marine carbonate cements, biofilms, biomineralization, and skeletogenesis: Some bivalves do it all. Journal of Sedimentary Research, 70, 1129.

Brand, U., Logan, A., Hiller, N. & Richardson, J. 2003. Geochemistry of modern brachiopods: applications and implications for oceanography and paleoceanography. Chemical Geology, 198, 305.

Brigaud, B., Puceat, E., Pellenard, P., Vincent, B. & Joachimski, M. M. 2008. Climatic fluctuations and seasonality during the Late Jurassic (Oxfordian-Early Kimmeridgian) inferred from $\delta 18O$ of Paris Basin oyster shells. Earth and Planetary Science Letters, 273, 58.

Bromley, R. G. & Heinberg, C. 2006. Attachment strategies of organisms on hard substrates: A palaeontological view. Palaeogeography, Palaeoclimatology, Palaeoecology, 232, 429.

Bruet, F. J. B., Qi, J. H., Boyce, C. M., Panas, R., Tai, K., Frick, L. & Ortiz, C. 2005. Nanoscale morphology and indentation of individual nacre tablets from the gastropod mollusc *Trochus Niloticus*. Journal of Materials Research, 20, 2400.

Burkett, J. R., Hight, L. M., Kenny, P. & Wilker, J. J. 2010. Oysters produce an organic-inorganic adhesive for intertidal reef construction. Journal of the American Chemical Society, 132, 12531.

Burton, E. A. & Walter, L. M. 1987. Relative precipitation rates of aragonite and Mg calcite from seawater: Temperature or carbonate ion control? Geology, 15, 111.

Butler, P. G., Wanamaker, A. D. J., Scoursea, J. D., Richardson, C. A. & Reynolds, D. J. 2011. Long-term stability of δ13C with respect to biological age in the aragonite shell of mature specimens of the bivalve mollusk *Arctica islandica*. Palaeogeography, Palaeoclimatology, Palaeoecology, 302, 21.

Carpenter, S. J. & Lohmann, K. C. 1995. δ18O and δ13C values of modern brachiopod shells. Geochimica et Cosmochimica Acta, 59, 3749.

Carriker, M. R. & Palmer, R. E. 1979. A new mineralized layer in the hinge of the oyster. Science, 206, 691.

Carriker, M. R., Palmer, R. E. & Prezant, R. S. 1980. Functional ultra morphology of the dissoconch valves of the oyster C*rassostrea virginica*. Proceedings National Shellfisheries Association, 70, 139.

Carriker, M. R., Swann, C. P., Prezant, R. S. & Counts, C. L. 1991. Chemical elements in the aragonitic and calcitic microstructural groups of the oyster *Crassostrea virginica* - A proton probe study. Marine Biology, 109, 287.

Carter, J. G. 1990. Shell microstructural data for the bivalvia Part 1. Introduction. *Skeletal Biomineralization: Patterns, Processes and Evolutionary Trends.* Van Nostrand & Reinhold, New York.

Carter, J. G., Barrera, E. & Tevesz, M. J. S. 1998. Thermal potentiation and mineralogical evolution in the Bivalvia (Mollusca). Journal of Paleontology, 72, 991.

Chacko, T., Cole, D. R. & Horita, J. 2001. Equilibrium oxygen, hydrogen and carbon isotope fractionation factors applicable to geologic systems. Reviews in Mineralogy & Geochemistry, 43, 1.

Chambon, C., Legeay, A., Durrieu, G., Gonzalez, P., Ciret, P. & Massabuau, J. 2007. Influence of the parasite worm *Polydora sp*. on the behaviour of the oyster *Crassostrea*

gigas: A study of the respiratory impact and associated oxidative stress. Marine Biology, 152, 329.

Chauvaud, L., Lorrain, A., Dunbar, R. B., Paulet, Y. M., Thouzeau, G., Jean, F., Guarini, J. M. & Mucciarone, D. 2005. Shell of the Great Scallop *Pecten maximus* as a high-frequency archive of paleoenvironmental changes. Geochemistry Geophysics Geosystems, 6, Q08001.

Checa, A. G., Esteban-Delgado, F. J., Ramirez-Rico, J. & Rodríguez-Navarro, A. B. 2009. Crystallographic reorganization of the calcitic prismatic layer of oysters. Journal of Structural Biology, 167, 261.

Checa, A. G., Esteban-Delgado, F. J. & Rodríguez-Navarro, A. B. 2007a. Crystallographic structure of the foliated calcite of bivalves. Journal of Structural Biology, 157, 393.

Checa, A. G. & Jimenez-Jimenez, A. P. 2003. Rib fabrication in Ostreoidea and Plicatuloidea (Bivalvia, Pteriomorphia) and its evolutionary significance. Zoomorphology, 122, 145.

Checa, A. G., Jimenez-Jimenez, A. P., Marquez-Aliaga, A. & Hagdorn, H. 2006. Further comments on the origin of oysters. Palaeogeography Palaeoclimatology Palaeoecology, 240, 672.

Checa, A. G., Jiménez-López, C., Rodríguez-Navarro, A. & Machado, J. 2007b. Precipitation of aragonite by calcitic bivalves in Mg-enriched marine waters. Marine Biology, 150, 819.

Checa, A. G. & Rodríguez-Navarro, A. B. 2005. Self-organisation of nacre in the shells of Pterioida (Bivalvia: Mollusca). Biomaterials, 26, 1071.

Checa, A. G., Rodríguez-Navarro, A. B. & Esteban-Delgado, F. J. 2005. The nature and formation of calcitic columnar prismatic shell layers in pteriomorphian bivalves. Biomaterials, 26, 6404.

Clarke, G. M. & Cooke, D. 2004. *A Basic Course in Statistics.* Oxford University Press. New York.

Coe, W. R. 1932. Season of attachment and rate of growth of sedentary marine organisms at the pier of the Scripps Institution of Oceanography, La Jolla, California. Bulletin of the Scripps Institution of Oceanography.

Cognie, B., Haure, J. & Barillé, L. 2006. Spatial distribution in a temperate coastal ecosystem of the wild stock of the farmed oyster *Crassostrea gigas* (Thunberg). Aquaculture, 259, 249.

Cohn, M. & Urey, H. C. 1938. Oxygen exchange reactions of organic compounds and water. Journal of the American Chemical Society, 60, 679.

Cölfen, H. & Mann, S. 2003. Higher-order organization by mesoscale self-assembly and transformation of hybrid nanostructures. Angewandte Chemie-international Edition, 42, 2350.

Craig, H. 1957. Isotopic standards for carbon and oxygen and correction factors for mass spectrometric analysis of carbon dioxide. Geochimica et Cosmochimica Acta, 12, 133.

Cranfield, H. J. 1973a. Observations on function of glands of foot of pediveliger of *Ostrea edulis* during settlement. Marine Biology, 22, 211.

Cranfield, H. J. 1973b. Observations on the behaviour of pediveliger of *Ostrea edulis* during attachment and cementing. Marine Biology, 22, 203.

Cranfield, H. J. 1973c. Study of morphology, ultrastructure and histochemistry of foot of pediveliger of *Ostrea edulis*. Marine Biology, 22, 187.

Cranfield, H. J. 1974. Observations on the morphology of the mantle folds of the pediveliger of *Ostrea edulis* and their function during settlement. Journal of the Marine Biological Association of the UK, 54, 1.

Cranfield, H. J. 1975. The ultrastructure and histochemistry of the larval cement of *Ostrea edulis*. Journal of the Marine Biological Association of the UK, 55, 497.

Currey, J. D. 1964. Mechanical aspects of the structure of bone. Journal of Bone and Joint Surgery-British Volume, 46, 356.

Curry, G. B. & Fallick, A. E. 2002. Use of stable oxygen isotope determinations from brachiopod shells in palaeoenvironmental reconstruction. Palaeogeography, Palaeoclimatology, Palaeoecology, 182, 133.

Cusack, M. & Freer, A. 2008. Biomineralisation: Elemental and organic influence in carbonate systems. Chemical Reviews, 108, 4433.

Cusack, M., Parkinson, D., Freer, A., Pérez-Huerta, A., Fallick, A. E. & Curry, G. B. 2008. Oxygen isotope composition in *Modiolus modiolus* aragonite in the context of biological and crystallographic control. Mineral Magazine, 72, 569.

Cusack, M., Pérez-Huerta, A. & Dalbeck, P. 2007. Common crystallographic control in calcite biomineralisation of bivalved shells. CrystEngComm, 9, 1215.

Dahlhoff, E. P. 2004. Biochemical indicators of stress and metabolism: Applications for marine ecological studies. Annual Review of Physiology, 66, 183.

Dalbeck, P. & Cusack, M. 2006. Crystallography (electron backscatter diffraction) and chemistry (electron probe microanalysis) of the avian eggshell. Crystal Growth & Design, 6, 2558.

Dame, R. F. & Allen, D. M. 1996. Between estuaries and the sea. Journal of Experimental Marine Biology and Ecology, 200, 169.

Dauphin, Y. 2002. Structures, organo-mineral compositions and diagenetic changes in biominerals. Current Opinion in Colloid & Interface Science, 7, 133.

Dauphin, Y. 2003. Soluble organic matrices of the calcitic prismatic shell layers of two pteriomorphid bivalves - *Pinna nobilis* and *Pinctada margaritifera*. Journal of Biological Chemistry, 278, 15168.

De Bruyne, N. A. 1962. The action of adhesives. Scientific American, 206, 114.

Diederich, S. 2006. High survival and growth rates of introduced Pacific oysters may cause restrictions on habitat use by native mussels in the Wadden Sea. Journal of Experimental Marine Biology and Ecology, 328, 211.

Dingley, D. J. & Randle, V. 1992. Microtexture determination by electron back-scatter diffraction. Journal of Materials Science, 27, 4545.

Donner, J. & Nord, A. G. 1986. Carbon and oxygen stable isotope values in shells of *Mytilus edulis* and *Modiolus modiolus* from holocene raised beaches at the outer coast of the Varanger Peninsula, North Norway. Palaeogeography, Palaeoclimatology, Palaeoecology, 56, 35.

Dove, P. M. 2010. The Rise of Skeletal Biominerals. ELEMENTS, 6, 37.

Edwards, A. & Sharples, F. 1986. Scottish Sealochs: A catalogue. Scottish Marine Biological Association / Nature Conservancy Council.

Edwards, H. G. M., Villar, S. E. J., Jehlicka, J. & Munshi, T. 2005. FT-Raman spectroscopic study of calcium-rich and magnesium-rich carbonate minerals. Spectrochimica Acta Part A: Molecular and Biomolecular Spectroscopy, 61, 2273.

Elliot, M., DeMenocal, P. B., Linsley, B. K. & Howe, S. S. 2003. Environmental controls on the stable isotopic composition of *Mercenaria mercenaria*: Potential application to paleoenvironmental studies. Geochemistry Geophysics Geosystems, 4, 1.

Eltzholtz, J. R. & Birkedal, H. 2009. Architecture of the biomineralised byssus of the saddle oyster (*Anomia sp*.). Journal of Adhesion, 85, 590.

England, J., Cusack, M., Dalbeck, P. & Pérez-Huerta, A. 2007. Comparison of the crystallographic structure of semi nacre and nacre by electron backscatter diffraction. Crystal Growth & Design, 7, 307.

Epstein, S., Buchsbaum, R., Lowenstam, H. & Urey, H. C. 1951. Carbonate -water isotopic temperature scale. Geological Society of America Bulletin, 62, 417.

Epstein, S., Buchsbaum, R., Lowenstam, H. A. & Urey, H. C. 1953. Revised carbonate-water isotopic temperature scale. Geological Society of America Bulletin, 64, 1315.

Esteban-Delgado, F. J., Harper, E. M., Checa, A. G. & Rodríguez-Navarro, A. B. 2008. Origin and expansion of foliated microstructure in pteriomorph bivalves. Biological Bulletin, 214, 153.

Evans, L. A. & Alvarez, R. 1999. Characterization of the calcium biomineral in the radular teeth of *Chiton pelliserpentis*. Journal of Biological Inorganic Chemistry, 4, 166.

Faivre, D. & Schüler, D. 2008. Magnetotactic bacteria and magnetosomes. Chemical Reviews, 108, 4875.

Falini, G., Albeck, S., Weiner, S. & Addadi, L. 1996. Control of aragonite or calcite polymorphism by mollusk shell macromolecules. Science, 271, 67.

Fan, C., Koeniger, P., Wang, H. & Frechen, M. 2011. Ligamental increments of the mid-Holocene Pacific oyster *Crassostrea gigas* are reliable independent proxies for seasonality in the western Bohai Sea, China. Palaeogeography, Palaeoclimatology, Palaeoecology, 299, 437.

Ferraro, J. R., Nakamoto, K. & Brown, C. W. 2003. *Introductory Raman Spectroscopy.* Elsevier Science.

Field, D. P. 1997. Recent advances in the application of orientation imaging. Ultramicroscopy, 67, 1.

Ford, H. L., Schellenberg, S. A., Becker, B. J., Deutschman, D. L., Dyck, K. A. & Koch, P. L. 2010. Evaluating the skeletal chemistry of *Mytilus californianus* as a temperature proxy: Effects of microenvironment and ontogeny. Paleoceanography, 25, 14.

Freer, A., Greenwood, D., Chung, P., Pannell, C. L. & Cusack, M. 2010. Aragonite prismatic nacre interface in freshwater mussels *Anodonta anatina* (Linnaeus, 1758) and *Anodonta cygnea* (L. 1758). Crystal Growth & Design, 10, 344.

Freitas, P. S., Clarke, L. J., Kennedy, H. A. & Richardson, C. A. 2008. Inter- and intra-specimen variability masks reliable temperature control on shell Mg/Ca ratios in laboratory- and field-cultured *Mytilus edulis* and *Pecten maximus* (bivalvia). Biogeosciences, 5, 1245.

Friedman, G. M. 1998. Rapidity of marine carbonate cementation - implications for carbonate diagenesis and sequence stratigraphy: perspective. Sedimentary Geology, 119, 1.

Friedman, I. & O'Neil, J. 1977. Compilation of stable isotope fractionation factors of geochemical interest. *Data of Geochemistry.* sixth edition ed. US Geological Survey.

Galtsoff, P. S. 1964. *The American oyster Crassostrea virginica* Gmelin. Government Printing office. Washington. D.C.

Gilbert, P. U. P. A., Abrecht, M. & Frazer, H. 2005. The organic-mineral interface in biominerals. Reviews in Mineralogy & Geochemistry 7, 59, 157.

Gillet, P., Biellmann, C., Reynard, B. & McMillan, P. 1993. Raman spectroscopic studies of carbonates.1. High pressure and high temperature behaviour of calcite, magnesite, dolomite and aragonite. Physics and Chemistry of Minerals, 20, 1.

Gillibrand, P. A. 2001. Calculating exchange times in a Scottish fjord using a two-dimensional, laterally-integrated numerical model. Estuarine, Coastal and Shelf Science, 53, 437.

Gillikin, D. P., De Ridder, F., Ulens, H., Elskens, M., Keppens, E., Baeyens, W. & Dehairs, F. 2005. Assessing the reproducibility and reliability of estuarine bivalve shells (*Saxidomus giganteus*) for sea surface temperature reconstruction: Implications for paleoclimate studies. Palaeogeography, Palaeoclimatology, Palaeoecology, 228, 70.

Gonzalez, L. A. & Lohmann, K. C. 1985. Carbon and oxygen isotopic composition of Holocene reefal carbonates. Geology, 13, 811.

Gray, J. E. 1833. Some observations on the economy of molluscous animals, and on the structure of their shells. Philosophical Transactions of the Royal Society of London, 123, 771.

Griesshaber, E., Schmahl, W., Neuser, R., Job, R., Bluem, M. & Brand, U. 2005. Microstructure of brachiopod shells - An inorganic/organic fibre composite with nanocrystalline protective layer. Mechanical Properties of Bioinspired and Biological Materials, 844, 99.

Griesshaber, E., Schmahl, W. W., Neuser, R., Pettke, T., Blum, M., Mutterlose, J. & Brand, U. 2007. Crystallographic texture and microstructure of terebratulide brachiopod shell calcite: An optimized materials design with hierarchical architecture. American Mineralogist, 92, 722.

Grossman, E. L. & Ku, T. L. 1986. Oxygen and carbon isotope fractionation in biogenic aragonite: Temperature effects. Chemical Geology: Isotope Geoscience section, 59, 59.

Gunasekaran, S. & Anbalagan, G. 2007. Spectroscopic characterization of natural calcite minerals. Spectrochimica Acta Part A: Molecular and Biomolecular Spectroscopy, 68, 656.

Harper, E. M. 1991. The role of predation in the evolution of cementation in bivalves. Palaeontology, 34, 455.

Harper, E. M. 1992. Postlarval cementation in the Ostreidae and its implications for other cementing Bivalvia. Journal of Molluscan Studies, 58, 37.

Harper, E. M. 1997. Attachment of mature oysters (*Saccostrea cucullata*) to natural substrata. Marine Biology, 127, 449.

Harper, E. M., Checa, A. G. & Rodríguez-Navarro, A. B. 2009. Organization and mode of secretion of the granular prismatic microstructure of *Entodesma navicula* (Bivalvia: Mollusca). Acta Zoologica, 90, 132.

Harper, E. M. & Morton, B. 2000. The biology and functional morphology of *Myochama anomioides* Stutchbury, 1830 (Bivalvia : Anomalodesmata : Pandoroidea), with reference to cementation. Journal of Molluscan Studies, 66, 403.

Hickson, J. A., Johnson, A. L. A., Heaton, T. H. E. & Balson, P. S. 1999. The shell of the Queen Scallop *Aequipecten opercularis* (L.) as a promising tool for palaeoenvironmental reconstruction: evidence and reasons for equilibrium stable-isotope incorporation. Palaeogeography, Palaeoclimatology, Palaeoecology, 154, 325.

Higuera-Ruiz, R. & Elorza, J. 2009. Biometric, microstructural, and high-resolution trace element studies in *Crassostrea gigas* of Cantabria (Bay of Biscay, Spain): Anthropogenic and seasonal influences. Estuarine Coastal and Shelf Science, 82, 201.

Higuera-Ruiz, R. & Elorza, J. 2011. Shell thickening and chambering in the oyster *Crassostrea gigas*: natural and anthropogenic influence of tributyltin contamination. Environmental Technology, 32, 583.

Hillgartner, H., Dupraz, C. & Hug, W. 2001. Microbially induced cementation of carbonate sands: are micritic meniscus cements good indicators of vadose diagenesis? Sedimentology, 48, 117.

Hou, W. T. & Feng, Q. L. 2006. Morphologies and growth model of biomimetic fabricated calcite crystals using amino acids and insoluble matrix membranes of *Mytilus edulis*. Crystal Growth and Design, 6, 1086.

Jackson, A. P., Vincent, J. F. V. & Turner, R. M. 1988. The mechanical design of nacre. Proceedings of the Royal Society of London Series B-Biological Sciences, 234, 415.

Jackson, J. B. C. 2001. What was natural in the coastal oceans? Proceedings of the National Academy of Sciences, 98, 5411.

Ji, B., Cusack, M., Freer, A., Dobson, P. S., Gadegaard, N. & Yin, H. 2010. Control of crystal polymorph in microfluidics using molluscan 28 kDa Ca2+-binding protein. Integrative Biology, 2, 528.

Jones, D. S. 1983. Sclerochronology: reading the record of the molluscan shell. American Scientist, 71, 384.

Kamenos, N. A., Cusack, M., Huthwelker, T., Lagarde, P. & Scheibling, R. E. 2009. Mg-lattice associations in red coralline algae. Geochimica et Cosmochimica Acta, 73, 1901.

Kamino, K. 2008. Underwater adhesive of marine organisms as the vital link between biological science and material science. Marine Biotechnology, 10, 111.

Kamino, K., Inoue, K., Maruyama, T., Takamatsu, N., Harayama, S. & Shizuri, Y. 2000. Barnacle cement proteins - Importance of disulfide bonds in their insolubility. Journal of Biological Chemistry, 275, 27360.

Kanazawa, T. & Sato, S. I. 2008. Environmental and physiological controls on shell microgrowth pattern of *Ruditapes philippinarum* (Bivalvia: Veneridae) from Japan. Journal of Molluscan Studies, 74, 89.

Kasemann, S. A., Schmidt, D. N., Bijma, J. & Foster, G. L. 2009. In situ boron isotope analysis in marine carbonates and its application for foraminifera and palaeo-pH. Chemical Geology, 260, 138.

Kauffman, E. G. 1971. Form, Function and Evolution. *In:* Moore, R. C. (ed.) *Treatise on Invertebrate Paleontology. Mollusca 6. Bivalvia. Part N, 1.* Geological Society of America, University of Kansas.

Kawaguchi, T. & Watabe, N. 1993. The organic matrices of the shell of the American oyster *Crassostrea virginica* Gmelin. Journal of Experimental Marine Biology and Ecology, 170, 11.

Kennedy, W. J., Taylor, J. D. & Hall, A. 1969. Environmental and biological controls on bivalve shell mineralogy Biological Reviews, 44, 499.

Key, D., Nunny, R., Davidson, P. & Leonard, M. 1976. Abnormal shell growth in the Pacific oyster (*Crassostrea gigas*): Some preliminary results from experiments undertaken in 1975. Journal of Paleontology. ICES Paper CM

Khandeparker, L. & Anil, A. C. 2007. Underwater adhesion: The barnacle way. International Journal of Adhesion and Adhesives, 27, 165.

Kim, S. T. & O'Neil, J. R. 1997. Equilibrium and nonequilibrium oxygen isotope effects in synthetic carbonates. Geochimica et Cosmochimica Acta, 61, 3461.

Kirby, M. X. 2000. Paleoecological differences between Tertiary and Quaternary *Crassostrea* oysters, as revealed by stable isotope sclerochronology. Palaios, 15, 132.

Kirby, M. X. 2001. Differences in growth rate and environment between Tertiary and Quaternary *Crassostrea* oysters. Paleobiology, 27, 84.

Kirby, M. X., Soniat, T. M. & Spero, H. J. 1998. Stable isotope sclerochronology of Pleistocene and Recent oyster shells (*Crassostrea virginica*). Palaios, 13, 560.

Klein, R. T., Lohmann, K. C. & Thayer, C. W. 1996. Bivalve skeletons record sea-surface temperature and δ18O via Mg/Ca and 18O/16O ratios. Geology, 24, 415.

Kobayashi, I. 2008. Scanning electron microscopic structure of the prismatic layer in the Bivalvia. Frontiers of Materials Science in China, 2, 246.

Kobayashi, I. & Samata, T. 2006. Bivalve shell structure and organic matrix. Materials Science and Engineering: C, 26, 692.

Komatsu, T., Chinzei, K., Zakhera, M. S. & Matsuoka, H. 2002. Jurassic soft-bottom oyster *Crassostrea* from Japan. Palaeontology, 45, 1037.

Korringa, P. 1951. On the nature and function of "chalky" deposits in the shell of *Ostrea edulis* Linnaeus. Proceedings of the California Academy of Science, 27, 133.

Krantz, D. E., Williams, D. F. & Jones, D. S. 1987. Ecological and paleoenvironmental information using stable isotope profiles from living and fossil molluscs. Palaeogeography, Palaeoclimatology, Palaeoecology, 58, 249.

Lartaud, F., De Rafelis, M., Ropert, M., Emmanuel, L., Geairon, P. & Renard, M. 2010a. Mn labelling of living oysters: Artificial and natural cathodoluminescence analyses as a tool for age and growth rate determination of *C. gigas* (Thunberg, 1793) shells. Aquaculture, 300, 206.

Lartaud, F., Emmanuel, L., De Rafelis, M., Pouvreau, S. & Renard, M. 2010b. Influence of food supply on the δ13C signature of mollusc shells: implications for palaeoenvironmental reconstitutions. Geo-Marine Letters, 30, 23.

Lartaud, F., Emmanuel, L., De Rafelis, M., Ropert, M., Labourdette, N., Richardson, C. A. & Renard, M. 2010c. A latitudinal gradient of seasonal temperature variation recorded in oyster shells from the coastal waters of France and the Netherlands. Facies, 56, 13.

Lassen, N. C. K. 1996. Automatic localisation of electron backscattering pattern bands from Hough transform. Materials Science and Technology, 12, 837.

Lecuyer, C., Reynard, B. & Martineaua, F. 2004. Stable isotope fractionation between mollusc shells and marine waters from Martinique Island. Chemical Geology, 213, 293.

Lee, M. R., Torney, C. & Owen, A. W. 2007. Magnesium-rich intralensar structures in schizochroal Trilobite eyes. Palaeontology, 50, 1031.

Lee, S. W. & Choi, C. S. 2007. The correlation between organic matrices and biominerals (myostracal prism and folia) of the adult oyster shell, *Crassostrea gigas*. Micron, 38, 58.

Lee, S. W., Jang, Y. N., Ryu, K. W., Chae, S. C., Lee, Y. H. & Jeon, C. W. 2011. Mechanical characteristics and morphological effect of complex crossed structure in biomaterials: Fracture mechanics and microstructure of chalky layer in oyster shell. Micron, 42, 60.

Lee, S. W., Kang, G., Lee, K. B. & Park, S. B. 2009. New approach for fabrication of folded-structure SiO2 using oyster shell. Micron, 40, 713.

Lee, S. W., Kim, G. H. & Choi, C. S. 2008a. Characteristic crystal orientation of folia in oyster shell, *Crassostrea gigas*. Materials Science and Engineering: C*,* 28**,** 258.

Lee, S. W., Kim, Y. M., Kim, R. H. & Choi, C. S. 2008b. Nano-structured biogenic calcite: A thermal and chemical approach to folia in oyster shell. Micron*,* 39**,** 380.

Lepzelter, C. G., Anderson, T. F. & Sandberg, P. A. 1983. Stable isotope variations in modern articulate brachiopods. American Association of Petroleum Geologists-Bulletin*,* 67**,** 500.

Lesin, P. A., Khalaman, V. V. & Flyachinskaya, L. P. 2006. Heterogeneity of the byssal threads in *Mytilus edulis* L. on different stages of attachment. Proceedings of the Zoological Institute: Russian Academy of Science*,* 310**,** 107.

Lewy, Z. 1972. Xenomorphic growth in ostreids. Lethaia*,* 5**,** 347.

Lleonart, M., Handlinger, J. & Powell, M. 2003. Spionid mudworm infestation of farmed abalone (*Haliotis spp*.). Aquaculture*,* 221**,** 85.

Loudon, R. 1963. Theory of the first-order Raman effect in crystals. Proceedings of the Royal Society of London Series a-Mathematical and Physical Sciences*,* 275**,** 218.

Lowenstam, H. A. 1954. Factors affecting the aragonite: calcite ratios in carbonate-secreting marine organisms. The Journal of Geology*,* 62**,** 284.

Lowenstam, H. A. 1961. Mineralogy, 18O/16O ratios, and strontium and magnesium contents of recent and fossil brachiopods and their bearing on the history of the oceans. Journal of Geology*,* 69**,** 241.

Lowenstam, H. A., Traub, W. & Weiner, S. 1984. Nautilus hard parts: A study of the mineral and organic constitutents. Paleobiology*,* 10**,** 268.

Lowenstam, H. A. & Weiner, S. 1989. *On Biomineralization.* Oxford University Press. New York.

Lutz, R. A. & Rhoads, D. C. 1980. Growth patterns within the molluscan shell: an overview. *In:* Rhoads, D. C. & Lutz, R. A. (eds.) *Skeletal growth and aquatic organisms.* Plenum Press, New York.

MacDonald, J., Freer, A. & Cusack, M. 2010. Alignment of crystallographic c-axis throughout the four distinct microstructural layers of the oyster *Crassostrea gigas*. Crystal Growth & Design*,* 10**,** 1243.

Mahway, E. 2005. *OIM User's Manual.* EDAX-TSL. New Jersey.

Margolis, S. V. & Carver, R. E. 1974. Microstructure of chalky deposits found in shells of the oyster *Crassostrea virginica*. Nautilus*,* 88**,** 62.

Margolis, S. V., Kroopnick, P. M., Goodney, D. E., Dudley, W. C. & Mahoney, M. E. 1975. Oxygen and carbon isotopes from calcareous nannofossils as paleoceanographic indicators. Science, 189, 555.

Margosian, A., Tan, F. C., Cai, D. & Mann, K. H. 1987. Seawater temperature records from stable isotopic profiles in the shell of *Modiolus modiolus*. Estuarine, Coastal and Shelf Science, 25, 81.

Marie, B., Zanella-Cléon, I., Guichard, N., Becchi, M. & Marin, F. 2011. Novel proteins from the calcifying shell matrix of the Pacific oyster *Crassostrea gigas*. Marine Biotechnology, 13, 1.

Marin, F. & Luquet, G. 2005. Molluscan biomineralization: The proteinaceous shell constituents of *Pinna nobilis* L. Materials Science and Engineering, 25, 105.

Marin, F., Luquet, G., Marie, B. & Medakovic, D. 2007. Molluscan shell proteins: Primary structure, origin, and evolution. *In:* Gerald, P. S. (ed.) *Current Topics in Developmental Biology.* Academic Press.

Marquez-Aliaga, A., Jimenez-Jimenez, A. P., Checa, A. G. & Hagdorn, H. 2005. Early oysters and their supposed Permian ancestors. Palaeogeography Palaeoclimatology Palaeoecology, 229, 127.

Mascolo, J. M. & Waite, J. H. 1986. Protein gradients in byssal threads of some marine bivalve molluscs. Journal of Experimental Zoology, 240, 1.

McConnaughey, T. 1989. δ13C and δ18O isotopic disequilibrium in biological carbonates: I. Patterns. Geochimica et Cosmochimica Acta, 53, 151.

McConnaughey, T. & Gillikin, D. 2008. Carbon isotopes in mollusk shell carbonates. Geo-Marine Letters, 28, 287.

McConnaughey, T. A., Burdett, J., Whelan, J. F. & Paull, C. K. 1997. Carbon isotopes in biological carbonates: Respiration and photosynthesis. Geochimica et Cosmochimica Acta, 61, 611.

McCrea, J. M. 1950. On the isotopic chemistry of carbonates and a paleotemperature scale. The Journal of Chemical Physics, 18, 849.

McKinney, C. R., McCrea, J. M., Epstein, S., Allen, H. A. & Urey, H. C. 1950. Improvements in mass spectrometers for the measurement of small differences in isotope abundance ratios. Reviews of Scientific Instruments, 21, 724.

Medcoff, J. C. 1944. Structure, deposition, and quality of oyster shell (*Ostrea edulis* Gmelin). Journal of the Fisheries Research Board Canada, 6c, 209.

Meldrum, F. C. & Hyde, S. T. 2001. Morphological influence of magnesium and organic additives on the precipitation of calcite. Journal of Crystal Growth, 231, 544.

Minchin, D. 2003. Monitoring of tributyltin contamination in six marine inlets using biological indicators. Marine Environment. Health Series 6, 1.

Mitchell, A. & Ferris, F. 2006. The influence of *Bacillus pasteurii* on the nucleation and growth of calcium carbonate. Geomicrobiology Journal, 23, 213.

Mitterer, R. M. 1971. Influence of natural organic matter on $CaCO_3$ precipitation *In:* Bricker, O. P. (ed.) *Carbonate Cements. Studies in Geology 19.* The John Hopkins Press.

Mook, W. G. 1971. Paleotemperatures and chlorinities from stable carbon and oxygen isotopes in shell carbonate. Palaeogeography, Palaeoclimatology, Palaeoecology, 9, 245.

Mook, W. G. & Vogel, J. C. 1968. Isotopic equilibrium between shells and their environment. Science, 159, 874.

Morse, J. W. & Mackenzie, F. T. 1990. *Geochemistry of Sedimentary Carbonates.* Elsevier. Amsterdam.

Morton, B. 1987. The mantle and radial mantle glands of *Entodesma saxicola* and *E. inflata* (Bivalvia: Anomalodesmata: Lyonsiidae). Journal of Molluscan Studies, 53, 139.

Morton, B. & Harper, E. M. 2001. Cementation in *Cleidothaerus albidus* (Lamarck, 1819) (Bivalvia: Anomalodesmata: Pandoroidea). Molluscan Research, 21, 1.

Mount, A. S., Wheeler, A. P., Paradkar, R. P. & Snider, D. 2004. Hemocyte-mediated shell mineralization in the Eastern Oyster. Science, 304, 297.

Nakahara, H. 1983. Calcification of gastropod nacre. *In:* Westbroek, P & De-Jong E.W. (eds.) *Biomineralization and biological metal accumulation*. Dordrecht, 225-230.

Nelson, T. C. 1924. The attachment of oyster larvae. The Biological Bulletin, 46, 143.

Neri, R., Schifano, G. & Papanicolaou, C. 1979. Effects of salinity on mineralogy and chemical composition of *Cerastoderma edul*e and *Monodonta articulata* shells. Marine Geology, 30, 233.

Nishikawa, S. & Kikuchi, S. 1928a. Diffraction of cathode rays by calcite. Nature, 122, 726.

Nishikawa, S. & Kikuchi, S. 1928b. Diffraction of cathode rays by mica. Nature, 121, 1019.

Nudelman, F., Chen, H., Goldberg, H., Weiner, S. & Addadi, L. 2007. Spiers Memorial Lecture. Lessons from biomineralization: comparing the growth strategies of mollusc shell prismatic and nacreous layers in *Atrina rigida*. Faraday Discussions, 136, 9.

O'Neil, J. R., Clayton, R. N. & Mayeda, T. K. 1969. Oxygen isotope fractionation in divalent metal carbonates. The Journal of Chemical Physics, 51, 5547.

Okoshi, K., Mori, K. & Nomura, T. 1987. Characteristics of shell chamber formation between the 2 local races in the japanese oyster *Crassostrea gigas*. Aquaculture, 67, 313.

Okumura, T., Suzuki, M., Nagasawa, H. & Kogure, T. 2010. Characteristics of biogenic calcite in the prismatic layer of a pearl oyster, *Pinctada fucata*. Micron, 41, 821.

Orton, J. H., Amirthalingam, C. & Bull, H. O. 1927. Notes on shell-depositions in oysters: Note on the chemical composition of ?chalky? deposits in shells of *O. edulis*. Journal of the Marine Biological Association of the UK (New Series), 14, 935.

Owen, R., Kennedy, H. & Richardson, C. 2002. Isotopic partitioning between scallop shell calcite and seawater: effect of shell growth rate. Geochimica et Cosmochimica Acta, 66, 1727.

Palmer, R. E. & Carriker, M. R. 1979. Effects of cultural conditions on morphology of the shell of the oyster *Crassostrea virginica*. Proceedings National Shellfisheries Association, 69, 58.

Parkinson, D., Curry, G. B., Cusack, M. & Fallick, A. E. 2005. Shell structure, patterns and trends of oxygen and carbon stable isotopes in modern brachiopod shells. Chemical Geology, 219, 193.

Pearce, T. & LaBarbera, M. 2009. A comparative study of the mechanical properties of Mytilid byssal threads. Journal of Experimental Biology, 212, 1442.

Pérez-Huerta, A. & Cusack, M. 2009. Optimizing electron backscatter diffraction of carbonate biominerals-resin type and carbon coating. Microscopy and Microanalysis, 15, 197.

Pérez-Huerta, A., Cusack, M. & Zhu, W. 2008a. Assessment of crystallographic influence on material properties of calcite brachiopods. Mineralogical Magazine, 72, 563.

Pérez-Huerta, A., England, J. & Cusack, M. 2008b. Crystallography of craniid brachiopods by electron backscatter diffraction (EBSD). Transactions of the Royal Society of Edinburgh Earth and Environmental Science, 98, 437.

Perez, F. R. & Martinez-Frias, J. 2003. Identification of calcite grains in the Vaca Muerta mesosiderite by Raman spectroscopy. Journal of Raman Spectroscopy, 34, 367.

Pokroy, B., Fieramosca, J. S., Von Dreele, R. B., Fitch, A. N., Caspi, E. N. & Zolotoyabko, E. 2007. Atomic structure of biogenic aragonite. Chemistry of Materials, 19, 3244.

Politi, Y., Mahamid, J., Goldberg, H., Weiner, S. & Addadi, L. 2007. Asprich mollusk shell protein: in vitro experiments aimed at elucidating function in CaCO3 crystallization. CrystEngComm, 9, 1171.

Pope, M. C., Grotzinger, J. P. & Schreiber, B. C. 2000. Evaporitic subtidal stromatolites produced by in situ precipitation: textures, facies associations, and temporal significance. Journal of Sedimentary Research, 70, 1139.

Popp, B. N., Anderson, T. F. & Sandberg, P. A. 1986. Brachiopods as indicators of original isotopic compositions in some Paleozoic limestones. Geological Society of America Bulletin, 97, 1262.

Prezant, R. 1979. The structure and function of the radial mantle glands of *Lyonsia hyaline* (Bivalvia: Anomalodesmata). Journal of Zoology, 187, 505.

Price, H. A. 1980. Seasonal variation in the strength of byssal attachment of the common mussel *Mytilus edulis* L. Journal of the Marine Biological Association of the United Kingdom, 60, 1035.

Prior, D. J., Boyle, A. P., Brenker, F., Cheadle, M. C., Day, A., Lopez, G., Peruzzo, L., Potts, G. J., Reddy, S., Spiess, R., Timms, N. E., Trimby, P., Wheeler, J. & Zetterstrom, L. 1999. The application of electron backscatter diffraction and orientation contrast imaging in the SEM to textural problems in rocks. American Mineralogist, 84, 1741.

Putten, E. V., Dehairs, F., Keppens, E. & Baeyens, W. 2000. High resolution distribution of trace elements in the calcite shell layer of modern *Mytilus edulis*: environmental and biological controls. Geochimica et Cosmochimica Acta, 64, 997.

Qian, C., Wang, R., Cheng, L. & Wang, J. 2010. Theory of microbial carbonate precipitation and its application in restoration of cement-based materials defects. Chinese Journal of Chemistry, 28, 847.

Rahimpour-Bonab, H., Bone, Y. & Moussavi-Harami, R. 1997. Stable isotope aspects of modern molluscs, brachiopods, and marine cements from cool-water carbonates, Lacepede Shelf, South Australia. Geochimica et Cosmochimica Acta, 61, 207.

Raman, C. V. 1928. A change of wave-length in light scattering. Nature, 121, 619.

Raman, C. V. & Krishnan, K. S. 1928. A new type of secondary radiation. Nature, 121, 501.

Riascos, J. M., Heilmayer, O., Oliva, M. E., Laudien, J. & Arntz, W. E. 2008. Infestation of the surf clam *Mesodesma donacium* by the spionid polychaete *Polydora bioccipitalis*. Journal of Sea Research, 59, 217.

Riera, P. & Richard, P. 1997. Temporal variation of δ13C in particulate organic matter and oyster *Crassostrea gigas* in Marennes-Oleron Bay (France): effect of freshwater inflow. Marine Ecology Progress Series, 147, 105.

Rodriguez-Navarro, C., Rodriguez-Gallego, M., Ben Chekroun, K. & Gonzalez-Muñoz, M. T. 2003. Conservation of ornamental stone by *Myxococcus xanthus*-induced carbonate biomineralization. Applied Environmental Microbiology*,* 69**,** 2182.

Romanek, C. S., Grossman, E. L. & Morse, J. W. 1992. Carbon isotope fractionation in synthetic aragonite and calcite: Effects of temperature and precipitation rates. Geochimica et Cosmochimica Acta*,* 56**,** 419.

Royer, J., Ropert, M., Mathieu, M. & Costil, K. 2006. Presence of spionid worms and other epibionts in Pacific oysters (*Crassostrea gigas*) cultured in Normandy, France. Aquaculture*,* 253**,** 461.

Ruddy, G. M., Feng, S. Y. & Campbell, G. S. 1975. The effect of prolonged exposure to elevated temperatures on the biochemical constituents, gonadal development and shell deposition of the American oyster, *Crassostrea virginica*. Comparative Biochemistry and Physiology Part B: Comparative Biochemistry*,* 51**,** 157.

Runnegar, B. 1984. Crystallography of the foliated calcite shell layers of bivalve molluscs. Alcheringa: An Australasian Journal of Palaeontology*,* 8**,** 273.

Samata, T., Ikeda, D., Kajikawa, A., Sato, H., Nogawa, C., Yamada, D., Yamazaki, R. & Akiyama, T. 2008. A novel phosphorylated glycoprotein in the shell matrix of the oyster *Crassostrea nippona*. FEBS Journal*,* 275**,** 2977.

Schiaparelli, S., Guidetti, P. & Cattaneo-Vietti, R. 2003. Can mineralogical features affect the distribution patterns of sessile gastropods? The Vermetidae case in the Mediterranean Sea. Journal of the Marine Biological Association of the United Kingdom*,* 83**,** 1267.

Schmahl, W. W., Griesshaber, E., Neuser, R., Lenze, A., Job, R. & Brand, U. 2004. The microstructure of the fibrous layer of terebratulide brachiopod shell calcite. European Journal of Mineralogy*,* 16**,** 693.

Schöne, B. R. 2008. The curse of physiology—challenges and opportunities in the interpretation of geochemical data from mollusk shells. Geo-Marine Letters*,* 28**,** 269.

Schöne, B. R., Dunca, E., Fiebig, J. & Pfeiffer, M. 2005. Mutvei's solution: An ideal agent for resolving microgrowth structures of biogenic carbonates. Palaeogeography Palaeoclimatology Palaeoecology*,* 228**,** 149.

Schöne, B. R., Tanabe, K., Dettman, D. L. & Sato, S. 2003. Environmental controls on shell growth rates and $\delta^{18}O$ of the shallow-marine bivalve mollusk *Phacosoma japonicum* in Japan. Marine Biology*,* 142**,** 473.

Schwarzer, R. A. 1997. Automated crystal lattice orientation mapping using a computer-controlled SEM. Micron*,* 28**,** 249.

Sharp, Z. 2006. *Principles of Stable Isotope Geochemistry.* Prentice Hall.

Sheldon, J. & Alber, M. 2006. The calculation of estuarine turnover times using freshwater fraction and tidal prism models: A critical evaluation. Estuaries and Coasts*,* 29**,** 133.

Shengrong, L., Fengqin, D., Lina, Y., Ye, C., Junyan, L., Yonghua, G., Liangfeng, Y. & Jinggui, T. 2011. The genetic mineralogical characteristics of fish otoliths and their environmental typomorphism. African Journal of Biotechnology*,* 10**,** 4405.

Simkiss, K. & Wilbur, K. M. 1989. *Biomineralization: Cell Biology and Mineral Deposition.* San Diego Academic Press.

Smith, A. M. 2002. The structure and function of adhesive gels from invertebrates. Integrative and Comparative Biology*,* 42**,** 1164.

Spero, H. J. & Lea, D. W. 1993. Intraspecific stable isotope variability in the planktonic foraminifera *Globigerinoides sacculifer*: Results from laboratory experiments. Marine Micropaleontology*,* 22**,** 221.

Stanley, S. M. 1972. Functional morphology and evolution of byssally attached bivalve mollusks. Journal of Paleontology*,* 46**,** 165.

Stenzel, H. B. 1971. Oysters. *In:* Moore, R. (ed.) *Treatise of Invertebrate Paleontology.Part N. Mollusca 6. Bivalvia.* Geological Association of America, University of Kansas.

Stirling, H. P. & Okumus, I. 1995. Growth and production of mussels (*Mytilus edulis L*.) suspended at salmon cages and shellfish farms in two Scottish sea lochs. Aquaculture*,* 134**,** 193.

Surge, D. & Lohmann, K. C. 2008. Evaluating Mg/Ca ratios as a temperature proxy in the estuarine oyster, *Crassostrea virginica*. Journal of Geophysical Research*,* 113**,** G02001.

Surge, D., Lohmann, K. C. & Dettman, D. L. 2001. Controls on isotopic chemistry of the American oyster, *Crassostrea virginica*: implications for growth patterns. Palaeogeography, Palaeoclimatology, Palaeoecology*,* 172**,** 283.

Surge, D., Lohmann, K. C. & Goodfriend, G. A. 2003. Reconstructing estuarine conditions: Oyster shells as recorders of environmental change, Southwest Florida. Estuarine, Coastal and Shelf Science*,* 57**,** 737.

Suzuki, M., Saruwatari, K., Kogure, T., Yamamoto, Y., Nishimura, T., Kato, T. & Nagasawa, H. 2009. An acidic matrix protein, Pif, is a key macromolecule for nacre formation. Science*,* 325**,** 1388.

Tarutani, T., Clayton, R. N. & Mayeda, T. K. 1969. The effect of polymorphism and magnesium substitution on oxygen isotope fractionation between calcium carbonate and water. Geochimica et Cosmochimica Acta*,* 33**,** 987.

Taylor, J. D., Kennedy, W. J. & Hall, A. 1969. *The shell structure and mineralogy of the Bivalvia.* Bulletin of the British Museum (Natural History). London.

Taylor, J. D. & Layman, M. 1972. The mechanical properties of bivalve mollusc shell structures. Palaeontology*,* 15**,** 73.

Tett, P. & Wallis, A. 1978. The general annual cycle of chlorophyll standing crop in Loch Crenan. Journal of Ecology*,* 66**,** 227.

Todd, A. J. 1993. The bivalve shell as a preservation trap, as illustrated by the Late Jurassic gryphaeid, *Deltoideum delta* (Smith). Scripta Geologica, Special. Issue 2*,* 2**,** 417.

Troost, K. 2010. Causes and effects of a highly successful marine invasion: Case-study of the introduced Pacific oyster *Crassostrea gigas* in continental NW European estuaries. Journal of Sea Research*,* 64**,** 145.

Tucker, M. E. & Wright, V. P. 1990. *Carbonate Sedimentology.* Blackwell Scientific Publications.

Ullmann, C. V., Wiechert, U. & Korte, C. 2010. Oxygen isotope fluctuations in a modern North Sea oyster (*Crassostrea gigas*) compared with annual variations in seawater temperature: Implications for palaeoclimate studies. Chemical Geology*,* 277**,** 160.

Urey, H. C. 1948. Oxygen isotopes in nature and in the laboratory. Science*,* 108**,** 489.

Urmos, J., Sharma, S. K. & Mackenzie, F. T. 1991. Characterisation of some biogenic carbonates with Raman spectroscopy. American Mineralogist*,* 76**,** 641.

Venables, J. A. & Harland, C. J. 1973. Electron backscattering patterns - New technique for obtaining crystallographic information in scanning electron microscope. Philosophical Magazine*,* 27**,** 1193.

Vermeij, G. J. 1977. The Mesozoic marine revolution evidence from snails, predators and grazers. Paleobiology*,* 3**,** 245.

Waite, J. H. 1983. Adhesion in bysally attached bivalves. Biological Reviews*,* 58**,** 209.

Waite, J. H. 2002. Adhesion à la Moule. Integrative and Comparative Biology*,* 42**,** 1172.

Wang, H., Keppens, E., Nielsen, P. & Van Riet, A. 1995. Oxygen and carbon isotope study of the Holocene oyster reefs and paleoenvironmental reconstruction on the northwest coast of Bohai Bay, China. Marine Geology*,* 124**,** 289.

Wang, H., Zeng, C., Liu, Q., Liu, D., Qiu, X. & Gong, L. Bacterially induced calcium carbonate precipitation and its implications for microbialite formation. 3rd International Palaeontological Congress, 28 June-3 July 2010 London. 402.

Watabe, N. 1965. Studies on shell formation: XI. Crystal-matrix relationships in the inner layers of mollusk shells. Journal of Ultrastructure Research, 12, 351.

Watabe, N. & Wilbur, K. M. 1961. Studies on shell formation; IX. An electron microscope study of crystal layer formation in the oyster. Journal of Cell Biology, 9, 761.

Webb, G. W., Jell, J. S. & Baker, J. C. 1999. Cryptic intertidal microbialites in beachrock, Heron Island, Great Barrier Reef: implications for the origin of microcrystalline beachrock cement. Sedimentary Geology, 126, 317.

Weigemann, M. 2004. Adhesion in bluse mussels (*Mytilus edulis*) and barnacles (genus *Balanus*): Mechanisms and technical applications. Aquatic Sciences, 67, 166.

Weiner, S., Addadi, L. & Wagner, H. D. 2000. Materials design in biology. Materials Science and Engineering, 11, 1.

Weiner, S. & Hood, L. 1975. Soluble protein of the organic matrix of mollusk shells: A potential template for shell formation. Science, 190, 987.

Weiner, S. & Traub, W. 1984. Macromolecules in mollusk shells and their functions in biomineralisation. Philosophical Transactions of the Royal Society of London Series B-Biological Sciences, 304, 425.

Wheeler, A. P., Rusenko, K. W., Swift, D. M. & Sikes, C. S. 1988. Regulation of in vitro and in vivo CaCO3 crystallization by fractions of oyster shell organic matrix. Marine Biology, 98, 71.

Williams, D. F., Arthur, M. A., Jones, D. S. & Healy-Williams, N. 1982. Seasonality and mean annual sea surface temperatures from isotopic and sclerochronological records. Nature, 296, 432.

Wise, S. W. & Hay, W. W. 1968. Scanning electron microscopy of molluscan shell ultrastructures.2. Observations of growth surfaces. Transactions of the American Microscopical Society, 87, 419.

Wisshak, M., Correa, M. L., Gofas, S., Salas, C., Taviani, M., Jakobsen, J. & Freiwald, A. 2009. Shell architecture, element composition, and stable isotope signature of the giant deep-sea oyster *Neopycnodonte zibrowii* sp n. from the NE Atlantic. Deep-Sea Research Part I Oceanographic Research Papers, 56, 374.

Wright, S. & Adams, B. 1992. Automatic-analysis of electron backscatter diffraction patterns. Metallurgical Transactions a Physical Metallurgy and Materials Science, 23, 759.

Yamaguchi, K. 1993. Shell structure and behaviour related to cementation in oysters. Marine Biology, 118, 89.

Yamaguchi, K. 1998. Cementation vs mobility: Development of a cemented byssus and flexible mobility in *Anomia chinensis*. Marine Biology, 132, 651.

Yonge, C. M. 1960. *Oysters.* Collins. London.

Yonge, C. M. 1962. On the primitive significance of the byssus in the Bivalvia and its effects in evolution. Journal of the Marine Biological Association of the United Kingdom, 42, 113.

Yonge, C. M. 1979. Cementation in bivalves. *In:* Van Der Spoel, S., Van Bruggen, C. & Lever, J. (eds.) *Pathways in malacology.* Scheltema & Holkema, Utrecht.

Yoon, Y., Mount, A. S., Hansen, K. M. & Hansen, D. C. 2011. Electrochemical characterization of a bioceramic material: The shell of the Eastern oyster *Crassostrea virginica*. Bioelectrochemistry, 81, 91.

Young, G. A. 1985. Byssus-thread formation by the mussel *Mytilus edulis*: effects of environmental factors. Marine Ecology-Progress Series, 21, 261.

Zeebe, R. E. 1999. An explanation of the effect of seawater carbonate concentration on foraminiferal oxygen isotopes. Geochimica et Cosmochimica Acta, 63, 2001.

Zhang, C. & Zhang, R. 2006. Matrix proteins in the outer shells of molluscs. Marine Biotechnology, 8, 572.

Zottoli, R. A. & Carriker, M. R. 1974. Burrow morphology, tube formation, and microarchitecture of shell dissolution by the spionid polychaete *Polydora websteri*. Marine Biology, 27, 307.

Peer reviewed publications from this thesis

1. Alignment of crystallographic c-axis throughout the four distinct microstructural layers of the oyster *Crassostrea gigas*

2. Attachment of oysters to natural substrata by biologically induced marine carbonate cement